UNIVERSIDAD COMPLUTENSE DE MADRID

FACULTAD DE CIENCIAS FÍSICAS

STUDY OF THE PRODUCTION OF THE Σb(*)± WITH THE CDF DETECTOR AT THE TEVATRON.

MEMORIA PARA OPTAR AL GRADO DE DOCTOR

PRESENTADA POR

Constantino Calancha Paredes

Bajo la dirección del doctor

Juan Pablo Fernández Ramos

Madrid, 2011

ISBN: 978-84-694-5894-5

Study of the production of the $\Sigma_b^{(*)\pm}$ with the CDF detector at the Tevatron

Estudio de la producción del barión $\Sigma_b^{(*)\pm}$ con el detector CDF en el Tevatron

CIEMAT
and
Departamento de Física Teórica I
(Universidad Complutense de Madrid)

PhD Dissertation

Constantino Calancha Paredes

to apply for the degree of Doctor of Philosophy in Physics

Supervised by

Dr. Juan Pablo Fernández Ramos

January 2011

Dr. Juan Pablo Fernández Ramos, investigador titular del Departamenteo de Investigación Básica, del Centro de Investigaciones Energéticas, Medioambientales y Tecnológicas (CIEMAT),

Certifica:

Que la presente memoria: **" Study of the production of the $\Sigma_b^{(*)\pm}$ with the CDF detector at the Tevatron"**, ha sido realizada bajo mi dirección en el Departamento de Física Teórica I de la Facultad de Ciencias Físicas de la Universidad Complutense de Madrid por *Constantino Calancha Paredes*, para optar al grado de Doctor en Ciencias Físicas.

Y para que así conste, en cumplimiento de la legislación vigente, presento ante la Universidad Complutense de Madrid esta memoria, formando el presente certificado:

Madrid, a 29 de octubre de 2010

Acknowledgements

I owe a debt of gratitude to my advisor, Dr. Juan Pablo Fernandez Ramos. His supervision made it possible for me to finish a wonderful analysis while successfully navigating the procedures and politics of a large collaboration. I always appreciate his enthusiasm and excitement over the amazing opportunities we have in the present day for new discoveries.

I would also like to thank the rest of the CIEMAT. In particular, I appreciate the advice and guidance of Dr. Oscar Gonzalez Lopez. His deep knowledge in high energy physics was a great inspiration to me during these years; and not only this, I also thank his support selflessly to any unespected situation that I found during my stay at Fermilab.

And last but not least, no exaggeration to say that this thesis would not have been possible without the help of Dr. Igor V. Gorelov. I feel very fortunate to have had the opportunity to work with this great scientist. His huge experience in the study of resonances has been crucial to me, and also I took good note of his love for the work well done, self-critical spirit and his eagerness to always document the work clearly.

I don't want to forget the Fermilab staffs and the technical staffs of the participating institutions for their vital contributions doing possible accumulate the large data sample used in this thesis.

Contents

List of Figures

List of Tables

Chapter 1

Introduction

The composition of matter is a topic in which the man has been interested throughout History. Since the introduction of the atom by Democritus in the 5th century BC until the establishment of the Standard Model, our successful theory that contains our current knowledge on the matter and their interactions, it has come a long way trying to solve this fundamental question. The efforts of many of the greatest minds to perform crucial experiments and develop theoretical models have helped to get deeper insight into the origin of the matter.

Today we know that indivisible atoms postulated by Democritus are no longer true, and they are actually composed of a nucleus made of protons and neutrons (nucleons) with orbiting electrons through electromagnetic interactions. Also the nucleons are not fundamental particles but are composed of more fundamental ones called quarks.

According to the present state of our knowledge, matter is composed of two types of particles: quarks and leptons. Leptons are believed to be fundamental particles and can occur freely in nature. Quarks are also fundamental particles, and there are no free in nature, but are confined to form hadrons. The hadrons may consist of a quark and an antiquark (mesons) or three quarks or three antiquarks (baryons). These quarks and leptons interact through the exchange of particles called bosons. Figure 1.1 summary the elementary particles in the Standard Model.

Despite its enormous success we know that the Standard Model is incomplete. Some of the issues left unresolved by the Standard Model are the mechanism for electroweak symmetry breaking, the mass spectrum of the Standard Model or that the Universe is much more matter than antimatter. That means that it should exist a more general theory which include the Standard Model as a valid approximation for low energy. This more general theory must give answers to the previous unresolved questions.

Accumulate more experimental information is crucial to get a deeper understanding of the Standard Model and its limitations. In particular, it is very important the measurement of those observables which they are not able to be calculated from theory by perturbation theory.

Particle accelerators have played and play nowadays a major role for past and new physics discoverements and has been for many years the source of many precision mea-

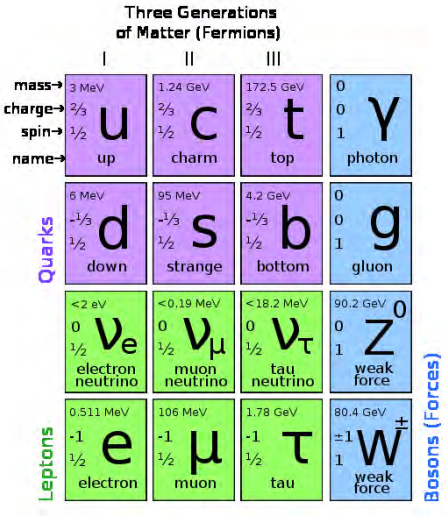

Figure 1.1: *Elementary particles in the Standard Model.*

surements. Unprecedent discoveries have been made and are yet to come. These measurements allow to select the models that best fit the results and also they can be used as input for those models to get further predictions.

Tevatron has been for many years the highest energy particle collider operational in the world. It is located in the high energy physics laboratory *Fermilab* in Batavia, in the State of Illinois (USA). Tevatron produce proton-antiproton collisions with an energy of 1.96 TeV at the center od the mass. This thesis is based on the data taken by the CDF II detector, one of the two multipurpose detectors located in the two interaction points at Tevatron.

In this thesis a precise measurement of the mass and width of four heavy baryon states are performed. These states are described together by the symbol $\Sigma_b^{(*)\pm}$. They are build by two light quarks and one heavy b quark as it is shown in Fig. 1.2.

Baryons containing one bottom quark and two light quarks are described by Heavy Quark Effective Theories (HQET) [1] (see [2] for a comprehensive review). In HQET, a bottom baryon consists of a b quark acting as a static source of the color field surrounded by a diquark system comprised of the two light quarks. In the lowest-lying $\Sigma_b^{(*)}$ states, the diquark system has strong isospin $I = 1$ and $J^P = 1^+$, which couple to the heavy quark spin and result in a doublet of baryons with $J^P = \frac{1}{2}^+$ (Σ_b) and $J^P = \frac{3}{2}^+$ (Σ_b^*). This doublet is degenerate for infinite b quark mass. As the b quark mass is finite, there is a hyperfine mass splitting between the $\frac{3}{2}^+$ and $\frac{1}{2}^+$ states. There is also an isospin mass splitting between the $\Sigma_b^{(*)-}$ and $\Sigma_b^{(*)+}$ states. Both isospin states decay into Λ_b^0 with the emision of a pion in a P-wave. Figure 1.3 shows the energy levels diagram for these states.

The $\Sigma_b^{(*)\pm}$ baryons were discovered on 2007 by the CDF Collaboration [3]. In that work the significance of the four states together was higher than the 5 σ, which traditionally mark the umbral of observation, but the individually significance of the observed signals

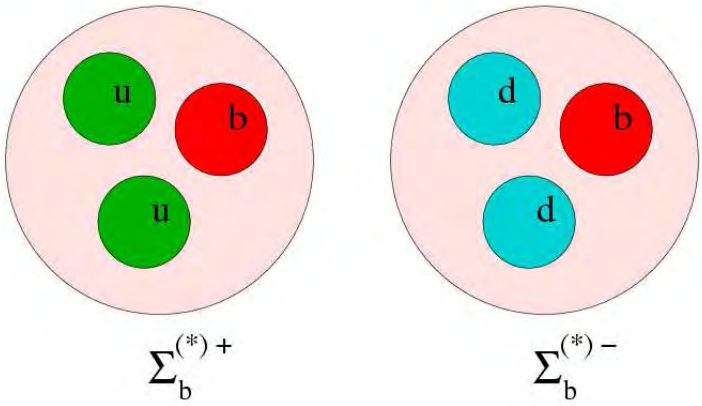

Figure 1.2: $\Sigma_b^{(*)\pm}$ *quark composition.*

was lower than that limit. No experimental measurement of the widths of those states has been performed yet. Table 1.1 summarizes the $\Sigma_b^{(*)}$ mass predictions from several theoretical approaches. The mass measurements from Ref. [3] are also shown.

In addition to improve the previous mass measurement, it is also interesting to measure the widths of $\Sigma_b^{(*)\pm}$, because it could help to discern between different models. In Tab.1.2 the width predictions from several models are shown.

The analysis described in this thesis is the first confirmation of the CDF II discovery [3] and the first measurement of the widths for these states. Also, the measurement of the masses of the four different $\Sigma_b^{(*)}$ hadrons (with no constraints or assumptions) has no precedent.

The basic theoretical concepts needed to fully understand the material exposed on this thesis are introduced in the Chapter 2. A description of the experimental apparatus is given in Chapter 3. The data samples collected by this experiment are described in Chapter 4. The analysis is detailed in Chapter 5. The systematic uncertainties are shown in Chapter 6. The results are presented in Chapter 7. Finally, the conclusions are summarized in Chapter 8.

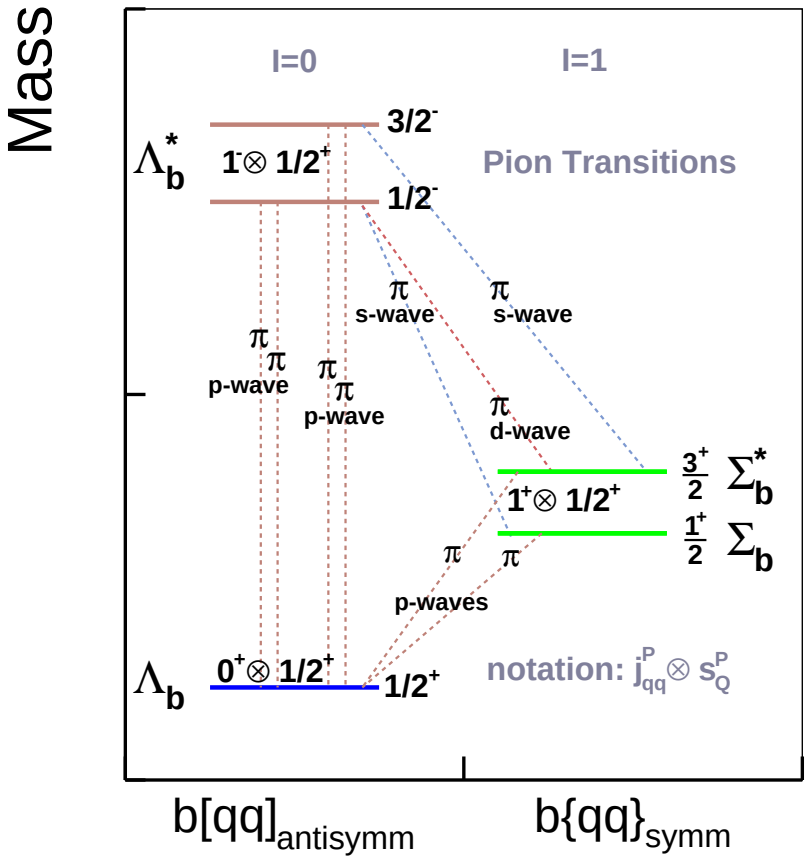

Figure 1.3: *Energy levels diagram for the* $\Sigma_b^{(*)}$ *states.*

Reference	$M(\Lambda_b^0)$, MeV/c^2	$M(\Sigma_b, \frac{1}{2}^+)$, MeV/$c^2$	Q, MeV/c^2	$M(\Sigma_b^*, \frac{3}{2}^+)$, MeV/$c^2$	Q^*, MeV/c^2
Albertus [4]	5643 ± 20	5851 ± 20	~ 68.5	5882 ± 20	~ 99.5
Faustov [5, 6]	5622	5805	43.4	5834	72.4
Capstick [7]	5585	5795	70.4	5805	80.4
Jenkins [8]	5623.0 ± 6.4, CDF I	5824.2 ± 9.0	~ 61.6	5840.0 ± 8.8	~ 77.4
Roncaglia [9]	5620 ± 40	5820 ± 40	~ 60.4	5850 ± 40	~ 90.4
Karliner [10]	5619.7, CDF II	5814	~ 54.7	5836	~ 76.7
Narodetskii [11]	5619.7, CDF II	5808, CDF II	~ 48.7	5833	73.7
Garcilazo [12]	5624	5789	24.4	5844	79.4
Zhang [13]	5690 ± 130	5730 ± 210	-100 ± 247	5810 ± 190	-20 ± 230
Liu [21]	5637^{+68}_{-56}	$5809 \pm^{+82}_{-76}$	~ 32.4	5835^{+82}_{-77}	~ 58.4
Mathur [22]	$5664 \pm^{+103}_{-108}$	–	$(\Sigma_b - \Lambda_b^0 - m_\pi)$	–	$(\Sigma_b^* - \Sigma_b)$
$\beta = 2.1$			1.4^{+38}_{-33}	–	22 ± 12
Mathur [22]	$5672 \pm^{+108}_{-110}$	–	53.4^{+37}_{-36}	–	$(\Sigma_b^* - \Sigma_b)$
$\beta = 2.3$				–	24^{+13}_{-12}
Lewis [14]	$5641 \pm^{+26}_{-39}$	$5795 \pm^{+23}_{-30}$	~ 14.4	$5842 \pm^{+33}_{-32}$	~ 61.4
$\beta = 1.9$					
$\Sigma_b^{(*)-}$ CDF II	5619.7 ± 1.5	$5815.2^{+2.0}_{-2.0}$	$55.9^{+1.0}_{-1.0}$	$5836.4^{+2.7}_{-2.6}$	$Q^{*\pm} - Q^{\pm} =$
$\Sigma_b^{(*)+}$ CDF II	5619.7 ± 1.5	$5807.8^{+2.6}_{-2.8}$	$48.5^{+2.0}_{-2.2}$	$5829.09^{+2.3}_{-2.5}$	$= 21.2^{+2.0}_{-1.9}$

Table 1.1: The mass predictions for $\Sigma_b^{(*)}$ states. The Q-value is defined as $Q = M(\Sigma_b^{(*)}) - M(\Lambda_b^0) - m(\pi^\pm)_{PDG}$. The results from CDF discovery publication are shown at the bottom lines.

Reference	$\Gamma(\Sigma_b, \frac{1}{2}^+)$ MeV/c^2	$\Gamma(\Sigma_b, \frac{3}{2}^+)$ MeV/c^2
Körner et al.	≈ 8	≈ 15
Guo et al.	$(6.73 - 13.45)$	$(10.00 - 17.74)$
C.-W. Hwang,$\Sigma_b^{(*)+}$	4.35	8.50
C.-W. Hwang,$\Sigma_b^{(*)-}$	5.77	10.44

Table 1.2: *Several predictions for the widths of $\Sigma_b^{(*)\pm}$. Note that they are models which predict same width for different states within a isotriplet, but also exist one prediction which assign different widths for those different isospin partners.*

Chapter 2

Theoretical Overview

In this chapter we present the basic theoretical concepts to fully understand this thesis. We begin with a short overview over the Standard Model of Particle Physics. After, we briefly describe the Quantum Chromodynamics and the different theoretical approaches describing heavy hadrons.

2.1 The Standard Model of Particle Physics

The Standard Model of Particle Physics is the most succesfull theory to date for describing elementary particles. It describes the interactions between the fundamental particles in terms of three kind of forces: the electromagnetic, the weak and the strong interaction. They are introduced as coming from fundamental gauge symmetries $U(1)_Y \times SU(2)_L \times SU(3)_C$ based on the solid grounds of Quantum Field Theory. It developed through the 1960's and 1970's by a fruitfull combination of experimental and theoretical discoveries.

Within the Standard Model there are two different types of fundamental constituents of Nature: bosons and fermions. Bosons are those particles responsible for carrying the interactions among the fermions, which constitute matter. Fermions are divided into six quarks and six leptons, forming a three-folded structure. All these fermions and bosons have an antimatter partner.

2.1.1 The Fundamental Particles

For each fundamental particle, there exists an antiparticle with the same mass but opposite quantum numbers[1]. In Tab. 2.1 are shown the three generations of fundamental fermions.

The leptons all carry integer values of electric charge, and are arranged in three generations (electron, muon, and tau). The muons (μ) and taus (τ) are heavier versions of the electron (e); they have the same spin and electric charge. The neutral leptons are called neutrinos, and there is one associated with each lepton generation. In the Standard Model, lepton flavour is conserved by all interactions. The leptons are assigned a lepton

[1] Antiparticles are generally denoted by putting a line over the particle symbol

Quarks	Symbol	Charge	Mass(MeV/c^2)
up	u	$+\frac{2}{3}$	$1.5-3$
down	d	$-\frac{1}{3}$	$3-7$
charm	c	$+\frac{2}{3}$	$(1.25\pm0.09)\times10^3$
strange	s	$-\frac{1}{3}$	95 ± 25
top	t	$+\frac{2}{3}$	$(174.2\pm3.3)\times10^3$
bottom	b	$-\frac{1}{3}$	$(4.20\pm0.07)\times10^3$
Leptons	**Symbol**	**Charge**	**Mass(MeV/c^2)**
electron	e	-1	0.511
electron neutrino	ν_e	0	$< 2eV/c^2$
muon	μ	-1	105.7
muon neutrino	ν_μ	0	< 0.19
tau	τ	-1	1776.90 ± 0.20
tau neutrino	ν_τ	0	< 18.2

Table 2.1: *The fundamental fermions. Charges are in units of the absolute electron charge. All masses are taken from Ref. [17]. The electron and muon masses are shown without errors because the errors are so small. 1* MeV/c^2 $= 1.783\times10^{-30}$ *kg.*

number of $+1$, while the antimatter leptons have a lepton number of -1. At the end of the last century was observed that neutrinos can oscillate from one lepton flavour to another [16] so far this is the only observed violation of lepton number conservation.

The quarks all carry a fractional electric charge of either $+\frac{2}{3}$ or $-\frac{1}{3}$. As with leptons, the quarks may be arranged in three generations. The charm and top quarks are heavy versions of the up quark, while the strange and bottom quarks are heavy versions of the down quark. Although leptons can exist freely, quarks are confined in bound quark-antiquark states (mesons) or bound three quark states (baryons).

Amazingly, a simple classification scheme called quark model was developed which it was able to accommodate all the known hadrons, accounting for several of their observed properties like the spin, and even predict the existence of other not observed particles.

The original quark model is a generalization of the isospin $SU(2)$ symmetry between the u and d to a $SU(3)$ symmetry including the quark s. It is assumed that these three quarks lie in the fundamental representation, 3 of $SU(3)$. The antiquarks lie in the complex conjugate representation $\overline{3}$. Then the 9 mesons made out of a pair can be decomposed (following a known result of Group Theory) into the trivial representation, 1 and the adjoint 8 in accord with:

$$3\otimes\overline{3}=8\oplus1 \tag{2.1}$$

The baryons are built from those three quarks in a similar way:

$$3\otimes3\otimes3=10_S\oplus8_M\oplus8_M\oplus1_A \tag{2.2}$$

Meson	Quark Content	Mass(MeV/c^2)
$\pi^{\pm}$	$u\overline{d}$,$\overline{u}d$	139.57018 ± 0.00035
π^0	$(u\overline{u} - d\overline{d})/\sqrt{}(2)$	134.9766 ± 0.0006
$K^{\pm}$	$u\overline{s}$,$\overline{u}s$	493.677 ± 0.016
K^0, $\overline{K}^0$	$d\overline{s}$,$\overline{d}s$	497.648 ± 0.022
$D^{\pm}$	$c\overline{d}$, $\overline{c}d$	1869.3 ± 0.4
D^0, $\overline{D}^0$	$c\overline{u}$, $\overline{c}u$	1864.5 ± 0.4
J/ψ	$c\overline{c}$	3096.916 ± 0.011
$B^{\pm}$	$u\overline{b}$, $\overline{u}b$	5279.0 ± 0.5
B^0,$\overline{B}^0$	$d\overline{b}$, $\overline{d}b$	5279.4 ± 0.5
B_s^0, $\overline{B}_s$	$s\overline{b}$, $\overline{s}b$	5367.5 ± 1.8

Table 2.2: *Quark content and masses for several mesons. Masses are taken from Ref. [17].*

Baryon	Quark Content	Mass(MeV/c^2)
p	uud	938.27203 ± 0.00008
n	udd	939.56536 ± 0.00008
Σ^+, $\Sigma(1385)^+$	uus	1189.37 ± 0.07, 1382.8 ± 0.4
Σ_b^-, $\Sigma(1385)^-$	dds	1197.449 ± 0.030, 1387.2 ± 0.5
Σ_c, Σ_c^*	udc	2286.46 ± 0.14, 2595.4 ± 0.6
Σ_c^{++}	uuc	2454.02 ± 0.18
Σ_c^0	ddc	2453.76 ± 0.18
Λ_b^0	udb	5624 ± 9
Σ_b^+, Σ_b^{*+}	uub	5807.8 ± 2.7, 5829.0 ± 3.4
Σ_b^-, Σ_b^{*-}	ddb	5815.2 ± 2.0, 5836.4 ± 2.8

Table 2.3: *Quark content and masses for several baryons. Masses are taken from Ref. [17].*

where the subindex indicate the behaviour of the wave function under transformations in the flavour space: S if symmetric, A if antisymmetric and M if has mixed symmetry. Tables 2.2 and 2.3 show the quark content as predicted by the quark model, together with their experimental masses for several mesons and baryons.

Despite this great success, it was realized soon that the naive quark model is clearly unsatisfactory, and they would be something more. One way to realized that is considering the Δ^{++} baryon: this is a baryon compose of three u quarks with a spin $J = \frac{3}{2}$ in their ground state. Thus, in order to acommodate the observed Δ-particle properties, we are forced to combine three identical fermions u in a completely symmetric ground state uuu. Such state is of course forbidden by Fermi statistics.

There are more experimental facts which the quark model is unable to explain. We know that the qqq, $\overline{qqq}$, and $q\overline{q}$ reproduce the observed sequence of baryon, antibaryon, and meson states, but the quark model give not and answer why some quark configurations

Force	Mediator	J^P	Mass(GeV/c^2)	Realtive Strength
Strong Nuclear	Gluon (g)	1^-	0	1
Electromagnetic	Photon (γ)	1^-	$< 6 \times 10^{-17}$ eV/c^2	10^{-2}
Weak Nuclear	Charged: $W^{\pm}$	1^-	80.403 ± 0.029	10^{-7}
	Neutral: Z^0	1^+	91.1876 ± 0.0021	
Gravity	Graviton	2^+	unobserved	10^{-39}

Table 2.4: *The four forces in nature and their corresponding gauge bosons. The strength roughly gives the relative magnitudes of each force in the case where two protons are just in contact. Masses are taken from Ref. [17]. , where the gluon mass is a theoretical value.*

(qq, $\overline{qq}$, ...) are not observed in the Nature.

All these unconsistencies are solved introducing a new property or quantum number for quarks: the "color". We assume that this label can take three possible values: red (R), green (G) and blue (B). Now we made the assumption that all hadron states should be arranged in that way that the total wave function is "colorless" (or more precise, unchanged by rotations in R, G, B space). After introducing these new quantum number we can accommodate the Δ^{++} baryon with the Fermi statistics, because it is no longer true that the three u be equal because they are distinguisable by their color quantum number.

There is several ways to obtain colorless hadrons combining quarks and antiquarks:

- Equal mixture of red, green, and blue (RGB).
- Equal mixture of antired, antigreen, and antiblue ($\overline{RGB}$).
- Equal mixture of color and anticolor ($R\overline{R}, G\overline{G}, B\overline{B}$).

Now it is clear why the no observed quark configurations like qq or $\overline{qq}$ could not exist, because they are neccesarily colored.

2.1.2 Particle Interactions

In the Standard Model, interactions between the fundamental fermions are mediated by the exchange of the force mediators, also known as gauge bosons. There is a different gauge boson for each of the four forces in nature: the strong nuclear force, the weak nuclear force, electromagnetism, and gravity. The mediators and relative strengths of these forces are given in Tab. 2.4

Electromagnetic interactions are responsible for most interactions outside of the nucleous. Electromagnetism binds electrons to nuclei and is thus the basic of all chemistry. These interactions are mediated by a massless, spin-1 boson called the photon. Although the photon carries no electric charge, it couples to all particles with a non-zero electric

charge. Because the photon is massless, the electromagnetic force has an infinite range, although its strength drops off rapidly as $1/r^2$.

The strong nuclear force is responsible both for binding quarks together in hadrons and for binding protons and neutrons together in a nucleus. These interactions are mediated by massless, spin-1 bosons called gluons. The color charge carried by quarks may also change during a string interaction. Consequently, the gluons themselves must be "bicolored", meaning they carry one color and one anti-color charge. Since leptons do not have a color charge, they do not interact with gluons and thus do not feel the strong force. The interactions of colored particles can be modeled by requiring that the observable world be invariant under the $SU(3)$ group of local gauge transformations. The resultanting field theory is called quantum chromodynamics (QCD), and in terms of the $SU(3)$ symmetry there are eight gluons corresponding to each of the states in a color octet. Since the gluons are massless, the strong force would also be expected to have infinite range. However, due to the confinement of quarks and gluons to colorless hadron states, we observe the force to be of very short range, essentially the size of the nucleus.

The weak nuclear force is responsible for all interactions which change quark flavours, such as nuclear β-decay. All leptons and quarks feel the weak force, which is mediated by the massive, spin-1 intermediate vector bosons. The charged weak interactions are mediated by the W^+ and W^- bosons, which have a mass of ≈ 80 GeV/c^2. The neutral weak interactions are mediated by the Z^0 boson, with a mass of ≈ 91 GeV/c^2. Because these force carriers are so massive, the weak interaction has a range even less than the size of the nucleous.

Gravity, the weakest of the four forces, is the only force which is not included in the Standard Model of particle physics. Physicists are still searching for a satisfactory theory of gravity. Most models postulate the mediator of the gravitational force to be a massless, spin-2 boson called the graviton, but such a particle has yet to be observed.

The Standard Model provides no explanation for the existence of four separate forces, and physicists are searching for a "grand unifying theory" in which the four forces are different manifestations of one underlying force. This effort began in the early 18th century, when it was realized that electricity and magnetism were actually two aspects of a single force, now called electromagnetism. Einstein attempted but never succeeded in unifying gravity and electromagnetism into one single field theory. However, in the 1960's the physicists Glashow, Weinberg, and Salam developed a very successfull theory which joined the weak and electromagnetic forces (electroweak unification). The obvious next step is to combine the strong and electroweak forces. There are some promising early results, but this is still a work in progress.

2.2 Quantum Chromodynamics

Quantum chromodynamics (QCD) describes the interactions of colored objects, and in principle it can be used to calculate the properties of hadrons. However, QCD problems are notoriously difficult to solve analytically, as they consist of path integrals in a contin-

uum theory. The strong interaction constant α_s is not a constant; α_s actually decreases as the momentum transfer $|q^2|$ of an interaction increases. A higher $|q^2|$ occurs when the quarks are closer together. Consequently, the color force between two quarks is weak at short distances; this property is known as "asymptotic freedom". The color force then increases as the $|q^2|$ decreases, or as the quarks move farther apart. This property, known as "'confinement', is thought to be the reason why quarks are confined in hadrons.

For high $|q^2|$ interactions, the quarks and gluons involved behave as free particles. Because α_s is so small, it is possible to use a pertubative expansion in powers of α_s to solve QCD problems. This approach, known as perturbative QCD, has resulted in some of the most precise tests to date of QCD interactions at high energies. However, few tests exist of theories in regions of non-perturbative QCD. These non-perturbative QCD effects can obscure or confuse indirect searches of precision measurements in B decays, and it is important to understand their contributions as we continue the search for physics beyond the Standard Model.

The QCD confinement scale $\Lambda_{QCD} \approx 400$ MeV/c^2 is the typical energy at which QCD becomes non-perturbative. The description of quarks in a hadron is inherently a low energy interaction, where α_s is of order unity. In this case, we typically exploit some symmetry of QCD rather than attempting a dynamical calculation. There are several prominent methods for predicting QCD results at low $|q^2|$, including lattice QCD, $1/N_c$ expansions, and effective theories. Lattice QCD uses a discrete set of space-time points and heavy or light quark propagators to reduce continuum path integrals to numerical computations which can be performed on supercomputers. Such simulations are time-intensive, and each sample takes years to complete. However, the results can give insight into the non-perturbative regime of QCD. The $1/N_c$ expansion starts from the premise that the number of colors is infinite; even though QCD has only 3 colors, the number $1/N_c$ is treated as small enough to expand around. Effective theories also simplify QCD calculations by expanding around some parameter which is assumed to be either very small or infinite. For example, chiral perturbation theories assume the light quark masses are zero, while heavy quark effective theories assume an infinite mass for the heavy quarks. Heavy quark effective theories are used to explain the heavy hadron nomenclature and this approach is described in more detail in Section 2.2.1.

2.2.1 Heavy Quark Effective Theory

The QCD treatment of quark-quark interactions significantly simplifies if one of the participating quarks is much heavier than Λ_{QCD}. The momentum exchange between the heavy quark and the light quark is much less than the heavy quark mass m_Q if $m_Q \gg \Lambda_{QCD}$. In this case, the recoil of the heavy quark is negligible, and the heavy quark acts as a static source of electromagnetic and color (chromomagnetic) fields. In the limit of an infinite heavy quark mass, the interactions of the light quarks are independent of m_Q. With a finite heavy quark mass, this information allows corrections to the limit using a systematic expansion in powers of Λ_{QCD}/m_Q. Methods employing this formalism are known as Heavy Quark Effective Theories (HQET) [1].

The HQET approach is used to predict the spectroscopy of "heavy hadrons", hadrons containing one or more heavy quarks. For an infinite heavy quark mass, the light quark excitations alone determine the spectrum of the heavy hadrons. These solutions do not depend on the flavour of the heavy quark, so to the first order the spectrum of all heavy-light mesons is expected to be the same. The heavy quark still has a spin quantum number $S_Q = \frac{1}{2}$, which leads to a chromomagnetic moment

$$\mu_Q = \frac{g}{2m_Q} \tag{2.3}$$

As $m_Q \to \infty$, the chromomagnetic moment approaches zero, and the spin interaction between the light quarks and the heavy quark is suppresed. This leads to a doublet of hadrons with the same mass for each light quark excitation level, one state for each possible value of the heavy quark spin.

One example of the HQET approach is for the B meson, made of a b quark and a u or d quark. The b quark has a spin angular momentum $J_Q = \frac{1}{2}$, while the light quark has a total angular momentum

$$J_l = |L \pm \frac{1}{2}| \tag{2.4}$$

where L is the orbital angular momentum of the light quark. The resulting physical hadron state has a total angular momentum of

$$J = |J_l \pm \frac{1}{2}| \tag{2.5}$$

In the ground state of $L = 0$, $J_l = \frac{1}{2}$. In the limit $m_Q \to \infty$, the doublet states with $J = 0$ (B) and $J = 1$ (B^*) would be degenerate. When effects of the order $1/m_b$ are included, the chromomagnetic interactions split the states with different values of J. This splitting, called "hyperfine" in analogy with the hyperfine levels in atoms which arise from the weak nuclear magnetic moment, is proportional to the heavy quark chromomagnetic moment μ_Q. As predicted, the B^* state is slightly heavier than the B state, and decays to B via photon emission.

The HQET approach has been successfully applied to describe available experimental data on $Q\overline{q}$ mesons for the ground states and the lowest P-wave excitations in both the charm and b sectors.

2.2.2 $1/N_c$ Expansion of QCD

The $1/N_c$ expasion of QCD [18] is a valuable tool for studying the non-perturbative dynamics of the strong interactions. In the limit $N_c \to \infty$, the baryon sector of QCD has an exact contracted $SU(2N_F)$ spin-flavour-symmetry. For finite N_c, the contracted spin-flavour-symmetry is broken by effects suppressed by powers of $1/N_c$. The spin-flavour structure of the $1/N_c$ breaking terms is predicted at each order in the $1/N_c$ expansion. The spin-flavour structure of many baryon properties have been derived in a systematic expansion in $1/N_c$, and the results are in excellent agreement with experiment.

One important application of the baryon $1/N_c$ expansion is the prediction of masses [19, 20, 8]. By choosing appropiate linear combinations of the baryon masses, one can study coefficients of the baryon mass $1/N_c$ operator expansions with definite spin and flavour transformation properties. In this case of perturbative $SU(3)$ flavour-symmetry breaking, the $1/N_c$ analysis gives a hierarchy of baryon mass relations in powers of $1/N_c$ and the dimensionless $SU(3)$ breaking parameter $\epsilon \propto m_s/\Lambda_\chi$.

The $1/N_c$ expansion also has been used to obtain very accurate predictions for the charm and bottom baryon masses which have been confirmed by recent experiments.

2.3 Production of $b\bar{b}$ Pairs in a $p\bar{p}$ Collider

In high energy $p\bar{p}$ collisions, the strong coupling constant, α_s, becomes small enough for b quark production at sufficiently high momentum transfer that perturbative QCD is expected to provide reliable predictions.

That is the situation at the Tevatron, where protons and antiprotons collide with a center of mass energy of $\sqrt(s) = 1.96$ TeV.

Very rarely is the entire momentum of the proton and the antiproton involved in a collision. More commonly, only one parton from the proton and one from the antiproton will interact, via the exchange of virtual bosons. At Tevatron, the b quarks are produced mainly in $b\bar{b}$ pairs.

Figure 2.1 shows the lowest order mechanisms to produce $b\bar{b}$ pairs. Those processes correspond to $q\bar{q}$ annhiliation and gluon fusion. Due to the confinement of QCD, these $b\bar{b}$ pairs produced are combined into colorless hadrons. This is ussually achieved by the creation of additional $q\bar{q}$ pairs in a process called "fragmentation" or "hadronization". These fragmentation also happen for any other quarks or gluons being in the final state, so in practice, many other hadrons are produced in addition to the hadrons coming from the $b\bar{b}$ pair. This source of background coming from the fragmentation of those partons not involved in the creation of the $b\bar{b}$ pair is referred to as the "underlying event".

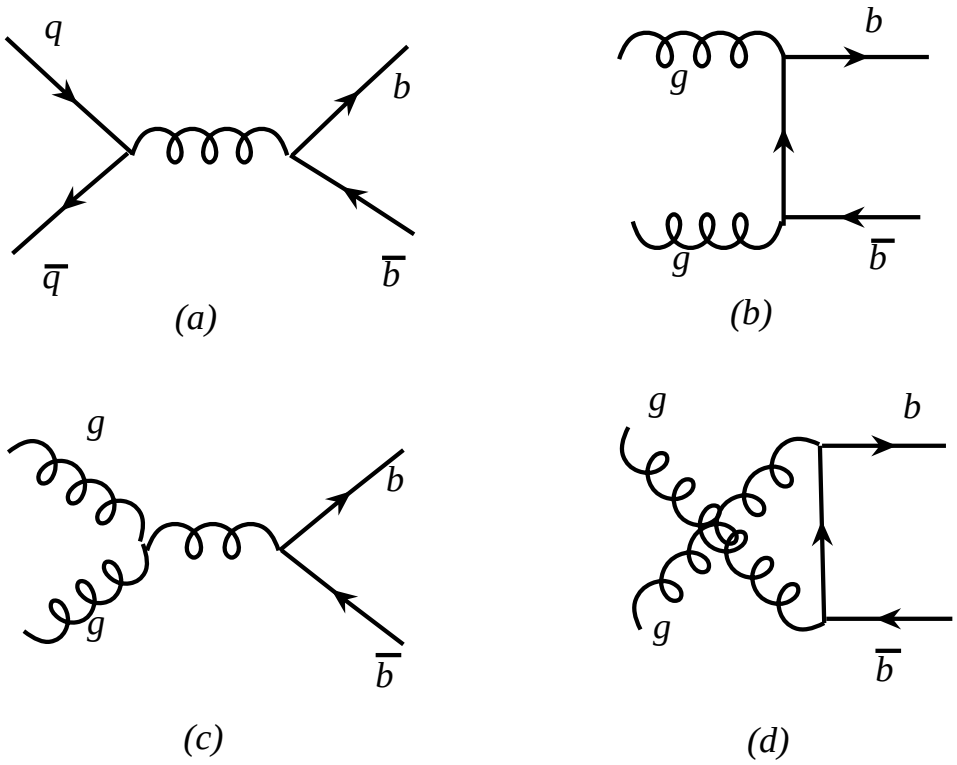

Figure 2.1: *$b\bar{b}$ production at Tevatron.*

Chapter 3

The CDF Experiment at the Tevatron Collider

The *Collider Detector at Fermilab*, or CDF, is a general purpose experiment for the study of $p\overline{p}$ collisions at the Tevatron, for many years the highest-energy particle collider operational in the world. Using the Tevatron accelerator, CDF discovered top-quark events in 1995.

To exploit this unique tool fully, and to meet the goals of the high energy physics research program through the 1990's and into the twenty-first century, a phased upgrade of the accelerator complexes and the detector has taken place. The upgrade is expected to give an opportunity not only to discover new physics but also to perform precision measurements. In this chapter, various complexes and functions of the Tevatron accelerator and CDF detector are briefly described. For a complete review see [23] and [24, 25].

3.1 The Particle Accelerator

The Tevatron [26] is located in the high energy physics laboratory *Fermilab*, (short name for the Fermi National Accelerator Laboratory) in Batavia, approximately 40 miles west of Chicago in the State of Illinois. In the Tevatron, it is possible to study the hard scattering events resulting from collisions between proton and antiprotons of nearly 1 TeV. The energy available in the center of mass on these collisions is 1.96 TeV.

The Tevatron ring has a 6.3 km perimeter and is located inside an underground tunnel. An aerial shot of Fermilab is shown in Fig. 3.1.

3.1.1 Accelerator chain

In order to reach the final colliding energy of 980 GeV, five systems are used: Cockcroft-Walton, Linac, Booster, Main Injector and Tevatron. The schematic view of the accelerator complex at Fermilab is illustrated in Figure 3.2. The accelerating process starts with electrical discharges in a hydrogen gas bottle, where H ions are produced. These H's are pulled out from the gas bottle by a Cockcroft-Walton which is a 750KV DC voltage

Figure 3.1: *Aerial shot of Fermilab. The CDF detector is located at one of the collision points, called B0, on the Tevatron Ring.*

source, and Hs get accelerated to 750 keV. In a second step, these ions enter a linear accelerator (Linac) 145 m long, where they reach the energy of 400 MeV. The Linac has two parts: a 116 MeV drift-tube linac operating at 201.25 MHz and a 400 MeV side-coupled cavity linac operating at 805 MHz [27]. The H's are accelerated through electromagnetic waves generated by a series of cavities in the Linac; as a result, the continuous beams are separated into several bunches. At the end of the Linac, the electrons from the H ions are stripped off by a thin carbon foil, and the resulting protons are passed into the Booster ring, which is a circular synchrotron ring with a 75 m radius. The protons are circulated until they acquire an energy of 8 GeV before being collected in bunches of 6×10^{10} particles each to be used in the Tevatron. The acceleration in the Booster is accomplished by a series of electromagnetic kicks applied by RF cavities: about 500 kV per turn. The next step is further acceleration in the Main Injector, where protons are accelerated from 8 GeV to 150 GeV for injection into the Tevatron or to 120 GeV for $\bar{p}$ production. The Main Injector is a proton synchrotron ring with a circumference of 3319.4 m which operates at 53 MHz. For the Tevatron Run I operation, the 8 GeV proton bunches were injected into the Main Ring synchrotron, where they were accelerated to 150 GeV. In the Run II phase, the existing Main Ring has been replaced by a new accelerator, the Main Injector, for the purpose of reducing the inefficiency of the antiproton production. As the result of this, more than a factor of 2 increases in the luminosity are expected. The 120 GeV proton bunches are finally injected into the evacuated beam pipe of the Tevatron ring and brought to an energy of 980 GeV.

Antiprotons production

Antiprotons are created at a target station. On its way towards the Tevatron, a fraction of the proton beam is extracted to bombard a nickel target. The 120 GeV protons extracted from the Main Injector hit the target and produce antiprotons over large spread angles and energies on the forward direction. On average, 20 antiprotons per million protons are produced, with a mean kinetic energy of 8 GeV. These antiprotons then undergo a process called stochastic cooling to reduce random motion [28]. A cylindrical lithium lens is used to focus the antiprotons into a parallel beam and a pulsed magnet separates them from other particle species. The resulting antiproton beam is then directed to the Debuncher, a rounded triangular-shaped synchrotron with a mean radius of 90 m. Its primary purpose is to reduce the momentum spread of the antiprotons by rotating the bunches. There are also beam cooling systems that act to reduce the oscillations in the plane perpendicular to the orbit (transverse plane) apart from reducing the momentum spread of the antiprotons. Then, the antiprotons are transferred to the Accumulator, which is the storage ring for the antiprotons. Antiprotons are stored there at 8 GeV and cooled until needed. After a period of 10 to 20 hours, when the stack is large enough, bunches of antiprotons are transferred into the Main Injector and accelerated to 150 GeV, and finally into the Tevatron ring and accelerated to 980 GeV. The total number of antiprotons in the collider is determined by the product of the antiproton production rate, the typical store duration, and the transmission efficiency from Accumulator to storage

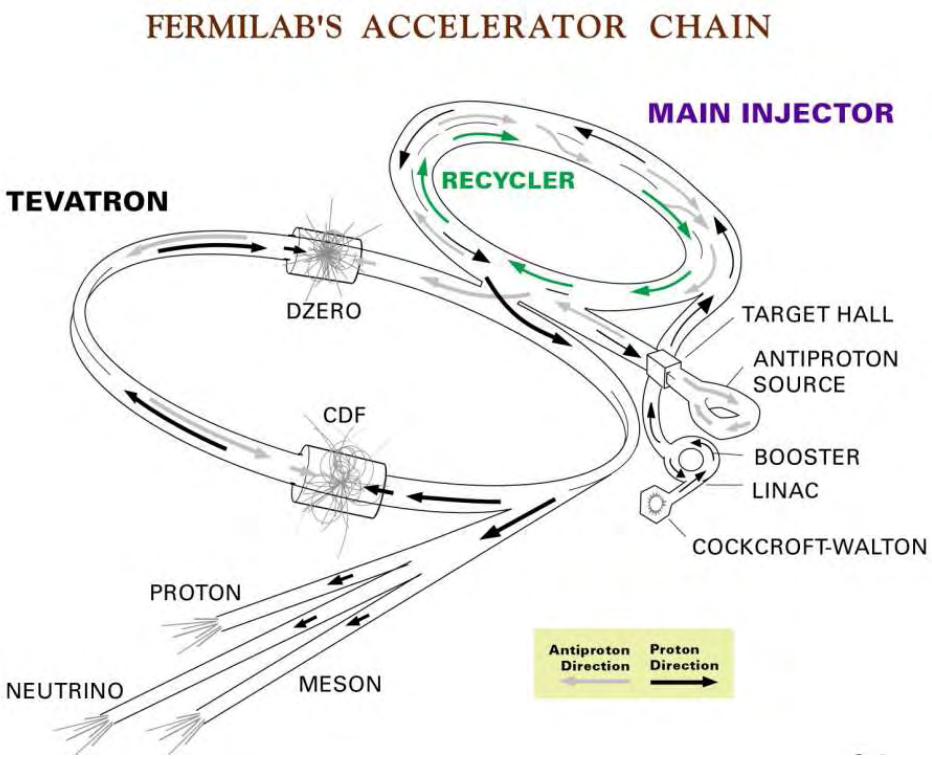

Figure 3.2: *A schematic view of the Run II Tevatron accelerator complex at Fermilab.*

in the Tevatron.

3.1.2 The Tevatron

The Tevatron is the only cryogenically cooled accelerator at Fermilab. It is a circular synchrotron of radius 1 km that has 8 accelerating cavities in the RF section of the accelerator. At the start of a store, about once per day, the Tevatron receives currently 36 bunches of about 3×10^{11} protons and 36 bunches of about 3×10^{10} antiprotons from the Main Injector and accelerates them from 150 GeV to 980 GeV. Protons and antiprotons share the same ring but move in opposite directions[1]. Two systems of independent superconducting magnets bend the protons and antiprotons so that they do not collide inside the ring except in two points. Once 36 bunches of protons and 36 bunches of antiprotons are obtained, the two beams are focused using quadrupole magnets. There are two collision halls on the Tevatron ring, B0 and D0, located at the two collision points of the Tevatron. The former is the collision hall for the CDF experiment, and the later is for the D0 experiment.

[1]An advantage of a proton-antiproton collider is that protons and antiprotons can share the same ring and therefore greatly reduce the cost of the facility, but the luminosity is limited by the possible intensity of the antiproton beam. On the other hand, in a proton-proton collider, the two proton beams have to be accelerated and stored in separate rings, but the luminosity can reach a much higher value.

Collisions continue typically for 10 hours. At the collision point at the CDF detector, the typical beam size is 120 cm in the direction of the beam axis, and 30 μm in directions perpendicular to it.

3.1.3 Tevatron Luminosity

Together with energy, another quantity is crucial on characterizing the performance of an accelerator: the instantaneous luminosity $\mathcal{L}$. The value of $\mathcal{L}$ is related to the production of a particular physical state by the formula:

$$rate[\,\mathrm{s}^{-1}] = \mathcal{L}[\,\mathrm{cm}^{-2}\mathrm{s}^{-1}] \cdot \sigma[\,\mathrm{cm}^{2}] \tag{3.1}$$

where σ is the production cross-section for the interesting process. The instantaneous luminosity is a function of the accelerator parameters. In the absence of a crossing angle or position offset it can be obtained as

$$\mathcal{L} = \frac{fBN_pN_{\bar{p}}}{2\pi(\sigma_p^2+\sigma_{\bar{p}}^2)}F(\sigma_l/\beta^*)(cm^{-2}s^{-1}), \tag{3.2}$$

where f is the revolution frequency, B is the number of bunches in each beam, $N_p(N_{\bar{p}})$ is the number of protons (antiprotons) in a bunch, $\sigma_{p(\bar{p})}$ is the RMS proton (antiproton) beam size at the interaction point, and F is a form factor that depends on the ratio of the bunch length σ_l, to the beta function at the interaction point β^*. The β function is a measure of the beam width, and is proportional to the beam's x and y extent in phase space. The luminosity can be rewritten in a form that more directly displays its dependencies on the limiting factors within the Tevatron complex,

$$\mathcal{L} = \frac{3\gamma f}{\beta^*}(BN_{\bar{p}})(\frac{N_p}{\epsilon_{Np}})\frac{F(\sigma_l/\beta^*)}{(1+\frac{\epsilon_{N\bar{p}}}{\epsilon_{Np}})}, \tag{3.3}$$

where $\epsilon_{Np}(\epsilon_{N\bar{p}})$ is the normalized transverse emittance[2] containing 95% of the proton (antiproton) beam (see [29] for the detailed definition and explanation of accelerator concepts). The major luminosity limitations are dominated by the number of antiprotons ($BN_{\bar{p}}$), and the proton beam brightness N_p/ϵ_p. Note that for a given total number of antiprotons, the luminosity does not depend explicitly on the number of bunches. The luminosity in the Tevatron is proportional to the total antiproton intensity.

The integrated luminosity is defined as:

$$L = \int_{\Delta T} \mathcal{L}(t)dt$$

This is an important quantity because it related both to the peak performances of the accelerator and to the duty cycle of the machine. Using this quantity is possible to know

[2]Emittance is, roughly, the density of the tiny clouds of particles and is akin to the cross-sectional area occupied by the beam.

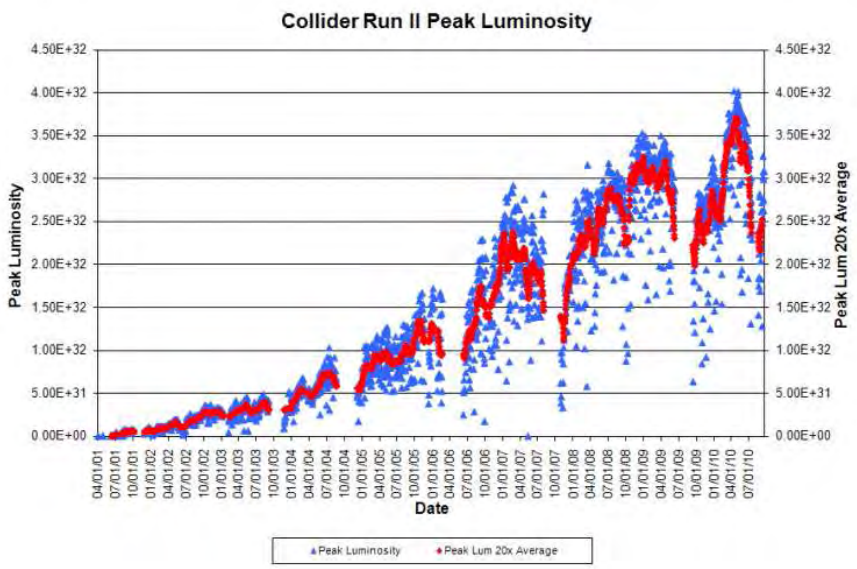

Figure 3.3: *Initial luminosity per store in* $\mathrm{cm}^{-2}\mathrm{s}^{-1}$.

the amount of data ex[ected to be collected for a particular process: time integrating $\mathcal{L} \cdot \sigma$ (Eq. 3.1) is equal to the expected number of events.

The typical luminosity for Run Ib was $\mathcal{L} = 1.6 \times 10^{31}$ $\mathrm{cm}^{-2}\mathrm{s}^{-1}$. During Run Ia and Ib from 1992 to 1996, CDF collected data corresponding to an *integrated luminosity* of approximately 130 pb^{-1}.

Run II started in June 2001. The instantaneous luminosities achieved by the Tevatron have overcome the design goals. This can be seen in Figure 3.3 that presents the peak instantaneous luminosities of every store of Run II. Figure 3.4 displays the increase of the integrated luminosity delivered by the Tevatron since the start of Run II.

Antiproton availability was the most important limiting factor for attaining high luminosities [23]. The improvements on the accelerator (the replacement of the Main Ring by the Main Injector and, if built, a new antiproton storage ring, the recycler) have allowed to increase the instantaneous luminosity up to $\mathcal{L} \approx 40 \times 10^{31}$ $\mathrm{cm}^{-2}\mathrm{s}^{-1}$. The plan is to deliver at the end of the Run II era (by 2011) an integrated luminosity ≥ 10 fb^{-1}. Table 3.1 summarizes the designed Run II accelerator parameters [23].

3.2 The CDF Detector

In this section, we give a brief description of the CDF II detector, focusing in its subsystems relevant for our analysis. A comprehensive description of the detector may be found in Ref. [25].

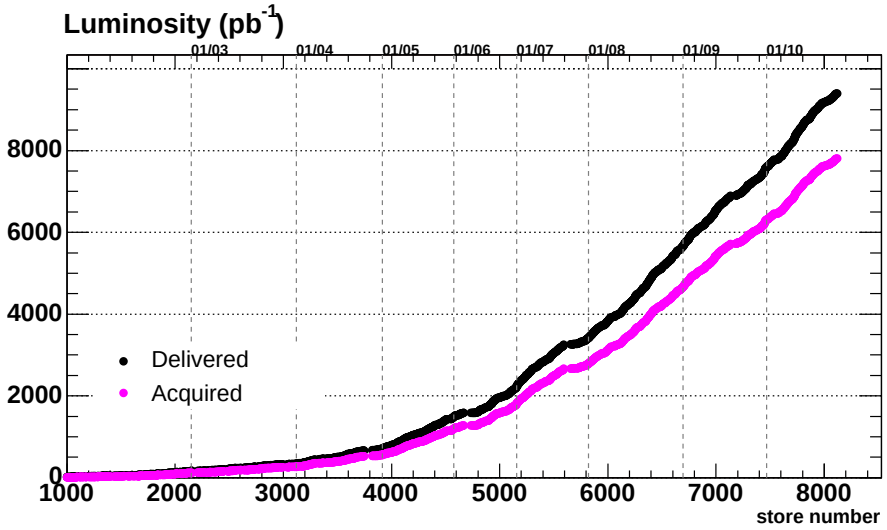

Figure 3.4: *Total integrated luminosity delivered by the Tevatron (upper curve) and recorded by CDF (lower curve) since the start of Run II. In the analysis presented in this thesis, we use the data taken from March 2002 to February 2010 corresponding to* 6.0 fb^{-1}.

Parameter	Run II
number of bunches (N_b)	36
revolution frequency [Mhz] (f_{bc}	1.7
bunch rms [m] σ_l	0.37
bunch spacing [ns]	396
protons/bunch (N_p)	2.7×10^{11}
antiprotons/bunch ($N_{\overline{p}}$)	3.0×10^{10}
total antiprotons	1.1×10^{12}
β^* [cm]	35

Table 3.1: *Parameters describing the accelerator configuration in Run II.*

3.2.1 Overview

The CDF Run II detector [24] is an azimuthally and forward-backward symmetric apparatus designed to study the $p\overline{p}$ collisions at the Tevatron. It is a general purpose detector capable of studying top, QCD, electroweak and heavy flavor physics, as well as searching for Higgs, SUSY and exotic particles. It combines precision charged particle tracking with fast projective calorimetry and fine grained muon detection. The detector has both azimuthal and forward-backward symmetry with respect to the nominal interaction point. The CDF is built and maintained by a collaboration of more than 63 institutions and fifteen countries.

A schematic view of the CDF II detector is shown in Figure 3.5. The tracking system is contained in a superconducting solenoid, 1.5 m in radius and 3.5 m in length, which generates a 1.4 T magnetic field parallel to the beam axis (and opposite to the protons direction) provided by a superconducting solenoid. Calorimetry and muon systems are all outside the solenoid.

To deal with the higher luminosities of the Tevatron in Run II, some parts of the Run I detector and most of the data acquisition system have been replaced. Also, there have been improvements to extend the coverage and capabilities of the existing subdetectors. The calorimetry systems are now exclusively scintillator-based. The electronics and trigger systems are fully compliant with the new pipelined configuration, and all the software has been re-written using C++ and an Object Oriented architecture. A more detailed description of the CDF II detector can be found in its technical design report [24]. The Run I detector is described in detail elsewhere [30, 31].

Figure 3.6 shows CDF from another perspective, an elevation view of one half of the detector. At CDF, the proton beam moves from west to east; this is used as the z direction, the north horizontal direction is defined as the x direction, and the direction parallel to gravity, with positive being "up", is defined as the y direction, forming a right-handed coordinate system. The polar angle θ in cylindrical coordinates is measured from the proton beam axis; the azimuthal angle ϕ, from the plane of the Tevatron, and around the beam direction (see Figure 3.7). Throughout this thesis, longitudinal means parallel to the proton beam and transverse means perpendicular to the proton beam. The rapidity, which is defined as :

$$y = \frac{1}{2} \ln \frac{E + P_z}{E - P_z} \tag{3.4}$$

is often used instead of the polar angle θ in the laboratory coordinate frame. The advantage of the rapidity is that a change of rapidity is a constant $\delta y = \tanh^{-1} \beta$ under a boost in the z direction with velocity β. For the case where $E \gg m$, the rapidity can be approximated by the pseudorapidity, defined by $\eta = -\ln(\tan(\theta/2))$. It has to be noted that, for tracks, a pseudo-rapidity value is obtained from the direction of the track, and not from the angle θ in the coordinate system defined above. When the track comes from the origin of coordinates, both values coincide, but this is a rather rare case, since the interaction point at CDF is not at the coordinate (0,0,0). The quantity obtained from the θ coordinate is sometimes referred to as detector pseudo-rapidity.

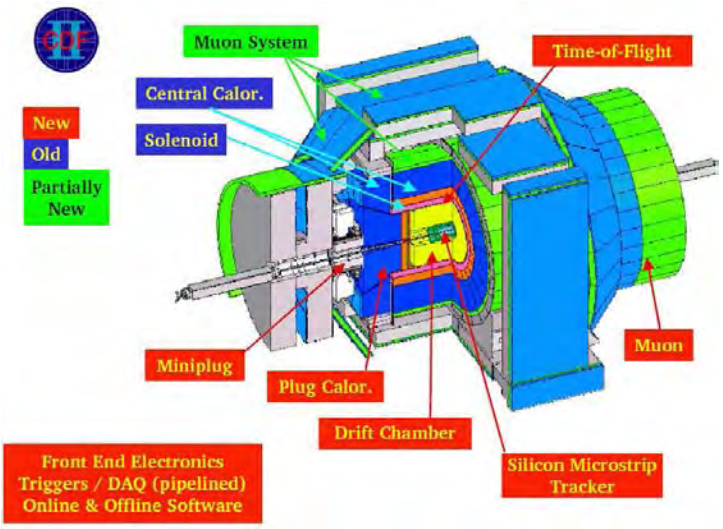

Figure 3.5: *A schematic view of the* CDF II *detector.*

At the most basic level, the CDF detector can be separated into 4 subsystems (that can be seen in the Figure 3.8): tracking, calorimetry, muon identification, and particle identification. When a particle is created in the $p\overline{p}$ collision, the momentum and charge can only be measured by the tracking system if the particle is charged. Right outside the tracking system, there is the Time-of-Flight detector which measures the time-of-flight of particles. Besides the TOF system, there is the calorimeter in which hadrons, electrons and photons deposit most of their energy. Unlike hadrons and electrons, muons only deposit minimum ionization energy in the calorimeters, so a muon system outside the calorimeter is used to identify muons. Further details of these systems, plus the Cherenkov Luminosity Counters (CLC) and trigger methods are described below, with special emphasis on those relevant to this analysis.

3.2.2 Tracking Systems

There are two primary tracking systems in CDF: the inner tracking system, consisting of the silicon-based detectors (L00, SVX II and ISL), and the Central Outer Tracker (COT), a wire-based drift chamber. A schematic view of the tracking systems is illustrated in Figure 3.9. Starting from the innermost, the subsystems are the *Layer 00* (L00), the *Silicon Vertex Detector* (SVX II), and the *Intermediate Silicon Layers* (ISL) detectors constitute the inner tracking system, and the COT constitutes the outer tracking system. The COT covers the central region, in the range $|\eta| \leq 1$, with high momentum resolution and reconstruction efficiency. The silicon tracker is used not only to precisely reconstruct the track impact parameter or interation point, but also to be able to perform the silicon stand-alone tracking for the region $(1 < |\eta| < 2)$ which is not covered by the COT.

The tracking system provides precise momentum measurement of charged particles by combining the COT and silicon tracks and extrapolating tracks down to the interaction

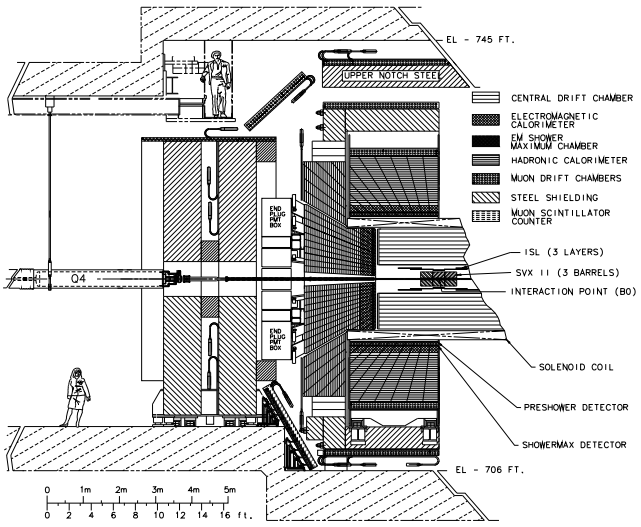

Figure 3.6: *Elevation view of one half of the* CDF II *detector.*

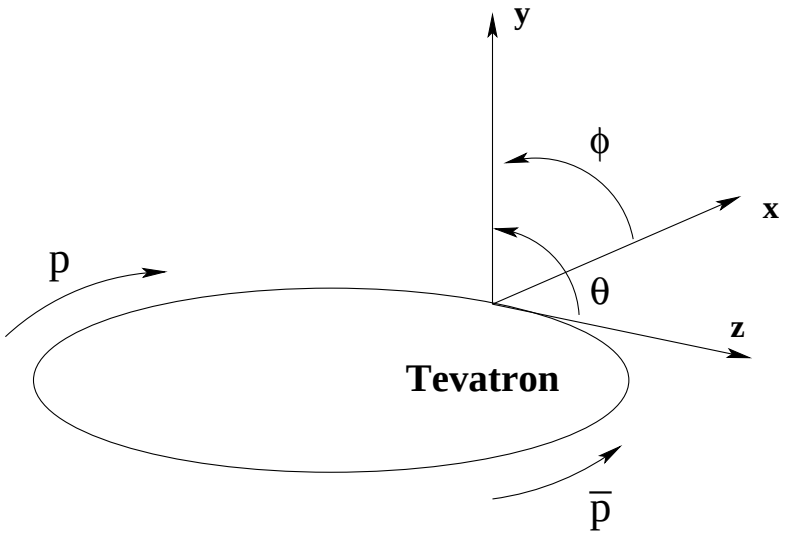

Figure 3.7: *Definition of the coordinate system in CDF.*

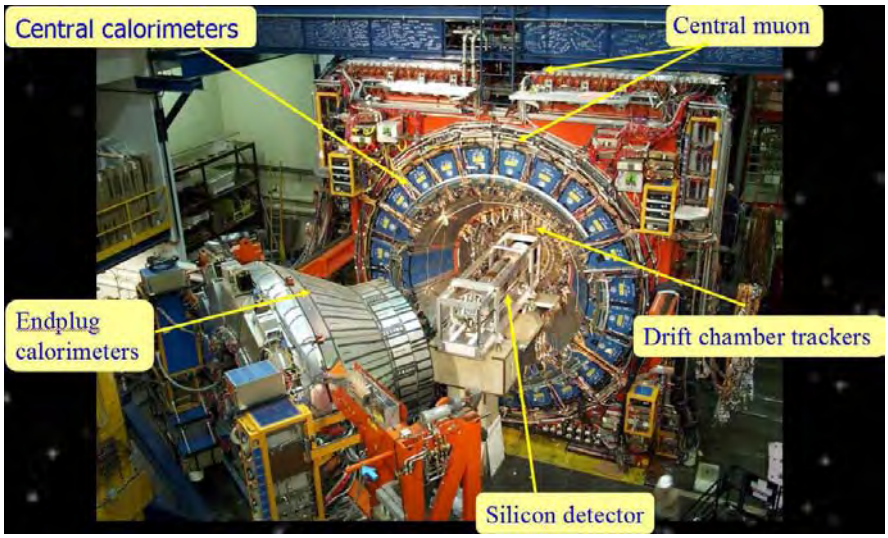

Figure 3.8: *Picture the Collider Detector at Fermilab.*

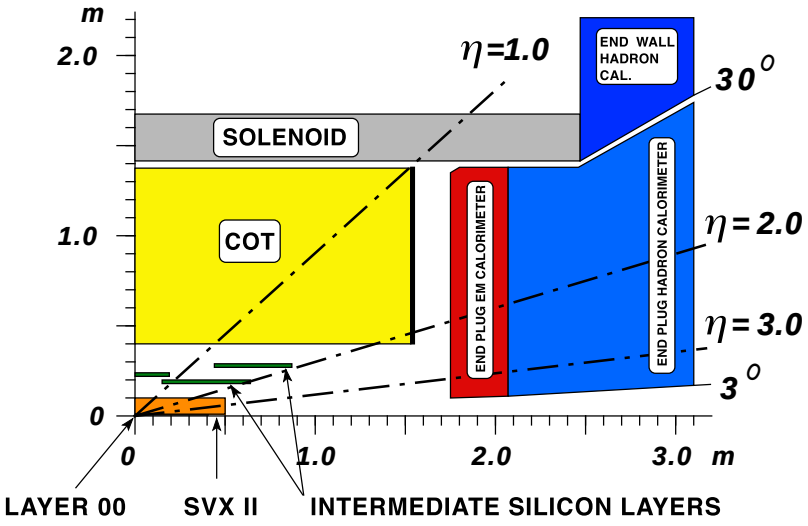

Figure 3.9: *A cut-away view of one quadrant of the inner portion of the CDF II detector showing the tracking region surrounded by the solenoid and end-cap calorimeters.*

point. We can reconstruct both the primary vertex, corresponding to the interaction point, and displaced vertices, corresponding to the long lived particles like b hadrons. Since the b quark has a relatively long lifetime, the tracking system provides a way to identify b-type quantities (e.g. jets) in an event. This is very important for Higgs searches and for top physics because both Higgs and top mainly decay via the b quark. For b physics, this is extremely important, not only for b identification, but also the lifetime measurements directly depend on the displaced vertex. Even for other analyses, like mass measurements, it is still very useful for reduce the huge QCD background in the $p\overline{p}$ collision environment. This is possible requiring a good displaced vertex. Moreover, when combined with the muon system, the tracking system can provide information for muon identification.

Tracks

We reconstruct the trajectories of charged particles ("tracks"), in the COT and SVX II. In a homogeneous magnetic field, tracks bend to form helices. Their transverse momenta can be related to half-curvature C by $p_T = B/2cC$, where c is the speed of light and B the magnitude of the magnetic field. The half-curvature is generally referred to as curvature. The tracking algorithms use 5 parameters to describe the helices: impact parameter (d_0), curvature(C), ϕ_0, z_0, and $\lambda = \cot\theta$. These are illustrated in Figure 3.10.

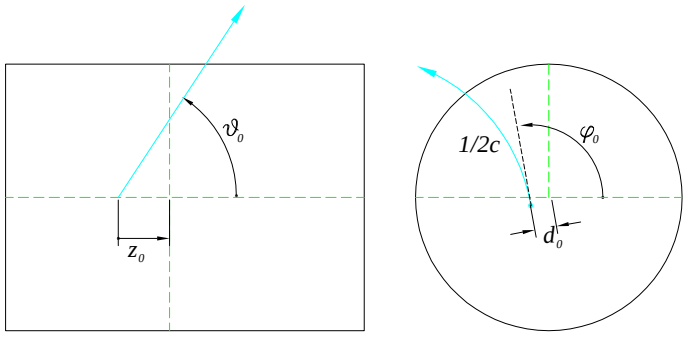

Figure 3.10: *An illustration of the tracking parameters: the figure on the left shows a charged track in the $r-z$ view of the tracking volume. The figure on the right shows an $r-\phi$ view of the track, with d_0 indicating the track's impact parameter, or point of closest approach to the origin, and c the curvature.*

The helix is a circle in the xy plane, whose curvature is related inversely to the transverse momentum, as described above. The sign of the curvature is the charge of the particle.

The circle in the xy plane has a well-defined point of closest approach to the origin, $\vec{P}$. ϕ_0 is the angle between the x axis and a line tangent to the track at $\vec{P}$. The impact parameter of a track has a sign that is defined by the following formula:

$$d_0 = \frac{\hat{z} \cdot (\vec{r} \times \vec{P_T})}{\left|\vec{P_T}\right|}, \tag{3.5}$$

where $\vec{P_T}$ is the transverse momentum vector of the particle, $\vec{r}$ is the vector pointing from the primary vertex to the reconstructed particle trajectory at the point of closest approach to the primary in the $r-\phi$ plane and $\hat{z}$ is the unit vector along the z axis. In other words, the signed impact parameter d_0 is the y-intercept of the track, after rotating the coordinate system so that $\phi_0 = 0$ [3]. z_0 is the position of the track along the z-axis at P, and λ is defined as $\lambda \equiv \cot\theta = p_z/p_T$, being θ the polar angle at the minimum approach. The axial parameters, which provide information in the xy plane only, are C, d_0 and ϕ_0. λ and z_0 are called stereo parameters, since they provide z information.

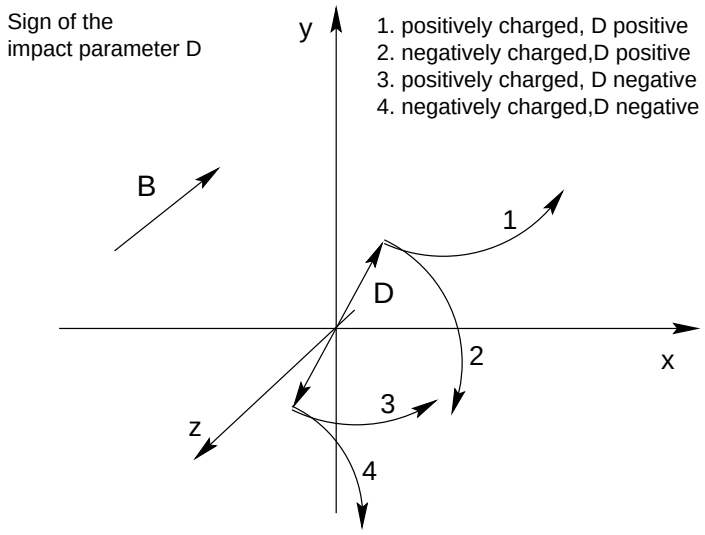

Figure 3.11: *Track of a particle with positive/negative charge and positive/negative impact parameter.*

Central outer tracking system: COT

The Central Outer Tracker (COT)F [24, 32], is the main tracking chamber in CDF. It is an open-cell cylindrical drift chamber segmented into 8 concentric superlayers for particle reconstruction in the central region $|\eta| \leq 1$ with transverse momenta as low as 400 MeV/c. The active volume extends 310 cm in z, and from 40 to 137 cm from the beam line in radius. The entire azimuth, ϕ, is covered. Each superlayer is sectioned in ϕ into separate cells. A cell is defined as one sense plane (active and read-out) with two adjacent field planes, which are grounded. A diagram of a section of the endplate, with slots for the field and sense planes, is shown in Figure 3.12

Figure 3.13 shows a diagram of 3 cells in the $r-\phi$ plane. The rows of small circles and crosses represent high voltage wireplanes. There are a total of 29 wires in each cell, 12 of which, called sense wires, are read out. The sense wires have approximately the same

[3] If a track has a positive(negative) charge and the reference point is outside(inside) the circle of the track, then the impact parameter has a positive sign, see Figure 3.11.

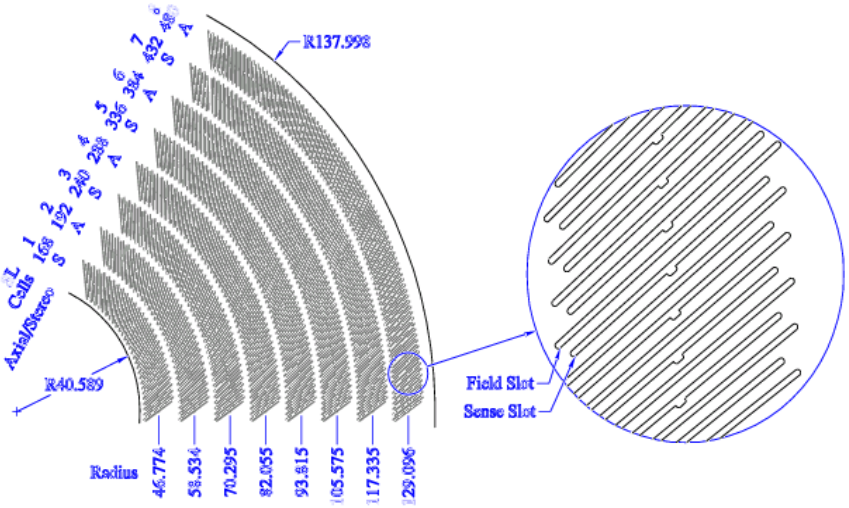

Figure 3.12: *1/6 section of the COT endplate, showing the cell counts in superlayers 1-8. The radii at the center of each superlayer are shown in cm. The endplate has inner and outer radii of 40.589 cm and 137.998 cm.*

maximum drift distance, therefore the number of cells in a given super layer is roughly proportional to the radius of the super layer. The remaining wires are needed to shape the electric field, adjusting for the taper of the cell with decreasing radius. The lines adjacent to the sense planes represent the grounded field planes.

The sense plane wires are composed of 40 μm gold-plated tungsten wire. The main body of the field sheets is 0.25 mil gold-coated mylar. The field sheets are separated by $\simeq$ 2 cm. Mylar is stretched and supported by two 12 mil stainless steel wires, which are epoxied in a parabolic shape along each side of the field sheet. In axial superlayers, they are approximately parallel to the z-axis. The field sheets are much closer to a true grounded plane than arrays of wire, which have often been used in wire chambers, including the predecessor to the COT. Use of field sheets results in a smaller total radiation length, and allows the COT to operate at much higher drift field than with an array of wire. This is an important factor in maximum drift time. In addition to this, the total endplate load is less, because a single field plane requires less tension than an array of field wires.

The eight superlayers of the COT alternate between stereo and axial, beginning with superlayer 1, which is a stereo layer. In an axial layer, the wires and field plates are parallel to the z axis, and thus provide only $r - \phi$ information. In stereo layers, a given wireplane or field sheet which starts at a slot in one endplate does not end at the mirror-image slot in the other. Instead, it is offset by 6 cells. This generates a stereo angle of $\pm 3^\circ$, depending upon the direction, which corresponds to a rotation about an axis in the radial direction.

The COT is filled with Argon/Ethane(50-50) with a drift velocity of $\simeq$ 100 μm/ns. This will give a maximum drift time of 180 ns. When a charged particle passes through, the gas is ionized. Electrons drift to wards the sense wires, resulting in an avalanche at the wire

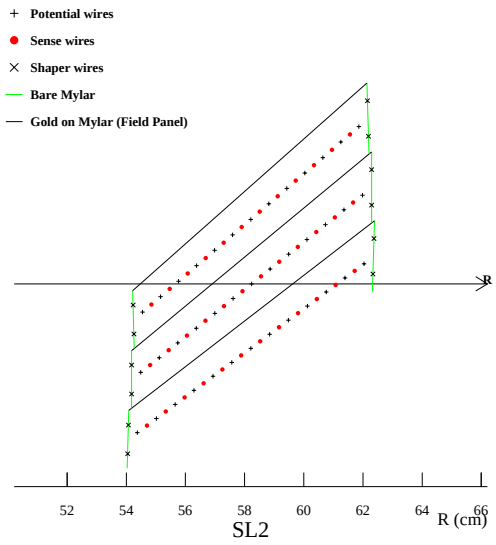

Figure 3.13: *A transverse view of three cells in super layer 2 of the COT. The continuous lines represent field sheets, which are grounded., and approximately 11.8 cm wire. The 11.8 cm length arrays of circles and crosses represent high-voltage wireplanes. The circles are the sense wires, which are read out. The crosses are the field wires.*

surface, which provides a gain of $\approx 10^4$. For a charged particle traveling through the entire COT radially, the 4 axial and stereo super layers will provide 96 (8×12) measurements. The drift time of ionization electrons in the gas is used to measure the charged particle's spatial position and the pulse height can be used to measure the amount of ionization.

Due to the magnetic field, the electrons drift with a Lorentz angle of $\approx 35°$. It is for this reason that the cells are tilted with respect to the radial direction. An illustration of the electron drift using the GARFIELD simulation is shown in Figure 3.14 [33]. The voltage on the wire planes is set in order to insure the maximum drift time to be smaller than the time between beam crossings, which is 396 ns.

Table 3.2 summarizes the main features of the COT.

Signals on the sense wires are processed by ASDQ (Amplifier-Shaper-Discriminator with Charge Encoding), which provides input protection, amplification, pulse shaping, baseline restoration, discrimination, and charge measurement [32]. This charge measurement is encoded in the width of the discriminator output pulse, which also allows the measurement of the energy loss through ionization of the gas per unit length (dE/dx)[4]. The pulse is sent through $\approx$ 35 ft. of micro-coaxial cable, through repeater cards, and finally to the TDC's (Time to Digital Converters), which reside in the collision hall. Hit times are then processed by pattern recognition and fitting algorithms to form helices. These algorithms are collectively referred to as "tracking". Figure 3.15 shows the COT hit resolution vs. drift distance, measured by an online monitoring program. The single hit resolution is about 150 μm in the center of the cell.

[4]The dE/dx of a charged particle is a function of particle velocity, which can be used to infer the particle mass when combined with the information on the particle momentum.

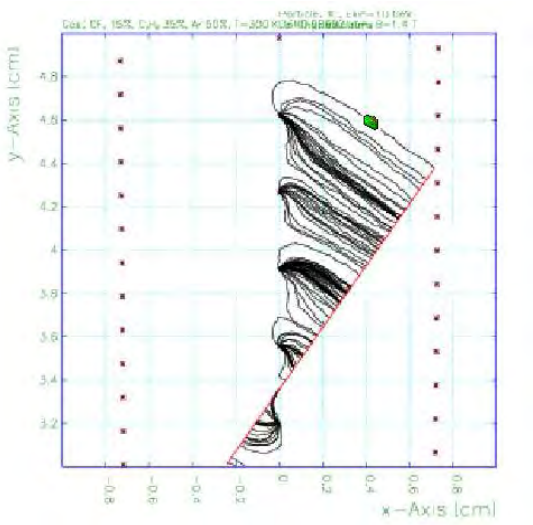

Figure 3.14: *The drift of electrons toward the sense wires, as predicted by the GARFIELD Simulation [33]. The straight line represents a charged particle passing through the detector. Along the track, ionizations occur, and the liberated electrons, or clusters of electrons, drift toward the sense wires. The direction of drift is determined by the electric field (due to the sense wires, potential wires, and field sheets) and the magnetic fields, which is required for the COT to function as a spectrometer.*

Inner Tracker: L00 + SVX II + ISL

One the most important components of CDF is the Silicon Detector [34, 24]. Among its major features, we find a more complete geometric coverage of the interaction region than previous versions of this detector [35], a faster and improved electronic and trigger system and harder sensors to survive the radiation fields created by the higher Run II luminosity (capable of withstanding several Mrads of integrated dose). The CDF silicon detector is essential for enhancing not only the overall tracking capabilities but also the heavy flavor tagging of the experiment.

The inner tracking system consists of three silicon detectors [34]: The Silicon Vertex Detector (SVX II), the Intermediate Silicon Layer (ISL) and Layer 00 (L00), described below. Comprising a total of 7-8 silicon layers arranged in cylinders, these detectors allow to achieve among other things a good impact parameter resolution and a silicon stand-alone tracking. The basic structural unit of a sub-detector is a *ladder*, which consists of several silicon microstrip sensors with strip width and multiplicity depending on the layer, or distance from the beam pipe.

SVX II: The Silicon Vertex Detector (SVX II) is built in three cylindrical barrels with beryllium "bulkheads" at each end for support and cooling of the silicon units. It is positioned end-to-end along the beam axis and centered longitudinally with the detector with a total length of 96 cm and a coverage in pseudorapidity of $|\eta| \leq 2$. Each barrel is

COT	
Number of superlayers	8
Measurements per superlayer	12
Stereo Angle [degrees]	+3 0 -3 +3 0 -3 0
Cell/Layer	168 192 240 288 336 384 432 480
Radius at Center of SL [cm]	46 58 70 82 94 106 119 131
Tilt angle [degrees]	35
Length of Active Region	310 cm
Number of channels	30,240
Material thickness	1.3 % X_0

Table 3.2: *Summary of the main COT features.*

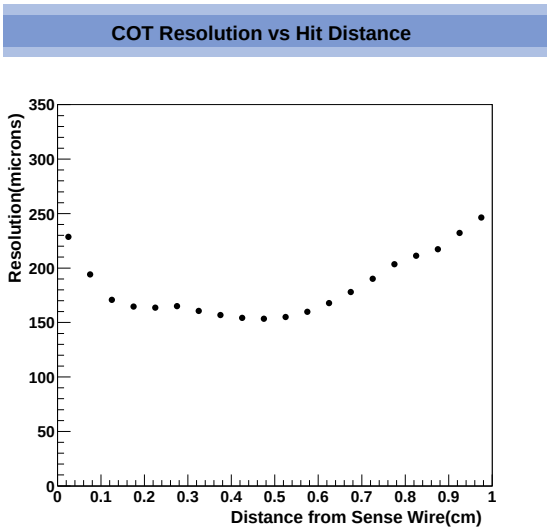

Figure 3.15: *Single hit resolution vs. drift distance measured in data. The measurements are an average over all superlayers.*

divided in azimuth into 30° wedges and each wedge consists of five radial layers of double sided silicon microstrip detectors between radii of 2.4 and 10.7 cm. One layer consists of two wire-bonded pairs of double-sided silicon microstrips sensors of 7.28 cm length. The bulk of the sensor is n-doped. On the side facing the beamline, the strips are spaced in $r - \phi$ by approximately 60 μm, and have p^+-implant widths of 14-15 μm (resulting in a high density array of pn diodes). On the other side, both 90° and small angle stereo sensors are used, in the pattern (90 90 -1.2 90 +1.2) degrees from the innermost to the outermost SVX II layer. They are spaced by (141, 125.5, 60, 141, 65) μm, and have n^+-implant widths of 2-μm for the 90° strips and 15 μm for the small angle stereo layers. This is designed to allow good resolution in locating the z-position of secondary vertices and to enhance the 3-D pattern recognition capability of the silicon tracker.

When the detector is reverse-biased, passage of a charged particle through the material results in the creation of electron-hole pairs. Due to the electric field, the charge then drifts toward the readout strips, providing position measurements.

Figure 3.16 shows a detailed end view of the SVX II system and table 3.3 shows a summary of some of the SVX II features.

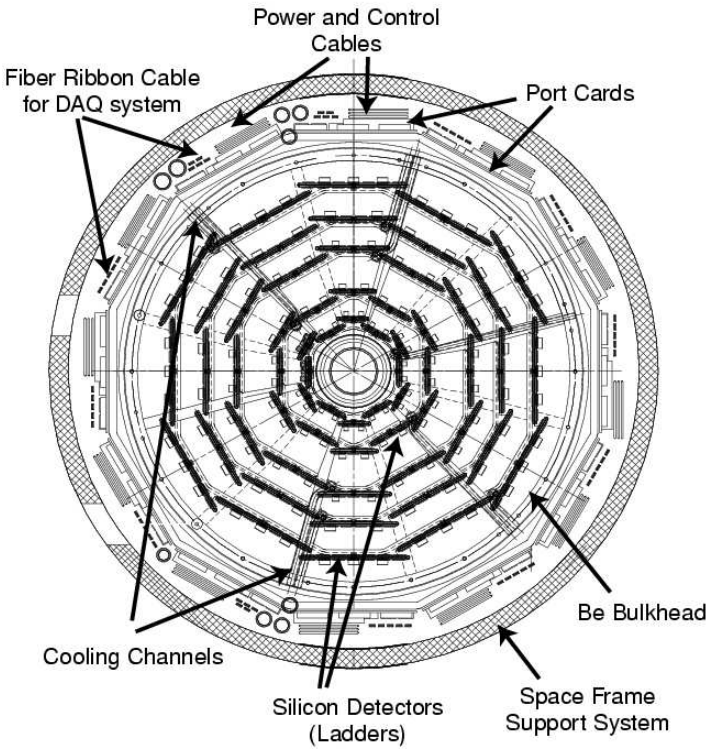

Figure 3.16: *An end view of SVX II including the cooling and support systems.*

ISL: With an outer radius of 10.7 cm, additional tracking information is needed to robustly link silicon information to tracks formed from hits in the drift chamber. This is achieved by an additional double-sided silicon layer at a radius of 22 cm covering the

SVX II	
Readout coordinates	$r-\phi$,$r-z$
Number of barrels	3
Number of layers per barrel	5
Number of wedges per barrel	12
Ladder length	29.0 cm
Combined barrel length	87.0 cm
Radius at axial layers	2.54 4.12 6.52 8.22 10.1
Radius at stereo layers	3.00 4.57 7.02 8.72 10.65
number of ϕ strips	256 384 640 768 896
number of z strips	256 384 640 512 896
ϕ strip pitch	60 62 60 60 65 μm
z strip pitch	141 125.5 60 141 65 μm
Number of channels	405,504
Material thickness	3.5% X_0

Table 3.3: *Summary of the main SVX II features.*

interval $|\eta| < 1$ and two layers of silicon placed at the radii of 20 and 28 cm in the forward and backward region covering $1 < |\eta| < 2$ [36]. Fig. 3.17 shows an schematic view of the ISL disposition with respect the SVX II. The ISL incorporates many features of the SVX II design. The crystals are double-sided with axial strips on one side and small angle stereo at 1.2° on the other. The readout electronics are identical to the SVX II (see below). In the forward and backward region, where the COT tracking is not efficient, the silicon stand-alone tracking is performed. The ISL thus extends tracking, lepton identification, and b-tagging capabilities over the full region $|\eta| < 2$.

L00: The innermost Layer 00 (L00) [37] is a single-sided, radiation-hard silicon layer, placed immediately outside the beam pipe at 1.35-1.62 cm radius. The readout electronics is identical to that used for SVX II. Being so close to the interaction region, L00 significantly enhances CDF's impact parameter resolution. It also should add longevity to the silicon system.

SVX3D readout chip

All components of the CDF II silicon system achieve their data readout through a set of custom integrated circuit chips with the designation SVX3D [38]. It includes preamplification, a multi-cell analog storage pipeline, and simultaneous analog and digital operation capability. An optional data acquisition mode allows common-mode noise to be reduced independently for each chip by dynamic data-driven determination of pedestal levels. For SVX II, the SVX3D chips are mounted on electrical hybrids on the surface of the sili-

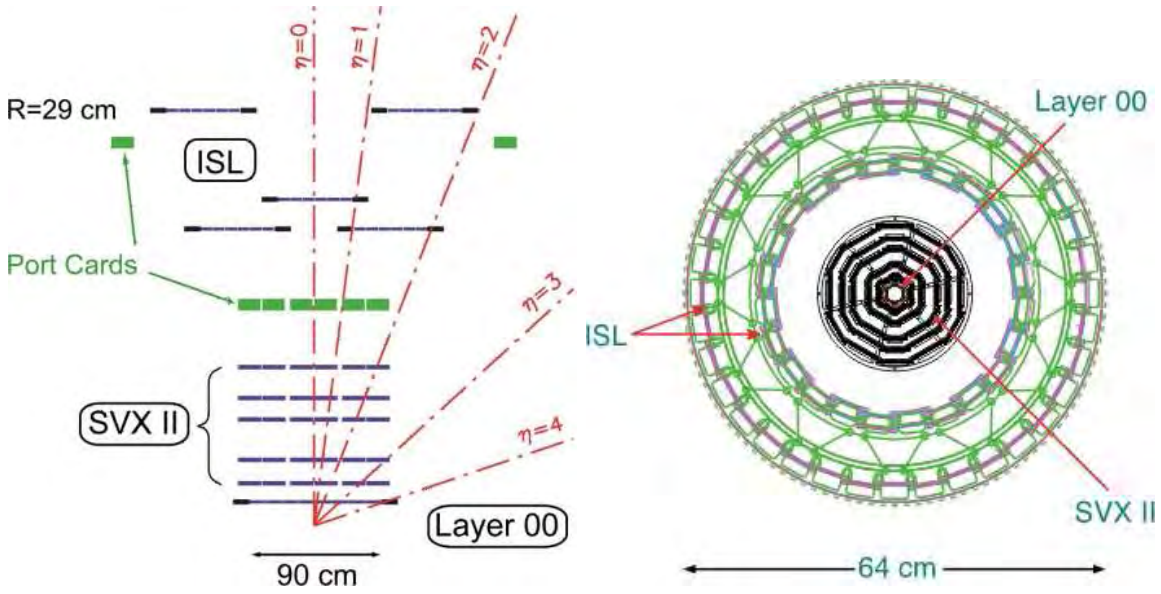

Figure 3.17: *Schematic layout of the CDF Silicon Detector. $r-\phi$ and $r-z$ views are shown. Note that the z axis is compressed for illustration purposes.*

con detectors. ISL, with more space available, has the hybrids attached right after the sensors. L00 hybrids are well separated from the sensors at the end of the detector and the SVX3D chips are connected via fine-pitched cables to their corresponding L00 sensor. Each readout chip has 128 channels, each with a charge-sensitive amplifier, 42-cell dual-ported pipeline with four additional cells for buffers, and an ADC.

Silicon DAQ

The data acquisition system for the CDF II silicon detectors is a fully pipelined DAQ+trigger architecture that can operate without deadtime losses at machine bunch crossing intervals as low as 132 ns. The 42-cycle "Level 1" pipeline within each SVX3 chip allows storage of the analog signals for later digitization and transmission at rates up to 50 kHz. A highly parallel fiber-based data acquisition system reads out the entire detector in approximately 10 μs. This high speed and dual porting of the readout allows the SVX II information to be used for impact parameter discrimination in the SVT processor of the "Level 2" trigger. This allows an online trigger to identify displaced tracks at "level 2", as described in references [39, 40, 41, 42], which is crucial for this analysis. This trigger operates with 20 μs latency at rates up to 300 Hz. It is followed in the data stream by a third level of software-based trigger processing that implements a portion of the offline analysis and reduces the final rate of logged events to less than 50 Hz. Further detail on the components and logic of the silicon DAQ system can be found in [43].

3.2.3 Pattern Recognition in Tracking

Track reconstruction begins in the outer tracking chamber - the COT. The first step in the pattern recognition is to form line segments from hits in each with lying tangent to a common circle are linked together to form a track. A 2d circle fit is then performed. Line segments in stereo layers are then linked to the 2d track, and finally a helix fit is performed. At this point we have a set of tracks which have only COT hits [44]. These are referred to as COT-only tracks.

The next step is to extrapolate the COT-only track into the SVX and add hits which are consistent with lying on that track. This process starts with the outermost layer in SVX II. A road, or window, around the track is established based on the errors on the COT track parameters. If hits lie within the road, they are added to the track. A new track fit is then performed, resulting in a new error matrix and a new road. This road is then used to add hits from the next SVX layer. This procedure is repeated until there are no SVX layers left. There may be multiple tracks with different combinations of SVX hits associated with one COT track. In this case, the track with the largest number of SVX hits is chosen [45].

The set of tracks resulting from this process is referred to as "default tracks", or **defTracks**. This set is a mix of tracks with varying numbers of SVX hits. Some tracks have had no SVX hits added; they remain COT-only tracks, and they are called that way. Every track in **defTracks** has a unique COT-only parent, which is stored in the event record.

3.2.4 Other Subdetectors

In this section we briefly described some other subdetectors which are not relevant in this analysis.

Calorimeter system

CDF has both electromagnetic and hadronic calorimetry, segmented into towers in η and ϕ. Towers in the central calorimeter span 15 ° in azimuth and 0.11 in pseudorapidity. The coverage is $0 < |\eta| < 1.3$. For Run II, there is a new Plug Calorimeter, with variable tower size, which extends coverage out to $|\eta| = 3.6$. For a more detailed description of the calorimetry, we refer the reader to the Run I description of the CDF detector [30] and the Run II Technical Design Report [24], which discusses the Plug Upgrade Calorimeter.

Muon Systems

Because the muon is roughly 200 times heavier than the electron, bremsstrahlung radiation is about 40000 times weaker than for an electron, so muons deposit relatively very little energy in the calorimeters, which totally absorb most other particles. In order to identify muons, there are several muon detectors [46] outside the calorimeters. Moreover,

the muon is a charged particle, so the tracking system can measure its charge and momentum. Combining the information from a muon detector and tracking system, CDF can provide good muon identification. CDF uses four systems of scintillators and proportional chambers in the detection of muons over the region $|\eta| < 2$. The absorbers for these systems are the calorimeter steel, the magnet return yoke, additional steel walls, and the steel from the Run I forward muon toroids. New chambers have been added for the CMP and CMX systems to close gaps in the azimuthal coverage in Run II, while the central chambers (CMU) have almost the same configuration without major changes from Run I. Finally, the forward muon systems used in Run I was replaced with a completely new Intermediate Muon System (IMU).

Time of Flight System

Particle Identification is done both in the COT, using dE/dx, and in the Time Of Flight system (TOF) [47]. This detector is situated between the solenoid and the COT, and measures the time between a beam crossing and a particle incident upon the detector itself. The TOF detector consists of scintillator panels which provide both timing and amplitude information. The timing resolution is 100 ps. The detector covers the central region out to $|\eta| < 1.1$ and is capable of identifying kaons from pions by their flight time difference with at least 2σ separation up to kaon momenta of 1.6 GeV/c. The mayor motivation for this system is to improve the b flavor tagging power, which is essential for b mixing and CP violation analyses.

Cherenkov Luminosity Counter

In Run II, a Cherenkov Luminosity Counter (CLC) [48] was designed to measure the luminosity with an uncertainty of 5% or less in the very high rate regime of $L \simeq 2 \times 10^{32}\,\mathrm{cm}^{-2}\mathrm{s}^{-1}$. There are CLC modules in the CDF detector, installed at small angle in the proton (East) and antiproton (West) directions with rapidity coverage between 3.75 and 4.75. Each module consists of 48 thin, long, gas-filled, Cherenkov counters. The counters consist of three concentric layers around the beam-pipe, each layer has 16 counters and points back to the collision point.

3.3 Trigger and Data Acquisition

At the Tevatron the $p\bar{p}$ collision rate is much higher than the rate at which the data can be recorded, and the cross section of the interesting physics events is only a small fraction of the total inelastic cross section. This leads to implementation of a trigger system that preselects events online and decides if the corresponding event information is written to tape or discarded.

The CDF trigger system consists of three trigger levels as it is shown in Figure 3.18. Each trigger level provides a rate reduction sufficient to allow for processing in the next

level with minimal deadtime. The data size is reduced accordingly to the triggering ability.

Below we briefly describe the three levels of the CDF trigger, followed by a description of the *two-track trigger* (TTT), which is the particular trigger used in the analysis presented within this thesis.

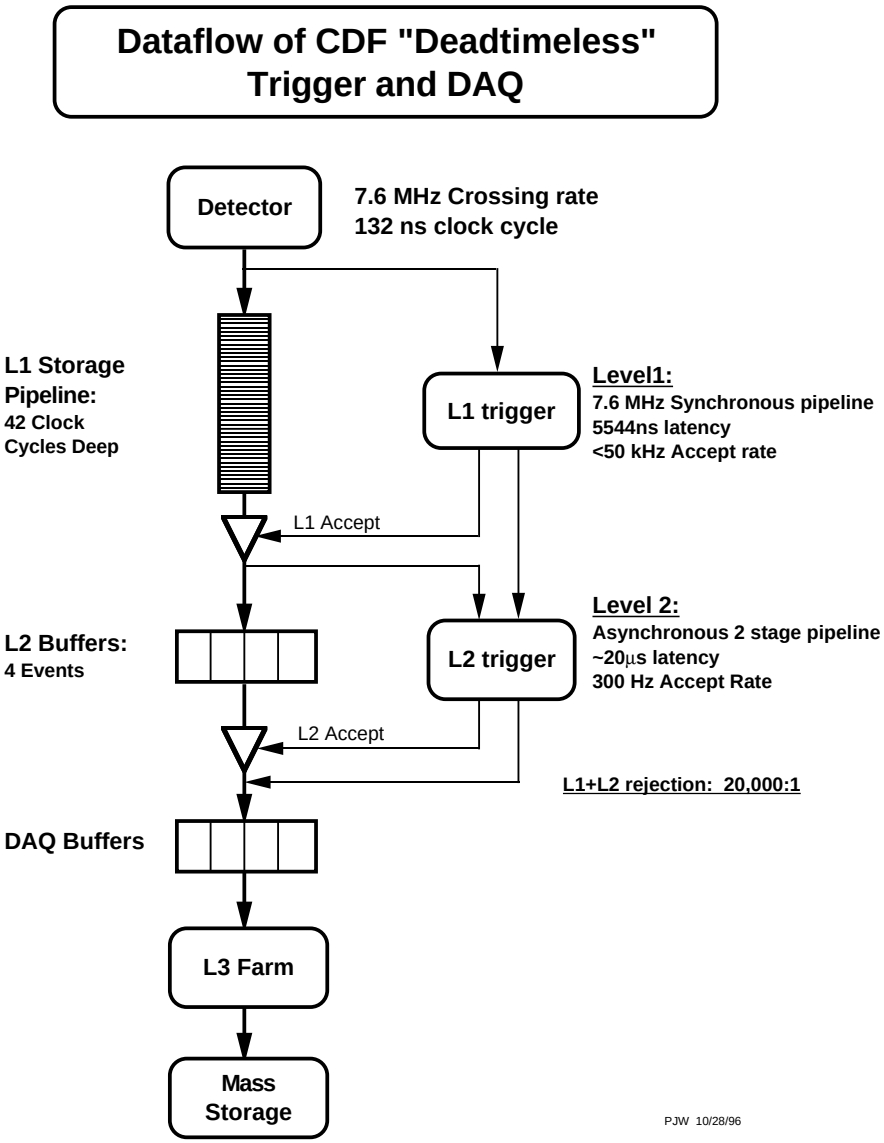

Figure 3.18: *The Run II readout functional block diagram of the three level pipelined and buffered trigger system of CDF.*

3.3.1 Level 1 Trigger

The lowest level trigger, "Level 1" uses output from the muon detectors, for muon triggers, and from all the calorimeters for electron and jet triggers.

The reconstruction of tracks using COT information is already present at "Level 1". This is done by the XFT (eXtremely Fast Tracker), an improved version of the central fast tracker [50, 51]. This level basically, requires two tracks with a transverse momentum $p_T > 2.04\,\mathrm{GeV}/c$ to accept one event.

It takes $\simeq$5 μs to make a "Level 1" decision. All front-end electronics are fully pipelined, with on-board buffering for 42 beam crossings. This allows the 41 next crossings to be stored while the "Level 1" decision of crossing i is taken. Once the "Level 1" decision is taken, the buffer i is released for the storage of another crossing.

The "Level 1" trigger is a synchronous system with a decision reaching each front-end card at the end of a 42-crossing pipeline. It reduces the event rate from 2.5MHz to $\simeq$10kHz.

3.3.2 Level 2 Trigger

Upon a "Level 1" accept, the data on each front-end card are transferred to one of four local "Level 2" buffers. The second trigger level, "Level 2", is an asynchronous system with an average decision time of 20 μs.

The most challenging addition for "Level 2" is the Silicon Vertex Tracker (SVT). The SVT provides the ability to trigger not only on electrons, muons, and jets, as during Run I, but to select events with tracks which have large impact parameters, what is crucial for this analysis.. This provides already the secondary vertex information at "Level 2" and allow to study charm physics with high statistics and the study of hadronic b decays as in this analysis. The "Level 2" output rate is approximately 300 Hz. A "Level 2" trigger accept flags an event for readout.

3.3.3 Level 3 Trigger

All events accepted by the "Level 2" trigger are collected in the Event Builder (EVB), and then the EVB assembles those event fragments into one data block and delivers it to the third level of triggering, the "Level 3". The "Level 3" uses the C++ object oriented algorithms run in the "offline" reconstruction. The software is run on a PC farm. On one CPU, one event is processed in approximately 1 second. The output rate of the "Level 3" trigger is approximately 50 Hz at present. The accepted events are then transferred via network to the *Feymman Computing Center* and stored on tape. To facilitate handling of the huge data volumes collected with the CDF, the data coming from "Level 3" is currently split into eight different streams. The triggers an event has passed decide to which streams this event belongs. These events can also be viewed by online monitoring programs running on specific workstations.

3.3.4 The Two-Track Trigger

The relatively long lifetimes of weakly decaying heavy-flavour hadrons [17] implies that their decay vertices are displaced by a measurable amount from the primary $p\overline{p}$ interaction

point. The track left by the charged daughter particles are therefore characterized by impact parameters which are inconsistent with zero. These displaced tracks may include the immediate decay particles of B meson, such as a pion or a lepton, or they may arise from the daughters of subsequent D meson decays. This topology is in contrast to the appearance of more common interactions such as inelastic scattering, in which all tracks are "prompt", originating directly from the primary vertex.

The precise silicon hit information and SVT electronics provide the trigger with impact parameter resolutions of approximately 35 μm for high-momentum tracks. This capability, which is the first of its kind among collider experiments and is unique at the Tevatron, allows for track displacement to be recognized at the online level and used in trigger decisions. Triggering on such a clear signature of long-lived events creates data samples which are enriched in events containing bottom and charm hadrons.

As the Tevatron luminosity decreases over the lifetime of a store, the rate of events which meet a given trigger's requirements decreases correspondingly. However, the CDF detector's ability to read out and store events remains constant. If one were to enforce very strict requirements on trigger paths such that they pass events at acceptable rates for high luminosities, the trigger bandwidth would become progressively under-utilized as the luminosity decreases. Conversely, loose trigger requirements would overwhelm the DAQ system during high luminosity running, such that high quality events could be missed as the system struggles to record less interesting events. A solution for efficient allocation of fixed trigger bandwidth is *prescalling*, in which the DAQ system may record only every N^{th} event that passes a trigger path. The prescale N can be varied dynamically to achieve a given acceptance rate, such that N may initially be set high ($\sim O(5)$) and eventually decreased to unity later in the store. The two-track trigger (TTT) encompasses a set of distinct trigger paths or "scenarios" [52] which aim to achieve efficient use of the trigger bandwidth at all Tevatron luminosities. The paths are applied simultaneously; that is, an event is tested against all scenarios rather than allowing only one as an option. A feature common to all scenarios is that the presence of at least two displaced tracks is required in order to make a simple vertex in the transverse plane. In addition to impact parameter bounds, the paths make various requirements on the opening angle $\Delta\phi$ and transverse momentum p_T of the displaced tracks and on the transverse displacement L_{xy} of the associated vertex. "Scenario A" established the baseline TTT path and is prescaled at high luminosity. The unprescaled "Scenario C" imposes stricter requirements and is designed to ensure acceptance of high quality events which might otherwise be discarded by the Scenario A prescale. The presence of an unprescaled trigger is also useful in that it simplifies potential cross-section measurements. "Scenario Low" is a more relaxed variation of Scenario A and is intended to use all available bandwidth by accepting a more inclusive sample at low luminosity. The requirements for all the TTT paths are detailed in Appendix A.

Chapter 4

Data Sample

The data used in this analysis is based on events collected by the CDF II detector from March 2002 to Feburary 2010, for a total integrated luminosity of 6.0 fb^{-1} of data.

The information provided by the detector has to be process in order to build observables physical meaningful. This reconstruction implies mathematical algorithms and definitions hardly related with the detector itself.

In this chapter we explain how the information from the detector is processed.

4.1 Event Reconstruction

The final reconstruction of particle decays is performed offline, once the events have been written to tape. The organizing principle is similar to that of the trigger, in that simple objects are constructed initially and then combined into structures of progressively greater complexity. However, this final procedure aims to use the most accurate available models of the detector and event attributes. The following discussion refers primarily to the central decay channel of this analysis, but all of the concepts apply equally to the supporting datasets.

4.1.1 Track and Primary Vertex Reconstruction

The trajectories of charged particles are found (in a first approximation) as a series of fragments in the axial superlayers of the COT. Two complementary algorithms associate the segments lying on a common circle to define an axial track. Segments in the stereo layers are associated with the axial tracks to reconstruct 3D tracks.

The COT tracks are extrapolated to the silicon detector and the track is refit using the information from the silicon measurements. The initial track parameters provide a width for a search region in a given layer. For each candidate hit in that layer, the track is refit and used to define the search region into the next layer. The search uses the two best candidate hits in each layer to generate a small tree of final track candidates, and the one with the best χ^2 is selected. The efficiency to associate at least three silicon hits with an isolated COT track is found to be $(91 \pm 1)\%$.

The primary vertex location for a given event is found by fitting well-measured tracks to a common point of origin. At high luminosities, more than one collision can occur on a given bunch crossing. For a luminosity of $\sim 10^{32}$ cm^{-2}s^{-1}, there are ~ 2.3 interactions per bunch crossing. The luminous region is long, with $\sigma_z = 29$ cm; therefore the primary vertices of each collision are tipically separate in z. The first estimate of the primary vertices (x_V, y_V, z_V) is binned in the z coordinate, and the z position of each vertex is then calculated from the weighted average of the z coordinate of all tracks within 1 cm of the first interaction vertex, with a typical resolution of 100 μm. The primary vertex is determined event by event by an iterative algorithm which uses tracks around a seed vertex, defined as above, to form a new vertex. The χ^2 for all tracks relative to the new vertex is calculated, tracks with bad χ^2 are removed, and the cycle is repeated until all tracks have a good χ^2. The locus of all primary vertices defines the beamline, the position of the luminous region of the beam-beam collisions through the detector. A linear fit to (x_V, y_V) vs. z_V yields the beamlines for each stable running period. The beamlines is used as a constraint to refine the knowledge of the primary vertex in a given event. The transverse beam cross section is circular, with a rms width of ~ 40 μm at $z = 0$, rising to $\sim 50 - 60$ μm at $|z| = 40$ cm. The beam is not necessarily parallel nor centered in the detector.

4.1.2 Track Refitting

The tracks reconstructed from the detector information are not ready to be used in an analysis until several additional effects are considered.

The first effect is Multiple Coulomb Scattering (MCS) in the COT volume. This is a statistical description of the scattering angle of a particle as a result of many small interactions with atomic electrons. These interactions have the most impact on incoming particles with low energy. For reconstructed COT tracks, not accounting for MCS results in an underestimation of the errors on track measurements. To correct for MCS, the elements of the track covariance matrix must be rescaled as reported in Ref. [53].

The second effect is the energy loss of a particle due to interactions with both the active and passive materials in a detector. As the particle loses energy its momentum decreases, and thus the curvature of the track changes along the particle's path. The previous track reconstruction assumed the same curvature along the entire path. The energy loss per unit length in a material is dependent on the type of particle being tracked, as the interaction cross-sections change for different particles. The tracks must be refit taking this into consideration. The refit is performed separately for pion, kaon, and muon track hypothesis using a Kalman fitter [54]. Ref. [53] also makes a measurement of the magnetic field inside the tracking volume and a description of the silicon geometry, both of which contribute to track reffiting.

4.1.3 Vertex Fitting and Preselection

Having prepared a set of tracks for every event, these traces of quasi-stable particles must be combined into various levels of heavy unstable parent particles. The main tool for this task is the CTVMFT vertex fitting package [55] which performs a three-dimensional fit of two or more track helices to a common origin. Requirements for acceptable vertices are imposed on the fit χ^2, spatial displacement, or kinematic variables such as momentum and mass.

The reconstruction of vertices begins with the most basic unstable particles which decay only to stable tracks. A few of the many possible examples include $\phi \to K^+K^-$, $\bar{D}^0 \to K^+\pi^-$, and $\Lambda_c^+ \to pK^-\pi^+$. Tracks are combined from the collections of pions and kaons as appropiate, where care is taken not to combine duplicate tracks. The charge of the tracks is often considered, so as not to expend CPU time making vertices with nonsensical charge correlations. After screening these candidate vertices with loose requirements, they are combined by the fitting package with an additional track to produce more massive unstable particles. The decays of $D_s^- \to \phi\pi^-$ and $\Lambda_b^0 \to \Lambda_c^+\pi_b^-$ are examples of this level. The fits may also include pointing constraints, such that the total vertex momentum is assumed to originate from the primary vertex, or mass constraints, such that constituent unstable particles are assumed to have a certain mass when fitted with another track. Such procedures may be repeated indefinitely to build decays of any complexity, with intermediate requirements on fit quality, position, and kinematics.

4.2 Σ_b Data Sample

The detailed reconstruction procedure for the $\Sigma_b^\pm \to \Lambda_b^0\pi^\pm$, $\Lambda_b^0 \to \Lambda_c^+\pi_b^-$, $\Lambda_c^+ \to pK^-\pi^+$ decay chain is outlined here. Figure 4.1 shows the topology of a Σ_b event produced in the CDF II detector. There is two decay vertex separated from the primary interaction point.

The reconstruction begins with three tracks, assumed to be proton, kaon and pion, that they are fitted to a common vertex. The resulting Λ_c^+ candidate is accepted if satisfy the following requirements:

- $\chi^2_{xy} < 20$,
- $2.200 < M(pK^-\pi^+) < 2.380$ GeV/c^2,
- $|\Delta z_0| < 1.5$ cm between the tracks.

Tracks from the pion collection are then fitted in turn to each Λ_c^+ candidate vertex, provided that they are not one of the three tracks from the Λ_c^+. Only resultant vertices that meet the following conditions are accepted for the $\Lambda_b^0 \to \Lambda_c^+\pi_b^-$ collection:

- $\chi^2_{xy} < 40$,
- $2.260 < M(pK^-\pi^+) < 2.311$ GeV/c^2,

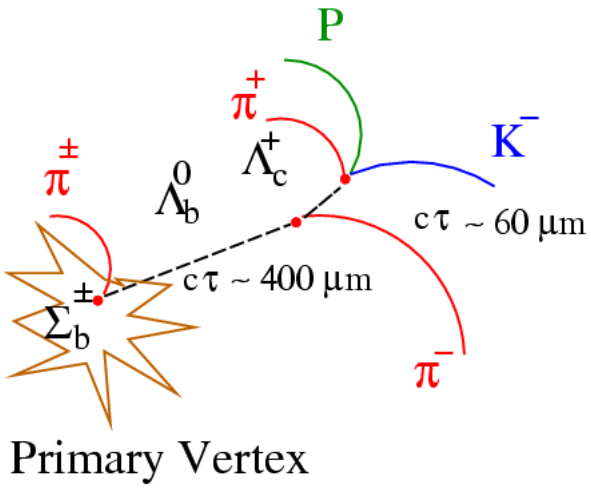

Figure 4.1: *Sketch of the event topology of a Σ_b produced in the* CDF II *detector. The tracks from the primary vertex are from the b quark hadronization and the hadronization of the $p\bar{p}$ debris.*

- Mass constraint: $M(pK^-\pi^+) = 2.28646$ GeV/c^2
- $4.500 < M(\Lambda_c^+\pi_b^\pm) < 7.000$ GeV/c^2,

Finally, the momentum vectors of Λ_b^0 candidates are combined with a pion track. The following requirements are imposed:

- $\chi^2_{xy} < 100$
- $5.200 < M(\Lambda_b^0 \to \Lambda_c^+\pi_b^-) < 6.500$ GeV/c^2,
- $5.00 < M(\Lambda_b^0\pi^\pm_{soft}) < 6.70$ GeV/c^2,

The final pions is often referred to as the "soft pion" due to its low momentum.

The tracks comprising each candidate are additionally subjected to *trigger confirmation*, which verifies that the SVT was triggered by two displaced tracks in this candidate and not some other part of the event. The final parameterization of each track is compared to the online tracks fitted by the SVT, and a threshold of agreement is applied to the χ^2 of the curvature and ϕ_0 parameters in order to identify a match. The SVT requirements on impact parameter and p_T are verified for the final versions of matched tracks, and only Σ_b candidates which contain both tracks are accepted for analysis.

Table 4.1 summarizes the selection criteria for $\Sigma_b^{(*)\pm}$ reconstruction.

Candidate/Collection	Criteria
$\Lambda_c^+ \to pK^-\pi^+$/`Lc-PKPi`	made from basic `Pions`,`Kaons`,`Protons`
charge Q	$= \pm 1$
vertex fit with $\chi^2_{r\phi}$	< 20.0
$\Delta(z_0)$	$< 1.5\,\mathrm{cm}$
$p_T(\pi), p_T(K), p_T(p)$	$> 0.350\,\mathrm{GeV}/c^2$
$M(pK^-\pi^+)$	$\in (2.200,\ 2.380)\,\mathrm{GeV}/c^2$
trigger confirmation	the `B_CHARM_LOWPT` imposed per event,
	≥ 1 trigger track $\in (\mathrm{p}, \mathrm{K}, \pi)$
$\Lambda_b^0 \to \Lambda_c^+\pi_b^\pm$/`Lb-LcPi-PKPi`	made from composite `Lc-PKPi` and basic `Pions`
charge Q	$= 0,\ \pm 2$
vertex fit with $\chi^2_{r\phi}$	< 40.0
and $M(\Lambda_c^+ \to pK^-\pi^+)$	$\in (2.260,\ 2.311)\,\mathrm{GeV}/c^2$ or
	$\approx (2.28646 \pm 4 \cdot \sigma)\,\mathrm{GeV}/c^2$
mass constraint: $M(pK^-\pi^+)$	"true", i.e. set $= 2.28646\,\mathrm{GeV}/c^2$ (PDG)
vertex information	linked to branches with Primary
	and 2-ndary VX info per event
$p_T(\pi), p_T(K), p_T(p)$	$> 0.350\,\mathrm{GeV}/c^2$
$p_T(\pi_b^\pm)$	no cut set, threshold is propagated via trigger
$M(\Lambda_c^+\pi_b^\pm)$	$\in (4.500,\ 7.000)\,\mathrm{GeV}/c^2$
trigger confirmation	the `B_CHARM_LOWPT` imposed per event,
	≥ 2 trigger track $\in (\mathrm{p}, \mathrm{K}, \pi^+, \pi^-_\mathrm{b})$, i.e.
	Λ_b^0 **candidate does fire the** `B_CHARM_LOWPT`
$\Sigma_b^{(*)\pm} \to \Lambda_b^0\pi^\pm_{soft}$	made from
`Sb-LbPi-LcPi-PKPi`	composite `Lb-LcPi-PKPi` and and basic `Pions`
charge Q	$= \pm 1$
vertex fit with $\chi^2_{r\phi}$	< 100.0
and $M(\Lambda_b^0 \to \Lambda_c^+\pi_b^\pm)$	$\in (5.200,\ 6.500)\,\mathrm{GeV}/c^2$ or
	$\approx (5.619^{+46\cdot\sigma}_{-22\cdot\sigma})\,\mathrm{GeV}/c^2$
mass constraint	"false", i.e. not set
vertex information	linked to branches with Primary
	and 2-ndary VX info per event
$p_T(\pi), p_T(K), p_T(p)$	$> 0.350\,\mathrm{GeV}/c^2$
$p_T(\pi_b^\pm)$	no cut set, threshold is propagated via trigger
$p_T(\pi^\pm_{soft})$	$\gtrsim 0.200\,\mathrm{GeV}/c^2$, coming from `Pions`
$M(\Lambda_b^0\pi^\pm_{soft})$	$\in (5.00,\ 6.70)\,\mathrm{GeV}/c^2$

Table 4.1: *The collections of candidates to be used in the analysis and their selection criteria set in BStNtuple [56] branches.*

4.3 Σ_b Monte Carlo Sample

Our resolution calculations are based on a large statistics Monte Carlo sample. The exclusive $\Sigma_b^{(*)+} \to \Lambda_b^0 \pi^+_{\Sigma_b}$ modes for positive charge states are generated with `Bgen` [57] with the natural width of a particular mode set to zero to measure only detector effects. The output of `Bgen` is fed into a full detector simulation `cdfSim` and then reconstructed and ntuplelized as the data.

The final files with the MC ntuple are analized and the detector response spectra are fitted with Gaussians. The results of this study are detailed in Sec. 5.4.1.

Chapter 5

$\Sigma_b^{(*)}$ Measurement

5.1 Analysis Cuts: Λ_b^0

The background in Q-value distribution is composed from

- the background under the Λ_b^0 signal candidates in $M(\Lambda_c^+\pi^-)$ spectrum combined with soft $\pi^\pm$ pion tracks with their momenta extending to a low range of $p_T \sim 200\,\mathrm{MeV}/c$.
- the Λ_b^0 signal candidates combined with soft $\pi^\pm$ originating from hadronization processes like b-quark fragmentation into various bottom baryon states.

The background shape of Q-spectra is expected to show a typical threshold $\sqrt{Q-thr}$- like behaviour. That is we have to be concerned with the analysis cuts for Λ_b^0 in a combination with soft pion and contributing to the low edge of mass difference Q spectrum with the finest resolution.

As we understand now (see our studies in [68]) the next criteria for Λ_b^0 candidates are the most powerfull in the background rejection and for the Λ_b^0 signal efficiency

- $c\tau(\Lambda_b^0)/\sigma_{c\tau}$, the Λ_b^0 decay path expressed in terms of its error. The Λ_b^0 decay path in the Λ_b^0 rest frame is defined as

$$c\tau(\Lambda_b^0) = L_{xy} \cdot \frac{M(\Lambda_b^0)}{p_T(\Lambda_b^0)}$$

  , where L_{xy} is defined in a transversal plane as

$$L_{xy}(\Lambda_b^0) = \vec{D}_{xy} \cdot (\vec{p}_{xy}/p_T)$$

- $|d_0|(\Lambda_b^0)$, the impact parameter of the Λ_b^0 candidate defined in the transversal plane as

$$|d_0|(\Lambda_b^0) = \left|\vec{D}_{xy} \times (\vec{p}_{xy}/p_T)\right|$$

- $\vec{D}_{xy}$ is a position of the Λ_b^0 decay vertex w.r.t. to primary vertex in the transversal plane.

- $p_T(\pi_b^-)$, the transverse momentum of a prompt pion from $\Lambda_b^0 \to \Lambda_c^+ \pi_b^-$ decay.

The track quality criteria for Λ_b^0 tracks are tightened at the analysis stage. The track quality cuts are shown in Table 5.1.

Track Parameter	Analysis Cut
Track Collections	`Protons`, `Kaons`, `Pions`
COT stereo hits	≥ 10
COT axial hits	≥ 10
SVX $r-\phi$ hits	≥ 3
$\lvert d_0 \rvert$	$< 0.1\,\text{cm}$
p_T	$> 400\,\text{MeV}/c$

Table 5.1: *Λ_b^0 Candidates: Track Quality Cuts*

The full set of Λ_b^0 cuts defining the starting point of the analysis cuts area is shown in Table 5.2. The cuts shown in the Table 5.2 are based on our previous experience with Σ_b analysis [68] and most of the cuts are set to very relaxed values. Cuts #1, 2, 6, 13 confirm the conditions imposed at the Two-Track Trigger (TTT) level or at *BStNtuple* production step. Cut #8 confirms the requirement $L_{xy} > 200\,\mu\text{m}$ set with TTT tracks at Level 3 Trigger. The tracks involved in Λ_c^+ and Λ_b^0 reconstruction have the lowest momenta initially set to $p_T \geq 400\,\text{MeV}/c$ where the CDF tracking efficiency flattens.

5.1.1 Optimization of Λ_b^0

At present with $\int \mathcal{L}\,dt \sim 6.0\,\text{pb}^{-1}$ we are in a possession of a largest sample of fully reconstructed with hadronic mode Λ_b^0 baryons reaching of ~ 17000 entries in a signal. Henceforth the optimization of the selection criteria based on the experimental data turns to be possible now. At the beginning we tried different optimization for `B_CHARM_SCENA` and `B_CHARM_LOWPT` samples, but results of the optimization have been very similar for both cases and both TTT trigger flavours are treated as one sample.

Here we use our optimization technique discussed in the early CDF note [68] on $\Sigma_b^{(*)}$ measurement. The figure of merit (F.O.M.) used in the optimization is defined as $S/\sqrt{S+B}$, where S and B were the total number of signal and background candidates that pass the cuts obtained from the binned fit. S is determined as the number of entries in the fitted signal model within $\pm 3 \cdot \sigma$, where σ results from the same fit. B is determined as the number of entries in the fitted background model with the same $\pm 3 \cdot \sigma$.

The cuts under the optimization are the following ones:

- $c\tau(\Lambda_b^0)/\sigma_{c\tau}$

#	Variable	Cut value
1	trigger confirmation	`B_CHARM_LOWPT`
2	$\chi^2_{r\phi}(\Lambda_c^+)$	< 20
3	$\lvert m(\Lambda_c^+\pi^-) - m(\Lambda_b^0)\rvert$	$< 3 \cdot 19.22\,\mathrm{MeV}/c^2$, $\pm 3\sigma$
4	$p_T(\Lambda_c^+)$	no cut
5	proton ID	no PID involved
6	$\chi^2_{r\phi}(\Lambda_b^0)$	< 40
7	Prob(χ^2_{3D}) of Λ_b^0 vertex fit	> 0.0001
8	$c\tau(\Lambda_b^0)$	$> 100\,\mu$m
9	$c\tau(\Lambda_b^0)/\sigma_{c\tau}$	> 2.0
10	$\lvert d_0(\Lambda_b^0)\rvert$	$< 250\,\mu$m
11	$c\tau(\Lambda_c^+ \leftarrow \Lambda_b^0)$	$> -300\,\mu$m
12	$c\tau(\Lambda_c^+ \leftarrow \Lambda_b^0)$	$< 500\,\mu$m
13	$p_T(\Lambda_b^0)$	$> 4.0\,\mathrm{GeV}/c$
14	$p_T(\pi_b^-)$	$> 0.4\,\mathrm{GeV}/c$
15	$p_T(p)$	$> 0.4\,\mathrm{GeV}/c$
16	$p_T(K^-)$	$> 0.4\,\mathrm{GeV}/c$
17	$p_T(\pi^+)$	$> 0.4\,\mathrm{GeV}/c$

Table 5.2: *The initial values of the analysis cuts for Λ_b^0 reconstruction. The Λ_b^0 mass and σ values refered in the Cut #3 are obtained using our full data sample (see Table 5.7).*

- $c\tau(\Lambda_b^0)$
- $c\tau(\Lambda_c^+ \leftarrow \Lambda_b^0)$
- $|d_0|(\Lambda_b^0)$
- $p_T(\pi_b^-)$

We perform a simultaneous optimization of all cuts using an iterative procedure similar to the one described in the discovery analysis [70].

The optimization scans are shown at Figure 5.1.

Fitter of $\mathbf{\Lambda_b^0}$

For our optimization and Λ_b^0 yield estimates we use the fitter developed by R. Tesarek and co-workers [72] and by M. Martin, P. Maksimovich and co-workers [73].

The Λ_b^0 signal is modeled by a Gaussian function.

The following backgrounds contribute to the mass spectrum of $M(\Lambda_b^0 \to \Lambda_c^+\pi_b^-)$:

- Cabibbo suppressed decay $\Lambda_b^0 \to \Lambda_c^+ K^-$ with a peak at $\sim 50\,\mathrm{MeV}/c^2$ below Λ_b^0 signal peak. The contribution is modeled by two Gaussians.
- Four-prong mis-identified B-mesons: all B-mesons with four tracks in the final state, fully reconstructed. The mode $B^0 \to D^-\pi^+$ contributes here at $\sim 50\%$. The $B \to 4\,\mathrm{prongs}$ modes produce a peak at the left from the Λ_b^0 signal peak and are modeled by a sum of a Gaussian and a Landau functions.
- The remaining B- meson decays , modeled by the sum of an exponential function and a product of a bifurcated Gaussian with a step-down function.
- The remaining Λ_b^0 decays modeled by the sum of two Gaussians and the product of a bifurcated Gaussian and a step-down function.
- The combinatorial background which is described by an exponential function.
- Several parameters of the combined background model are fixed, based on MC templates or ratios of $\mathcal{B}$-fractions taken from known measurements.

5.1.2 Yields with Optimized Cuts for $\mathbf{\Lambda_b^0}$

To understand the background level, the statistics available with *BStNtuple* datasets and the effect of optimization, we have reconstructed Λ_b^0 signals with still very mild cuts shown in Table 5.3. Only cuts changed w.r.t. to Table 5.2 are shown. The cuts on $c\tau(\Lambda_c^+ \leftarrow \Lambda_b^0)$ have been set to its optimal values, please see the second row of plots at Figure 5.1.

We process only data from run periods passing the official quality requirements set by the CDF II Data Quality Management group (see Appendix B for further details).

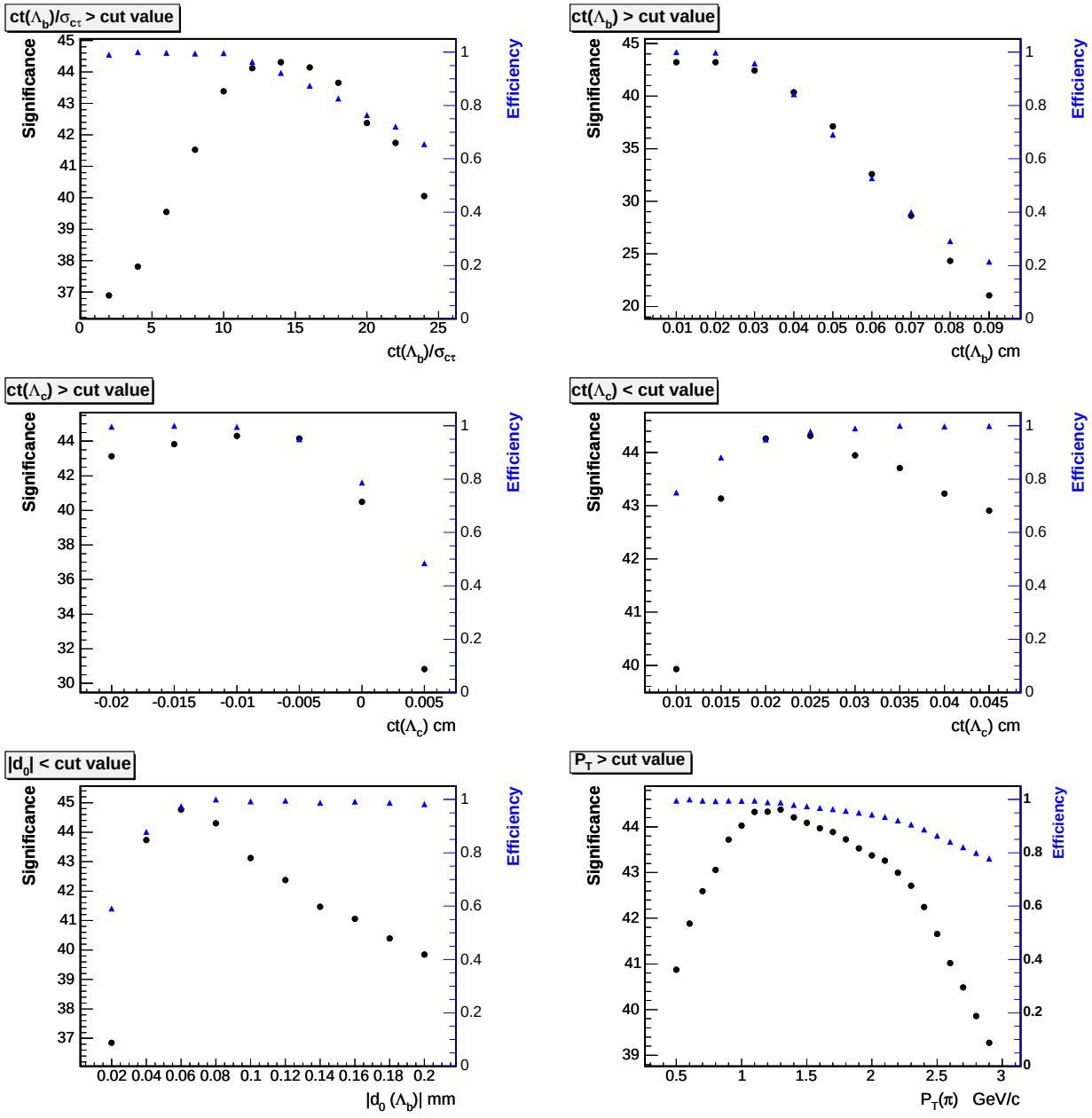

Figure 5.1: *Optimization scan for $c\tau(\Lambda_b^0)/\sigma_{C\tau}$, $c\tau(\Lambda_b^0)$ (first row), $c\tau(\Lambda_c^+ \leftarrow \Lambda_b^0)$ (second raw), $|d_0|(\Lambda_b^0)$ and $p_T(\pi_b^-)$ (third raw). Black circles (left scale) correspond to F.O.M. as a function of cut on a variable in question. Blue triangles (right scale) show signal efficiency as determined from binned fit. The choice of cuts is shown in Table 5.5.*

Variable	Cut value
$c\tau(\Lambda_b^0)/\sigma_{c\tau}$	> 3.0
$\lvert d_0(\Lambda_b^0)\rvert$	$< 150\,\mu$m
$c\tau(\Lambda_c^+ \leftarrow \Lambda_b^0)$	$> -150\,\mu$m
$c\tau(\Lambda_c^+ \leftarrow \Lambda_b^0)$	$< 250\,\mu$m
$p_T(\Lambda_b^0)$	$> 4.0\,\mathrm{GeV}/c$
$p_T(\pi_b^-)$	$> 0.7\,\mathrm{GeV}/c$

Table 5.3: *The cut values for Λ_b^0 signals shown at Figures 5.2*

The reconstructed according to Table 5.3 and fitted **inclusive** Λ_b^0 signals found with every dataset are shown at Figure 5.2. The signal and its background are fitted with the fitter developed by R. Tesarek and co-workers [72]. The corresponding yields are summarized in Table 5.4. Even with the mild cuts the mass distributions exhibit powerfull peaks on top of the background with a typical ratio of $S/B \sim 1/2$.

BStNtuple dataset	Period span	$\int \mathcal{L}\,dt$, pb^{-1}	$N_{\mathrm{signal}}(\, c\tau(\Lambda_b^0)/\sigma_{c\tau} > 3,$ $\lvert d_0\rvert(\Lambda_b^0) < 150\,\mu\mathrm{m}, p_T(\pi_\mathrm{b}^-) > 0.7\,\mathrm{GeV/c}\,)$
`xbhdid`	0	344.78	2253 ± 91
`xbhdih`	$1 - 4$	397.76	2813 ± 98
`xbhdii`	$5 - 10$	894.86	2977 ± 99
`xbhdij`	$11 - 13$	703.11	2238 ± 66
`xbhdik`	$14 - 17$	498.23	1766 ± 77
`xbhdfm`	$18 - 28$	3159.04	5800 ± 135
total stat.	$0 - 28$	5997.79	17855 ± 247

Table 5.4: *The yields of Λ_b^0 signals for every dataset composing the total data sample. Every dataset consists of several periods.*

To demonstrate the development (or deterioration) of the CDF Trigger and DAQ conditions w.r.t. observed Λ_b^0 yields we produced a graph with Λ_b^0 yields obtained with minimal cuts of Table 5.3 and normalized to $100\,\mathrm{pb}^{-1}$ of every dataset. The upper plot at Figure 5.3 corresponds to the Table 5.4. The bottom plot shows the Λ_b^0 signal obtained with minimal cuts and the total statistics of Periods $0 - 28$.

Now we make our choice of analysis cuts according to Figure 5.1. The cut on absolute value $c\tau(\Lambda_b^0) > 200\,\mu$m practically confirms the cut applied at *BStNtuple* production which in turns confirms the Level 3 threshold. The $c\tau(\Lambda_b^0)/\sigma_{c\tau} > 12$ is selected right at the maximum of F.O.M. The cut of $\lvert d_0\rvert(\Lambda_b^0) < 80\,\mu$m is selected at the F.O.M. point next after the maximum keeping $\sim 100\%$ efficiency and still high F.O.M. value. The upper cut on $c\tau(\Lambda_c^+ \leftarrow \Lambda_b^0)$ is fixed to be at the maximum of F.O.M., viz. $< 250\,\mu$m. The lower cut on this variable is taken to be the next to F.O.M. maximum, with $\sim 100\%$ efficiency and

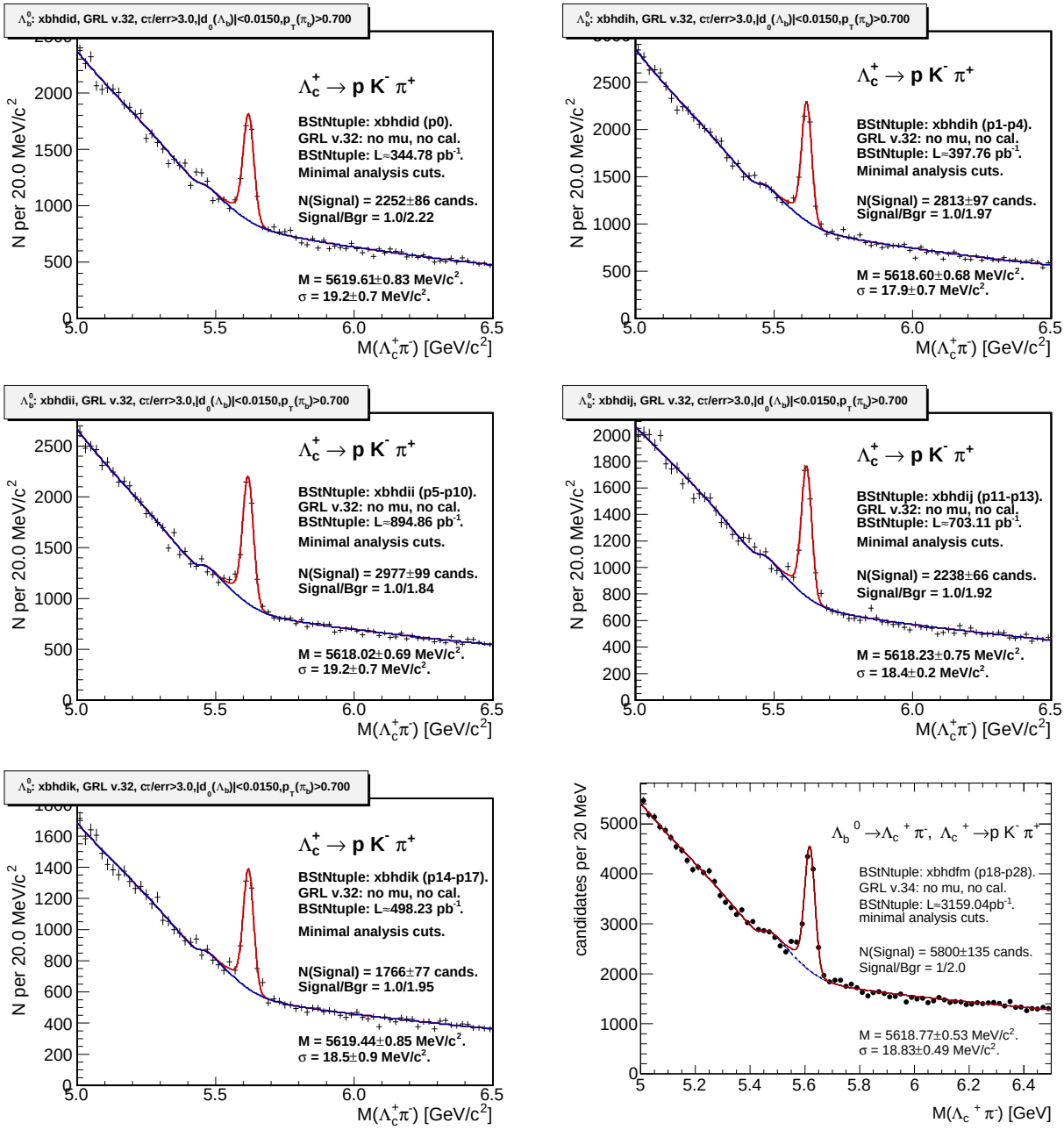

Figure 5.2: **Inclusive** *mass spectra* $\mathbf{M(\Lambda_b^0 \to \Lambda_c^+ \pi_b^-,\ \Lambda_c^+ \to pK^-\pi^+)}$ *with the several datasets composing the total data sample. The number of candidates* $N/20\,\mathrm{MeV}/c^2$ *is plotted. The minimal cuts* $c\tau(\Lambda_b^0) > 0.0200$, $c\tau(\Lambda_b^0)/\sigma_{c\tau} > 3.0$, $|d_0(\Lambda_b^0)| < 0.0150$, $p_T(\pi_b^-) > 0.7\,\mathrm{GeV}/c$ *are applied here. The large significant signals are seen on top of a high background level with ratio* $S/B \approx 1/2$.

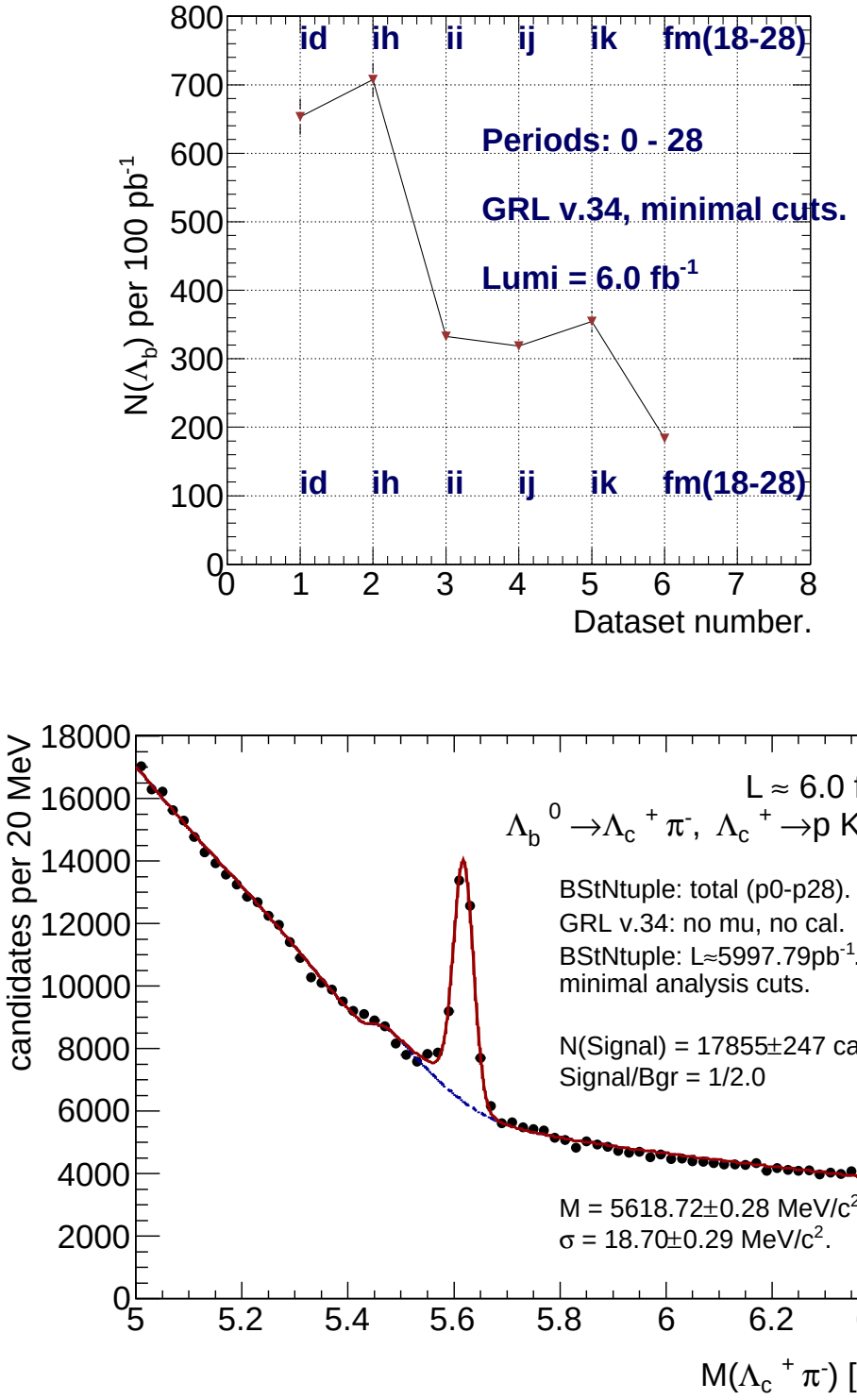

Figure 5.3: *Λ_b^0 yields per $100\,pb^{-1}$ for Λ_b^0 signal (upper plot) reconstructed with minimal cuts, Table 5.4. The several datasets composing the total data sample are plotted along x-axis. The bottom plot shows the Λ_b^0 signal reconstructed with minimal cuts using the total statistics.*

being symmetrical according to the shape of the experimental distribution and w.r.t. to the upper cut.

The choice of cuts for Λ_b^0 is arranged into the Table 5.5, the cut values specified in this table override the ones listed in Table 5.2.

Variable	Cut value
$c\tau(\Lambda_b^0)$	$> 200\,\mu$m
$c\tau(\Lambda_b^0)/\sigma_{c\tau}$	> 12.0
$\lvert d_0(\Lambda_b^0)\rvert$	$< 80\,\mu$m
$c\tau(\Lambda_c^+ \leftarrow \Lambda_b^0)$	$> -150\,\mu$m
$c\tau(\Lambda_c^+ \leftarrow \Lambda_b^0)$	$< 250\,\mu$m
$p_T(\pi_b^-)$	$> 1.5\,\mathrm{GeV}/c$

Table 5.5: *The optimized cut values for Λ_b^0 signals chosen with scans demonstrated at Figure 5.1.*

The reconstructed according to Table 5.5 and fitted [72] **inclusive** Λ_b^0 signals found with every dataset are shown at Figure 5.4. The corresponding yields are summarized in Table 5.6. The signal to background ratio became significantly better, viz. $S/B \sim 2.1/1$. The fit results for the Λ_b^0 mass and signal width values extracted from the signal spectra

BStNtuple dataset	Period span	$\int \mathcal{L}\,dt$, pb^{-1}	$N_{\mathrm{signal}}(\, c\tau(\Lambda_b^0)/\sigma_{c\tau} > 12,$ $\lvert d_0\rvert(\Lambda_b^0) < 80\,\mu\mathrm{m}, p_T(\pi_b^-) > 1.5\,\mathrm{GeV/c}\,)$
`xbhdid`	0	344.78	1997 ± 59
`xbhdih`	$1 - 4$	397.76	2578 ± 67
`xbhdii`	$5 - 10$	894.86	2696 ± 67
`xbhdij`	$11 - 13$	703.11	2073 ± 61
`xbhdik`	$14 - 17$	498.23	1580 ± 52
`xbhdfm`	$18 - 28$	3159.04	5409 ± 100
total stat.	$0 - 28$	5997.79	16333 ± 170

Table 5.6: *The yields of inclusive Λ_b^0 signals for every dataset with the optimized cuts applied.*

at Figure 5.4 are arranged in Table 5.7.

Again, we demonstrate the development (or deterioration) of the CDF Trigger and DAQ conditions w.r.t. observed Λ_b^0 yields producing a graph with Λ_b^0 yields obtained with optimal cuts of Table 5.5 and normalized to $100\,\mathrm{pb}^{-1}$ of every dataset. The upper plot at Figure 5.5 corresponds to the Table 5.6. The bottom plot shows the Λ_b^0 signal obtained with optimal cuts and the total statistics available.

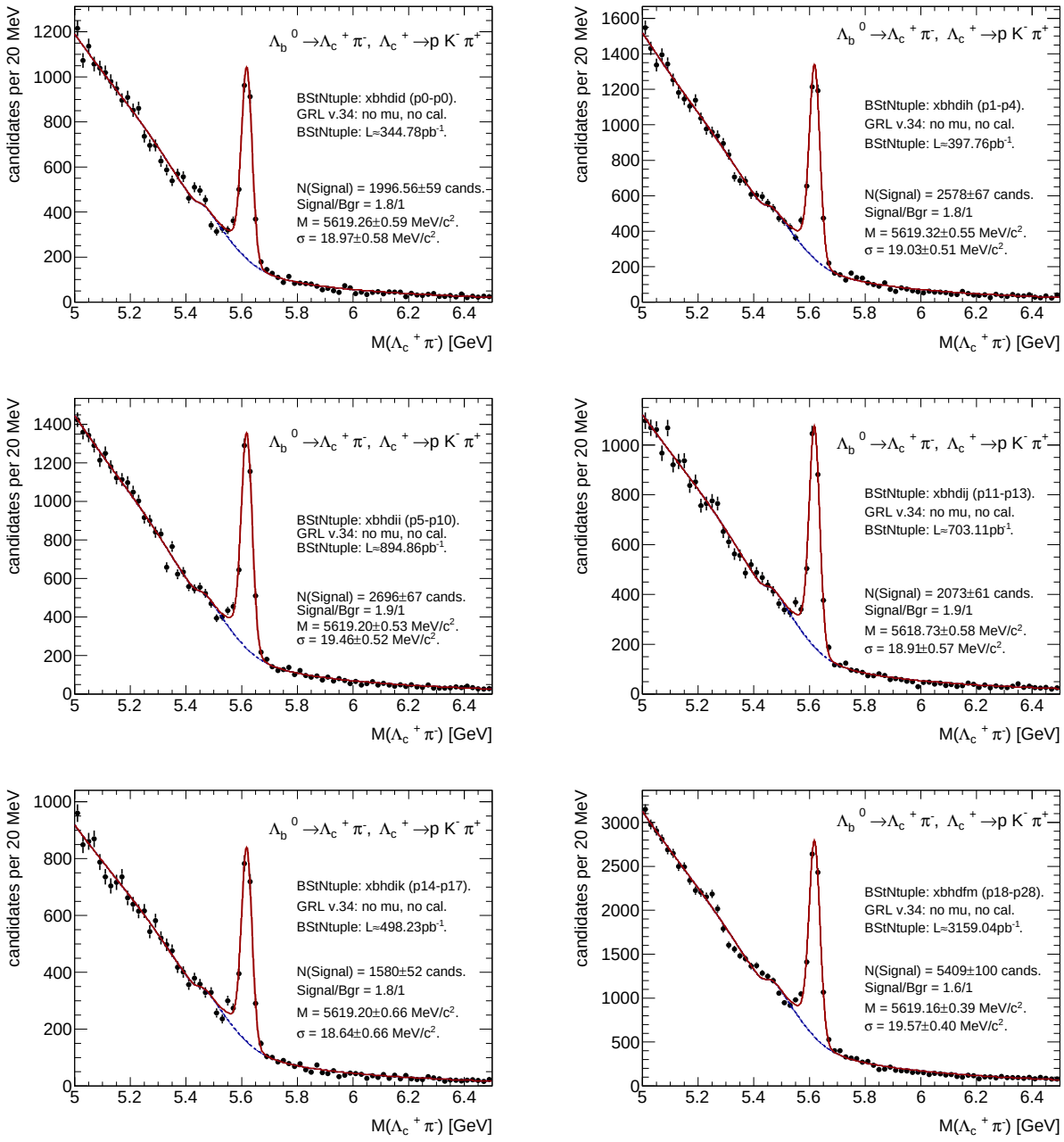

Figure 5.4: **Inclusive** *mass spectra* $\mathbf{M(\Lambda_b^0 \to \Lambda_c^+ \pi_b^-,\ \Lambda_c^+ \to pK^- \pi^+)}$ *with optimized requirements over the several datasets composing the total data sample. The number of candidates* $N/20\,\mathrm{MeV}/c^2$ *is plotted. The optimized cuts* $c\tau(\Lambda_b^0) > 0.0200$, $c\tau(\Lambda_b^0)/\sigma_{c\tau} > 12.0$, $|d_0|(\Lambda_b^0) < 0.0080$, $p_T(\pi_b^-) > 1.5\,\mathrm{GeV}/c$ *are applied here. The typical signal to background ratio is* $S/B \approx 1.8/1$.

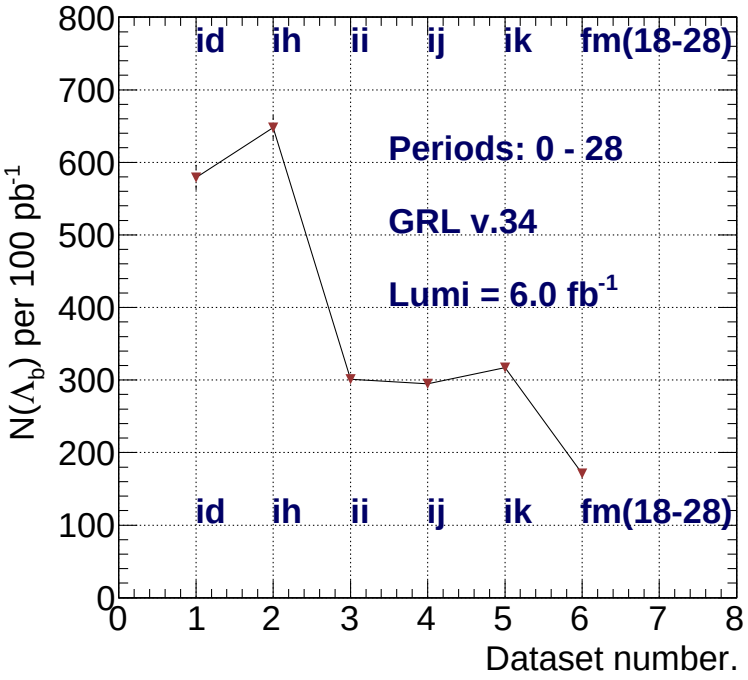

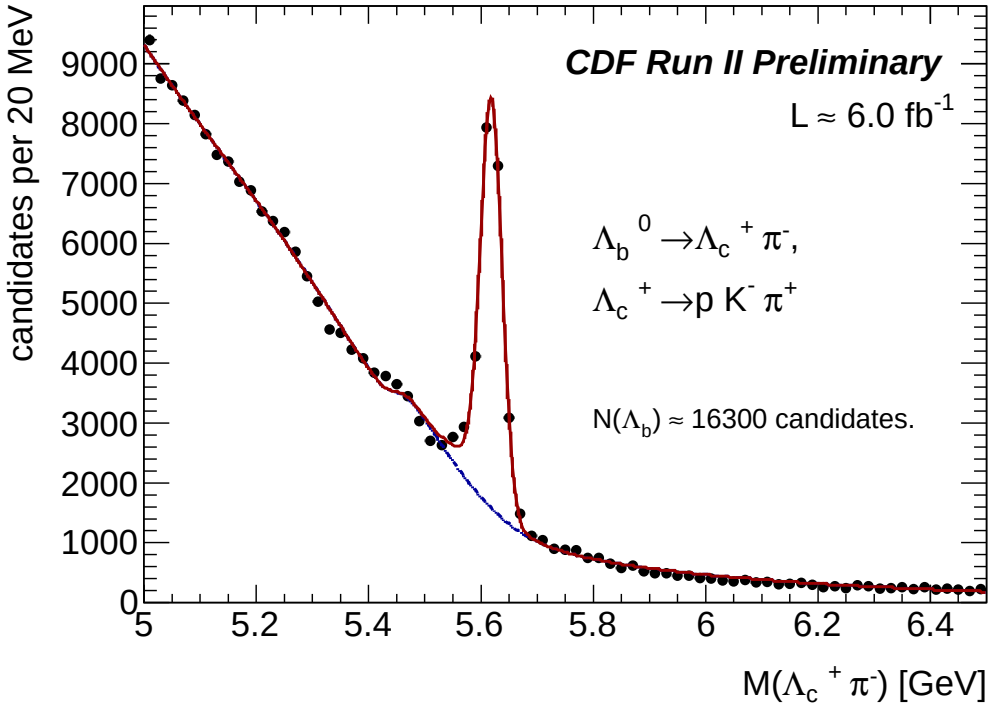

Figure 5.5: *Λ_b^0 yields per 100 pb^{-1} for Λ_b^0 signal (upper plot) reconstructed with cuts selected after optimization, Table 5.5. The several datasets composing the total data sample are plotted along x-axis. The bottom plot shows the Λ_b^0 signal reconstructed with optimized cuts using the total statistics.*

BStNtuple dataset	Period span	$M(\Lambda_b^0)$, MeV/c^2	σ_M, MeV/c^2
`xbhdid`	0	5619.26 ± 0.59	18.97 ± 0.58
`xbhdih`	1 − 4	5619.32 ± 0.55	19.03 ± 0.51
`xbhdii`	5 − 10	5619.20 ± 0.53	19.46 ± 0.52
`xbhdij`	11 − 13	5618.73 ± 0.58	18.91 ± 0.57
`xbhdik`	14 − 17	5619.20 ± 0.66	18.64 ± 0.66
`xbhdfm`	18 − 28	5619.16 ± 0.39	19.57 ± 0.40
total stat.	0 − 28	5619.15 ± 0.22	19.22 ± 0.22

Table 5.7: *The fit results for mass values and widths and their statistical errors of inclusive Λ_b^0 signals for every dataset with the optimized cuts applied. This table corresponds to the Table 5.6.*

5.2 Analysis Cuts: $\Sigma_b^{(*)}$

The basic track quality criteria for the soft pion track are somewhat loose w.r.t. nominal tracks contributing to the Λ_b^0 candidate, see a Table 5.1 of Section 5.1. The "stand alone" tracks with the only hits found in SVX II silicon tracker are used as well. The selection criteria applied to the soft pion track are arranged into a Table 5.8. Here we are driven by saving the soft track efficiency.

Track Parameter	Analysis Cut
Track Collections	`Pions`
Hit Selection:	
COT stereo hits	no hits found
COT axial hits	no hits found
SVX $r-\phi$ hits	≥ 4
OR	
Any of COT, stereo **or** axial, hits	≥ 1
SVX $r-\phi$ hits	≥ 3
$\lvert d_0 \rvert$	< 0.1 cm
p_T	> 200 MeV/c

Table 5.8: $\Sigma_b^{(*)\pm}$ *Candidates:* $\pi_{soft}^{\pm}$ *Track Quality Cuts*

The optimization of the cuts for the soft pion and a further confirmatiom of the cuts fixed for the Λ_b^0 candidates was performed based on the yield of the $\Sigma_b^{(*)\pm}$ $Q-$value spectrum, where $Q = M(\Lambda_b^0\pi_{soft}^{\pm}) - M(\Lambda_b^0) - m_\pi$. We use $S/\sqrt{S+B}$ as our figure of merit (FOM), where S is the addition of the yields of $\Sigma_b^{\pm}$ and $\Sigma_b^{*\pm}$, and B is the integral

of the background function within $(Q_1 - 3\cdot\sigma_1)$ and $(Q_2 + 3\cdot\sigma_1)$. Here, $Q_1 = Q(\Sigma_b^{\pm})$, $Q_2 = Q(\Sigma_b^{*\pm})$, and $\sigma_1 = \sqrt{\Gamma + \sigma_{res}}$, $\sigma_2 = \sqrt{\Gamma^* + \sigma_{res}}$ are "effective sigmas" built combining the intrinsic widths of the peaks with the resolution detector from Table 5.11. We kept fixed the natural widths of the peaks for convenience reasons to the values predicted by HQET using the following formula [74]:

$$\Gamma_{\Sigma_b \to \Lambda_b^0 \pi} = \frac{1}{64} \frac{M(\Lambda_b^0)}{M(\Sigma_b)} |f_p|^2 |\vec{p}|^3$$

where $f_p = g_A/f_\pi$, $g_A = 0.75$ is the constituent pion-quark coupling, $f_\pi = 92$ MeV is the pion decay constant, and the momentum of the pion in the Σ_b center of mass frame is $\vec{p}$.

Using this equation we obtain the width values:

$$\Gamma(\Sigma_b) \approx 7\,\mathrm{MeV}/c^2$$

and

$$\Gamma(\Sigma_b^*) \approx 12\,\mathrm{MeV}/c^2$$

Each cut was scanned separately of the other cuts. That means, that for every cut we perform a scan of it while the other cuts are kept fixed. The scans are performed in the following way: for each value of the cut being scanned we plot the Σ_b Q- value distribution. From this distribution we obtain the FOM as explained above. The efficiency of the cut at that step of the scan is defined as the ratio of S over S_{max}, being S_{max} the highest yield obtained during the whole scan. At Figures 5.6 and 5.7 the scans performed for several cuts corresponding with the $\Lambda_b^0 \pi^-_{\Sigma_b}$ sign are shown. The Figures 5.8 and 5.9 contains the corresponding plots for the $\Lambda_b^0 \pi^+_{\Sigma_b}$. The Table 5.9 shows the final cuts of the analysis after the optimization. The cuts for Λ_b^0 reconstruction are based on our optimization scans made with Λ_b^0 signal, see Figure 5.1 and the Table 5.5. The cut for the soft pion, namely for its impact parameter siginificance, $|d_0/\sigma_{d_0}|(\pi_{soft})$, are based on the scans shown at the Figure 5.7 and the Figure 5.9.

5.2.1 Duplicate Candidates in $\mathbf{\Sigma_b^{(*)}}$

The necessary low cut on the soft pion momentum moves the analysis into the realm where CDF tracking has a lower than 100% efficiency: it is well known that the tracking reaches a 100% efficiency plateau for $p_T > 0.4\,\mathrm{GeV}/c^2$.

There is a well known issue in the tracking reconstruction: the low p_T tracks are prone to be duplicated in the CDF default `defTracks` track collection.

While the duplicated events with the same run#, event# numbers are rejected with a special module provided with a `BottomMods` package, the duplicate $\Sigma_b^{(*)}$ candidates due to explained above feature do contribute to the Q-value spectra.

We reject all the candidates suspicious to be duplicate.

- The $\Sigma_b^{(*)\pm}$ candidates contributing to the $Q \in (0.0, 0.210)\,\mathrm{GeV}/c^2$ spectra at the final analysis cuts of Table 5.9 and having within the same run#, event# a partner contributing to the same spectrum but different by only $\Delta Q < 0.3\,\mathrm{MeV}/c^2$ have been listed individually for every charge state.

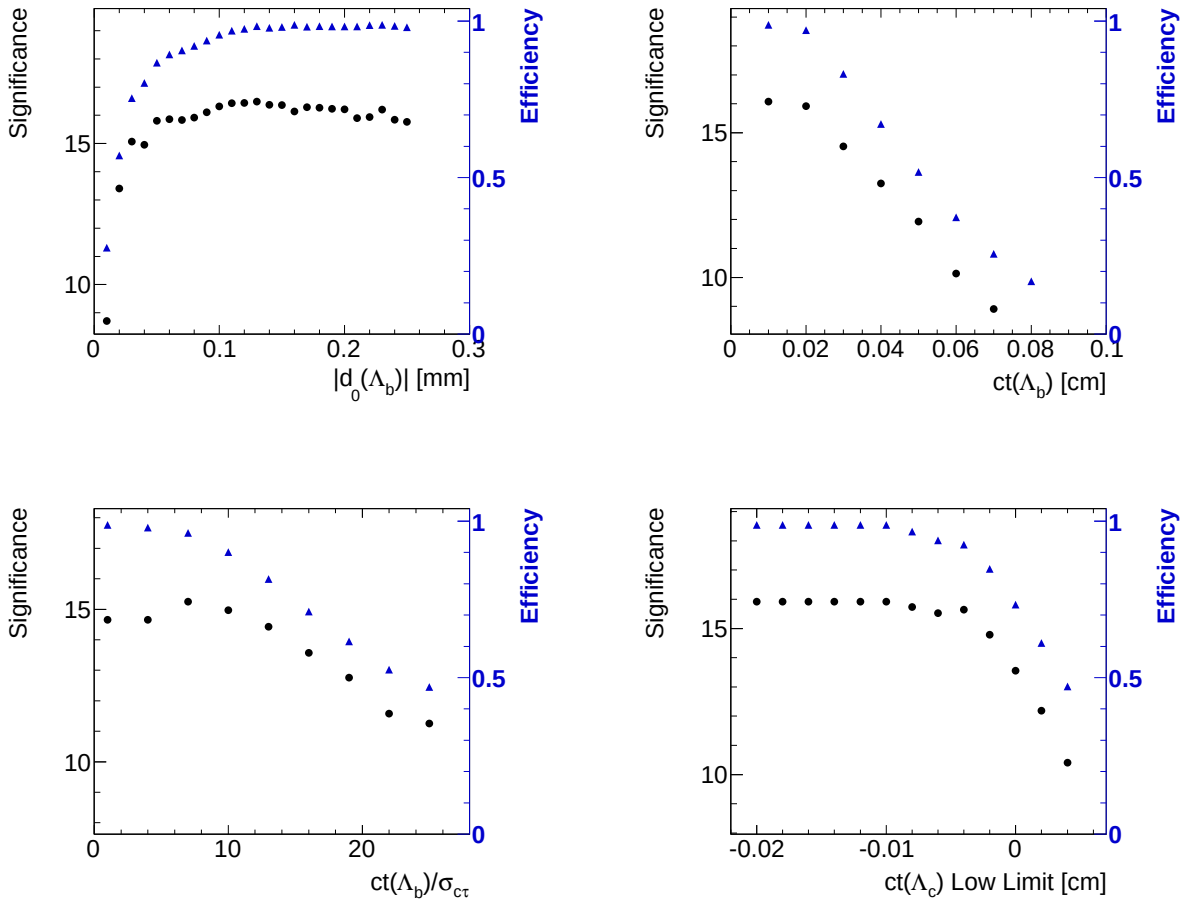

Figure 5.6: *Scans for the several cuts studied for the $\Lambda_b^0\pi^-_{\Sigma_b}$. Black circles (left scale) correspond to F.O.M. as a function of cut on a variable in question. Blue triangles (right scale) show signal "efficiency" as determined from binned fit. Both variables are defined in the text.*

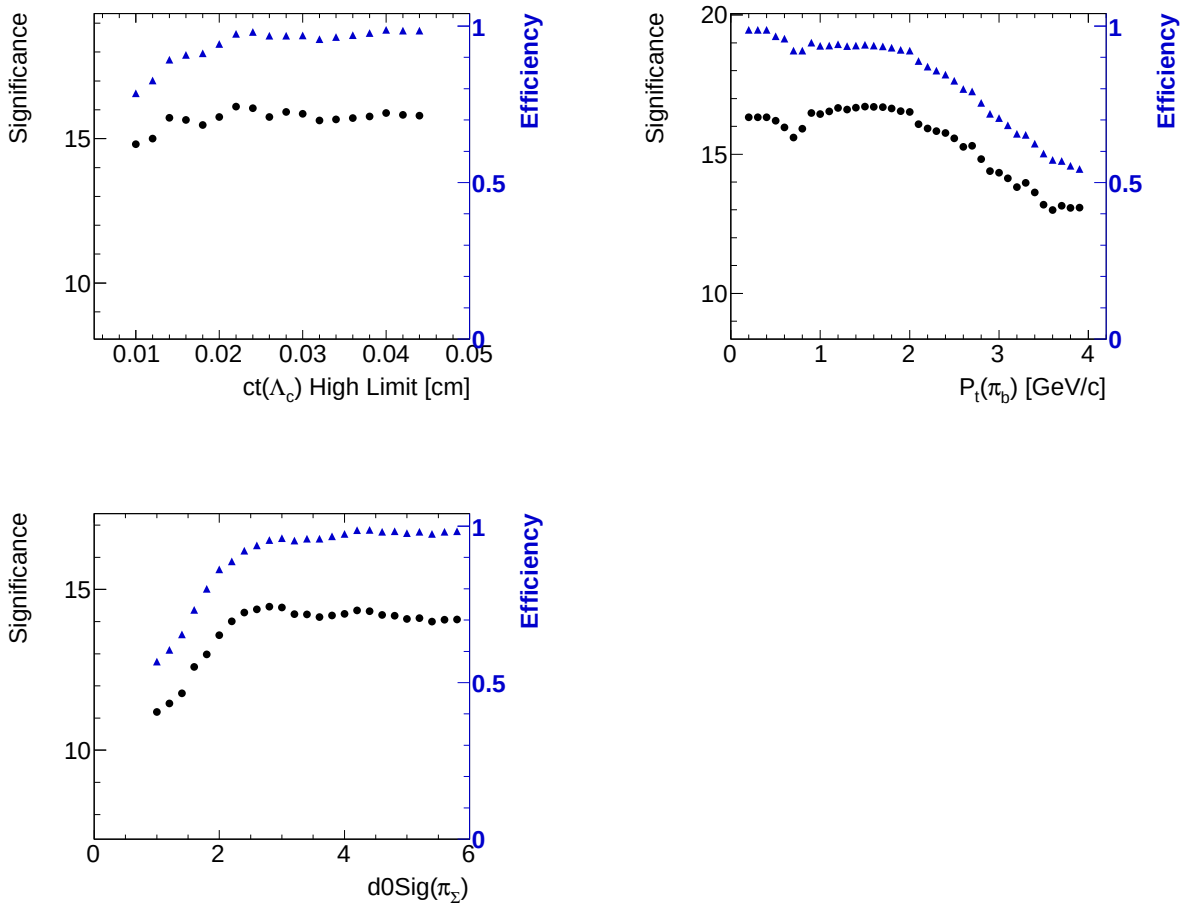

Figure 5.7: *Scans for the several cuts studied for the $\Lambda_b^0\pi^-_{\Sigma_b}$. Black circles (left scale) correspond to F.O.M. as a function of cut on a variable in question. Blue triangles (right scale) show signal "efficiency" as determined from binned fit. Both variables are defined in the text.*

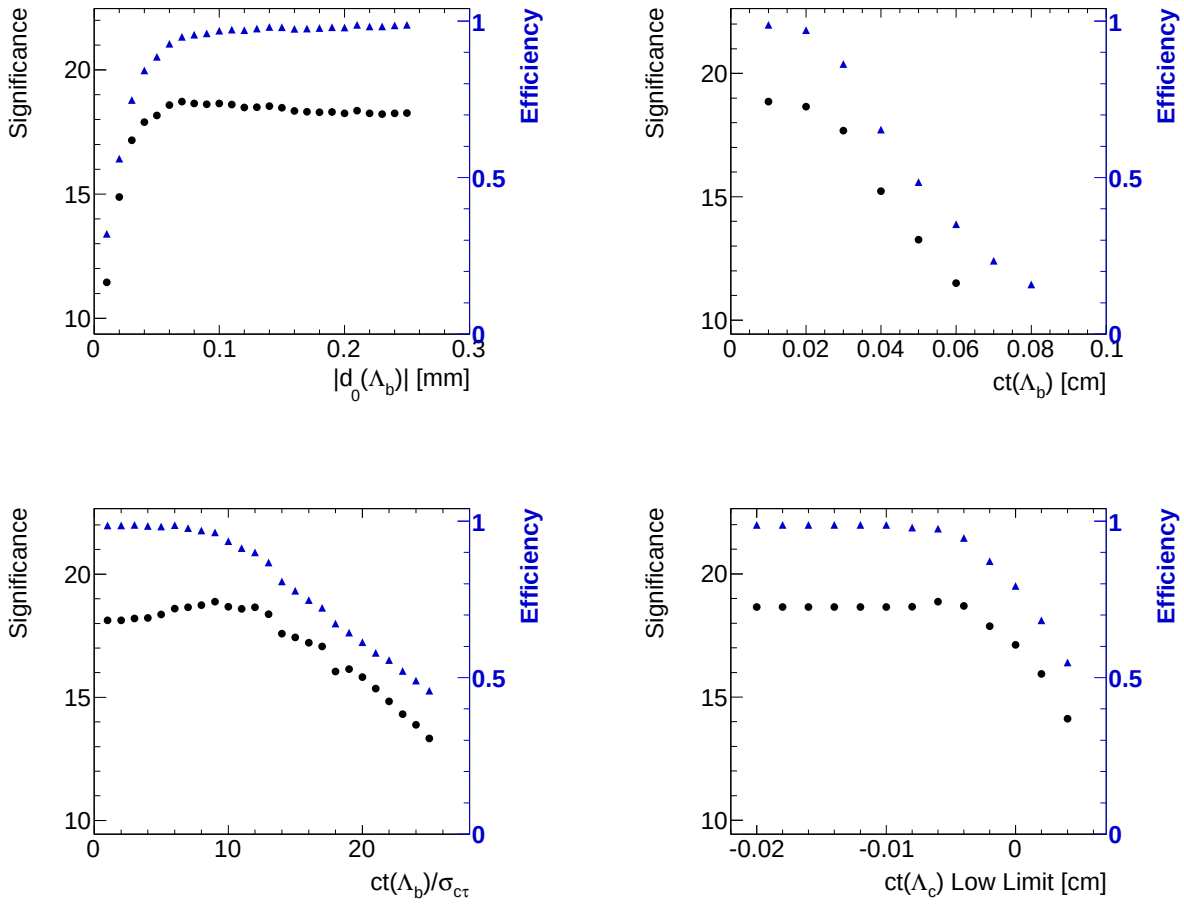

Figure 5.8: *Scans for the several cuts studied for the $\Lambda_b^0\pi^+_{\Sigma_b}$. Black circles (left scale) correspond to F.O.M. as a function of cut on a variable in question. Blue triangles (right scale) show signal "efficiency" as determined from binned fit. Both variables are defined in the text.*

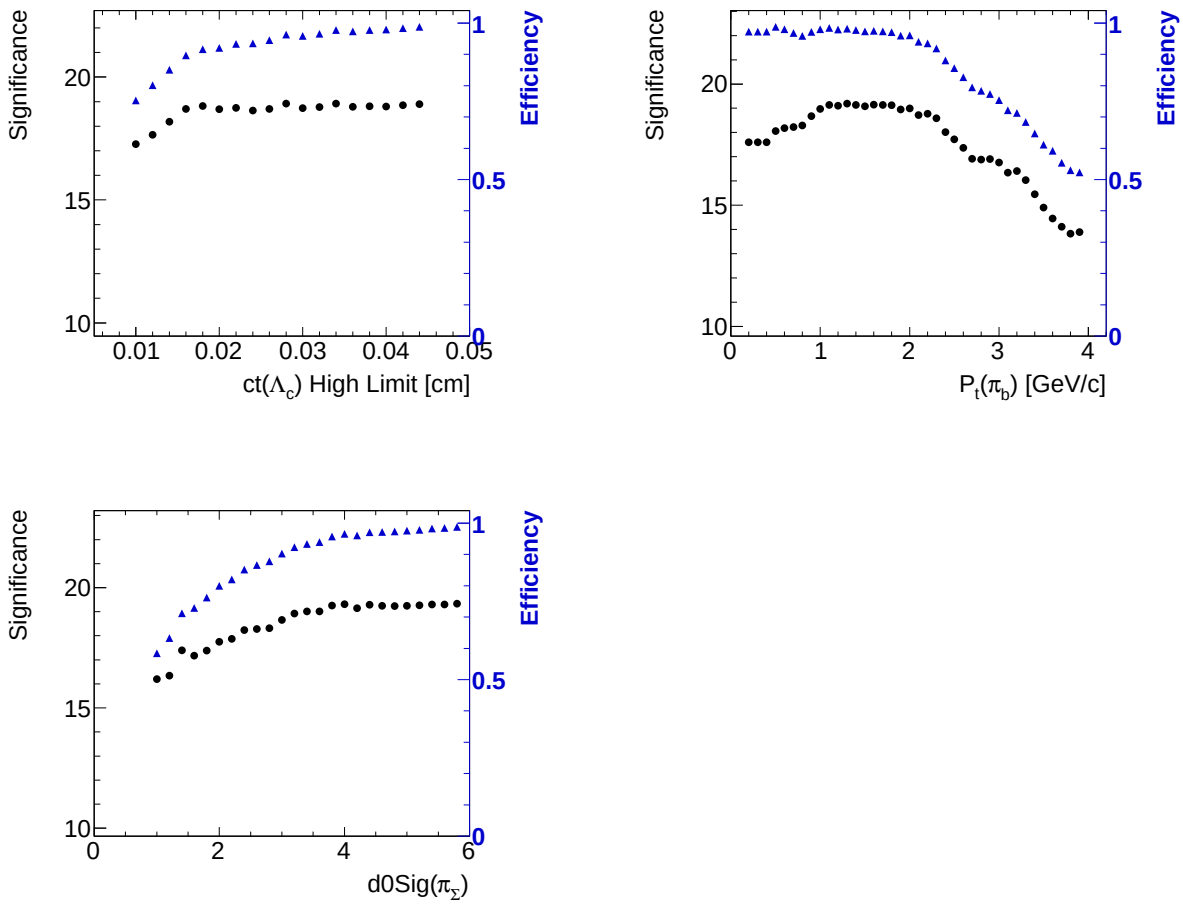

Figure 5.9: *Scans for the several cuts studied for the $\Lambda_b^0\pi^+_{\Sigma_b}$. Black circles (left scale) correspond to F.O.M. as a function of cut on a variable in question. Blue triangles (right scale) show signal "efficiency" as determined from binned fit. Both variables are defined in the text.*

Cut	value
Λ_b^0 analysis cuts, see also Tables 5.2, 5.5:	
$c\tau(\Lambda_b^0)$	$> 200\,\mu$m
$c\tau(\Lambda_b^0)/\sigma_{c\tau}$	> 12.0
$\lvert d_0(\Lambda_b^0)\rvert$	$< 80\,\mu$m
$c\tau(\Lambda_c^+ \leftarrow \Lambda_b^0)$	$> -150\,\mu$m
$c\tau(\Lambda_c^+ \leftarrow \Lambda_b^0)$	$< 250\,\mu$m
$p_T(\pi_b^-)$	$> 1.5\,\mathrm{GeV}/c$
$p_T(p)$	$> 0.4\,\mathrm{GeV}/c$
$p_T(K^-)$	$> 0.4\,\mathrm{GeV}/c$
$p_T(\pi^+)$	$> 0.4\,\mathrm{GeV}/c$
$p_T(\Lambda_b^0)$	$> 4.0\,\mathrm{GeV}/c$
$p_T(\Sigma_b^{(*)})$	$> 4.0\,\mathrm{GeV}/c$
$\lvert m(\Lambda_c^+\pi^-) - m(\Lambda_b^0)\rvert$	$< 3 \cdot 19.22\,\mathrm{MeV}/c^2$, $\pm 3\sigma$
$\mathrm{Prob}(\chi^2_{3D})$ of Λ_b^0 vertex fit	> 0.0001
π_{soft} analysis cuts:	
COT and SVX II hits	see Table 5.8
$\lvert d_0/\sigma_{d_0}\rvert(\pi_{soft})$	< 3.0
$p_T(\pi_{soft})$	$> 0.2\,\mathrm{GeV}/c$
$p_T(\pi_{soft})$	$< p_T(\pi_b^-)$

Table 5.9: *Final selection cuts after optimization. See also the Tables 5.2, 5.5*

- both lists again have been scanned manually to resolve inconsistencies
  - $\sim 2.3\%$ of candidates contributing individually to every charge state have been identified as duplicates
- the combined "bad events" list of pairs, run#, event# containing duplicate candidates has been generated including both charges.
  - 265 events having duplicate candidates contributing to the spectra at the analysis cuts have been identified.
  - given the low probability of the track duplicates for nominal tracks with $p_T > 0.4\,\mathrm{GeV}/c^2$, we can estimate the number of events taking the total number of signal and background combinations in and under the Λ_b^0 peak, to be ~ 25000.
  - the fraction of bad candidates to be rejected to exclude track duplicates after rejection of 265 events from the "bad events" list comprises $\sim 2.9\%$, please see the Figure 5.10.
- the events from the "bad events" list have been discarded while spinning over the final high end flat ntuples - the class has been written and implemented to our high end analysis codes.

Finally the comparison of Q- value distributions before and after rejection of bad events is shown at Figure 5.10.

5.3 MC Study: Signals Resolution

The Figure 5.13 shows the shape of the CDF detector response for Σ_b^+ signals and the Figure 5.14 shows the response to Σ_b^{*+}. The distribution is fitted with a sum of a double Gaussian function and a constant to account for a possible tiny combinatorial contribution. The results of the fits for both states are arranged in the Table 5.11. We will use the resolution model fitted with MC data for the soft pion momentum $p_T(\pi_{soft}) > 0.2\,\mathrm{GeV}/c^2$, what corresponds to our analysis cut, please see the last plots at both Figure 5.13 and Figure 5.14 and take a note of the third and sixth lines in the Table 5.11.

5.4 Description of the Fit

In this section we describe the assumed models for the signal and the background in our fitter. We fit the modes $\Lambda_b^0\pi^-_{\Sigma_b}$ and $\Lambda_b^0\pi^+_{\Sigma_b}$ separately using two unbinned negative likelihood fits. The model of our experimental spectra consists of two additive parts: a background and a signal. The fitter contains 9 floating parameters.

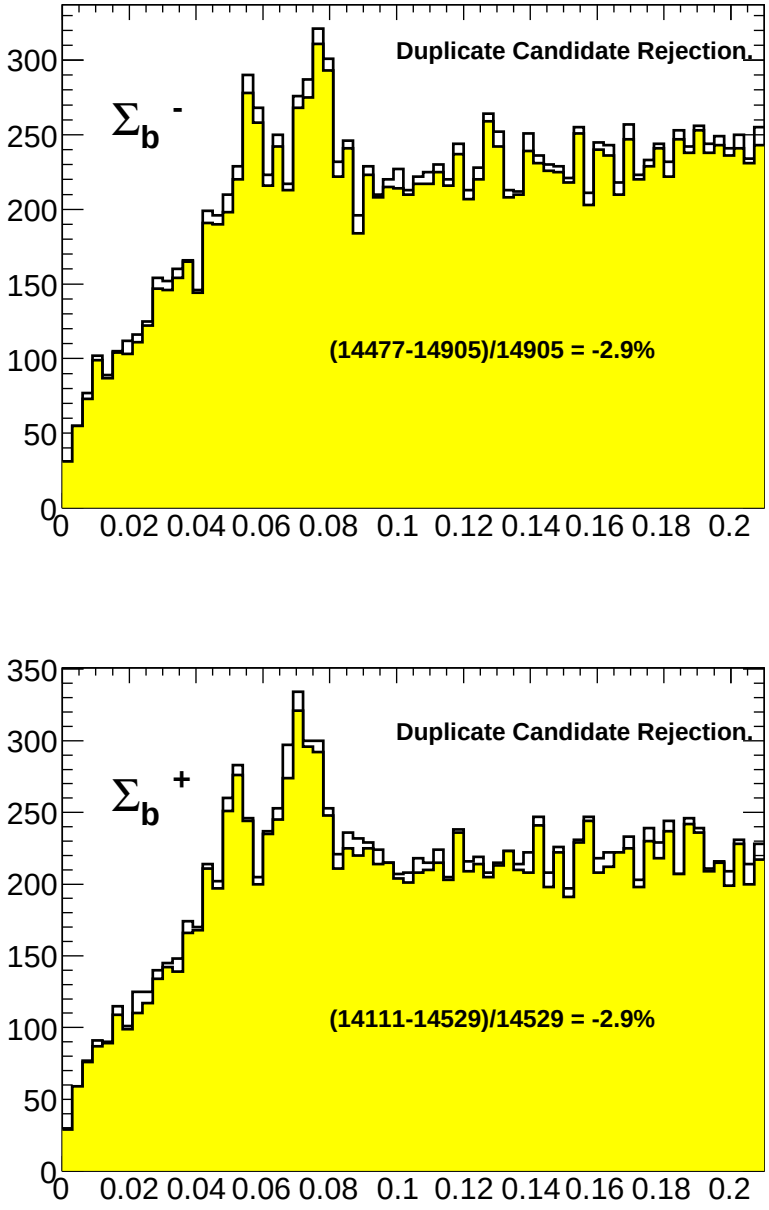

Figure 5.10: *Comparison of both $\Sigma_b^{(*)-}$ and $\Sigma_b^{(*)+}$ distributions with (yellow) and without (blank) candidates rejection.*

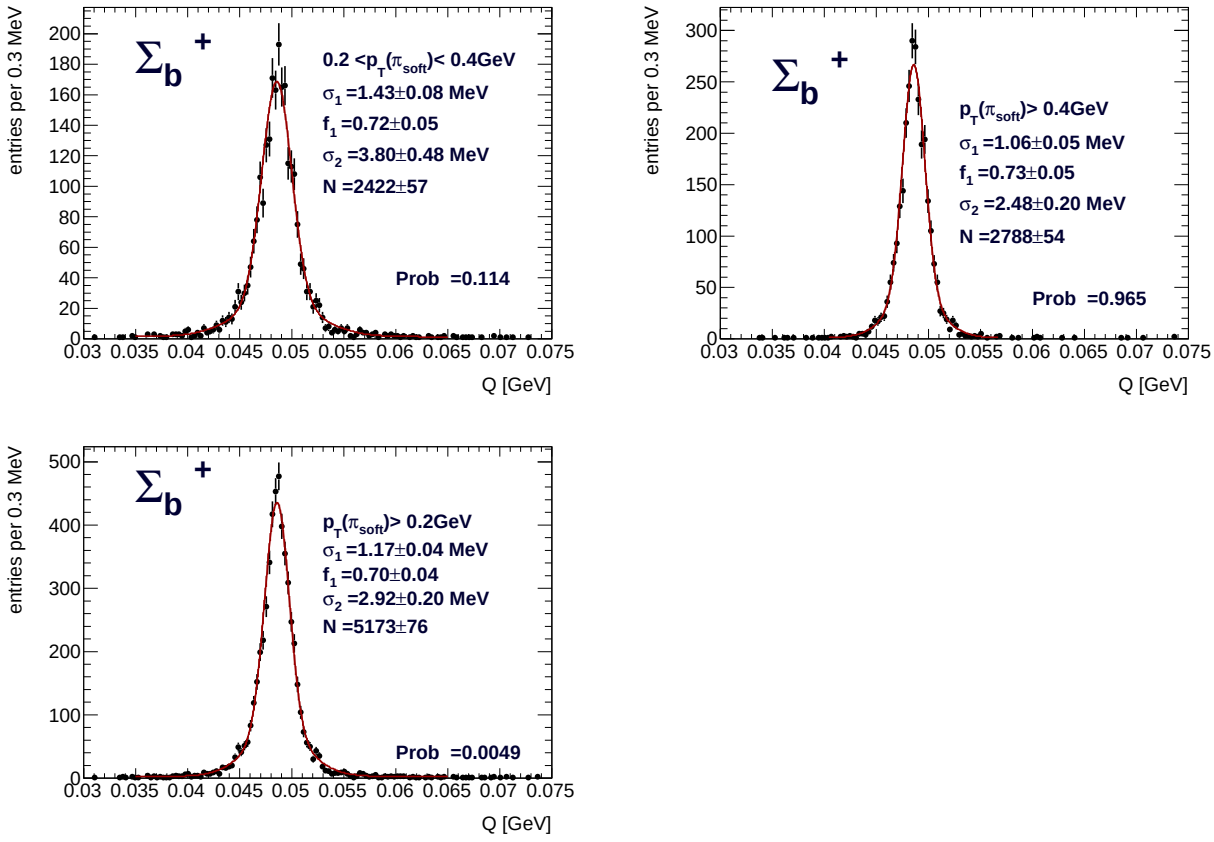

Figure 5.11: *The response of the CDF detector to the Σ_b^+ signals after the generated with the zero natural width modes $\Sigma_b^+ \to \Lambda_b^0 \pi^+_{\Sigma_b}$ are simulated, reconstructed and ntuplelized. The analysis cuts are applied. The Q-value spectrum, where $Q = M(\Lambda_b^0\pi^+) - M(\Lambda_b^0) - m_\pi$, is subjected to a fit with a double Gaussian plus a constant. We apply in our fitter the resolutions obtained when $p_T(\pi_{soft}) > 0.2\,\mathrm{GeV}/c^2$ (bottom plot)*

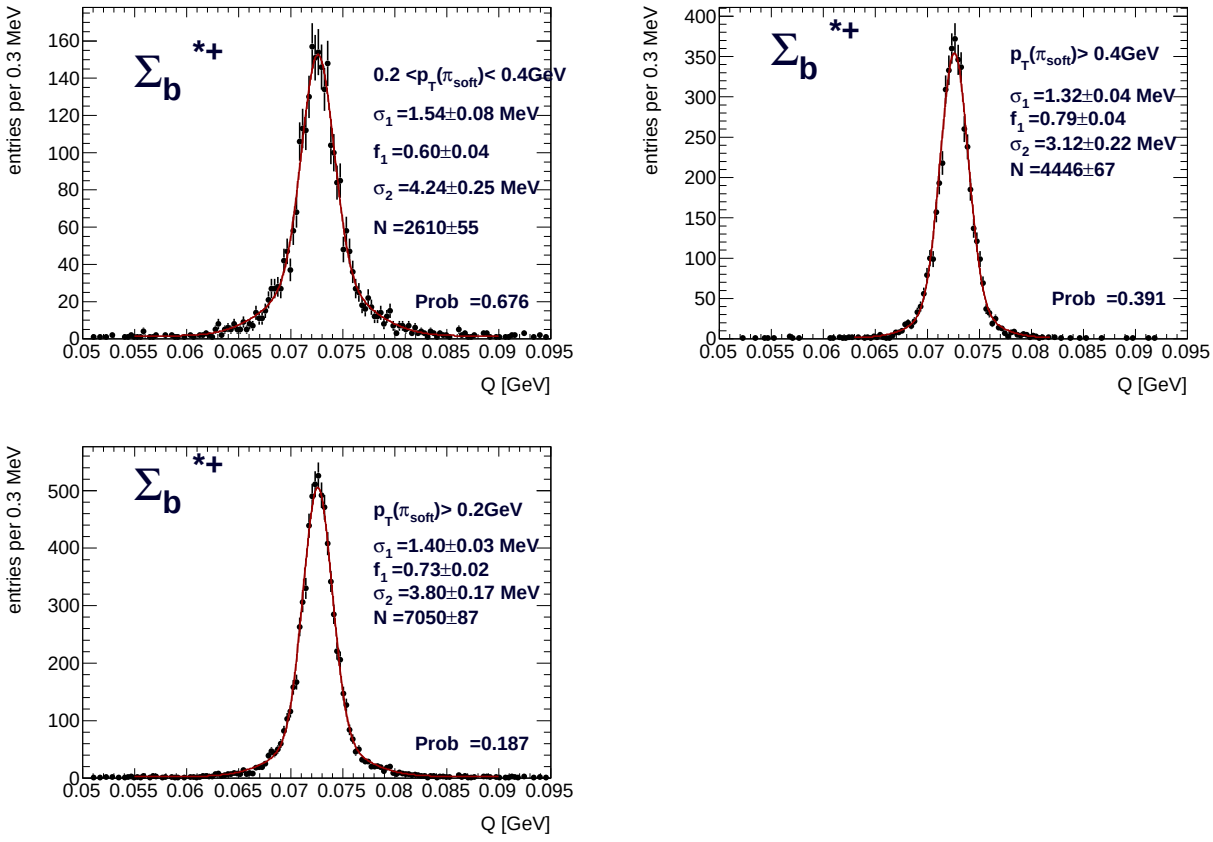

Figure 5.12: *The response of the CDF detector to the Σ_b^{*+} signals after the generated with the zero natural width modes $\Sigma_b^{*+} \to \Lambda_b^0 \pi^+_{\Sigma_b}$ are simulated, reconstructed and ntuplelized. The analysis cuts are applied. The Q-value spectrum, where $Q = M(\Lambda_b^0\pi^+) - M(\Lambda_b^0) - m_\pi$, is subjected to a fit with a double Gaussian plus a constant. We apply in our fitter the resolutions obtained when $p_T(\pi_{soft}) > 0.2\,\mathrm{GeV}/c^2$ (bottom plot)*

State	p_T, GeV/c^2	σ_1, MeV/c^2	σ_2, MeV/c^2	fraction, g_1
Σ_b^+	$\in (0.2, 0.4)$	1.43 ± 0.08	3.80 ± 0.48	0.72 ± 0.05
Σ_b^+	> 0.4	1.06 ± 0.05	2.48 ± 0.20	0.73 ± 0.05
Σ_b^+	> 0.2	1.17 ± 0.04	2.92 ± 0.20	0.70 ± 0.04
Σ_b^{*+}	$\in (0.2, 0.4)$	1.54 ± 0.08	4.24 ± 0.25	0.60 ± 0.04
Σ_b^{*+}	> 0.4	1.32 ± 0.04	3.12 ± 0.23	0.79 ± 0.04
Σ_b^{*+}	> 0.2	1.40 ± 0.03	3.80 ± 0.17	0.73 ± 0.02

Table 5.10: *Resolution of the detector for $\Sigma_b^{(*)+}$ signals. The same values are used for both charge modes, $\Sigma_b^{(*)\pm}$. The double Gaussian parameters $\sigma_{1,2}$ and relative fraction of the first, narrow core Gaussian, g_1 are listed in the table. The values quoted for $p_T >$ 0.2 GeV/c^2 will be plugged into a fitter.*

5.4.1 Signal Model

The expected $\Sigma_b^{(*)\pm}$ signals structure for both $\Lambda_b^0\pi^+_{\Sigma_b}$ and $\Lambda_b^0\pi^-_{\Sigma_b}$ mode consists of two peaks corresponding to $\Sigma_b^\pm$ ($J^P = 1/2^+$) and $\Sigma_b^{*\pm}$ ($J^P = 3/2^+$) candidates.

Since both states are produced at $Q \sim 50\,\mathrm{MeV}/c^2$ and $Q \sim 70\,\mathrm{MeV}/c^2$, i.e. very close to the threshold the signal shape is perfectly modeled with *modified* non-relativistic Breit-Wigner function. The parameter of the Breit-Wigner distribution describing the natural width of the state is modified with a factor according with the angular momentum of the P-wave of the emitted softpion (see Sec. 5.4.2).

Henceforth every signal of both $\Sigma_b(i \equiv 1)$ and $\Sigma_b^*(i \equiv 2)$ states is modeled by a non-relativistic Breit-Wigner function, see Eq. 5.2. The Breit-Wigner function is convoluted with the Q-value resolution parameterized by two Gaussians (see Eq. 5.1) taken with their widths $\sigma_{1,2}$ and weights g_1, $(1 - g_1)$ according to Monte-Carlo simulation studies. The Gaussian resolutions are listed in the Table 5.11.

$$\mathcal{S}(Q; Q_0, \Gamma, \sigma_1, g_1, \sigma_2) = \mathcal{BW}(Q; Q_0, \Gamma) \otimes (g_1 \cdot \mathcal{G}(q; 0, \sigma_1) + (1 - g_1) \cdot \mathcal{G}(q; 0, \sigma_2)) \quad (5.1)$$

where non-relativistic Breit-Wigner (Eq. 5.2) and Gaussian (Eq. 5.3) resolution functions are well known as

$$\mathcal{BW}(Q; Q_0, \Gamma) = \frac{\Gamma/2\pi}{(Q - Q_0)^2 - (\Gamma/2)^2}, \quad (5.2)$$

$$\mathcal{G}(q; 0, \sigma) = \frac{1}{\sigma\sqrt{2\pi}} \cdot \exp\left(-\frac{q^2}{2\sigma^2}\right) \quad (5.3)$$

MC Study: Signals Resolution

Each Σ_b state is described by a non-relativistic modified Breit-Wigner PDF convoluted with a double Gaussian detector resolution. The detector resolution is taken from the

Monte Carlo sample described in Sec. 4.3. Since the sample is generated with an input width of zero for all Σ_b states, the width of the reconstructed Q-value distributions is a measurement of the detector resolution.

The Figure 5.13 shows the shape of the CDF detector response for Σ_b^+ signals and the Figure 5.14 shows the response to Σ_b^{*+}. The distribution is fitted with a sum of a double Gaussian function and a constant to account for a possible tiny combinatorial contribution. The results of the fits for both states are arranged in the Table 5.11. We use the resolution model fitted with MC data for the soft pion momentum $p_T(\pi_{soft}) > 0.2\,\mathrm{GeV}/c^2$, what corresponds to our analysis cut, please see the last plots at both Figure 5.13 and Figure 5.14 and take a note of the third and sixth lines in the Table 5.11.

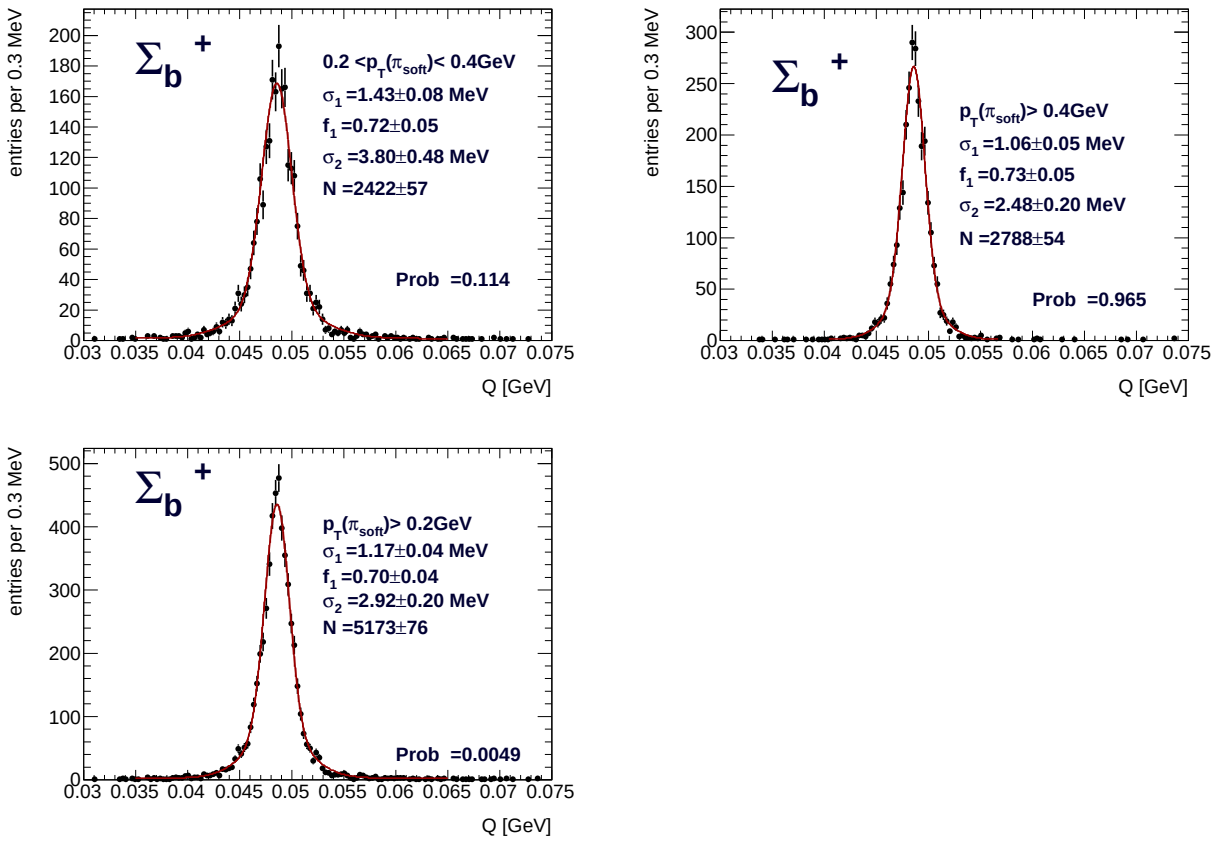

Figure 5.13: *The response of the CDF detector to the Σ_b^+ signals after the generated with the zero natural width modes $\Sigma_b^+ \to \Lambda_b^0\pi^+_{\Sigma_b}$ are simulated, reconstructed and ntuplelized. The analysis cuts are applied. The Q-value spectrum, where $Q = M(\Lambda_b^0\pi^+) - M(\Lambda_b^0) - m_\pi$, is subjected to a fit with a double Gaussian plus a constant.*

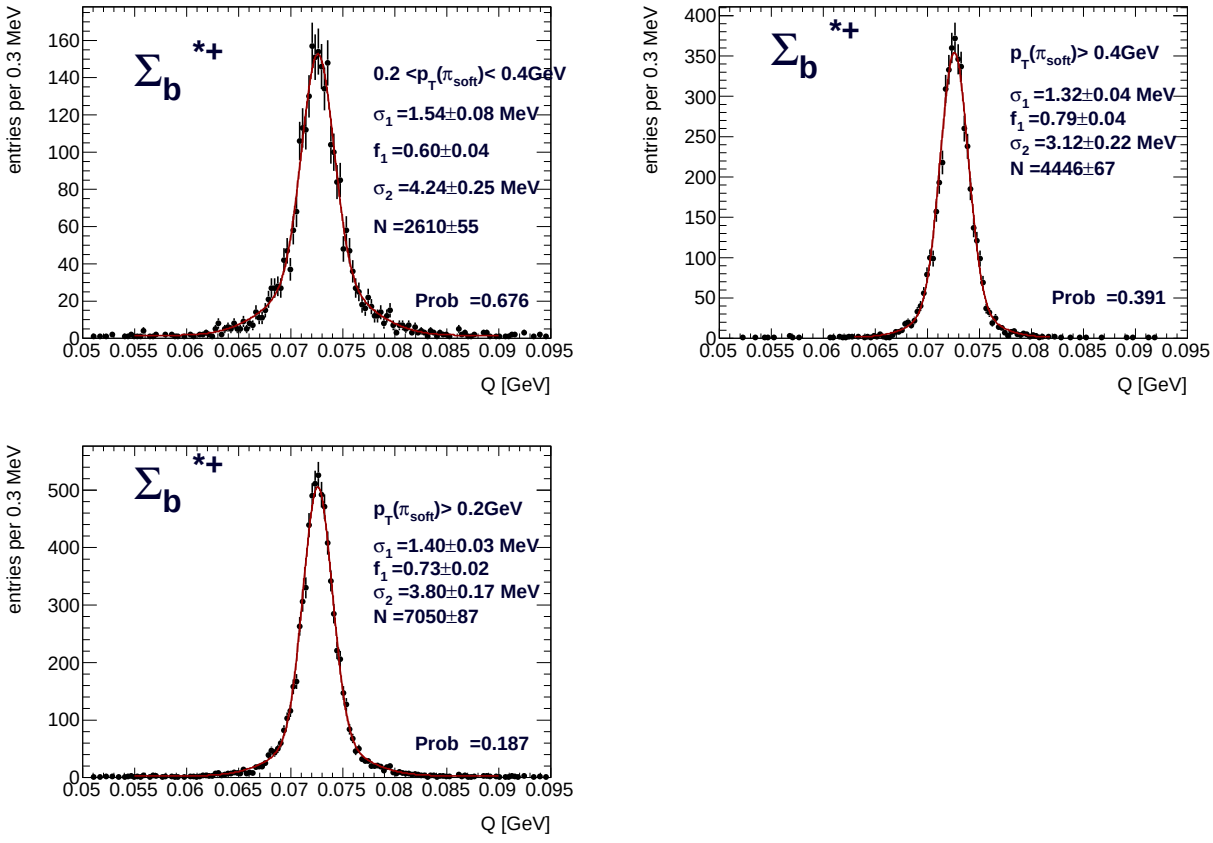

Figure 5.14: *The response of the CDF detector to the Σ_b^{*+} signals after the generated with the zero natural width modes $\Sigma_b^{*+} \to \Lambda_b^0 \pi^+_{\Sigma_b}$ are simulated, reconstructed and ntuplelized. The analysis cuts are applied. The Q-value spectrum, where $Q = M(\Lambda_b^0\pi^+) - M(\Lambda_b^0) - m_\pi$, is subjected to a fit with a double Gaussian plus a constant.*

State	p_T, GeV/c^2	σ_1, MeV/c^2	σ_2, MeV/c^2	fraction, g_1
Σ_b^+	$\in (0.2, 0.4)$	1.43 ± 0.08	3.80 ± 0.48	0.72 ± 0.05
Σ_b^+	> 0.4	1.06 ± 0.05	2.48 ± 0.20	0.73 ± 0.05
Σ_b^+	> 0.2	1.17 ± 0.04	2.92 ± 0.20	0.70 ± 0.04
Σ_b^{*+}	$\in (0.2, 0.4)$	1.54 ± 0.08	4.24 ± 0.25	0.60 ± 0.04
Σ_b^{*+}	> 0.4	1.32 ± 0.04	3.12 ± 0.23	0.79 ± 0.04
Σ_b^{*+}	> 0.2	1.40 ± 0.03	3.80 ± 0.17	0.73 ± 0.02

Table 5.11: *Resolution of the detector for $\Sigma_b^{(*)+}$ signals. The same values are used for both charge modes, $\Sigma_b^{(*)\pm}$. The double Gaussian parameters $\sigma_{1,2}$ and relative fraction of the first, narrow core Gaussian, g_1 are listed in the table. The values quoted for $p_T > 0.2$ GeV/c^2 will be plugged into a fitter.*

5.4.2 P-Wave Modified Breit-Wigner Function

The soft pion in strong decay modes is emitted in a P-wave. We follow the approach proposed by the very same J. D. Jackson in times of strange resonance [75] [76] discoveries. The approach has been employed also by CLEO Collaboration in their analyses on Σ_c charm baryons [77] [78]. The signal shape reconstructed in P-wave modes is asymmetrical and biased towards the higher masses due to a well known in nuclear physics "centrifugal factor" or for our case P-wave factor. To correct out the effect, the natural width Γ in the Breit-Wigner function is factorized with a phenomenological term $(\frac{p_\pi^*}{p_\pi^{*0}})^{2\cdot L+1}$, where p_π^* is the momentum of a soft pion in a $\Sigma_b^{(*)}$ rest frame and p_π^{*0} is the same evaluated at the resonance pole.

That is for our case, $L = 1$, (please see [17] for kinematic equations):

$$
\begin{aligned}
\Gamma(Q; Q_0, \Gamma_0) &= \Gamma_0 \cdot \left(\frac{p_\pi^*}{p_\pi^{*0}}\right)^3, \\
Q &= M_{\Sigma_b^{(*)}} - M_{\Lambda_b^0} - m_\pi, \\
Q_0 &= \text{mass at the pole, i.e. fit parameter,} \\
\Gamma_0 &= \text{corrected width i.e. fit parameter,} \\
E_\pi^*(Q) &= \frac{(Q + M_{\Lambda_b^0} + m_\pi)^2 - {M_{\Lambda_b^0}}^2 + {m_\pi}^2}{2 \cdot (Q + M_{\Lambda_b^0} + m_\pi)}, \\
p_\pi^*(Q) &= \sqrt{({E_\pi^*}^2 - {m_\pi}^2)}, \\
M_{\Lambda_b^0}(\text{Table 5.7}) &= 5.619150 \text{ GeV}/c^2, \\
m_\pi(\text{PDG[17]}) &= 0.13957018 \text{ GeV}/c^2
\end{aligned}
\tag{5.4}
$$

The shape of the $\mathcal{BW}(Q; Q_0, \Gamma)$ with Γ modified according to Equation 5.4 is shown at the Figure 5.15. The convolution is shown as well. The asymmetry becomes visible with a larger width of $\Gamma_0 = 20\,\text{MeV}$.

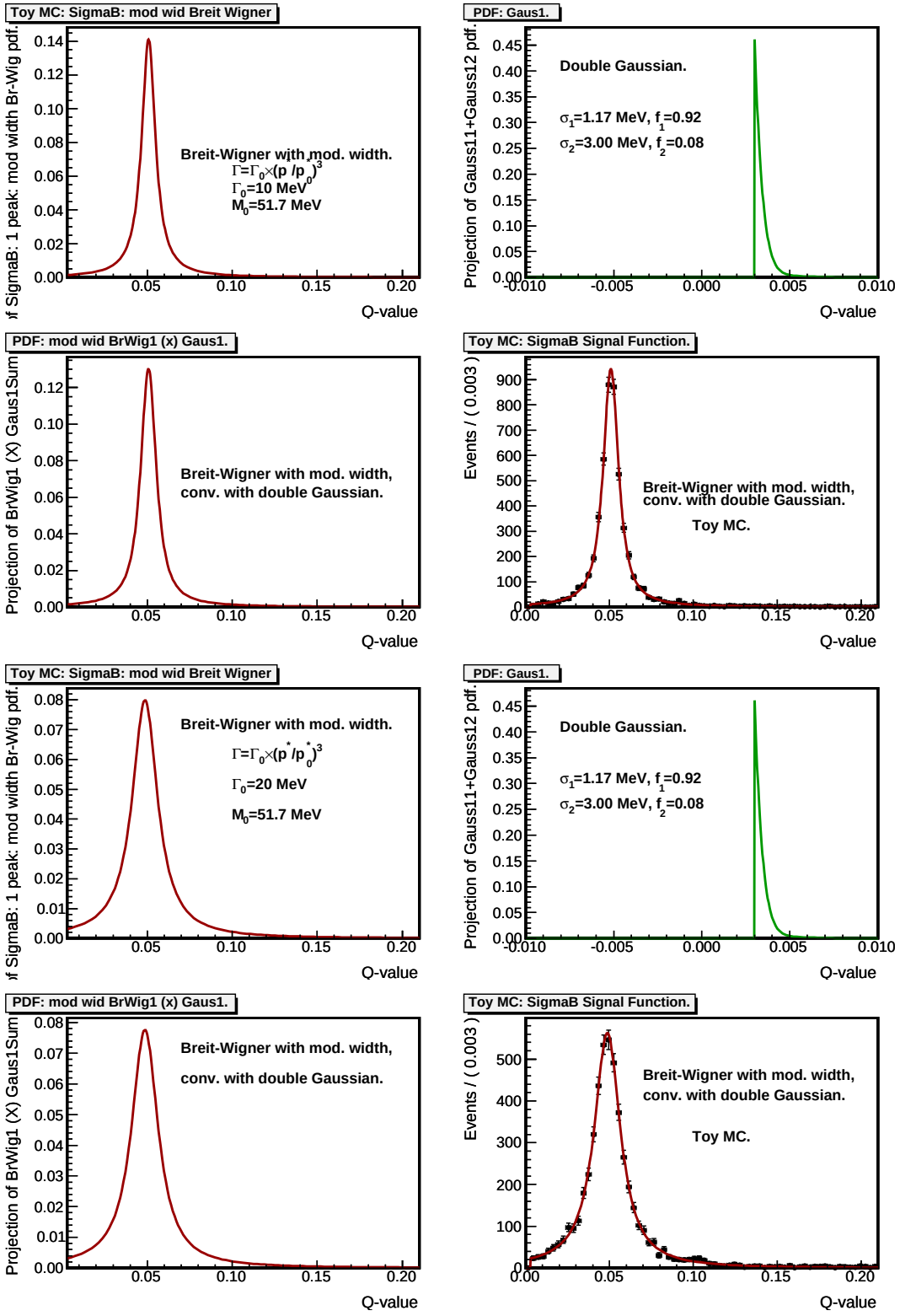

Figure 5.15: *The shape of* $\mathcal{BW}(Q;Q_0,\Gamma)$ *with* $\Gamma=\Gamma_0\cdot(p^*/p^{*0})^3$ *for* $\Gamma_0=10\,\mathrm{MeV}\,,20\,\mathrm{MeV}$. *The result of a numerical convolution using a Fast Fourier Transformation is shown as well. The resolution function is shown only over a positive range of its argument due to a* `RooFit` *setting for a plot method.*

The width in the Breit-Wigner function is now a variable, i.e. Voigtian analytical expression can not be used in the fitter and a price has to be paid.

5.4.3 Background Model

As resonances $\Sigma_b^{(*)}$ are observed and reconstructed in a typical two-body strong decay modes with a soft pion π_{Σ_b} and have masses close to a threshold of a reaction, we propose to use a background model which is kinematically motivated.

The 2-body decay rate following [17] is expressed by

$$d\Gamma = \frac{1}{32\pi^2} \cdot |\mathcal{A}|^2 \cdot \frac{|\vec{p_\pi^*}|}{M^2} \cdot d\Omega, \tag{5.5}$$

where M is a mass of initial state decaying with an amplitude $\mathcal{A}$ to a lower one m and emitting a soft pion of p_π^* momentum. Assuming the decay proceeds very near the threshold of $m+m_\pi$, with $m \sim M$, $m_\pi \ll M$, one can approximate the decay pion energy like

$$E_\pi = \frac{M^2 - m^2 + m_\pi^2}{2 \cdot M} \approx M - m \equiv \Delta m$$

Hence the soft pion momentum in a rest frame of a mass M can be written as

$$p_\pi^* = \sqrt{(\Delta m)^2 - {m_\pi}^2}$$

Therefore the phase space factor near the decay threshold is behaving like

$$\frac{|\vec{p_\pi^*}|}{M^2} \propto \sqrt{(\Delta m)^2 - {m_\pi}^2} \tag{5.6}$$

We have deduced the term which is used by many experiments (see for example CLEO analysis [79]) to describe a combinatorial background of 2-body reactions near the threshold when the reactions are analyzed in a mass difference spectra. Some groups modify this term to

$$((\Delta m)^2 - {m_\pi}^2)^\alpha$$

or to

$$((\Delta m) - m_\pi)^\alpha$$

with fits expected to yield $\alpha \sim 0.5$.

Following the Equation 5.6 we consider several kinematic motivated forms to describe the background for our case

$$\mathcal{BGR}(Q; thr, C, b_1, b_2) = \sqrt{(Q+m_\pi)^2 - thr^2} \cdot \left(C + b_1 \cdot Q + b_2 \cdot (2 \cdot Q^2 - 1)\right) \tag{5.7}$$

$$\mathcal{BGR}(Q; thr, C, b_1, b_2) = \left((Q+m_\pi)^2 - thr^2\right)^\alpha \cdot \left(C + b_1 \cdot Q + b_2 \cdot (2 \cdot Q^2 - 1)\right) \tag{5.8}$$

$$\mathcal{BGR}(Q; thr, f, C, b_1) = f \cdot \sqrt{(Q+m_\pi)^2 - thr^2} + C + b_1 \cdot Q \tag{5.9}$$

where C, b_1 and b_2 are the polynomial (Chebyshev) coefficients, thr is a threshold (a mass of a pion) which might be considered as a fit parameter and f is a coefficient of a kinematic threshold term applied additively in a form 5.9.

We consider our base background model to be a form 5.8 with parameters

- parameter fixed to $thr = 0.140$
- parameter fixed to $\alpha = 0.5$
- as the fitter is expected to run with extended likelihood, one of a polynomial coefficients will also be fixed, namely b_2
- With these fixed parameters a form 5.8 is actually equivalent to form 5.7.

5.4.4 Full PDF Function

Finally, the full model for $Q-$value spectra of every isospin partner state $\Sigma_b^{(*)+}$, $\Sigma_b^{(*)-}$ describes two peaks sitting on top of a smooth background with a threshold behavior. The next negative logarithm of a likelihood function (or NLL) is going to be minimized over an unbinned sample of N_{obs} "observed" experimental events:

$$-\log(\mathcal{L}) = -\sum_{k=1}^{N_{obs}} \log(N_{s1}\cdot\mathcal{S}_1+N_{s2}\cdot\mathcal{S}_2+N_b\cdot\mathcal{BGR})+(N_{s1}+N_{s2}+N_b)-N_{obs}\cdot\log(N_{s1}+N_{s2}+N_b) \tag{5.10}$$

The NLL function is individually constructed for the spectrum with Σ_b^+ and Σ_b^{*+} signals and for the spectrum with Σ_b^- and Σ_b^{*-} signals. The fits (i.e. a minimization of NLL) over unbinned ensemble of experimental $Q-$value, $Q_k\left(^{N_{obs}}_{k=1}\right)$ are performed for every charge state separately. The notations of Equation 5.10 are commented below:

- $\mathcal{S}_1 = \mathcal{S}(Q_k; Q_{01}, \Gamma_{01}, \sigma_{11}, g_{11}, \sigma_{21})$
  - Q_{01} is the pole mass value for the s_1 or Σ_b^+ (Σ_b^-) signal, floating parameter.
  - Γ_{01} is the natural width value for the s_1 or Σ_b^+ (Σ_b^-) signal, floating parameter.
  - σ_{11}, σ_{21} are the narrow core and wide contribution Gaussian widths with the relative weights of g_{11}, $(1-g_{11})$. These are parameters calculated from Monte-Carlo and fixed in fits.
  - N_{s1} is the floating yield of Σ_b^+ (Σ_b^-) signal
- $\mathcal{S}_2 = \mathcal{S}(Q_k; Q_{02}, \Gamma_{02}, \sigma_{12}, g_{12}, \sigma_{22})$
  - Q_{02} is the pole mass value for the s_2 or Σ_b^{*+} (Σ_b^{*-}) signal, floating parameter.
  - Γ_{02} is the natural width value for the s_2 or Σ_b^{*+} (Σ_b^{*-}) signal, floating parameter.

  - σ_{21}, σ_{22} are the narrow core and wide contribution Gaussian widths with the relative weights of g_{21}, $(1 - g_{21})$. These are parameters calculated from Monte-Carlo and fixed in fits.
  - N_{s2} is the floating yield of Σ_b^{*+} (Σ_b^{*-}) signal

- $\mathcal{BGR} = \mathcal{BGR}(Q_k; thr, C, ...)$, the background form from Eq. 5.8.
  - $thr = 0.140$ is the threshold factor parameter, to be fixed in the fitter.
  - C, b_1, b_2 are the polynomial coefficients, where b_2 will be fixed to propagate the normalization to N_b with only C, b_1 to be left floating in the fits.
  - N_b is the floating yield of a background contribution. The sum of fitted yields, $N_{s1} + N_{s2} + N_b$, is the Poisson mean value of total observed statistics of N_{obs} events for the particular candidates Σ_b^+, Σ_b^{*+} or Σ_b^-, Σ_b^{*-} corresponding to isospin triplets Σ_b and Σ_b^*.

- **The total number of floating parameters in the fit per every individual charge state is 9.**

As the Breit-Wigner width became dependent from Q the convolutions has to be made numerically. Moreover all likelihood fits must be unbinned to avoid the binning effect on the width measurements.

5.5 Statistical Tests of the Fitter

The complex structure of the fit model with numerical convolutions and the need to run the unbinned likelihood fits to avoid the bin size bias especially for the natural width fits requires to test the fitter performance running the fitter over many spectra generated according to the experimentally motivated parameters.

5.5.1 Toy MC Studies of the Fitter

The input values with which the statistical trials (or "toy MC" samples) have been generated, for every state $\Sigma_b^{(*)\pm}$, are arranged in Table 5.12. The inputs correspond to our baseline fit made with the data with the duplicate candidates events rejected, see the Tables 5.17, 5.18, 5.20

7000 trials and unbinned likelihood fits have been produced for both $\Sigma_b^{(*)-}$ and $\Sigma_b^{(*)+}$.

Only converged in `MIGRAD` unbinned likelihood fits with return code 0 are saved. The parabolic errors are calculated by `HESSE`.

Performance Plots: $\mathbf{\Sigma_b^{(*)-}}$

The distribution of all converged $-log(LH)$ is shown on the upper plot of Fig. 5.16 with the experimental data value overlapped. The perfect Gaussian shape is observed with

Signal parameters	$\Sigma_b^{(*)-} \to \Lambda_b^0 \pi^-_{\Sigma_b}$	$\Sigma_b^{(*)+} \to \Lambda_b^0 \pi^+_{\Sigma_b}$
Σ_b pole, Q_{01}, MeV/c^2	56.22	52.03
Σ_b width, Γ_{01} MeV/c^2	4.5	8.7
Σ_b yield, N_{s1}	324	443
Σ_b resolution, σ_{11} MeV/c^2	1.17	1.17
Σ_b resolution, σ_{21} MeV/c^2	2.92	2.92
Σ_b fraction of σ_{11}, g_{11}	0.70	0.70
Σ_b^* pole, Q_{02}, MeV/c^2	75.79	72.72
Σ_b^* width, Γ_{02} MeV/c^2	7.3	11.0
Σ_b^* yield, N_{s2}	530	781
Σ_b^* resolution, σ_{12} MeV/c^2	1.40	1.40
Σ_b^* resolution, σ_{22} MeV/c^2	3.80	3.80
Σ_b^* fraction of σ_{12}, g_{12}	0.73	0.73
Background, *thr*	0.140	0.140
Background, α	0.5	0.5
Background, C	4.01	4.20
Background, b_1	-3.55	-4.71
Background, b_2	3.12	2.89
Background yield, N_b	13621	12883

Table 5.12: *The list and values of the fit model parameters set to generate statistical trials or "toy MC" Q- spectra for both $\Sigma_b^{(*)-}$ and $\Sigma_b^{(*)+}$ given the results of the baseline fit with experimental over the whole sample of data, see the Tables 5.17, 5.18, 5.20*

the mean value practically the same as the experimental data fit yields. The bottom 2×2 plot of the same Fig. 5.16 demonstrates a fitter performance for a first Σ_b^- peak Q_{01} (left column) and width Γ_{01} (right column) values. The similar plots are shown at a Fig. 5.17 for the second, Σ_b^{*-} peak. The fitter response to yields with their pulls is shown at Fig. 5.18.

The results on absolute differences extracted from plots are summarized in a Table 5.13. For possible bias estimates we use the statistical means and RMS since the number of the statistical trials, 7000, is pretty high.

Signal parameters	Stat. Mean	Mean−Orig.	Stat. RMS
Σ_b^- pole, Q_{01}, MeV/c^2	56.25	0.03	0.66
Σ_b^- width, Γ_{01} MeV/c^2	4.43	−0.07	2.1
Σ_b^- yield, N_{s1}	323	−1	69
Σ_b^{*-} pole, Q_{02}, MeV/c^2	75.84	0.05	0.71
Σ_b^{*-} width, Γ_{02} MeV/c^2	7.32	0.02	1.06
Σ_b^{*-} yield, N_{s2}	532	2	89

Table 5.13: $\Sigma_b^{(*)-}$ *fitter performance: the absolute differences of the fitted values and their originally preset (see Table 5.12) values as extracted from high-statistics "toy MC" study of 7000 generated and fitted trials.*

The results on pulls extracted from plots and fits are summarized in a Table 5.14.

Signal parameters	Stat. Mean	Stat. RMS	Gauss. μ	Gauss. σ
Σ_b^- pole, Q_{01}, MeV/c^2	−0.05	1.07	0.05 ± 0.02	0.99 ± 0.02
Σ_b^- width, Γ_{01} MeV/c^2	−0.27	1.07	0.02 ± 0.02	1.02 ± 0.03
Σ_b^- yield, N_{s1}	−0.14	1.06	0.04 ± 0.02	1.01 ± 0.03
Σ_b^{*-} pole, Q_{02}, MeV/c^2	0.02	1.04	0.05 ± 0.02	1.00 ± 0.02
Σ_b^{*-} width, Γ_{02} MeV/c^2	−0.21	1.06	0.07 ± 0.02	1.02 ± 0.03
Σ_b^{*-} yield, N_{s2}	−0.09	1.04	0.06 ± 0.02	1.01 ± 0.03

Table 5.14: $\Sigma_b^{(*)-}$ *fitter performance: the pull distributions and their fits with Gaussian.*

The data in Table 5.13 show the possibility of slight shift in Γ_{01} but still much smaller than the statistical fit error. The longer positive tail of the Γ_{01} fitted values distribution w.r.t. the shorter negative one (and an inverse behavior at pull distribution plots) can be explained by the fact that parabolic errors are not quite right and the MINOS errors would do a better job. Another important factor is the expected positive correlation of the fitted widths with the corresponding fitted yields. Unfortunately the CPU time of fits with full MINOS is prohibitive, $10 - 15$ CPU (2.8 GHz) minutes per trial. Still the stability of the fitter is assured by Gaussian σ or its RMS analog being always very close

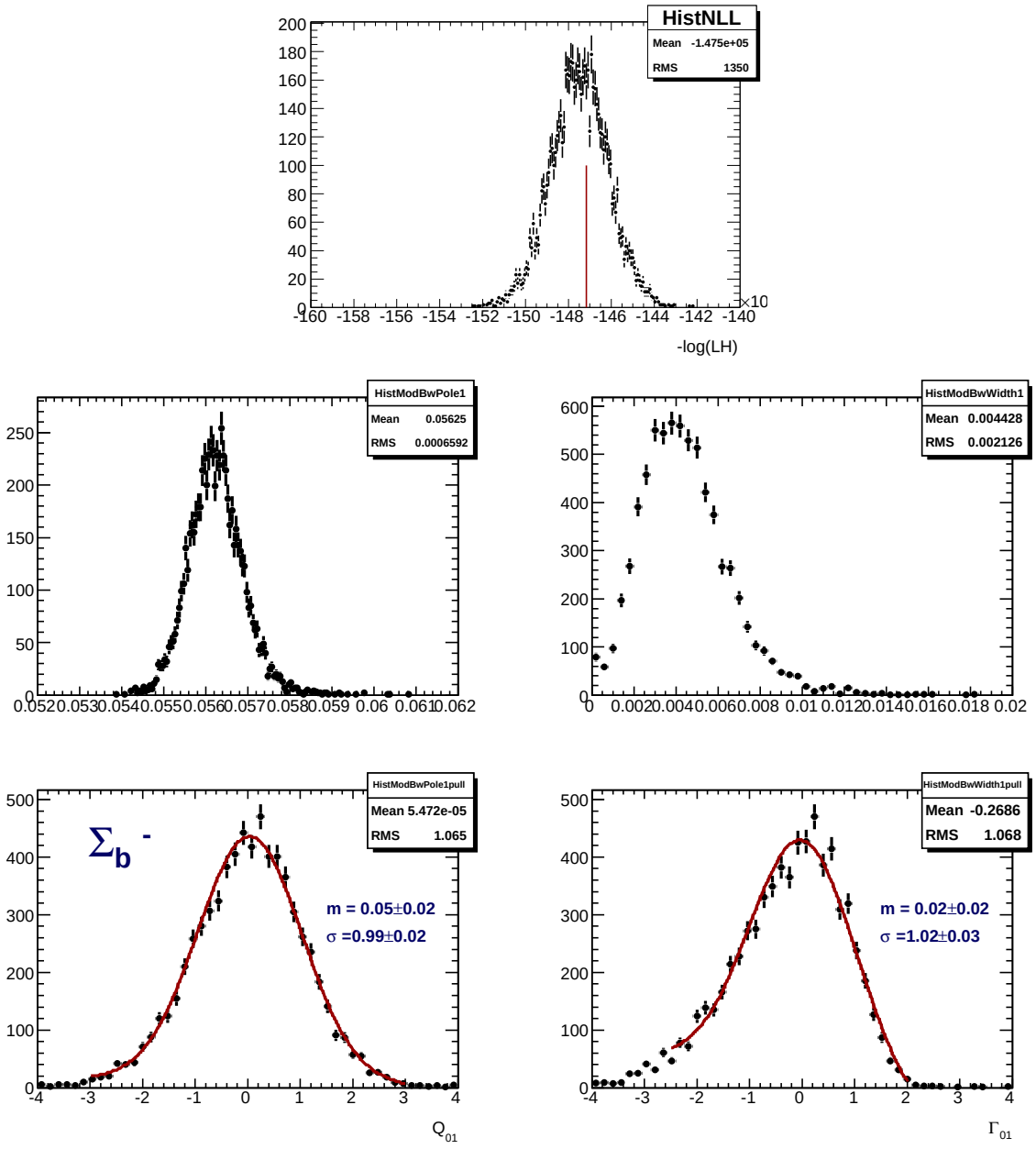

Figure 5.16: *The upper plot shows the distribution of NLL resulted by unbinned LH fits of 7000 trials. Σ_b^- statistical trials for Q_{01}, GeV/c^2 and for Γ_{01} GeV/c^2 yielded the bottom four plots showing the distribution of fitted values and their pulls.*

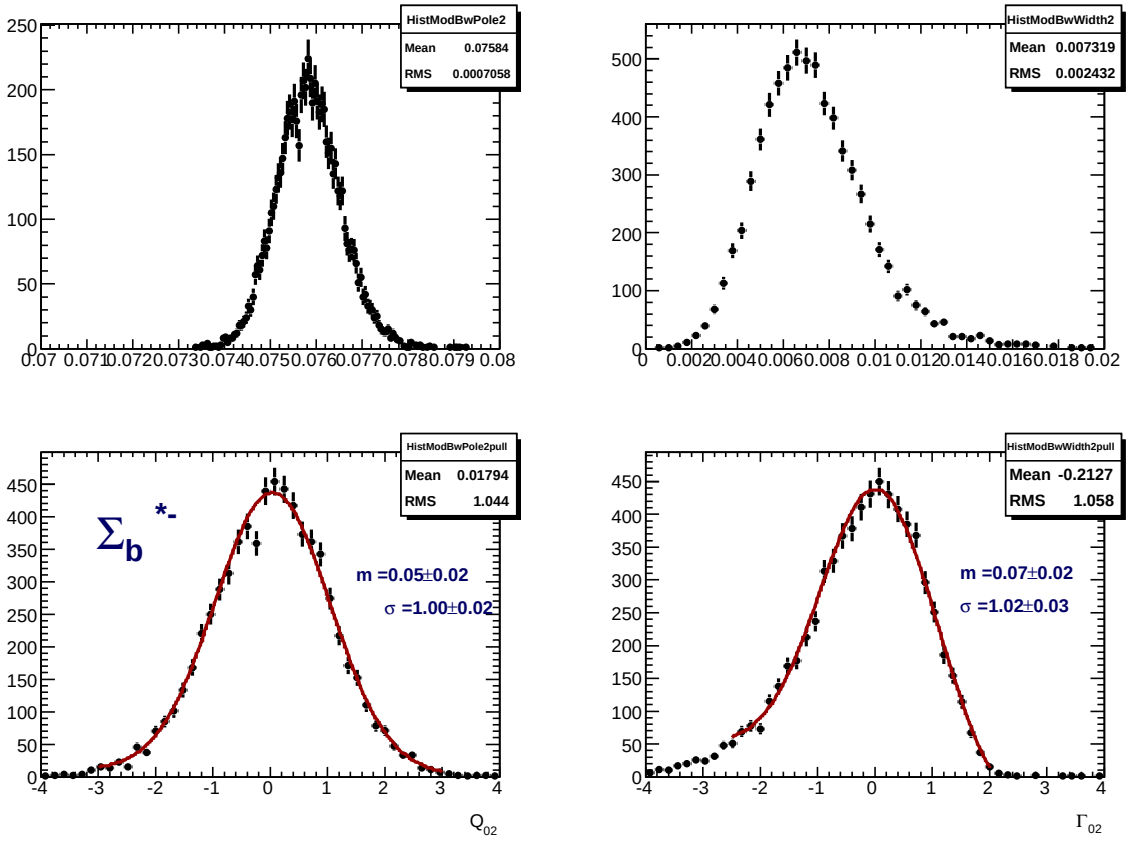

Figure 5.17: Σ_b^{*-} *7000 statistical trials for* Q_{02}, GeV/c^2 *and for* Γ_{02} GeV/c^2. *The plots show the distribution of fitted values and their pulls resulted from the same toy MC samples.*

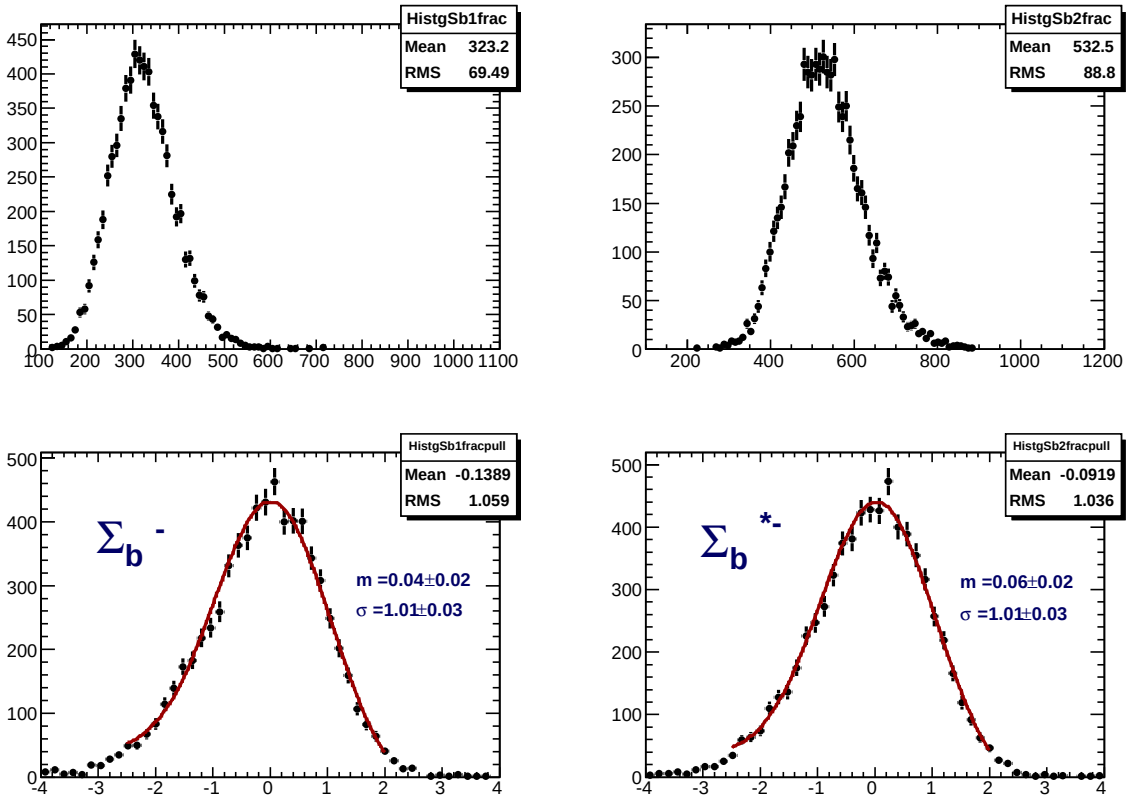

Figure 5.18: $\Sigma_b^{(*)-}$ *7000 statistical trials for yields* N_{s1} *and* N_{s2}*. The plots show the distribution of fitted values, and their pulls resulted from the same toy MC samples.*

to unit. The tails have a Gaussian behavior. The fitter performed stable and peacefully over a large number of 7000 trials consuming $\sim 1.7-2.0$ CPU (2.8 GHz)minutes per trial.

Performance Plots: $\mathbf{\Sigma_b^{(*)+}}$

The distribution of all converged $-log(LH)$ is shown on the upper plot of Fig. 5.19 with the experimental data value overlapped. The perfect Gaussian shape is observed with the mean value practically the same as the experimental data fit yields. The bottom 2×2 plot of the same Fig. 5.19 demonstrates a fitter response for a Σ_b^+ peak at Q_{01} (left column) and its width Γ_{01} (right column). Result of this study for Σ_b^{*+} is in the 5.20 and the fitter response for yields is shown at 5.21.

The results on absolute differences extracted from plots are summarized in Table 5.15.

Signal parameters	Stat. Mean	Mean−Orig.	Stat. RMS
Σ_b^+ pole, Q_{01}, MeV/c^2	52.07	0.04	1.09
Σ_b^+ width, Γ_{01} MeV/c^2	8.71	0.01	3.57
Σ_b^+ yield, N_{s1}	444	1	106
Σ_b^{*+} pole, Q_{02}, MeV/c^2	72.75	0.03	0.77
Σ_b^{*+} width, Γ_{02} MeV/c^2	11.13	0.13	2.93
Σ_b^{*+} yield, N_{s2}	785	4	120

Table 5.15: $\Sigma_b^{(*)+}$ *fitter performance: the absolute differences of the fitted values and their originally preset (see Table 5.12) values as extracted from high-statistics "toy MC" study of 7000 generated and fitted trials.*

The results on pulls extracted from plots and fits are summarized in Table 5.16.

Signal parameters	Stat. Mean	Stat. RMS	Gauss. μ	Gauss. σ
Σ_b^+ pole, Q_{01}, MeV/c^2	-0.11	1.08	-0.02 ± 0.02	1.02 ± 0.01
Σ_b^+ width, Γ_{01} MeV/c^2	-0.28	1.11	0.08 ± 0.02	1.07 ± 0.03
Σ_b^+ yield, N_{s1}	-0.12	1.10	0.06 ± 0.03	1.08 ± 0.04
Σ_b^{*+} pole, Q_{02}, MeV/c^2	0.01	1.03	0.04 ± 0.02	1.00 ± 0.03
Σ_b^{*+} width, Γ_{02} MeV/c^2	-0.16	1.03	0.13 ± 0.02	1.07 ± 0.03
Σ_b^{*+} yield, N_{s2}	-0.08	1.03	0.09 ± 0.03	1.04 ± 0.04

Table 5.16: $\Sigma_b^{(*)+}$ *fitter performance: the pull distributions and their fits with Gaussian.*

The data in Table 5.15 show practically no bias in masses, widths or yields for $\Sigma_b^{(*)+}$ Q-spectra. The longer positive tail of the Γ_{02} fitted values distribution w.r.t. the shorter negative one (and an inverse behavior at pull distribution plots) can be explained by

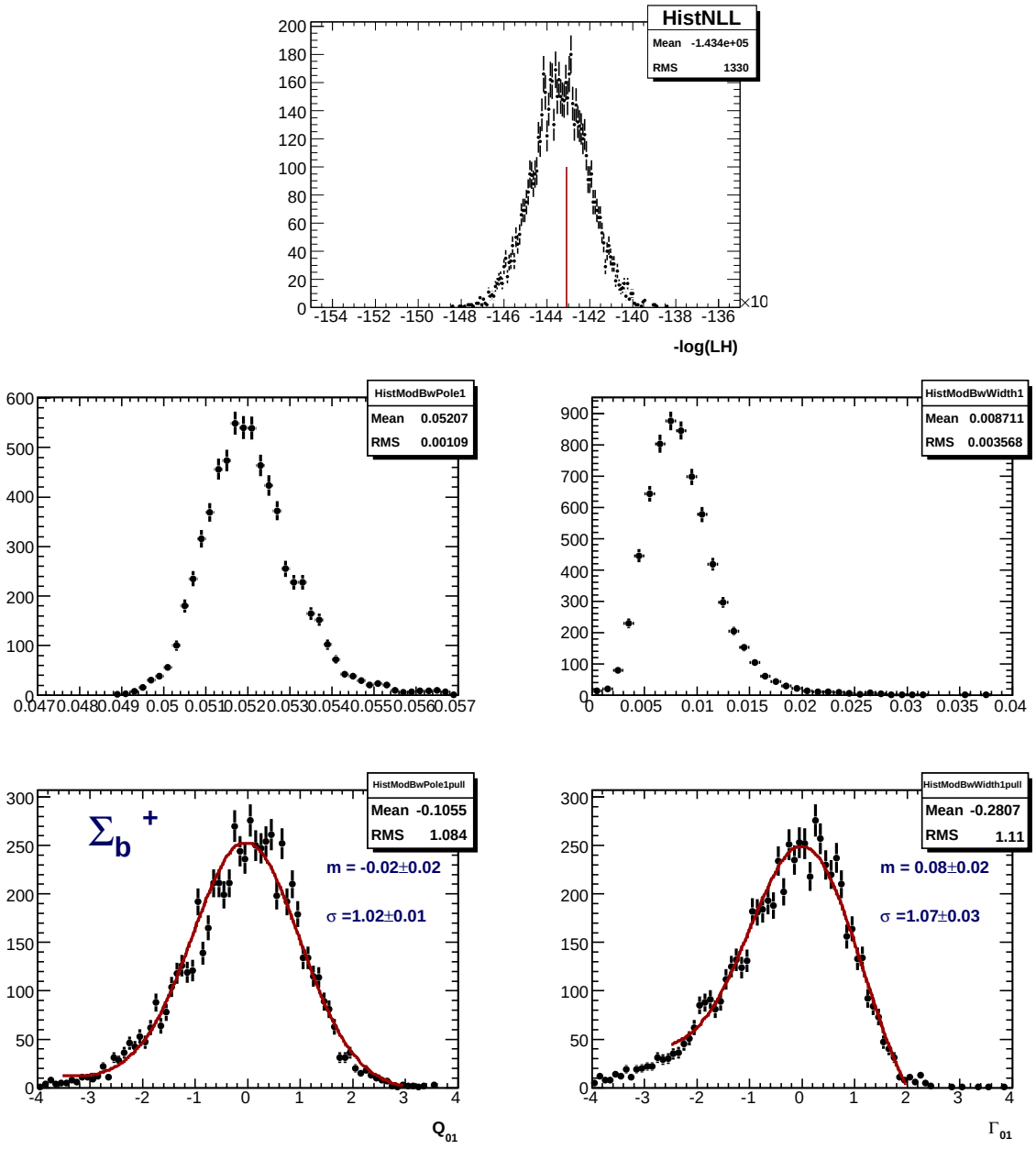

Figure 5.19: *The upper plot shows the distribution of NLL resulted by unbinned LH fits of 7000 trials. Σ_b^+ statistical trials for Q_{01}, GeV/c^2 and for Γ_{01} GeV/c^2 yielded the bottom plots showing the distribution of fitted values and their pulls.*

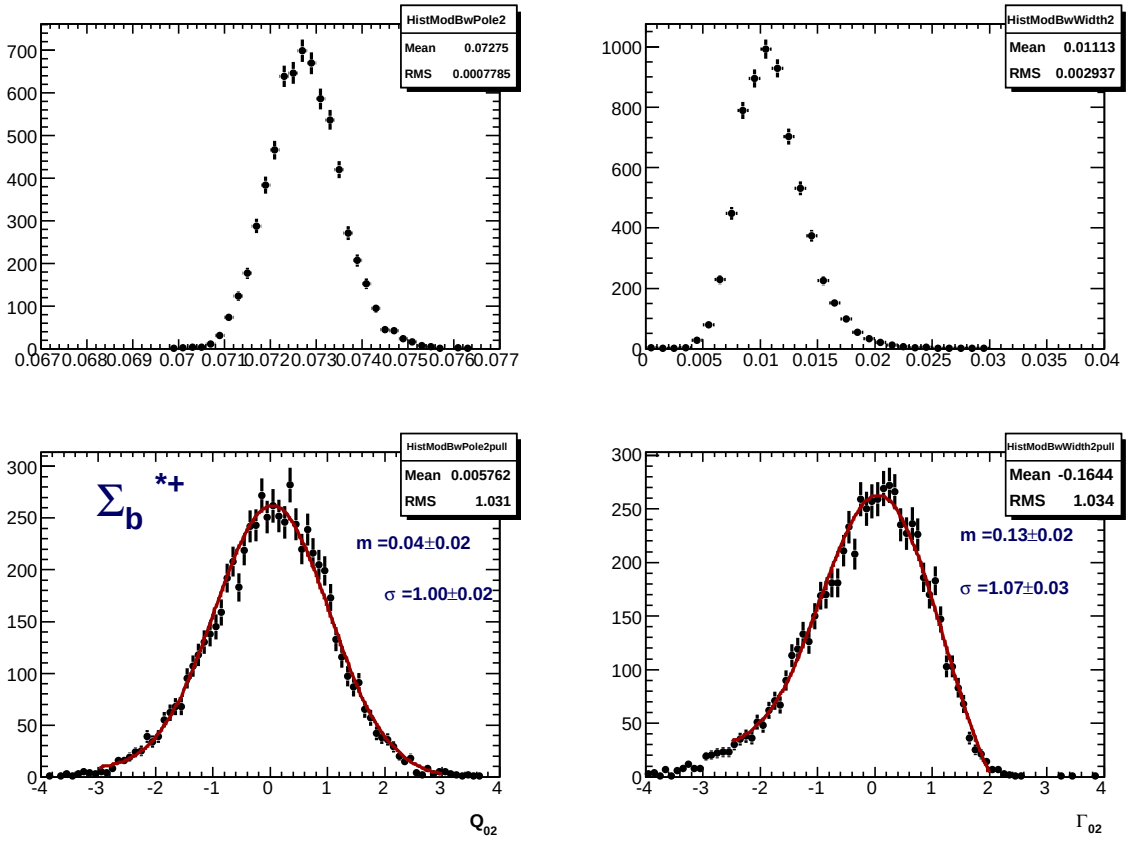

Figure 5.20: *Σ_b^{*+} 7000 statistical trials for Q_{21}, GeV/c^2 and for Γ_{02} GeV/c^2. The plots show the distribution of fitted values and their pulls resulted from the same toy MC samples.*

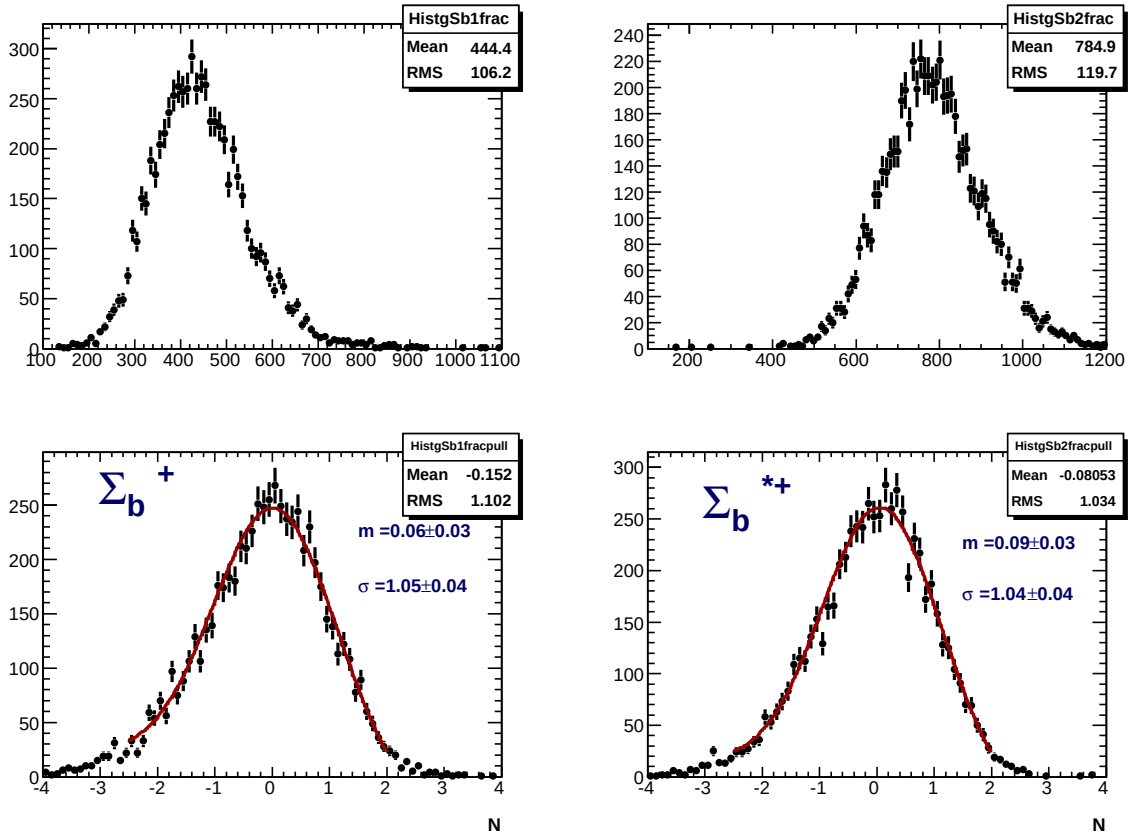

Figure 5.21: $\Sigma_b^{(*)+}$ *7000 statistical trials for yields* N_{s1} *and* N_{s2}*. The plots show the distribution of fitted values, their fit errors and their pulls resulted from the same toy MC samples.*

the naturally expected positive correlation with the yield and by parabolic errors. The stability of the fitter is assured by Gaussian σ or its RMS analog being always very close to unit. The tails have a Gaussian behavior. The fitter performed stable and peaceful over a large number of 7000 trials consuming $\sim 1.7 - 2.0$ CPU (2.8 GHz) minutes per trial.

Appendix C shows two additional toy MC checks of the fitter with varied input values.

5.5.2 Summary of the Statistical Tests

Based on our studies with different input conditions for our baseline fitter (see additional checks in Appendix C) we conclude

- the fitter response is stable w.r.t. to various input values
- the fitter response to Q_{01}, Q_{02} **has no bias and reveals Gaussian pulls** with $\sigma \approx 1.0$
- the fitter response to widths, Γ_{01}, Γ_{02} is stable with pulls having $\sigma \approx 1.0$. There is a typical positive tail in both Γ_{01} and Γ_{02} distribution causing a small bias. The tail is due to the fit correlations between widths and yields. This correlation is natural and expected. Additional asymmetry in pull distribution (negative tail) is caused by the fitter producing only parabolic errors only (HESSE) what is set due to CPU time considerations.
- We set the systematic uncertainty of width measurements, Γ_{01} and Γ_{02} due to the fitter according to Tables 5.14, 5.16:
  - for Σ_b^-: toy MC shows 0.02 ± 0.02, no bias, see Table 5.14
  - for Σ_b^{*-}: toy MC shows 0.07 positive bias, see Table 5.14
  - for Σ_b^+: toy MC shows 0.08 positive bias, see Table 5.16
  - for Σ_b^{*+}: toy MC shows 0.13 positive bias, see Table 5.16

  In order to be conservative, we assign **for all the widths** a systematic error using the highest observed bias, that is, the value 0.13 from the Σ_b^{*+}. For every state, we quote the systematic error:

  $$-0.13 \cdot \sigma_{stat}$$

- The fitter response and pulls for fitted yields of signals are pretty Gaussian, still with some less pronounced positive tails due to the fit correlation with widths. The bias is negligible in this case.

5.6 Fit Results

Our full baseline fit model consists of the signal expressed by Eq. 5.1 with Eq. 5.4 on top of the background expressed by a form in Eq. 5.8. The details and performance of the unbinned fitter are thoroughly covered in the Section 5.4. The fit is unbinned and being run in an extended mode as shown in Eq. 5.10. The list of parameters in the fit is arranged into the Table 5.17. The 9 floating parameters are subjected to fit with other 9 parameters fixed. The Q-spectrum of $\Sigma_b^{(*)-}$ and Q-spectrum of $\Sigma_b^{(*)+}$ are subjected to the fit independently. The Q-value fit range is set to be $Q \in (0.003,\, 0.210)\,\mathrm{GeV}/c^2$.

Only data from run periods passing the official quality requirements set by the CDF II Data Quality Management group (see Appendix B for further details) are included in the fitter.

The events having duplicate candidates contributing to $\Sigma_b^{(*)-}$ or $\Sigma_b^{(*)+}$ due to a faulty tracking reconstruction at soft low p_T range are rejected, see the explanation in Section 5.2.1. The events with the same `run#, event#` are filtered as well with a standard module provided with `BottomMods` package.

Signal parameters	$\Sigma_b^{(*)-} \to \Lambda_b^0 \pi^-_{\Sigma_b}$	$\Sigma_b^{(*)+} \to \Lambda_b^0 \pi^+_{\Sigma_b}$
Σ_b pole, Q_{01}, MeV/c^2	floating, $\in (3, 250)$	floating, $\in (3, 250)$
Σ_b width, Γ_{01} MeV/c^2	floating, $\in (-70, 70)$	floating, $\in (-70, 70)$
Σ_b yield, N_{s1}	floating, $\in (10, 5000)$	floating, $\in (10, 5000)$
Σ_b resolution, σ_{11} MeV/c^2	1.17	1.17
Σ_b resolution, σ_{21} MeV/c^2	2.92	2.92
Σ_b fraction of σ_{11}, g_{11}	0.70	0.70
Σ_b^* pole, Q_{02}, MeV/c^2	floating, $\in (3, 250)$	floating, $\in (3, 250)$
Σ_b^* width, Γ_{02} MeV/c^2	floating, $\in (-70, 70)$	floating, $\in (-70, 70)$
Σ_b^* yield, N_{s2}	floating, $\in (10, 5000)$	floating, $\in (10, 5000)$
Σ_b^* resolution, σ_{12} MeV/c^2	1.40	1.40
Σ_b^* resolution, σ_{22} MeV/c^2	3.80	3.80
Σ_b^* fraction of σ_{12}, g_{12}	0.73	0.73
Background, thr	0.140	0.140
Background, α	0.5	0.5
Background, C	floating, $\in (-\infty, +\infty)$	floating, $\in (-\infty, +\infty)$
Background, b_1	floating, $\in (-\infty, +\infty)$	floating, $\in (-\infty, +\infty)$
Background, b_2	3.12	2.89
Background yield, N_b	floating, $\in (5000, 50000)$	floating, $\in (5000, 50000)$

Table 5.17: *The list of the extended fit model parameters left floating or fixed to MC values (Gaussian resolutions) or fixed due to normalization propagated to the N_b parameter of the extended fit. The floating parameter ranges shown are set in the fitter.*

5.6.1 Fit Results for Candidates: $\mathbf{\Sigma_b^{(*)-}}$

Here we present the fit results based on the full available data sample.

The result of the unbinned fit for $\Sigma_b^{(*)-}$ charge state projected onto the binned distribution is shown at the Figure 5.22 with the unbinned likelihood fit profile superimposed onto corresponding Q-distribution sampled by 70 bins of $3\,\mathrm{MeV}/c^2$ width within $Q \in (0.0,\, 0.210)\,\mathrm{GeV}/c^2$ range. The data entries from the first bin, $Q \in (0.0,\, 0.003)\,\mathrm{GeV}/c^2$ do not contribute to the fit to avoid the latter from troubles at small or unphysical Q areas.

Please find the Table 5.18 for $\Sigma_b^{(*)-}$ candidates. The fit finds quite significant yields

$\mathbf{\Sigma_b^{(*)-}}$ **: Parameters**	**Value**	**+HiError**	**-LoError**	**Comments**
Q_{01}, MeV/c^2, Σ_b^- pole	56.21	+0.61	−0.51	MINOS
Q_{02}, MeV/c^2, Σ_b^{*-} pole	75.71	+0.61	−0.61	MINOS
Γ_{01}, MeV/c^2, Σ_b^- width	4.3	+3.1	−2.1	MINOS
Γ_{02}, MeV/c^2, Σ_b^{*-} width	6.4	+2.2	−1.8	MINOS
N_{s1}, evts, Σ_b^- yield	333	+93	−73	MINOS
N_{s2}, evts, Σ_b^{*-} yield	522	+85	−76	MINOS
N_b, evts, background	13591	+151	−151	parabolic
b_1, background	−3.55	+0.49	−0.49	parabolic
C, background	3.99	+0.19	−0.19	parabolic
$-\log(\mathcal{L})$	−147167			minimized NLL

19

Table 5.18: *Statistics of* $\int \mathcal{L}\,dt \approx 6.0\,fb^{-1}$*: the fit results from* $\Sigma_b^{(*)-}$ *spectrum. The errors of the signal fit parameters have been calculated by MINOS.*

for both Σ_b^- and Σ_b^{*-} peaks. The significances are to be expected well above 5 *st.dev.* as the numbers quoted in a column "Comments" correspond to the fit with floating widths. The MINUIT produces the successful fit and calculates the accurate covariance matrix, see the Table 5.19.

The fitted Breit-Wigner widths Γ_{01} and Γ_{02} are correlated with the corresponding signal yields N_{s1} and N_{s2} which is expected.

The largest correlations are found between polynomial coefficients but the fit errors of both b_1 and C are quite small, (3...7)% and the fit error of a total background normalization is less than 1.5%.

There are no strong correlations of the coefficients with the physical parameters. The fitted mass values have quite low correlations.

5.6.2 Fit Results for Candidates: $\mathbf{\Sigma_b^{(*)+}}$

Here we present the fit results based on the full data available.

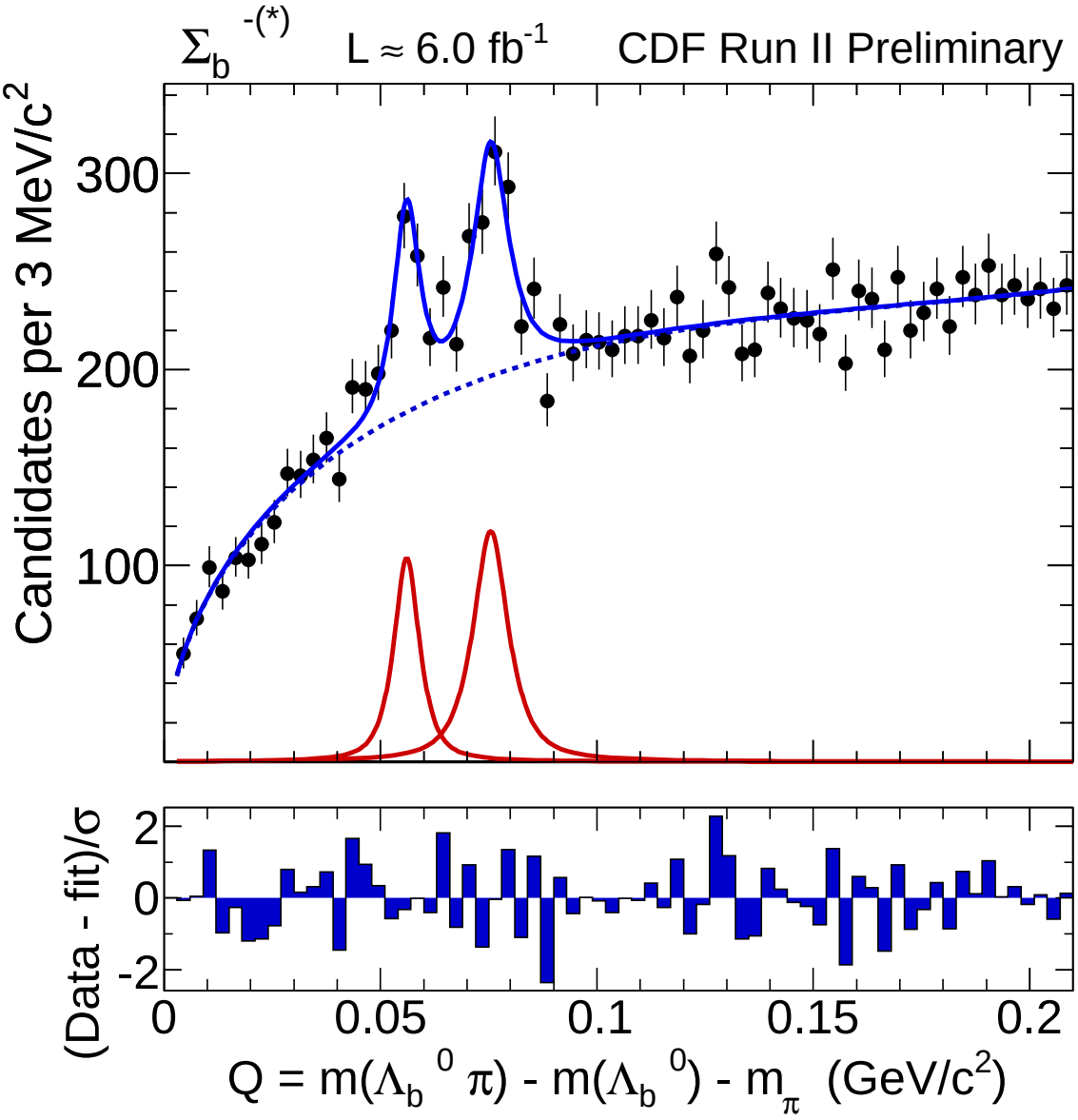

Figure 5.22: *$\Sigma_b^{(*)-}$ candidates: the Q-value spectrum, where $Q = M(\Lambda_b^0\pi^-) - M(\Lambda_b^0) - m_\pi$, with the unbinned fit profile superimposed.*

$\mathbf{\Sigma_b^{(*)-}}$: Par.	b_1	C	Q_{01}	Q_{02}	Γ_{01}	Γ_{02}	N_b	N_{s1}	N_{s2}
b_1	1.000	-0.989	-0.032	0.019	-0.162	0.123	0.016	-0.173	0.150
C	-0.989	1.000	0.041	-0.006	0.220	-0.100	-0.074	0.240	-0.110
Q_{01}	-0.032	0.041	1.000	0.107	0.316	-0.214	-0.046	0.283	-0.208
Q_{02}	0.019	-0.006	0.107	1.000	0.201	0.002	-0.108	0.204	-0.009
Γ_{01}	-0.162	0.220	0.316	0.201	1.000	-0.284	-0.341	0.861	-0.253
Γ_{02}	0.123	-0.100	-0.214	0.002	-0.284	1.000	-0.233	-0.303	0.754
N_b	0.016	-0.074	-0.046	-0.108	-0.341	-0.233	1.000	-0.396	-0.355
N_{s1}	-0.173	0.240	0.283	0.204	0.861	-0.303	-0.396	1.000	-0.243
N_{s2}	0.150	-0.110	-0.208	-0.009	-0.253	0.754	-0.355	-0.243	1.000

Table 5.19: *The fit results of $\Sigma_b^{(*)-}$ spectrum: the accurate full covariance matrix calculated by HESSE subroutine of MINUIT.*

The result of the unbinned fit for $\Sigma_b^{(*)+}$ charge state is shown at the Figure 5.23 with the unbinned likelihood fit profile superimposed onto corresponding Q-distribution sampled by 70 bins of $3\,\mathrm{MeV}/c^2$ width within $Q \in (0.0,\, 0.210)\,\mathrm{GeV}/c^2$ range. Again like in previous case the entries into the first bin do not contribute to the fit. Please find the Table 5.20 for $\Sigma_b^{(*)+}$ candidates. The fit finds quite significant yields for both Σ_b^{+} and Σ_b^{*+} peaks.

$\mathbf{\Sigma_b^{(*)+}}$: Parameters	Value	+HiError	-LoError	Comments
Q_{01}, MeV/c^2, Σ_b^{+} pole	51.96	+0.94	−0.84	MINOS
Q_{02}, MeV/c^2, Σ_b^{*+} pole	72.69	+0.73	−0.69	MINOS
Γ_{01}, MeV/c^2, Σ_b^{+} width	9.2	+3.8	−2.9	MINOS
Γ_{02}, MeV/c^2, Σ_b^{*+} width	10.4	+2.7	−2.2	MINOS
N_{s1}, evts, Σ_b^{+} yield	468	+110	−95	MINOS
N_{s2}, evts, Σ_b^{*+} yield	782	+114	−103	MINOS
N_b, evts, background	12831	+166	−166	parabolic
b_1, background	−4.89	+1.2	−1.2	parabolic
C, background	4.27	+0.46	−0.46	parabolic
$-\log(\mathcal{L})$	−143090			minimized NLL

Table 5.20:
Statistics of $\int \mathcal{L}\,dt \approx 6.0\,fb^{-1}$: the fit results from $\Sigma_b^{(*)+}$ spectrum. The errors of the signal fit parameters have been calculated by MINOS.

The significances are to be expected well above 5 *st.dev.* as the numbers quoted in a column "Comments" correspond to the fit with floating widths. The MINUIT produces the successful fit and calculates the accurate covariance matrix, see the Table 5.21.

The fitted Breit-Wigner widths Γ_{01} and Γ_{02} are correlated with the corresponding signal yields N_{s1} and N_{s2} which is expected.

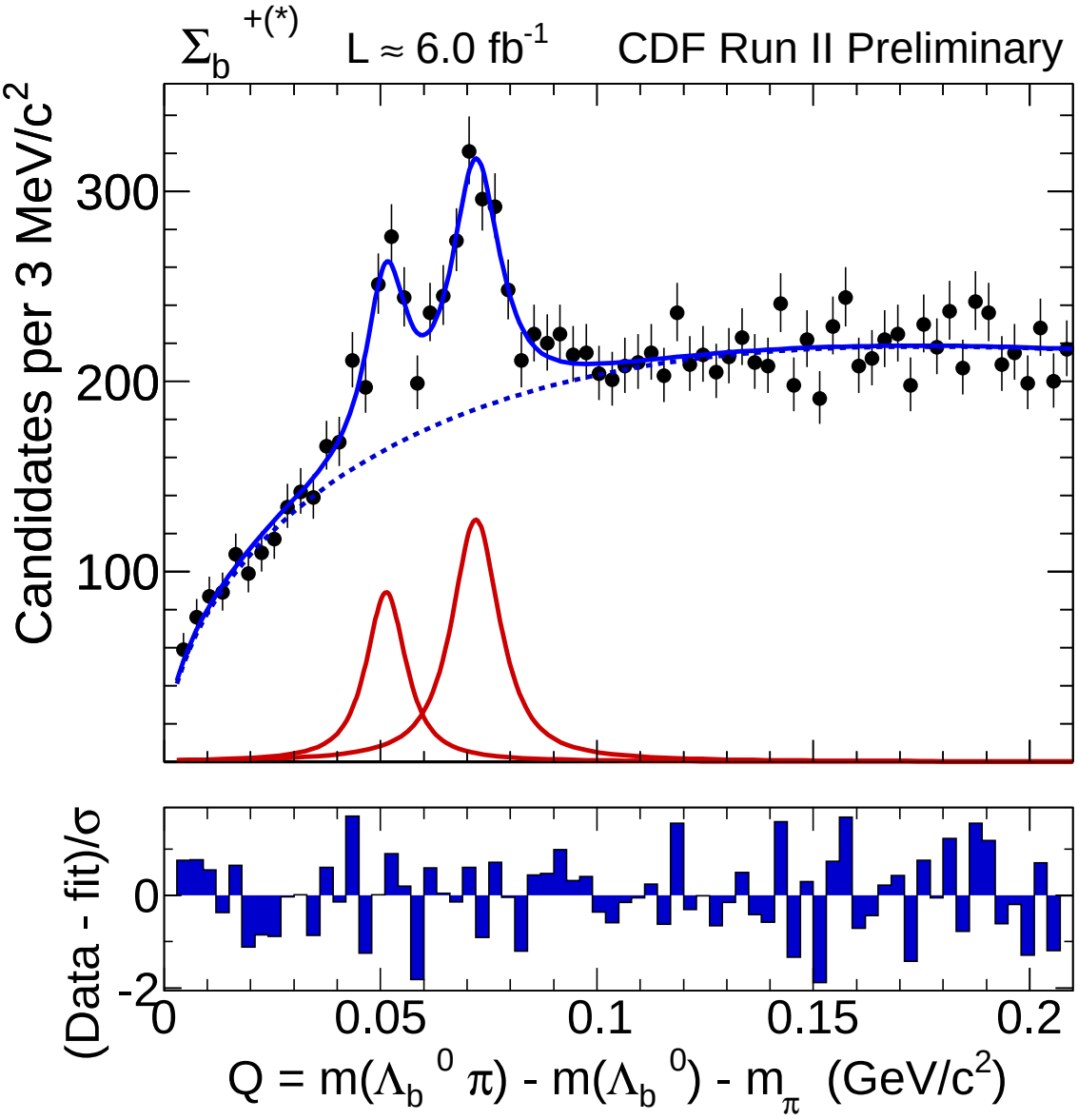

Figure 5.23: $\Sigma_b^{(*)+}$ *candidates: the* Q*-value spectrum, where* $Q = M(\Lambda_b^0\pi^+) - M(\Lambda_b^0) - m_\pi$*, with the unbinned fit profile superimposed.*

The largest correlations are found between polynomial coefficients but the fit errors of both b_1 and C are quite small, (3...7)% and the fit error of a total background normalization is less than 1.5%.

There are no strong correlations of the coefficients with the physical parameters. The fitted mass values have quite low correlations.

$\mathbf{\Sigma_b^{(*)+}}$: **Par.**	b_1	C	Q_{01}	Q_{02}	Γ_{01}	Γ_{02}	N_b	N_{s1}	N_{s2}
b_1	1.000	-0.994	-0.039	0.023	-0.216	0.068	0.096	-0.249	0.076
C	-0.994	1.000	0.040	0.001	0.255	-0.038	-0.150	0.296	-0.034
Q_{01}	-0.039	0.040	1.000	0.092	0.401	-0.292	0.008	0.368	-0.342
Q_{02}	0.023	0.001	0.092	1.000	0.171	0.355	-0.270	0.177	0.258
Γ_{01}	-0.216	0.255	0.401	0.171	1.000	-0.154	-0.346	0.799	-0.183
Γ_{02}	0.068	-0.038	-0.292	0.355	-0.154	1.000	-0.364	-0.252	0.788
N_b	0.096	-0.150	0.008	-0.270	-0.346	-0.364	1.000	-0.399	-0.468
N_{s1}	-0.249	0.296	0.368	0.177	0.799	-0.252	-0.399	1.000	-0.236
N_{s2}	0.076	-0.034	-0.342	0.258	-0.183	0.788	-0.468	-0.236	1.000

Table 5.21: *The fit results of $\Sigma_b^{(*)+}$ spectrum: the accurate full covariance matrix calculated by HESSE subroutine of MINUIT.*

5.6.3 Significance Estimates for Signals

The fit results in Table 5.18 and Table 5.20 show the strong signals of both low mass $\Sigma_b^{\pm}$ and higher mass $\Sigma_b^{*\pm}$ states found by our fitters. As far as in the discovery paper [3], the significance of individual signals was somewhat low as has been criticized by [80]. We make the significance calculations based on a log- ratio of minimal likelihoods, $\mathcal{L}_1/\mathcal{L}_0$, reached by the fitter for our base line fit model hypothesis, $-\log\mathcal{L}_1$, and for a particular null hypothesis, $-\log\mathcal{L}_0$, our default base line one is going to be tested against.

$$-2\cdot\log\frac{\mathcal{L}_0}{\mathcal{L}_1} = -2\cdot\Delta(\log\mathcal{L}) \tag{5.11}$$

We interpret Eq. 5.11 as a χ^2 of the null hypothesis spectrum to fluctuate to our base signal one with a number of degrees of freedom equal to the difference in the number of floating parameters between both hypotheses. The corresponding probability is converted to the equivalent number of σ's (N_σ) in a standard normal distribution using the following expresion:

$$P = \int_{N_\sigma}^{\infty} G(x;0,1)\,dx \tag{5.12}$$

where P is the probability and $G(x;0,1)$ is the usual Gaussian distribution:

$$G(x;\mu,\sigma) = \frac{1}{\sqrt{2\pi\sigma^2}} \cdot e^{\frac{-1}{2}\cdot(\frac{x-\mu}{\sigma})^2}$$

with $\mu = 0$ and $\sigma = 1$.

We consider the next null hypotheses to test the combined pair or individual one of observed charged states of $\Sigma_b^{(*)\pm}$

- Any single peak instead of the two ones is observed, the null hypotheses is a single peak p.d.f and the same polynomial background as in the base line model: the single peak spectrum fluctuates to two peaks with $\Delta\text{NDF} = 3$. The width of the single peak is floating, within $\Gamma_0 \in (0.001, 0.070)\,\text{GeV}/c^2$ as well as its position, $Q_0 \in (0.003, 0.210)\,\text{GeV}/c^2$. We expect that this test is going to be the most critical one.

- The signal Σ_b^* is observed but the Σ_b has been missed: the background at the left fluctuates to the peak of Σ_b with $\Delta\text{NDF} = 4$. We impose a loose requirement on an existence of the second peak, Σ_b^*, viz. we fix the width of Σ_b^* to the expected theoretical value of $12\,\text{MeV}/c^2$ (see Table 1.2) but let the fitter to find and fit the Σ_b^* position which is again floating, within $Q_0 \in (0.003, 0.210)\,\text{GeV}/c^2$.

- The signal Σ_b is observed but the Σ_b^* has been missed: the background at the right fluctuates to the peak of Σ_b^* with $\Delta\text{NDF} = 4$. We impose a loose requirement on an existence of the first peak, Σ_b, viz. we fix the width of Σ_b to the expected theoretical value of $7\,\text{MeV}/c^2$ (see Table 1.2) but let the fitter to find and fit the Σ_b position which is again floating, within $Q_0 \in (0.003, 0.210)\,\text{GeV}/c^2$.

- Any single peak is observed, the null hypotheses is our base line background model: the background fluctuates to this single peak with $\Delta\text{NDF} = 3$. This test should determine the significance of a single peak model w.r.t. to a pure background.

- Neither Σ_b nor Σ_b^* are observed, the null hypotheses is our base line background model: the background fluctuates to two peaks with $\Delta\text{NDF} = 6$. This test is expected to be the least critical one.

Candidates: $\mathbf{\Sigma_b^{(*)-}}$

In Table 5.22 the different hypotheses are tested and the comparison of likelihood values reached by fitter,$-2\cdot\Delta(\log\mathcal{L})$ and its analog in terms of Gaussian number of σ are shown. Figure 5.24 shows the fits under the different hypotheses. The base line model exposed to the tests reveals the robust significances, e.g. with Gaussian $7.5\,\sigma$ for the most critical comparison of the two-peak model hypothesis against a quite general null hypothesis assuming the single peak of any width in any place. The other cases are more significant.

Null Hypothesis	$-2\cdot\Delta(\log\mathcal{L})$	ΔNDF	Prob(χ^2)	N_σ	Comment
Any single peak	$-2\cdot(-147167.+147135.)$	3	$\approx 8.2\cdot10^{-14}$	7.5	w.r.t. double pk.
No Σ_b^-, **with** Σ_b^{*-}	$-2\cdot(-147167.+147132.)$	4	$\approx 2.3\cdot10^{-14}$	7.6	w.r.t. double pk., $\Gamma_{02}=12\,\mathrm{MeV}/c^2$
No Σ_b^{*-}, **with** Σ_b^-	$-2\cdot(-147167.+147110.)$	4	$\approx 1.0\cdot10^{-23}$	10.0	w.r.t. double pk., $\Gamma_{01}=7\,\mathrm{MeV}/c^2$
No any signal	$-2\cdot(-147135.+147080.)$	3	$\approx 1.1\cdot10^{-23}$	10.0	w.r.t. single pk.
No any signal	$-2\cdot(-147167.+147080.)$	6	$\approx 6.4\cdot10^{-35}$	12.3	w.r.t. double pk.

Table 5.22: *Estimation of the significance for our $\Sigma_b^{(*)-}$ double peak base line fit hypothesis being tested against several null hypotheses. The likelihood value for our base line fit is taken from the Table 5.18. The base line model exposed to the tests reveals the robust significances above $7.0\,\sigma$ in Gaussian terms (see Eq. 5.12).*

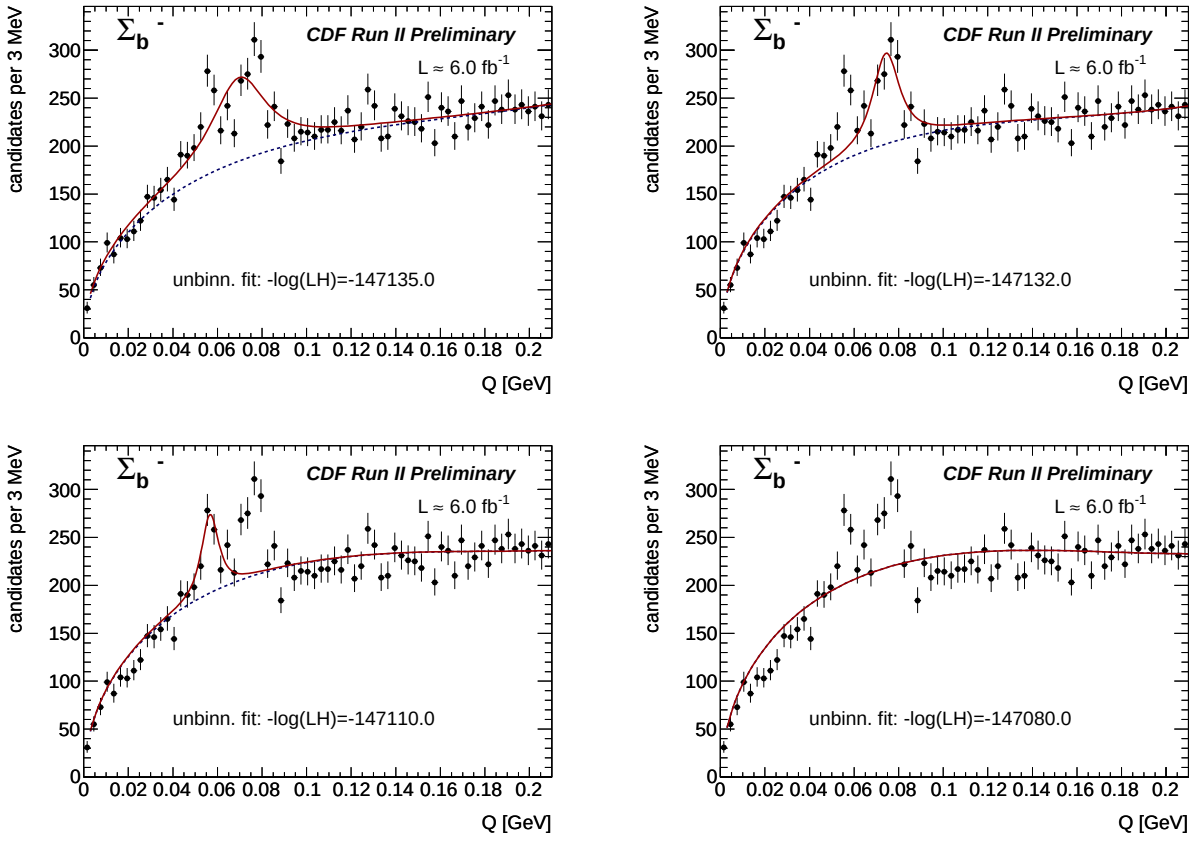

Figure 5.24: *Fits for $\Lambda_b^0\pi^-_{\Sigma_b}$ under four different null hypotheses: any single peak instead of two ones, no Σ_b^- but there is Σ_b^{*-}, no Σ_b^{*-} but there is Σ_b^-, no any peak observed, see the Table 5.22.*

Null Hypothesis	$-2\cdot\Delta(\log\mathcal{L})$	ΔNDF	Prob(χ^2)	N_σ	Comment
Any single peak	$-2\cdot(-143090.+143060.)$	3	$\approx 5.9\cdot10^{-13}$	7.2	w.r.t. double pk.
No Σ_b^+, **with** Σ_b^{*+}	$-2\cdot(-143090.+143057.)$	4	$\approx 1.6\cdot10^{-13}$	7.4	w.r.t. double pk., $\Gamma_{02}=12\,\mathrm{MeV}/c^2$
No Σ_b^{*+}, **with** Σ_b^+	$-2\cdot(-143090.+143006.)$	4	$\approx 2.8\cdot10^{-35}$	12.4	w.r.t. double pk., $\Gamma_{01}=7\,\mathrm{MeV}/c^2$
No any signal	$-2\cdot(-143060.+142981.)$	3	$\approx 4.9\cdot10^{-34}$	12.2	w.r.t. single pk.
No any signal	$-2\cdot(-143090.+142981.)$	6	$\approx 2.8\cdot10^{-44}$	14.0	w.r.t. double pk.

Table 5.23: *Estimation of the significance for our $\Sigma_b^{(*)+}$ base line fit hypothesis being tested against several null hypotheses. The likelihood value for our base line fit is taken from the Table 5.20. The base line model exposed to the tests reveals the robust significances above $7.0\,\sigma$ in Gaussian terms. (see Eq. 5.12).*

Candidates: $\mathbf{\Sigma_b^{(*)+}}$

In Table 5.23 the different hypotheses tested and the comparison of likelihood values reached by fitter,$-2\cdot\Delta(\log\mathcal{L})$ and an equivalent in terms of Gaussian number of σ are shown. Figure 5.25 shows the fits under the different hypotheses. The base line model exposed to the tests reveals the robust significances, e.g. with Gaussian $7.2\,\sigma$ for the most critical comparison of the two-peak model hypothesis against a quite general null hypothesis assuming the single peak of any width in any place. The other cases are much more significant.

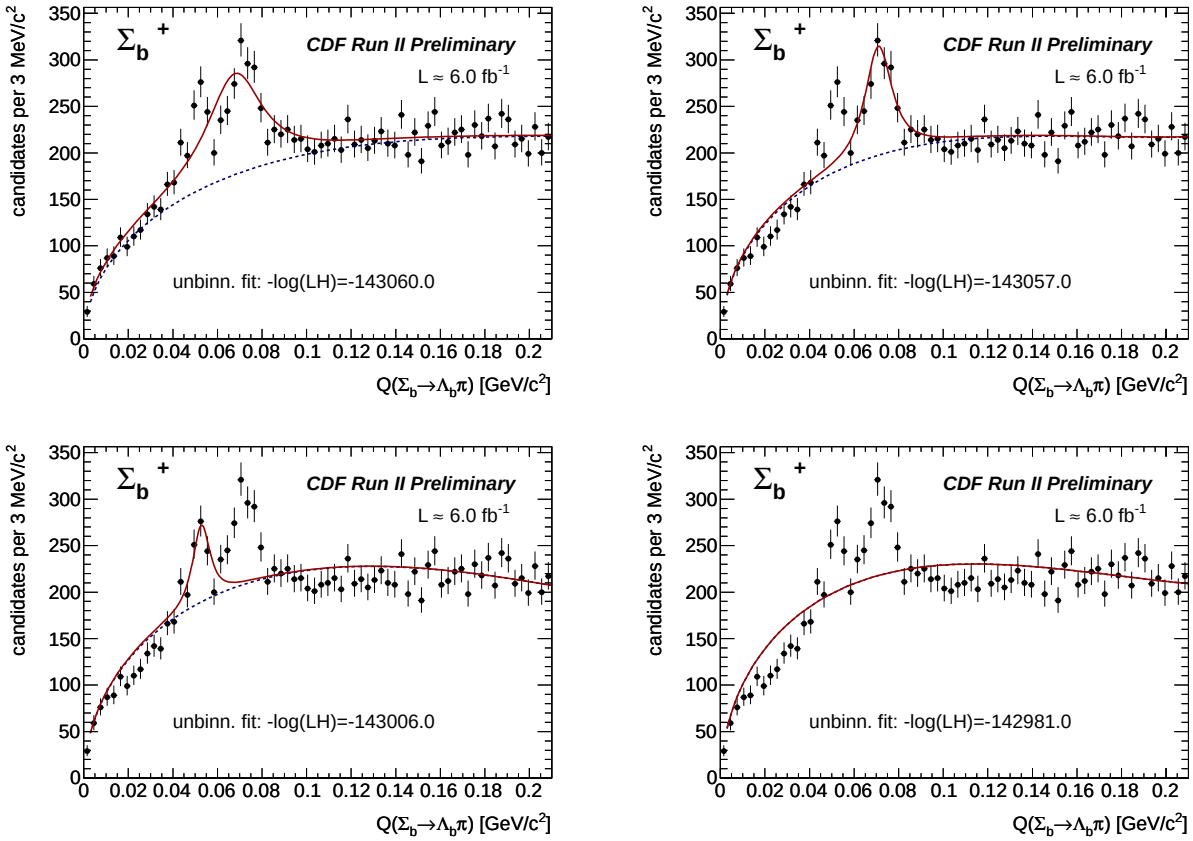

Figure 5.25: Fits for $\Lambda_b^0 \pi^+_{\Sigma_b}$ under four different null hypotheses: any single peak instead of two ones, no Σ_b^+ but there is Σ_b^{*+}, no Σ_b^{*+} but there is Σ_b^+, no any peak observed, see the Table 5.23.

Chapter 6

Systematic Error Estimates

The sources of systematic errors affecting our measurements can be divided in three different groups:

- The small bias introduced by the fitter on the widths.
- Those due to mass scale systematics on the soft pion.
- The systematics on assumptions made about the fitter.

The first one is discussed in Section 5.5.2. The other sources of systematic errors are estimated below.

6.1 Mass Scale Systematics

These sources of systematic error are due primarily to the fact that the calibration is only as precise as it has been tested out to. To estimate these errors, we reconstruct resonances of known negligible width such as the D^*. Using measurements of the D^*, Σ_c, and Λ_c^+ resonances, we extrapolate the mass scale offset expected for the Σ_b Q-value.

6.1.1 Experimental Spectra of D*

The $D^* - D^0$ mass difference is 145.421 ± 0.010 MeV/c^2 and the width of the D^* is 0.096 ± 0.022 MeV/c^2 [17]. This width is much smaller than the CDF mass resolution, so the measurement of the D^* width is actually a measurement of the resolution detector. By fitting the $D^* - D^0$ distribution, we measure both the systematic errors on the mass measurement and the mass resolution.

We use the dataset *xbhdij*, corresponding to ~ 760 pb^{-1} of data, reconstructed with the `BottomMods` package, and covering the run range 233133−246231 (or in terms of integrated luminosity, $2.2 - 2.7$ fb^{-1}). We also study a subsample of the dataset *xbhdfm* including approximately the same number of events than in the *xbhdij* sample, and covering the run range $261119 - 267718$ (or in terms of integrated luminosity, $3.7 - 4.2$ fb^{-1}). These data

samples are compared with a Monte Carlo simulation covering the run range 258880 − 261005 and being reconstructed using the same `BottomMods` package.

All samples are reconstructed in the channel: $D^{*\pm} \to D^0\pi^\pm$, $D^0 \to K^+\pi^-$.

We expect tracks with p_T less than 400 MeV/c to have a worse detector resolution than higher momentum tracks, which they are better measured. We divide the $D^* - D^0$ mass plot into bins of track p_T in order to compare the mass resolution of different momentum tracks for the pion from the D^* decay (soft pion). The bins used are:

- Track $p_T > 200$ MeV/c
- Track $p_T > 400$ MeV/c
- 200 MeV/$c <$ track $p_T < 400$ MeV/c
- 400 MeV/$c <$ track $p_T < 600$ MeV/c
- 600 MeV/$c <$ track $p_T < 800$ MeV/c
- 800 MeV/$c <$ track $p_T < 1$ GeV/c

We fit each mass plot with an unbinned likelihood fit, using a double Gaussian PDF to describe the $D^* - D^0$ signal, and the following expresion to describe the background:

$$RooDstD0BG(Q; dm_0, C, A, B) = (1 - e^{(-(Q-dm_0)/C)}) \cdot \left(\frac{Q}{dm_0}\right)^A + B \cdot (Q/dm_0 - 1)) \quad (6.1)$$

Where $Q = M(D^*) - M(D^0)$, and dm_0, A, B, C are floating parameters in the fit.

The mass plots for all these ranges of track p_T are shown in Figs. [6.1-6.6]. Mass and resolution parameters for all fits are listed in Tables [6.1,6.2,6.3].

Under inspection of these tables and the Figure 6.7, we conclude that the CDF Monte Carlo tipically underestimate the D^* resolutions. Tables 6.4 and 6.5 show the comparison between D^* resolutions from data periods *xbhdij* ,*xbhdfm* and MC simulation for several ranges of the soft pion p_T.

The maximum discrepancies found between data and Monet Carlo are lower than 25% for the σ narrow and lower than 40% for the wide one. These two values are used to estimate systematic errors for the signal parameters due to these underestimation of the resolution in Section 6.2.1.

Figure 6.7 also shows that the differences in the resolution detector between data from samples *xbhdij* and *xbhdfm* are negligible. Thus we do not estimate any systematic error comming from differences in resolution for data taken at different times/luminosities.

The resolution for D^{*-} is better than for D^{*+} as it is shown at Tables [6.1, 6.2,6.3] and Figure 6.7.

Tables 6.6 and 6.7 show these resolution differences between D^{*+} and D^{*-} for several ranges of the soft pion p_T. The maximum discrepancies found are 20% for the σ narrow and lower than 40% for the wide one.

These differences translate into different resolutions for states decaying into soft pions with opposite charge, so $\Sigma_b^{(*)\pm}$ and $\overline{\Sigma_b^{(*)\pm}}$ should have different resolution because the final states of their decays have opposite charge soft pions:

- $\Sigma_b^{(*)\pm} \to \Lambda_b^0 \pi^\pm$
- $\overline{\Sigma_b^{(*)\pm}} \to \overline{\Lambda}_b^0 \pi^\mp$

Our values for $\Sigma_b^{(*)\pm}$ resolution are obtained from Monte Carlo samples on the exclusive mode $\Sigma_b^{(*)+} \to \Lambda_b^0 \pi^+$ for positive charge states, as it is explained in Section 5.4.1. We use these same resolution parameters for all $\Sigma_b^{(*)\pm} \to \Lambda_b^0 \pi^\pm$ decay modes. Due we fit together $\Sigma_b^{(*)+} \to \Lambda_b^0 \pi^+$ with $\overline{\Sigma}_b^{(*)-} \to \overline{\Lambda}_b^0 \pi^-$ and $\Sigma_b^{(*)-} \to \Lambda_b^0 \pi^-$ with $\overline{\Sigma}_b^{(*)-} \to \overline{\Lambda}_b^0 \pi^+$, we always have together states decaying to positive and negative charge soft pions.

As we have seen that states decaying to negative charge soft pions have better resolution than those decaying to positive charge soft pions, we are actually overestimating the resolution of the states decaying to negative charge soft pions.

This could introduce a bias in our measurements. We use the maximum differences from Tables 6.6 and 6.7 to perform toy Monte Carlo studies in order to estimate a systematic error due to this uncertainty in the resolution in Section 6.2.1.

6.1.2 Determination of the Mass Scale Systematic Errors

We compare the measured masses of the D^*, Σ_c and Λ_c^+ particles by CDF with the world average values quoted in the PDG [17] to estimate the systematic error due to calibration of the energy scale.

These are decays which release little kinetic energy, and they are well characterized by the Q-value, which is the ΔM value (see Table 6.8) less the pion mass (or two pion masses, in the case of the Λ_c^+).

In a previous analysis, it has been shown that the systematic error on this Q-value may be approximed as linear, $\delta Q = a \cdot Q + \delta m(Q = 0)$ [81]. Thus, the followed procedure is plot the mass differences between CDF and PDG mass measurements as a function of the Q-value of the decays. Then we fit the graph to a linear function. This fuction is then evaluated at the Σ_b Q-value to extract the systematic error. For the Σ_c and Λ_c^+ states, we take the more precise CDF II values from [82]. For the D^* state we use the Q-value performing the error-weighted average using the four D^* masses from $xbhdij$ and $xbhdfm$ datasets. Table 6.8 list the used CDF II and PDG masses.

To avoid correlations in the fit function, we introduce an offset of the fit variable equal to the Σ_b Q-value. For example, the Σ_b^+ Q-value is 52 MeV/c^2, so the fit takes the form $\delta Q = a \cdot (Q - 52) + \delta m(Q = 0)$. In this case, the intercept $\delta m(Q = 0)$ is the bias on the Q-value. Figure 6.8 contains the mass difference plots with the four fits, one per each Σ_b

Track p_T (MeV/c)	Mean	σ_{narrow}	σ_{wide}
	$D^{*+} \to D^0\pi^+$		
Track $p_T > 200$	145.479	0.643 ± 0.002	2.094 ± 0.013
Track $p_T > 400$	145.481	0.639 ± 0.002	2.116 ± 0.014
$200 <$ track $p_T < 400$	145.464	0.671 ± 0.007	1.960 ± 0.036
$400 <$ track $p_T < 600$	145.467	0.640 ± 0.003	2.170 ± 0.017
$600 <$ track $p_T < 800$	145.492	0.628 ± 0.004	1.997 ± 0.027
$800 <$ track $p_T < 1000$	145.509	0.630 ± 0.007	2.035 ± 0.042
	$D^{*-} \to D^0\pi^-$		
Track $p_T > 200$	145.471	0.548 ± 0.002	1.532 ± 0.011
Track $p_T > 400$	145.471	0.544 ± 0.002	1.513 ± 0.014
$200 <$ track $p_T < 400$	145.474	0.581 ± 0.005	1.633 ± 0.032
$400 <$ track $p_T < 600$	145.463	0.572 ± 0.002	1.713 ± 0.015
$600 <$ track $p_T < 800$	145.473	0.510 ± 0.003	1.338 ± 0.017
$800 <$ track $p_T < 1000$	145.482	0.504 ± 0.005	1.312 ± 0.020

Table 6.1: *Mass and resolution parameters for the $D^* - D^0$ fits in bins of track p_T for xbhdij data sample. The quoted errors are statistic only. Both, the Mean and σ are in units of* MeV/c^2.

Track p_T (MeV/c)	Mean	σ_{narrow}	σ_{wide}
	$D^{*+} \to D^0\pi^+$		
Track $p_T > 200$	145.486	0.658 ± 0.002	2.064 ± 0.014
Track $p_T > 400$	145.486	0.656 ± 0.002	2.081 ± 0.014
$200 <$ track $p_T < 400$	145.487	0.682 ± 0.009	1.806 ± 0.053
$400 <$ track $p_T < 600$	145.467	0.656 ± 0.003	2.128 ± 0.019
$600 <$ track $p_T < 800$	145.499	0.648 ± 0.004	2.034 ± 0.026
$800 <$ track $p_T < 1000$	145.512	0.646 ± 0.007	1.936 ± 0.043
	$D^{*-} \to D^0\pi^-$		
Track $p_T > 200$	145.478	0.559 ± 0.002	1.546 ± 0.012
Track $p_T > 400$	145.477	0.559 ± 0.002	1.552 ± 0.012
$200 <$ track $p_T < 400$	145.490	0.555 ± 0.007	1.430 ± 0.034
$400 <$ track $p_T < 600$	145.468	0.586 ± 0.002	1.757 ± 0.014
$600 <$ track $p_T < 800$	145.480	0.518 ± 0.003	1.328 ± 0.016
$800 <$ track $p_T < 1000$	145.489	0.518 ± 0.005	1.336 ± 0.021

Table 6.2: *Mass and resolution parameters for the $D^* - D^0$ fits in bins of track p_T for xbhdfm data sample. The quoted errors are statistic only. Both, the Mean and σ are in units of* MeV/c^2.

Track p_T (MeV/c)	Mean	σ_{narrow}	σ_{wide}
	$D^{*+} \to D^0\pi^+$		
Track $p_T > 200$	145.475	0.544 ± 0.004	1.295 ± 0.022
Track $p_T > 400$	145.477	0.540 ± 0.004	1.331 ± 0.024
$200 <$ track $p_T < 400$	145.469	0.568 ± 0.009	1.305 ± 0.044
$400 <$ track $p_T < 600$	145.474	0.534 ± 0.005	1.326 ± 0.028
$600 <$ track $p_T < 800$	145.481	0.540 ± 0.009	1.313 ± 0.057
$800 <$ track $p_T < 1000$	145.495	0.573 ± 0.016	1.415 ± 0.110
	$D^{*-} \to D^0\pi^-$		
Track $p_T > 200$	145.461	0.449 ± 0.002	1.150 ± 0.010
Track $p_T > 400$	145.461	0.445 ± 0.003	1.165 ± 0.011
$200 <$ track $p_T < 400$	145.463	0.478 ± 0.005	1.182 ± 0.023
$400 <$ track $p_T < 600$	145.459	0.447 ± 0.003	1.182 ± 0.014
$600 <$ track $p_T < 800$	145.464	0.434 ± 0.005	1.117 ± 0.024
$800 <$ track $p_T < 1000$	145.464	0.439 ± 0.023	1.091 ± 0.219

Table 6.3: *Mass and resolution parameters for the $D^* - D^0$ fits in bins of track p_T for Monte Carlo sample. The quoted errors are statistic only. Both, the Mean and σ are in units of* MeV/c^2.

Track p_T (MeV/c)	$(\sigma(data) - \sigma(MC))_{narrow}$ (%)	$(\sigma(data) - \sigma(MC)_{wide}$ (%)
	$D^{*+} \to D^0\pi^+$	
$200 <$ track $p_T < 400$	15	33
$400 <$ track $p_T < 600$	17	39
$600 <$ track $p_T < 800$	14	34
$800 <$ track $p_T < 1000$	9	30
$1000 <$ track $p_T < \infty$	13	36
	$D^{*-} \to D^0\pi^-$	
$200 <$ track $p_T < 400$	17	27
$400 <$ track $p_T < 600$	22	31
$600 <$ track $p_T < 800$	15	17
$800 <$ track $p_T < 1000$	13	17
$1000 <$ track $p_T < \infty$	16	17

Table 6.4: *Differences between $D^{*\pm}$ resolution in xbhdij data sample and in Monte Carlo simulation for several ranges of the soft pion p_T.*

Track p_T (MeV/c)	$(\sigma(data) - \sigma(MC))_{narrow}$ (%)	$(\sigma(data) - \sigma(MC)_{wide}$ (%)
$D^{*+} \to D^0\pi^+$		
200 < track p_T < 400	17	28
400 < track p_T < 600	19	38
600 < track p_T < 800	17	35
800 < track p_T < 1000	11	27
1000 < track p_T < ∞	14	29
$D^{*-} \to D^0\pi^-$		
200 < track p_T < 400	14	17
400 < track p_T < 600	24	33
600 < track p_T < 800	16	16
800 < track p_T < 1000	15	18
1000 < track p_T < ∞	20	21

Table 6.5: *Differences between $D^{*\pm}$ resolution in xbhdfm data sample and in Monte Carlo simulation for several ranges of the soft pion p_T.*

Track p_T (MeV/c)	$(\sigma(D^{*+}) - \sigma(D^{*-}))_{narrow}$ (%)	$(\sigma(D^{*+}) - \sigma(D^{*-})_{wide}$ (%)
200 < track p_T < 400	13	17
400 < track p_T < 600	11	21
600 < track p_T < 800	19	33
800 < track p_T < 1000	20	36
1000 < track p_T < ∞	20	34

Table 6.6: *Differences between D^{*+} and D^{*-} resolutions in xbhdij data sample for several ranges of the soft pion p_T.*

Track p_T (MeV/c)	$(\sigma(D^{*+}) - \sigma(D^{*-}))_{narrow}$ (%)	$(\sigma(D^{*+}) - \sigma(D^{*-})_{wide}$ (%)
200 < track p_T < 400	19	21
400 < track p_T < 600	11	17
600 < track p_T < 800	20	35
800 < track p_T < 1000	20	31
1000 < track p_T < ∞	18	22

Table 6.7: *Differences between D^{*+} and D^{*-} resolutions in xbhdfm data sample for several ranges of the soft pion p_T.*

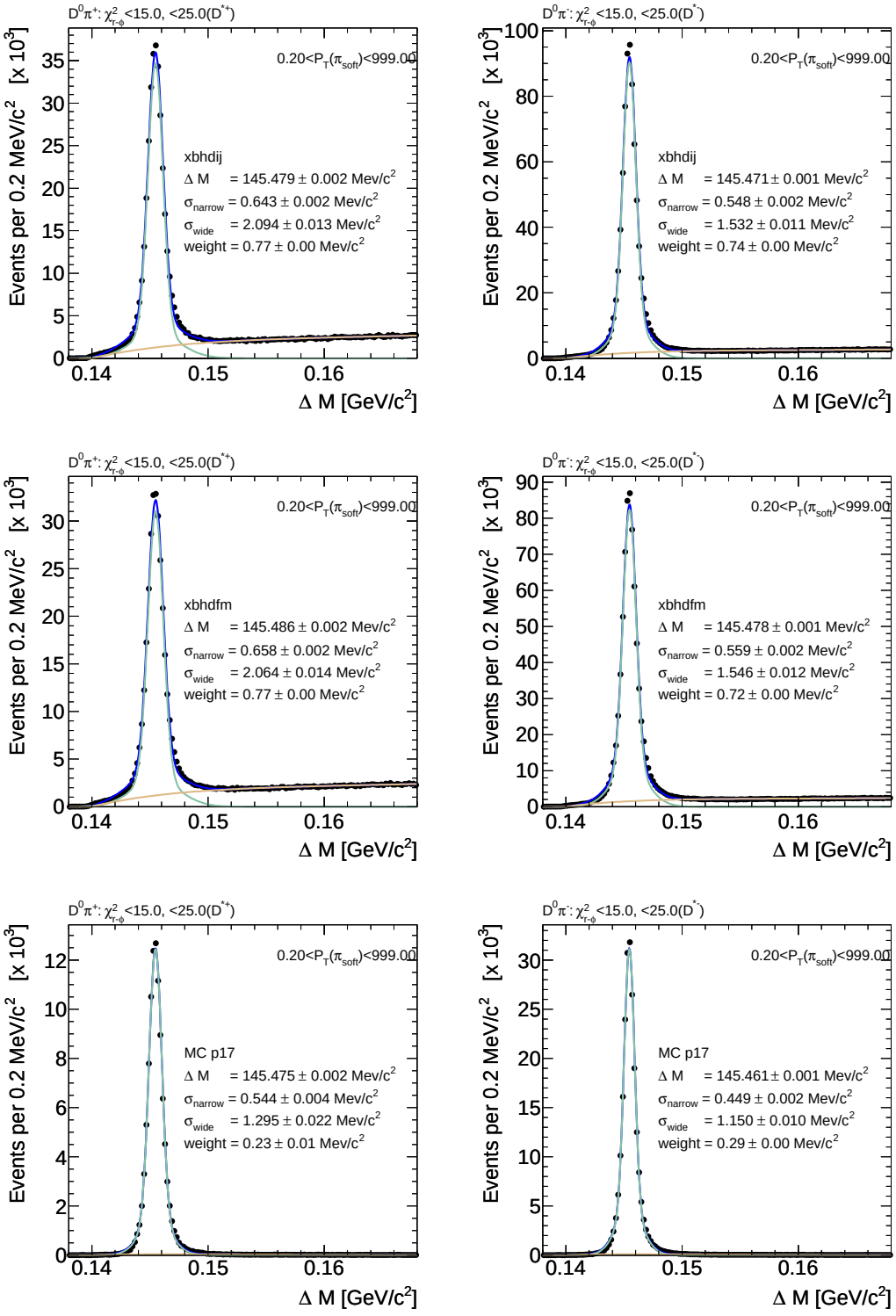

Figure 6.1: *Fit to $D^* - D^0$ peak using tracks with $p_T > 200$ MeV/c (all sample). First column shows $D^0\pi^+$ combination and second column $D^0\pi^-$. From top to the bottom: data from xbhdij sample, xbhdfm sample and Monte Carlo simulation.*

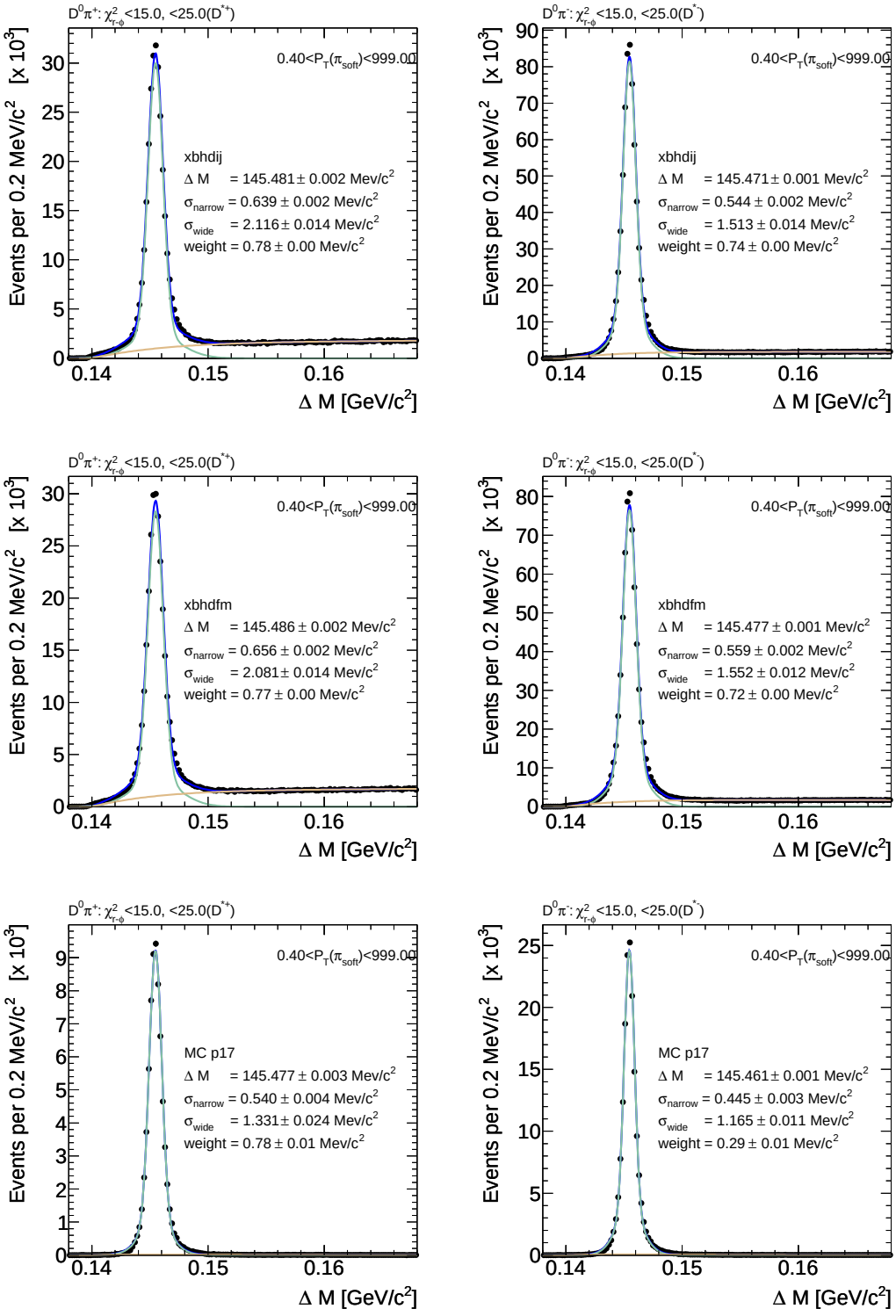

Figure 6.2: *Fit to $D^* - D^0$ peak using tracks with $p_T > 400$ MeV/c First column shows $D^0\pi^+$ combination and second column $D^0\pi^-$. From top to the bottom: data from xbhdij sample, xbhdfm sample and Monte Carlo simulation.*

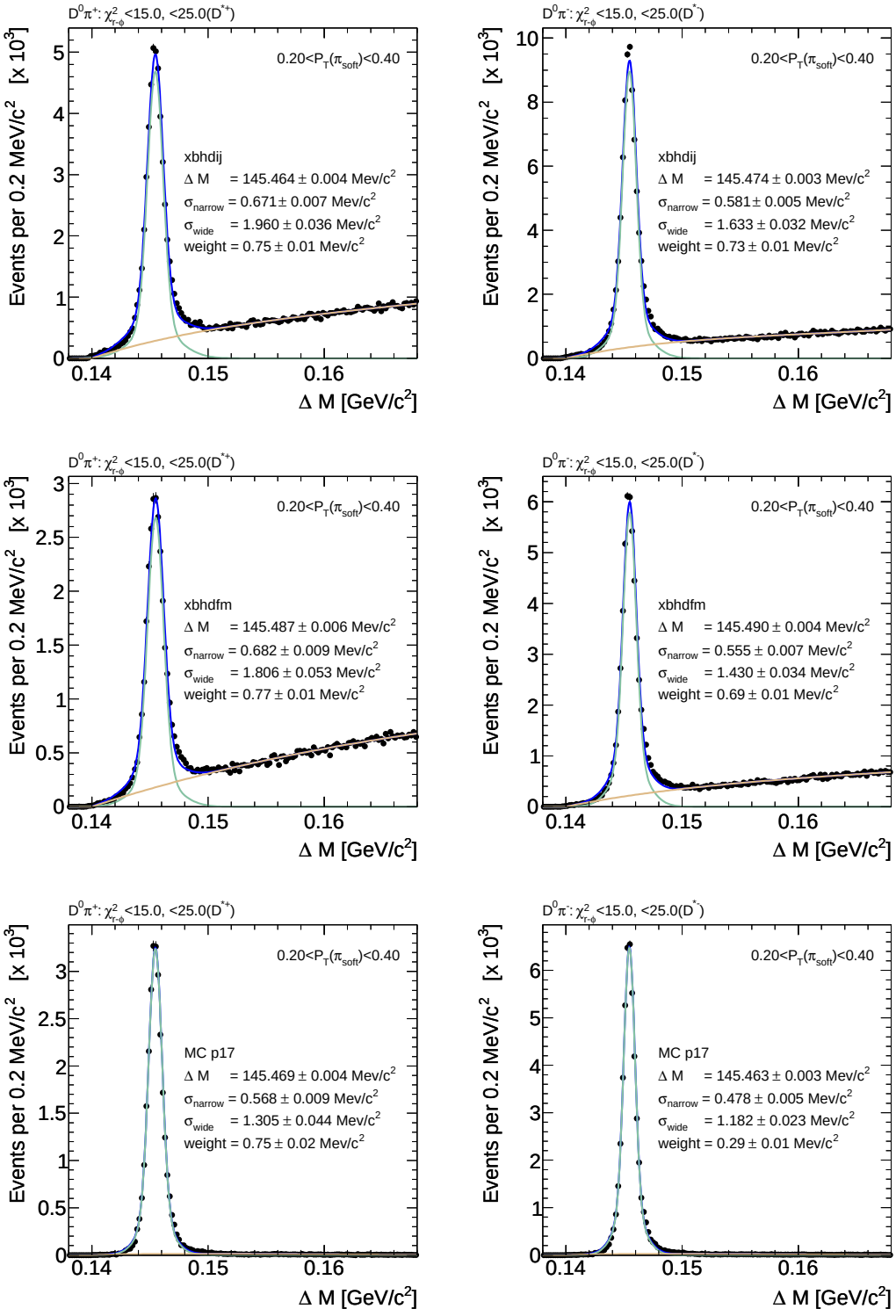

Figure 6.3: *Fit to $D^* - D^0$ peak using tracks with $200 < p_T < 400$ MeV/c First column shows $D^0\pi^+$ combination and second column $D^0\pi^-$. From top to the bottom: data from xbhdij sample, xbhdfm sample and Monte Carlo simulation.*

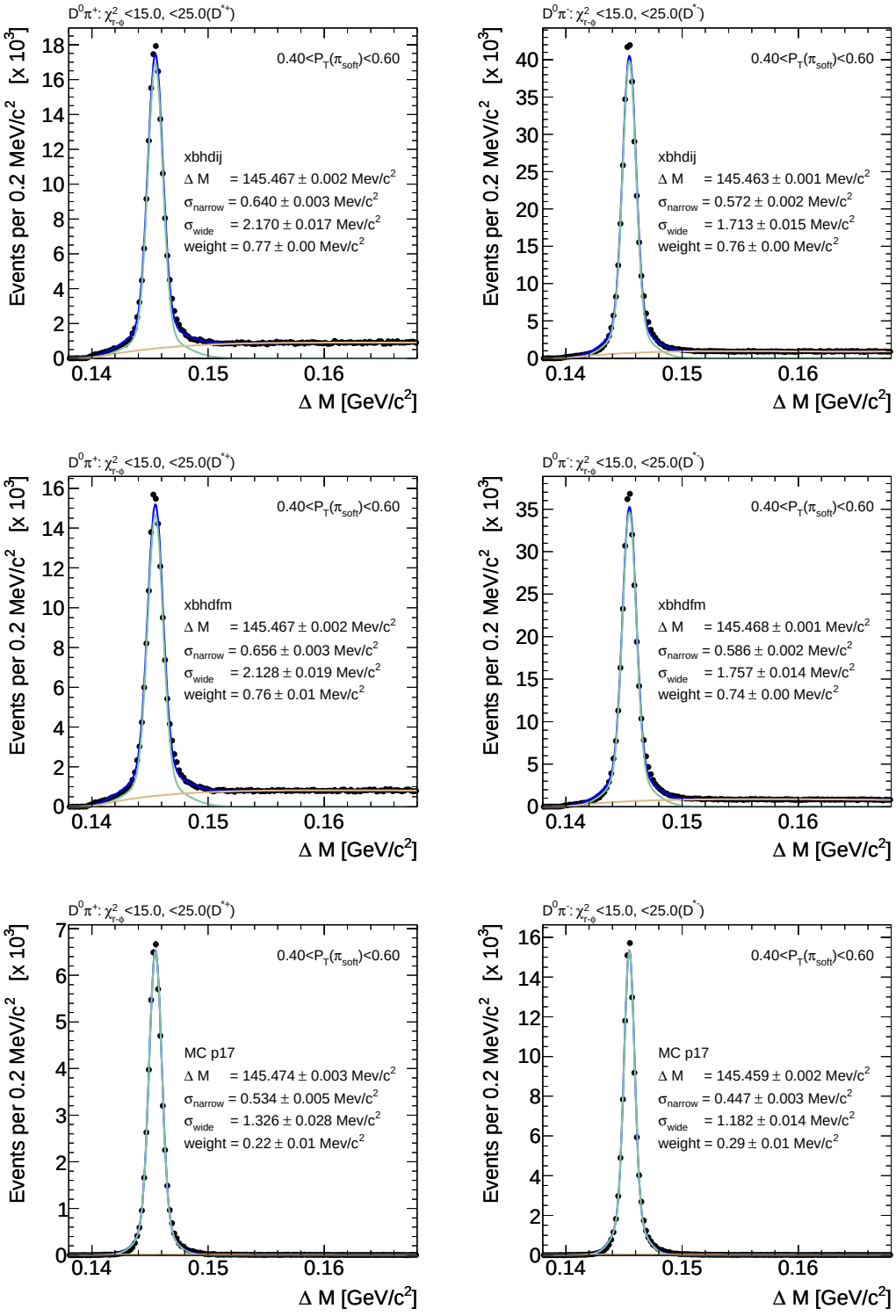

Figure 6.4: *Fit to $D^* - D^0$ peak using tracks with $400 < p_T < 600$ MeV/c First column shows $D^0\pi^+$ combination and second column $D^0\pi^-$. From top to the bottom: data from xbhdij sample, xbhdfm sample and Monte Carlo simulation.*

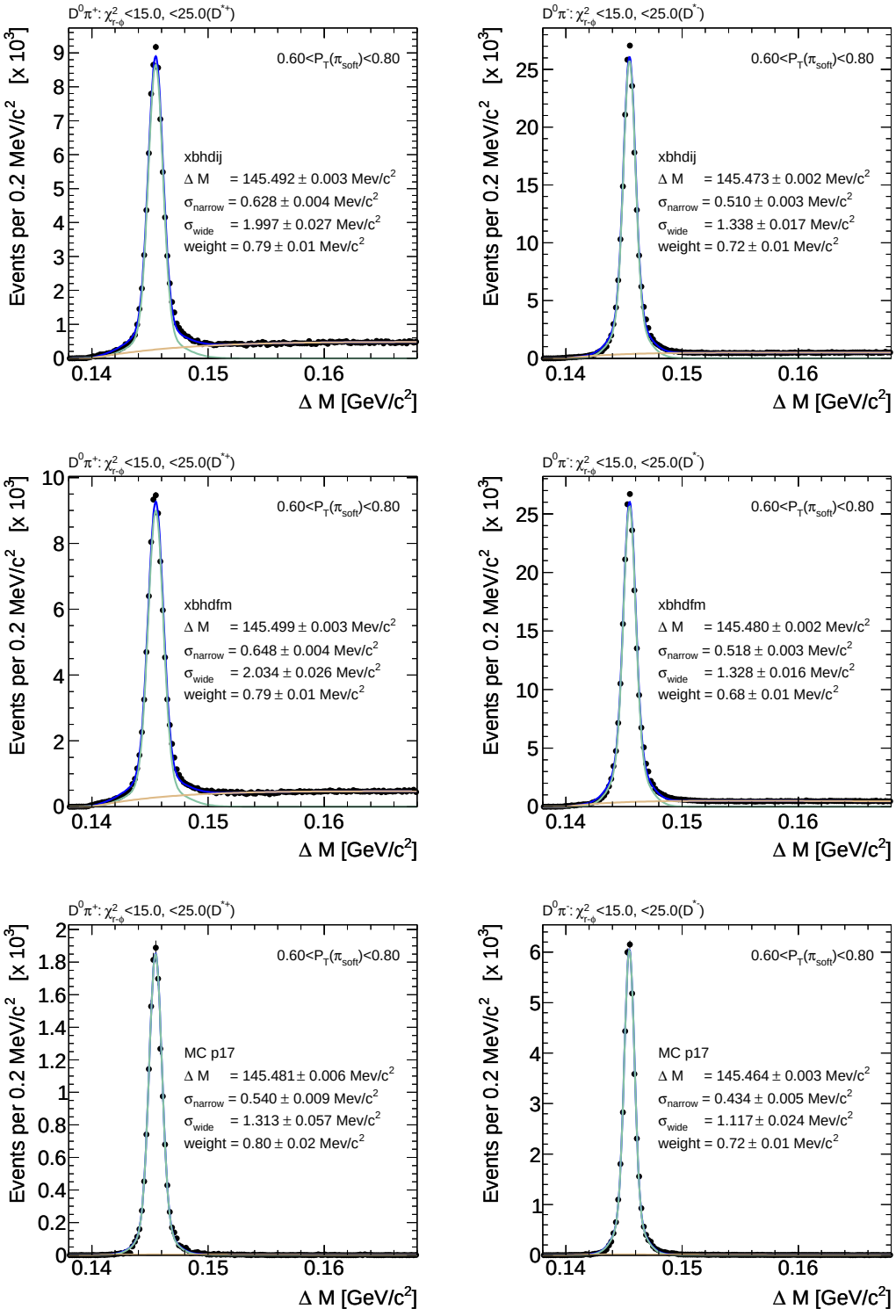

Figure 6.5: *Fit to $D^* - D^0$ peak using tracks with $600 < p_T < 800$ MeV/c First column shows $D^0\pi^+$ combination and second column $D^0\pi^-$. From top to the bottom: data from xbhdij sample, xbhdfm sample and Monte Carlo simulation.*

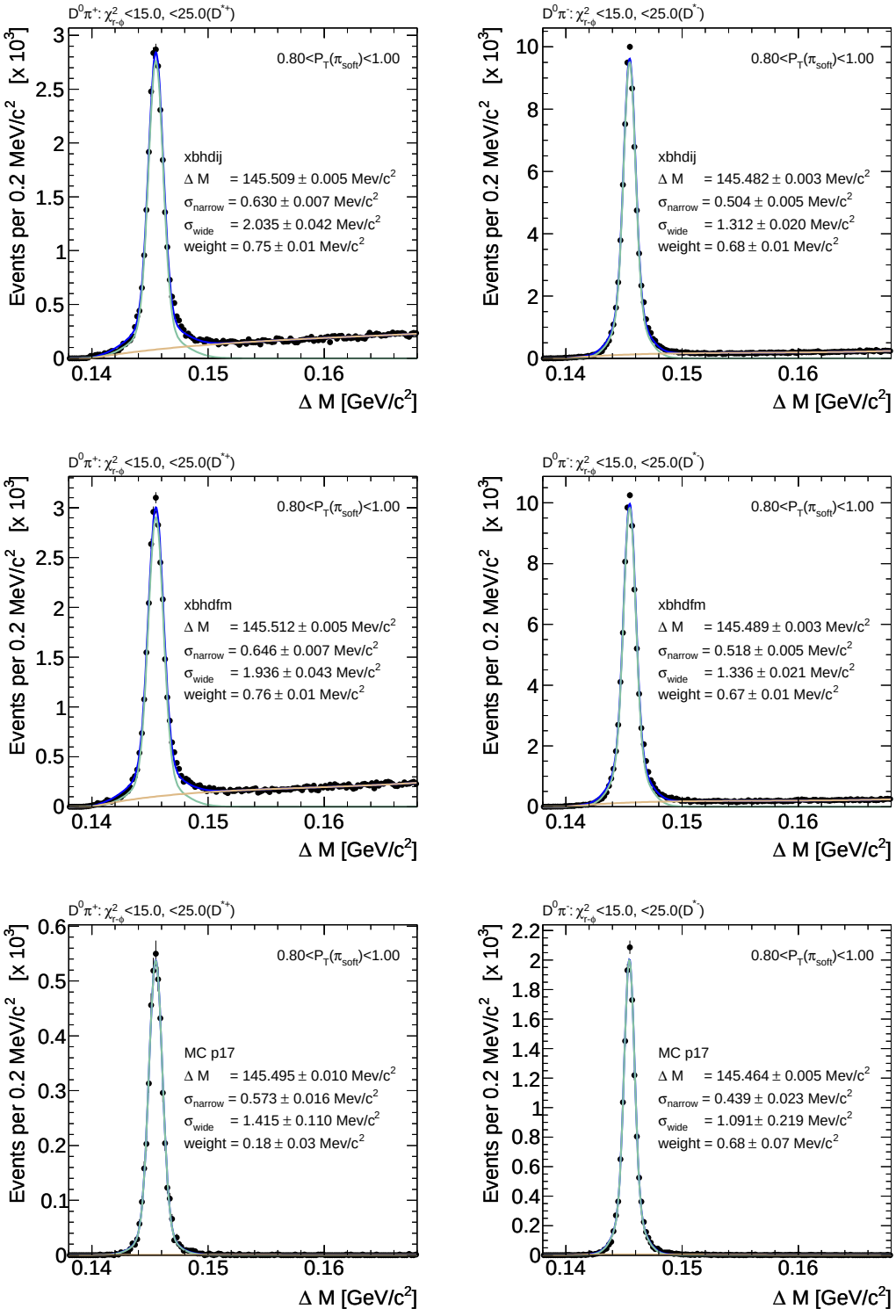

Figure 6.6: *Fit to $D^* - D^0$ peak using tracks with $800 < p_T < 1000$ MeV/c First column shows $D^0\pi^+$ combination and second column $D^0\pi^-$. From top to the bottom: data from xbhdij sample, xbhdfm sample and Monte Carlo simulation.*

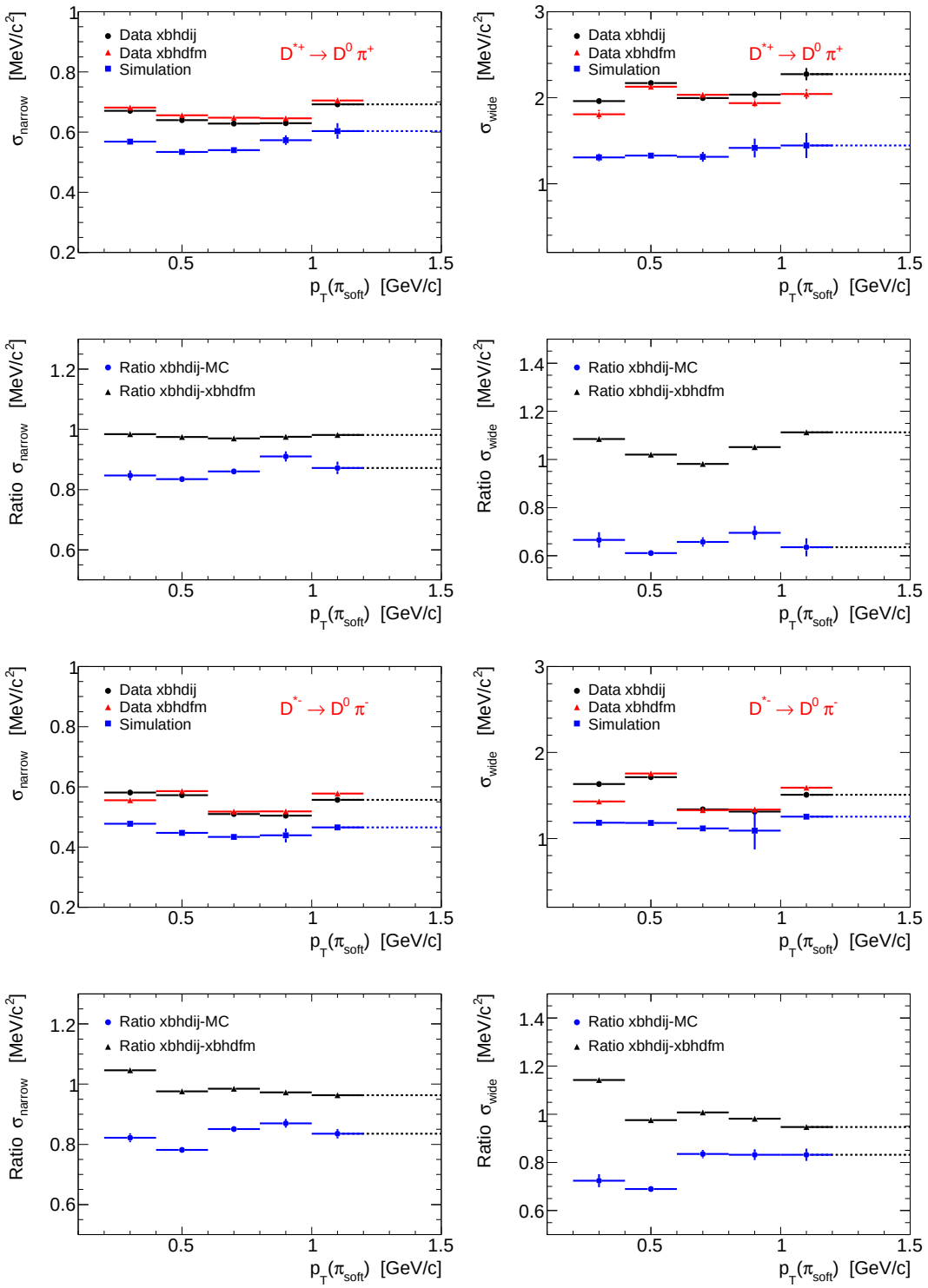

Figure 6.7: *Comparison Data-Monte Carlo for the resolution of the decay* $D^{*\pm} \to D^0\pi^\pm$ *when using the two data samples: xbhdij and xbhdfm. For all plots the bin width is* 0.2 GeV/c *except for the last bin which extends over* $(1.0, \infty)$ GeV/c.

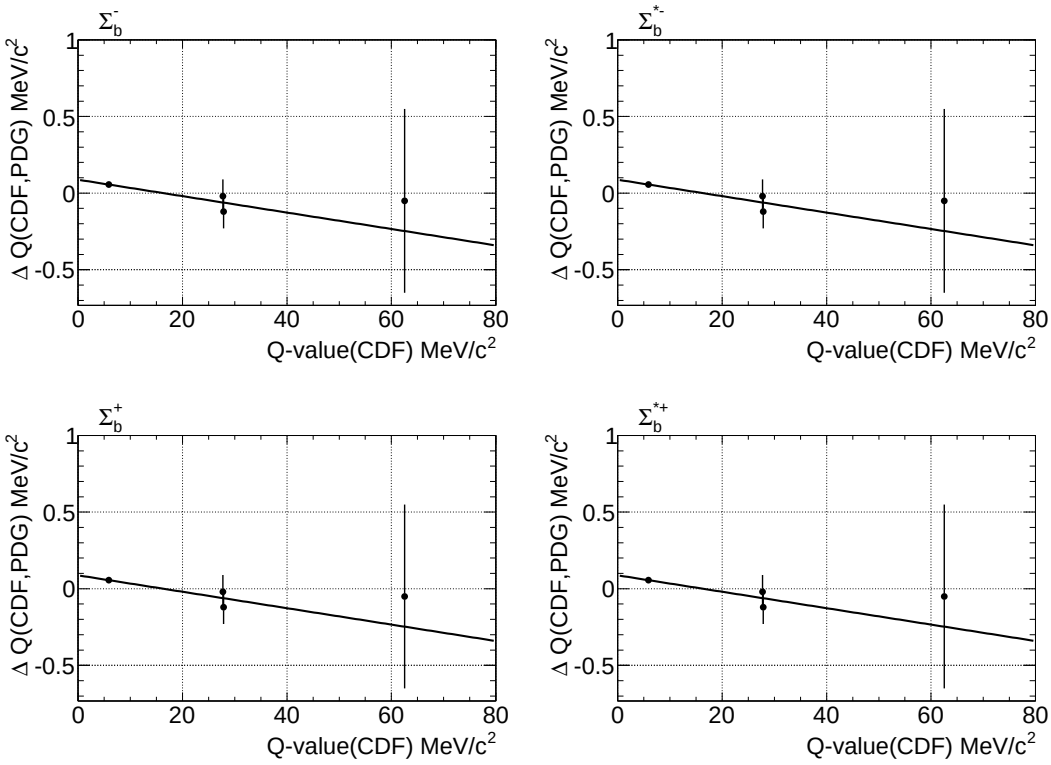

Figure 6.8: *Mass differences between CDF measurements and PDG values for the states D^*, Σ_c and Λ_c^+ plotted versus the CDF Q-value of each decay. The graph is fitted with four linear functions, one per each Σ_b state, to estimate the mass scale systematic error at each Σ_b Q-value. Table 6.9 summarizes the results of those fits.*

state, and the fit parameters are shown in Table 6.9.

The effect of the momentum scale uncertainty on the width measurements is also considered. Following same procedure as in a previous CDF analysis [83], we fit the D^{*+} Q-value distribution for several ranges of the soft pion p_T using the *xbhdij* data sample. We use the sum of two Breit-Wigner distributions (Eq. 5.2) with the same natural width (which is let float in the fit) convoluted with two different gaussian distributions to perform the fits. Figure 6.9 show the results of this study. We measure a natural width smaller than 0.2 MeV/c^2 for all momentum ranges, and use this value as a conservative systematic error on the widths due to tracking precision.

6.2 Fit Systematics

In this section we refer to sources of systematic error caused by assumptions made about the Σ_b fit.

We consider the following:

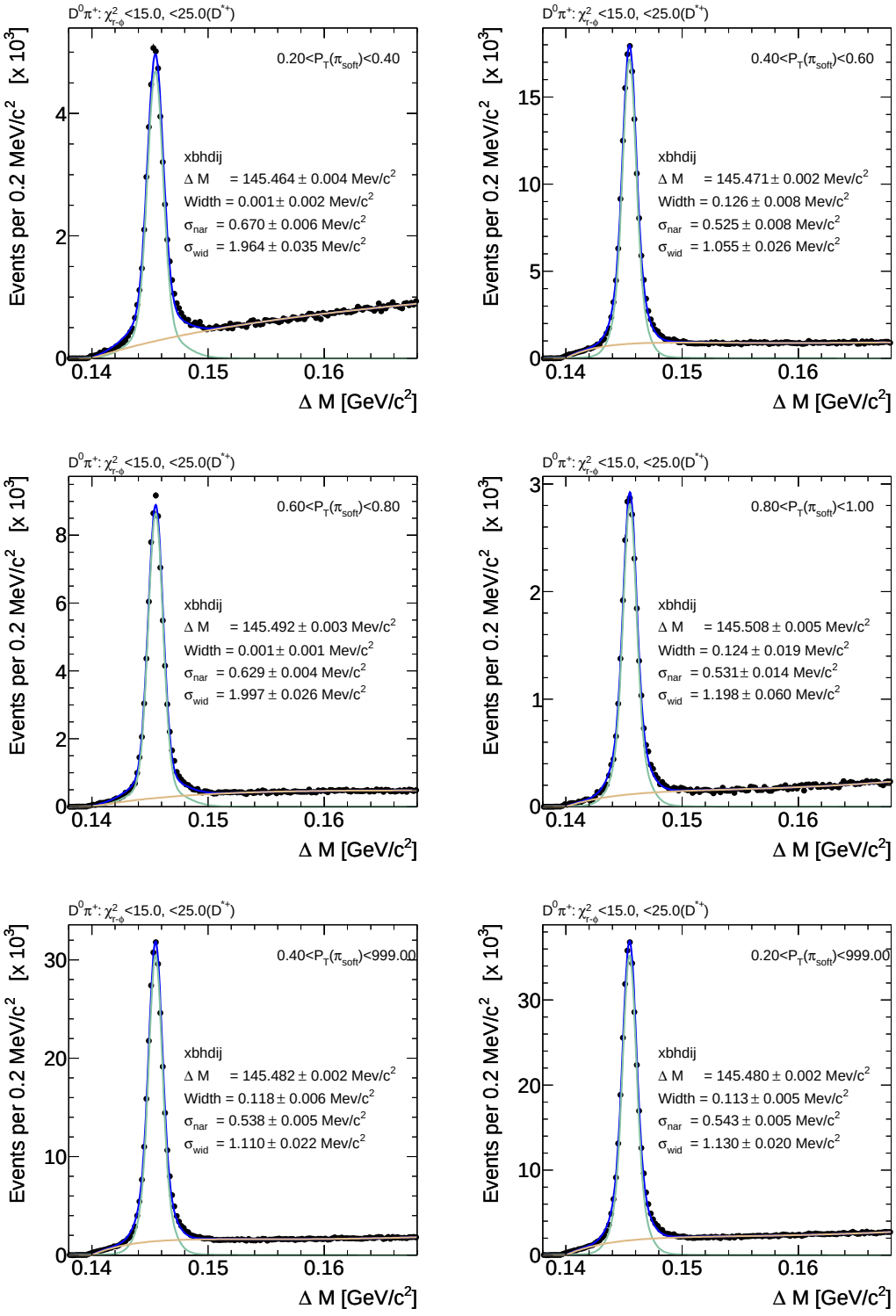

Figure 6.9: *Fit to $D^{*+} - D^0$ peak using tracks with several ranges of the soft pion p_T. All natural widths returned by the fits are lower than 0.2* MeV/c^2*, that it is taken as a systematic error on the widths due to tracking precision.*

Mass difference	CDF	PDG
$M(D^*) - M(D^0)$	145.477	145.421 ± 0.010
$M(\Sigma_c^0) - M(\Lambda_c^+)$	167.28 ± 0.12	167.30 ± 0.11
$M(\Sigma_c^{++}) - M(\Lambda_c^+)$	167.44 ± 0.13	167.56 ± 0.11
$M(\Lambda_c(2625)^+) - M(\Lambda_c^+)$	341.65 ± 0.13	341.7 ± 0.6

Table 6.8: *The* CDF II *and PDG mass differences used to estimate the systematic error due to the mass scale uncertainty. The quoted Σ_c^0, Σ_c^{++} and $\Lambda_c(2625)^+$ values from the first column, have being taken from the best* CDF II *mesurement [82], while the D^* mass value quoted correspond with the error-weighted average of the four D^* masses with $p_T > 200$ from Tables [6.1, 6.2,6.3]. We use the PDG mass error as the error for the difference between the* CDF II *and the PDG masses. All the masses are in units of* MeV/c^2.

State	Q	Slope	Intercept	Fit Prob.	Systematic
Σ_b^+	52	-0.005 ± 0.003	-0.19 ± 0.16	77%	-0.35
Σ_b^-	56	-0.005 ± 0.003	-0.21 ± 0.17	77%	-0.38
Σ_b^{*+}	72	-0.005 ± 0.003	-0.30 ± 0.22	77%	-0.52
Σ_b^{*-}	76	-0.005 ± 0.003	-0.32 ± 0.24	77%	-0.56

Table 6.9: *Fit parameters and mass scale systematic errors for every of the Σ_b states. For every state, the assigned systematic error due to mass scale uncertainty is the intercept returned by the fit less 1 statistical uncertainty. All mass units are in* MeV/c^2.

- Uncertainty in the resolution of the detector.
- Uncertainty in the assumed model to describe background.

We describe the detector resolution using two gaussians. We take into account the impact on our measurement of the systematic change of these widths. We also take in account the effect of the systematic change of the weight fraction combining the two gaussians.

The dependence of the signal parameters on the election of the background must be taking into account as well.

Both type of systematic errors are estimated using toy Monte Carlo simulations and they are explained in the next sections.

6.2.1 Resolution of CDF Detector

Our signal model describes the resolution detector using two gaussian distributions with fixed widths and weight fraction to the values obtained in Section 5.4.1 (see Table 5.11).

Any uncertainty affecting those values translates into bias in our measurements.

We consider the following three sources of uncertainty affecting our resolution parameters:

1. The finite size of the Monte Carlo samples used to obtain these resolution parameters.
2. The underestimation of resolution detector by the CDF Monte Carlo (see Section 6.1.1).
3. The differences in resolution between $\Sigma_b^{(*)\pm}$ states decaying to positive and negative charge soft pions (see Section 6.1.1).

The first source affects both, the weight fractions and the sigma of the gaussians while the other two sources just affect the sigmas of the gaussians distributions.

In order to estimate the systematic error for every source of uncertainty, we generate 7000 toy Monte Carlo samples, with the same statistics as in our data sample, with the corresponding resolution parameter changed. Then, we fit every sample with both, the default fitter and the fitter with varied resolution parameters. To every signal parameter, the systematic error is estimated as the mean returned by a gaussian fit over the distribution of the differences between the returned values by the two fitters for the considered parameter.

The selected variations of the resolution parameters for every source of systematic uncertainty are:

1. We generate samples with the resolution weight fraction increased (decreased) 1 statistical uncertainty. For the systematic variation of the gaussian sigmas we just generate samples with the sigmas decreased 2 statistical uncertainties. We do not generate samples with the sigmas increased 2 statistical uncertainties because we expect the effect of this source on the signal parameters to be much smaller than the source number 2).

2. We generate samples with the narrow sigma increased 25 % and the wide one increased 40 %. These values were obtained when comparing the $D^{*\pm}$ resolution values from data and Monte Carlo in Section 6.1.1.

3. We generate samples with the narrow sigma decreased 20 % and the wide one decreased 40 %. These values were obtained when comparing the D^{*+} and D^{*-} resolution values from CDF data in Section 6.1.1.

The systematics due to the uncertainty on the resolution weight calculated for the "opposite sign" states, $\Sigma_b^{(*)+}$ are shown in Figs. 6.10, 6.11 and the estimated systematic errors are summarized in Table 6.10.

The systematics due to the uncertainty on the resolution weight calculated for the "same sign" states, $\Sigma_b^{(*)-}$ are shown in Figs. 6.12, 6.13 and the estimated systematic errors are summarized in Table 6.11.

The systematics due to the uncertainty on the gaussian sigmas due to the finite size of our Monte Carlo for the "opposite sign" and the "same sign" are shown respectively in Figs. 6.14, 6.15.

The systematics due to the uncertainty on the gaussian sigmas due to the underestimation of the resolution detector by the CDF Monte Carlo for the "opposite sign" and the "same sign" are shown respectively in Figs. 6.16, 6.17. The estimated systematic errors due to the systematic variation of the gaussian sigmas due to the sources 1) and 2) listed above are summarized in Tabs. 6.12, 6.13.

Finally, the systematics due to the source 3) listed above are shown in Figure 6.18 and they are listed in Table 6.14.

6.2.2 Assumed Model

We use to describe our background a model following the Equation 5.7. There are many other different models which they are suitable to describe the background present in our data sample. In order to estimate the dependence of our signal parameters on the assumed background model, we generate 500 samples of toy Monte Carlo with the same statistics as in our data sample following a model with our background replaced by the *RooDstD0BG* PDF (Equation 6.1).

The initial parameters to generate these samples are obtained from a fit with this varied model over the data. Figure 6.19 shows these two fits and the obtained signal parameters are listed in Table 6.15.

Signal Parameters	$f_1 - 1 \cdot$ stat.err.	$f_1 + 1 \cdot$ stat.err.
Σ_b^+ pole, Q_{01}	-0.013 ± 0.017	0.042 ± 0.012
Σ_b^+ width, Γ_{01}	0.10 ± 0.06	0.41 ± 0.05
Σ_b^+ yield, N_{s1}	~ 9	~ 13
Σ_b^{*+} pole, Q_{02}	-0.015 ± 0.012	0.015 ± 0.012
Σ_b^{*+} width,Γ_{02}	-0.14 ± 0.05	0.08 ± 0.04
Σ_b^{*+} yield, N_{s2}	~ -3	~ 1

Table 6.10: *Systematic errors in the signal floating parameters for the* $\Sigma_b^{(*)+} \to \Lambda_b^0 \pi^+_{\Sigma_b}$ *modes, "opposite sign", due to the uncertainty by a single statistical error (CDF Monte Carlo) in the values of the gaussian resolution weigths. All the masses and widths are in units of* MeV/c^2.

Signal Parameters	$f_1 - 1 \cdot$ stat.err.	$f_1 + 1 \cdot$ stat.err.
Σ_b^- pole, Q_{01}	-0.013 ± 0.013	0.009 ± 0.012
Σ_b^- width, Γ_{01}	-0.19 ± 0.04	0.11 ± 0.04
Σ_b^- yield, N_{s1}	~ -3	~ 1
Σ_b^{*-} pole, Q_{02}	-0.010 ± 0.013	0.019 ± 0.013
Σ_b^{*-} width,Γ_{02}	-0.10 ± 0.05	0.15 ± 0.04
Σ_b^{*-} yield, N_{s2}	~ -1	~ 3

Table 6.11: *Systematic errors in the signal floating parameters for the* $\Sigma_b^{(*)-} \to \Lambda_b^0 \pi^-_{\Sigma_b}$ *modes, "same sign", due to the uncertainty by a single statistical error (CDF Monte Carlo) in the values of the gaussian resolution weigths. All the masses and widths are in units of* MeV/c^2.

Signal Parameters	$\sigma_1 \cdot 1.25$, $\sigma_2 \cdot 1.4$ MeV/c^2	$\sigma_{1,2} - 2 \cdot$ stat.err. (CdfSim), MeV/c^2
Σ_b^+ pole, Q_{01}	-0.121 ± 0.001	$+0.033 \pm 0.0002$
Σ_b^+ width, Γ_{01}	-0.887 ± 0.001	$+0.277 \pm 0.0003$
Σ_b^+ yield, N_{s1}	~ -7	$\sim +3$
Σ_b^{*+} pole, Q_{02}	-0.129 ± 0.0004	$+0.027 \pm 0.0001$
Σ_b^{*+} width, Γ_{02}	-0.999 ± 0.001	$+0.200 \pm 0.0002$
Σ_b^{*+} yield, N_{s2}	-13	$\sim +3$

Table 6.12: *Systematic errors in the signal floating parameters for the* $\Sigma_b^{(*)+} \to \Lambda_b^0 \pi^+_{\Sigma_b}$ *mode, "opposite sign" due to the uncertainty in the resolution of the detector. All the masses and widths are in units of* MeV/c^2. *Please see the plots and the fit results at Figure 6.16 and Figure 6.14.*

Signal Parameters	$\sigma_1 \cdot 1.25$, $\sigma_2 \cdot 1.4$ MeV/c^2	$\sigma_{1,2} - 2 \cdot$ stat.err. (CdfSim), MeV/c^2
Σ_b^- pole, Q_{01}	-0.072 ± 0.0004	$+0.019 \pm 0.0001$
Σ_b^- width, Γ_{01}	-0.854 ± 0.001	$+0.272 \pm 0.0002$
Σ_b^- yield, N_{s1}	~ -7	~ 3
Σ_b^{*-} pole, Q_{02}	-0.076 ± 0.0003	$+0.016 \pm 0.0001$
Σ_b^{*-} width, Γ_{02}	-0.950 ± 0.001	$+0.190 \pm 0.0002$
Σ_b^{*-} yield, N_{s2}	-8	$\sim +2$

Table 6.13: *Systematic errors in the signal floating parameters for the* $\Sigma_b^{(*)-} \to \Lambda_b^0 \pi^-_{\Sigma_b}$ *mode, "same sign" due to the uncertainty in the resolution of the detector. All the masses and widths are in units of* MeV/c^2. *Please see the plots and the fit results at Figure 6.17 and Figure 6.15.*

Signal Parameters	Systematic shift
Σ_b pole, Q_{01}	0.049 ± 0.0003
Σ_b width, Γ_{01}	0.795 ± 0.001
Σ_b yield, N_{s1}	~ 8
Σ_b^* pole, Q_{02}	0.047 ± 0.0003
Σ_b^* width,Γ_{02}	0.582 ± 0.001
Σ_b^* yield, N_{s2}	~ 6

Table 6.14: *Systematic errors in the signal floating parameters due to the overestimation in the resolution of the* $\Sigma_b^{(*)}$ *states decaying to negative charged soft pions. All the masses and widths are in units of* MeV/c^2.

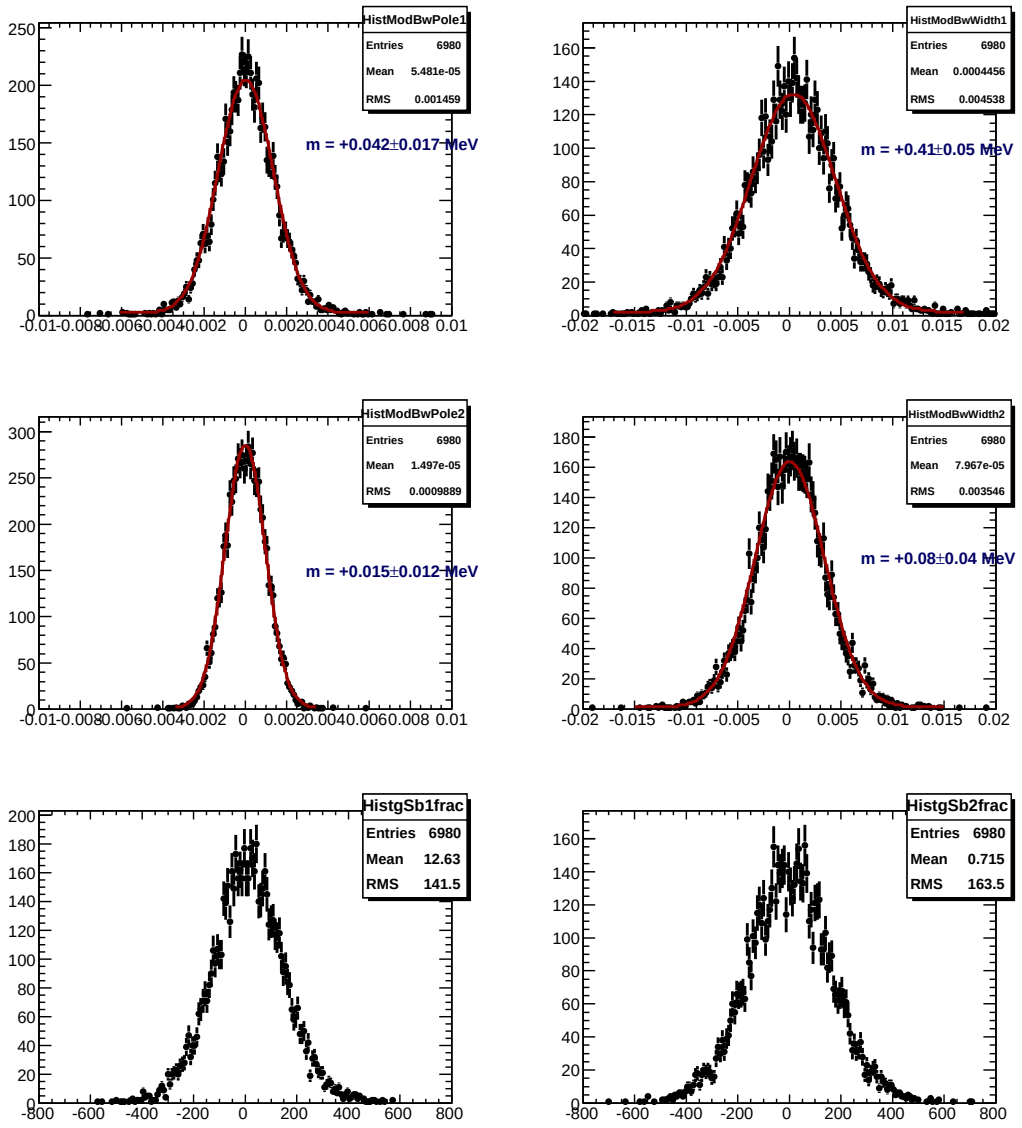

Figure 6.10: *The 7K toy Monte Carlo study for "opposite sign" state* $\Sigma_b^{(*)+} \to \Lambda_b^0 \pi^+_{\Sigma_b}$. *Impact on the signal floating parameters due to* **the increase** *by a single statistical (full CDF Monte Carlo) uncertainty (see Table 5.11 of Section 5.4.1) in the relative fraction* f_1 *of a first narrow Gaussian with parameter* σ_1. *From up to bottom in the first (second) column:* ΔQ_{01} *(*$\Delta\Gamma_{01}$*),* ΔQ_{02} *(*$\Delta\Gamma_{02}$*) and* ΔN_{s1} *(*ΔN_{s2}*). The plotted differences are in* GeV/c^2 *units.*

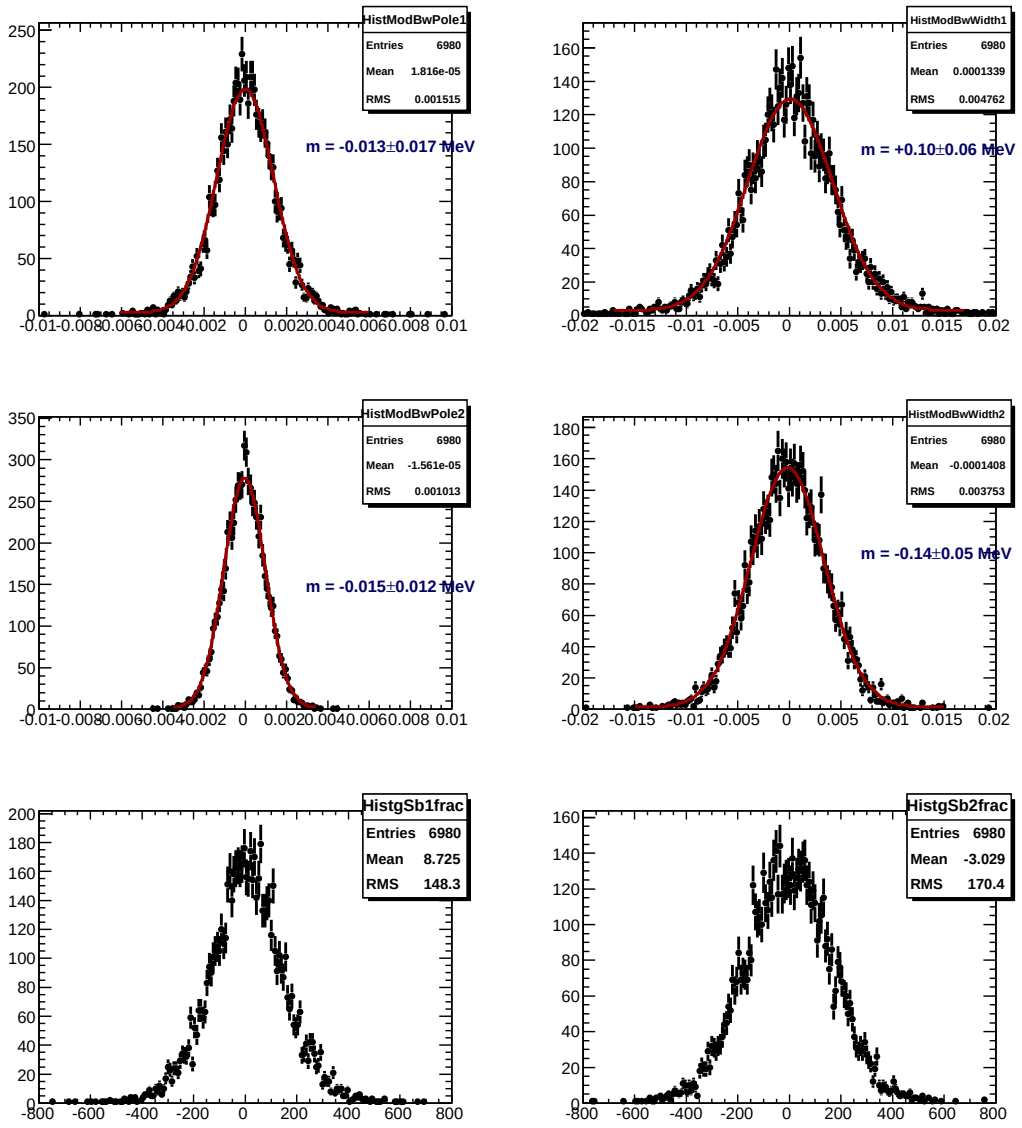

Figure 6.11: *The 7K toy Monte Carlo study for "opposite sign" state* $\Sigma_b^{(*)+} \to \Lambda_b^0 \pi^+_{\Sigma_b}$. *Impact on the signal floating parameters due to* **the decrease** *by a single statistical (full CDF Monte Carlo) uncertainty (see Table 5.11 of Section 5.4.1) in the relative fraction* f_1 *of a first narrow Gaussian with parameter* σ_1. *From up to bottom in the first (second) column:* ΔQ_{01} $(\Delta\Gamma_{01})$, ΔQ_{02} $(\Delta\Gamma_{02})$ *and* ΔN_{s1} (ΔN_{s2}). *The plotted differences are in* GeV/c^2 *units.*

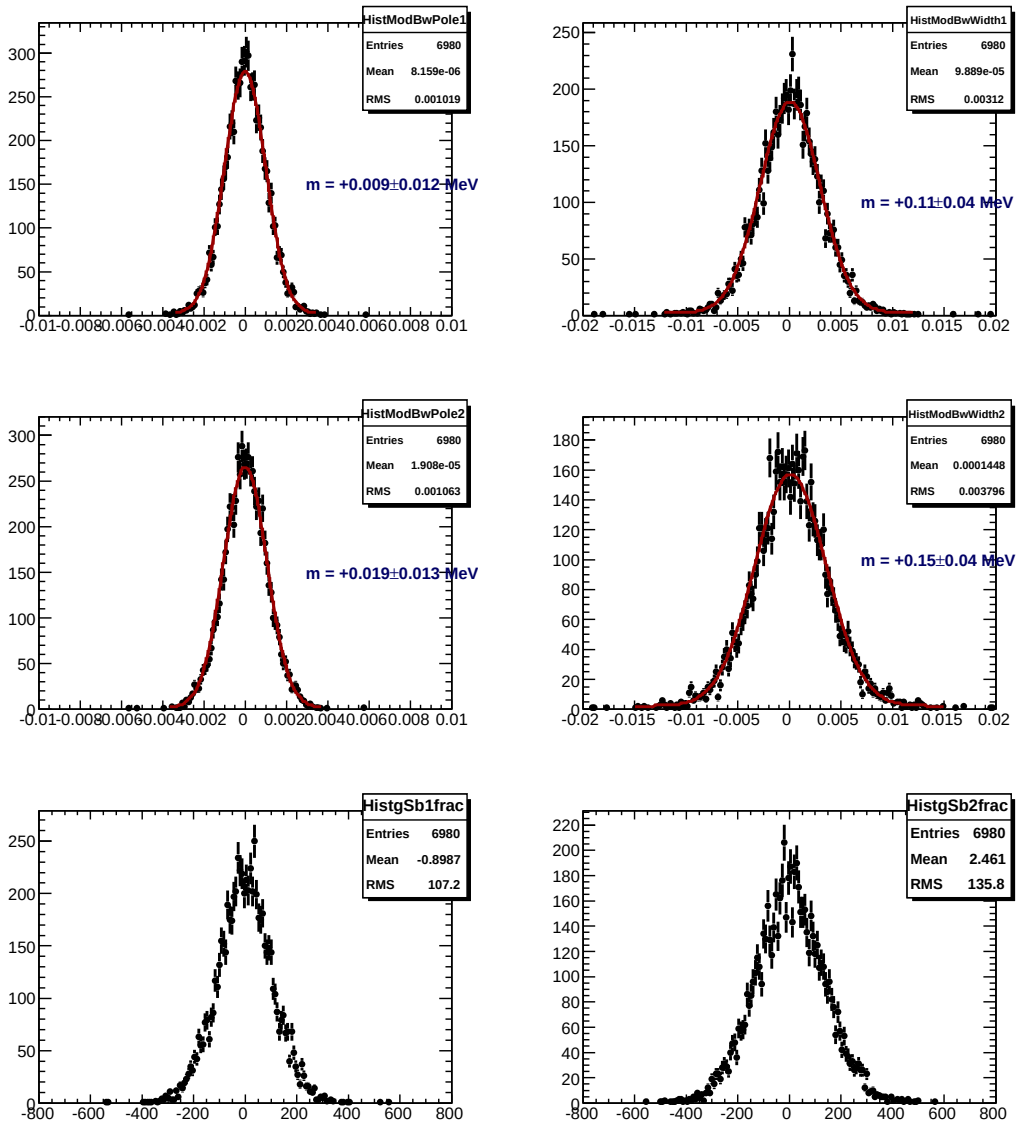

Figure 6.12: *The 7K toy Monte Carlo study for "same sign" state* $\Sigma_b^{(*)-} \to \Lambda_b^0 \pi^-_{\Sigma_b}$. *Impact on the signal floating parameters due to* **the increase** *by a single statistical (full CDF Monte Carlo) uncertainty (see Table 5.11 of Section 5.4.1) in the relative fraction* f_1 *of a first narrow Gaussian with parameter* σ_1. *From up to bottom in the first (second) column:* ΔQ_{01} *(*$\Delta\Gamma_{01}$*),* ΔQ_{02} *(*$\Delta\Gamma_{02}$*) and* ΔN_{s1} *(*ΔN_{s2}*). The plotted differences are in* GeV/c^2 *units.*

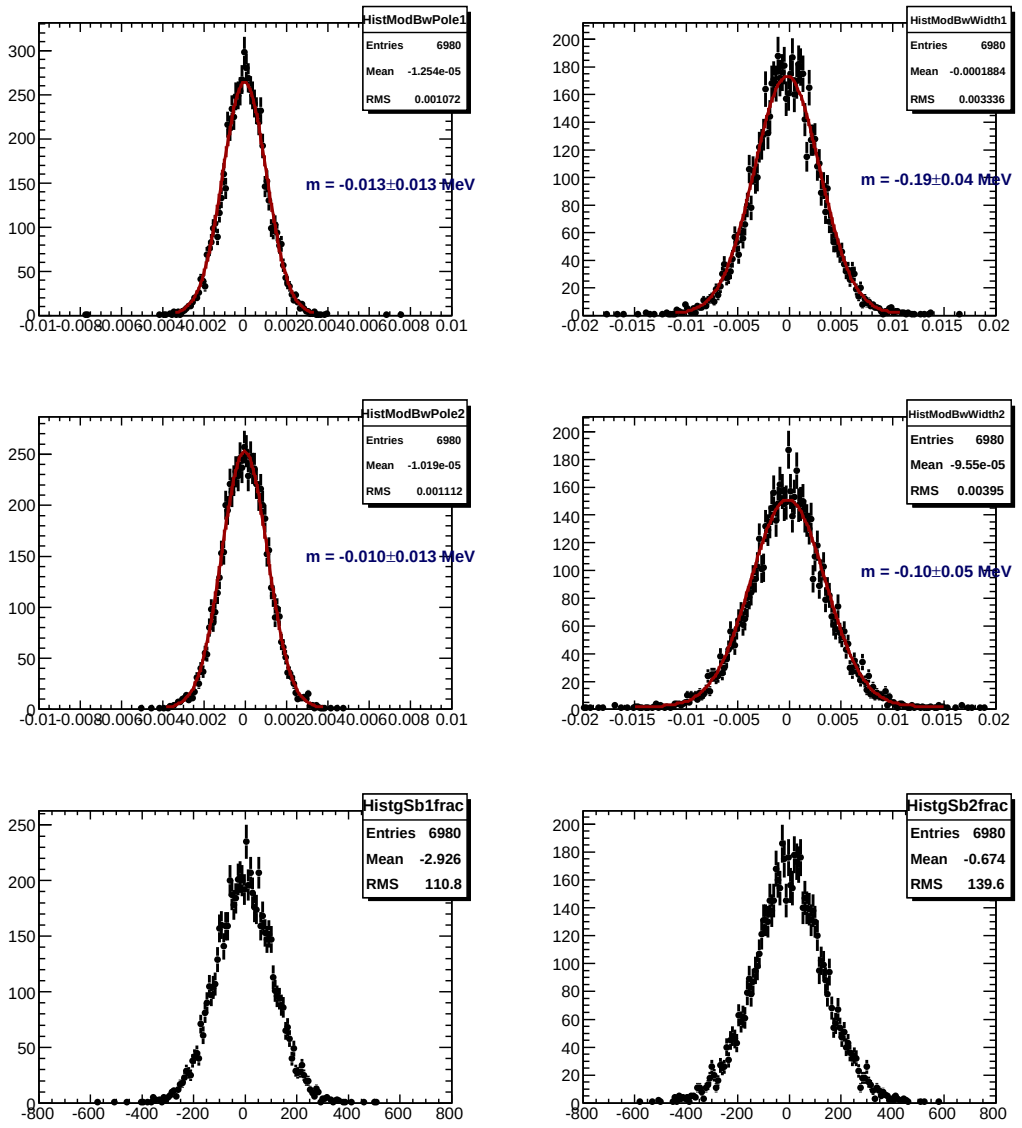

Figure 6.13: *The 7K toy Monte Carlo study for "same sign" state* $\Sigma_b^{(*)-} \to \Lambda_b^0 \pi^-_{\Sigma_b}$. *Impact on the signal floating parameters due to* **the decrease** *by a single statistical (full CDF Monte Carlo) uncertainty (see Table 5.11 of Section 5.4.1) in the relative fraction* f_1 *of a first narrow Gaussian with parameter* σ_1. *From up to bottom in the first (second) column:* ΔQ_{01} *(*$\Delta\Gamma_{01}$*),* ΔQ_{02} *(*$\Delta\Gamma_{02}$*) and* ΔN_{s1} *(*ΔN_{s2}*). The plotted differences are in* GeV/c^2 *units.*

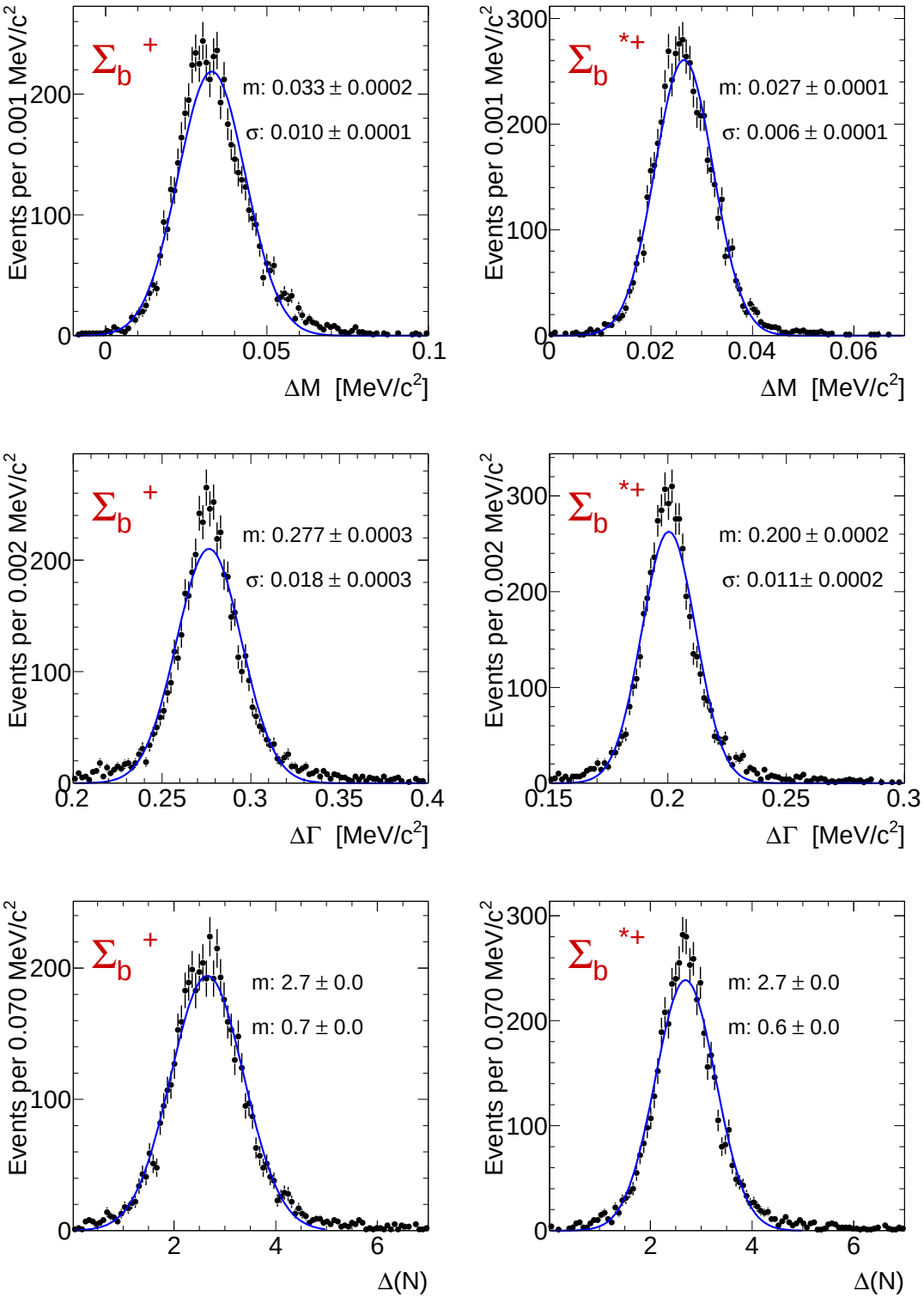

Figure 6.14: *The 7K toy Monte Carlo study for "opposite sign" state* $\Sigma_b^{(*)+} \to \Lambda_b^0 \pi^+_{\Sigma_b}$. *Impact on the signal floating parameters due to* **the decrease** *by two statistical (full CDF Monte Carlo) uncertainty (see Table 5.11 of Section 5.4.1) in the resolution parameters* $\sigma_{1,2}$ *of the detector.*

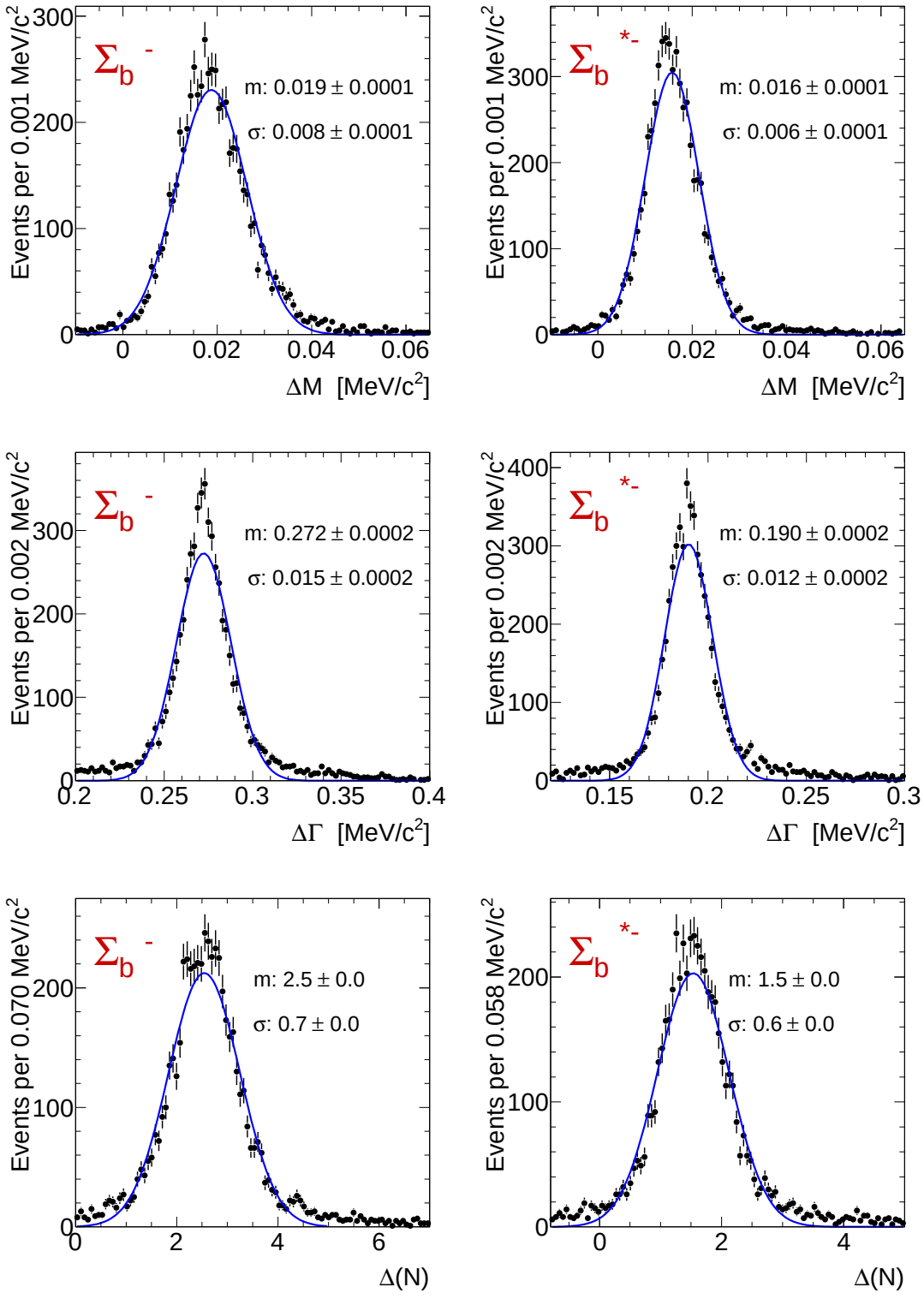

Figure 6.15: *The 7K toy Monte Carlo study for "same sign" state* $\Sigma_b^{(*)-} \to \Lambda_b^0 \pi^-_{\Sigma_b}$. *Impact on the signal floating parameters due to* **the decrease** *by two statistical (full CDF Monte Carlo) uncertainty (see Table 5.11 of Section 5.4.1) in the resolution parameters* $\sigma_{1,2}$ *of the detector.*

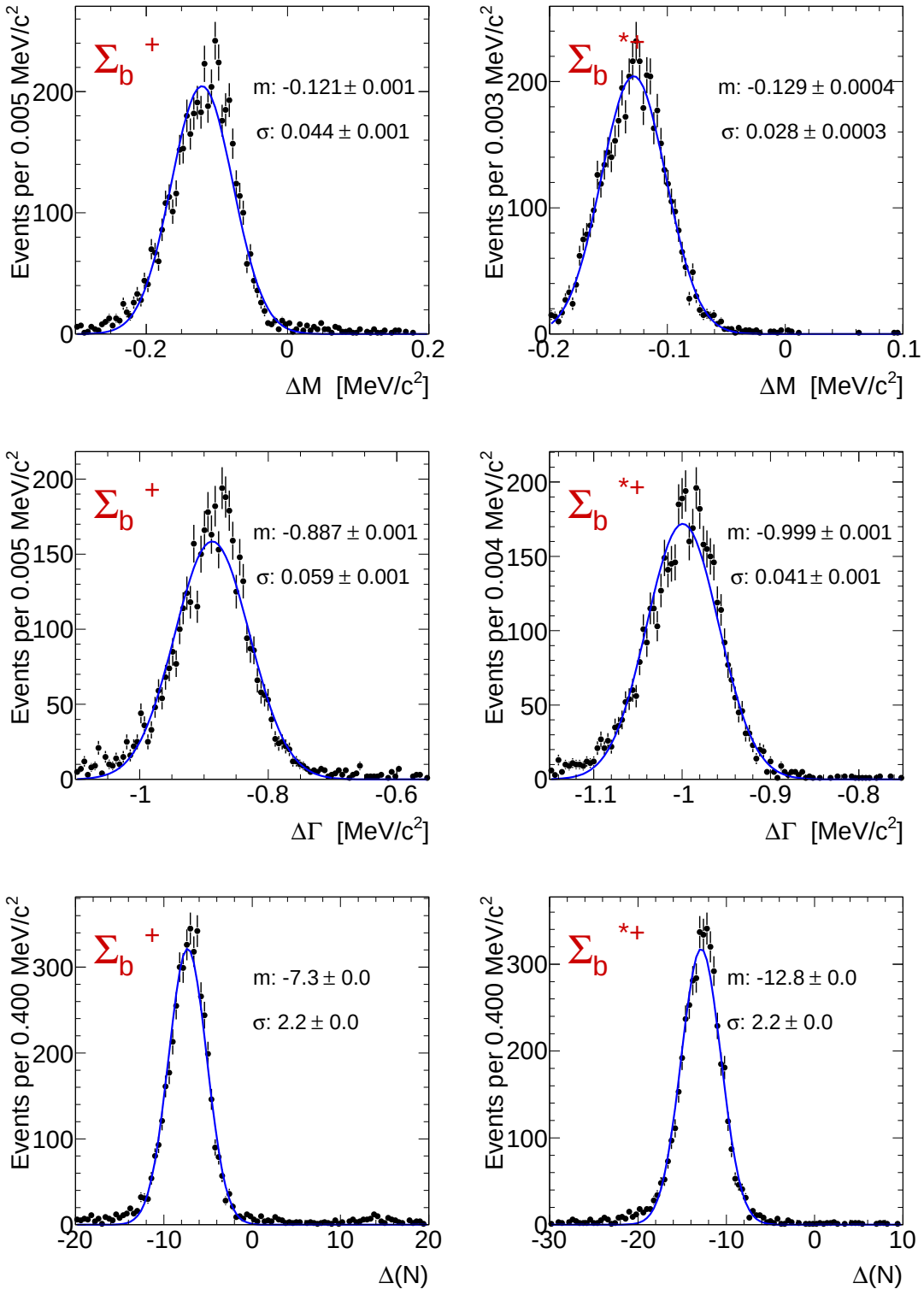

Figure 6.16: *The 7K toy Monte Carlo study for "opposite sign" state* $\Sigma_b^{(*)+} \to \Lambda_b^0 \pi^+_{\Sigma_b}$. *Impact on the signal floating parameters due to* **the increase** *by* $+25\%$ *in the sigma narrow and by* $+40\%$ *in the sigma wide describing resolution detector, that is,* $\sigma_{narrow} = \sigma_{narrow} \cdot 1.25$ *and* $\sigma_{wide} = \sigma_{wide} \cdot 1.4$.

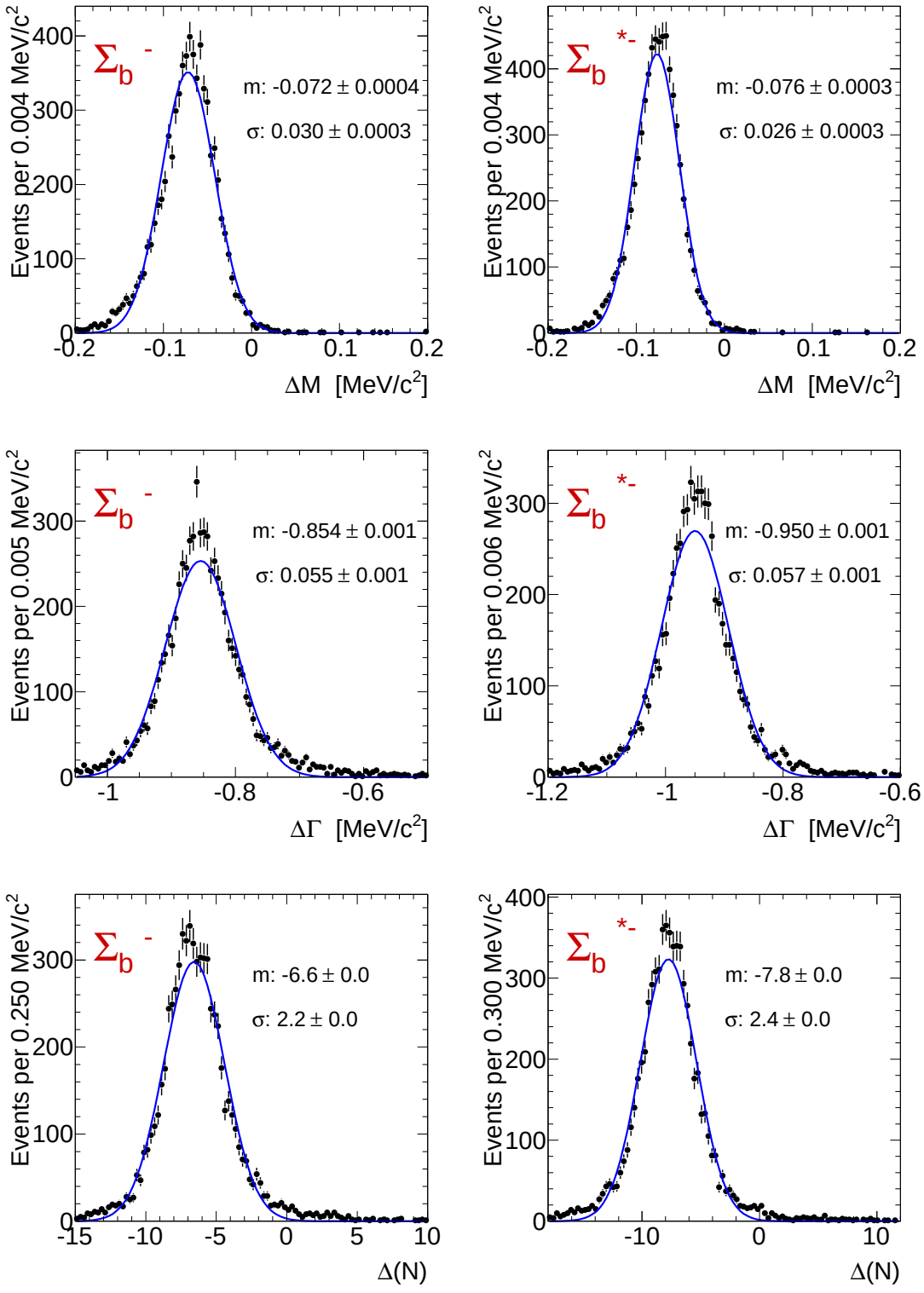

Figure 6.17: *The 7K toy Monte Carlo study for "same sign" state* $\Sigma_b^{(*)-} \to \Lambda_b^0 \pi^-_{\Sigma_b}$. *Impact on the signal floating parameters due to* **the increase** *by* $+25\%$ *in the sigma narrow and by* $+40\%$ *in the sigma wide describing resolution detector, that is,* $\sigma_{narrow} = \sigma_{narrow} \cdot 1.25$ *and* $\sigma_{wide} = \sigma_{wide} \cdot 1.4$.

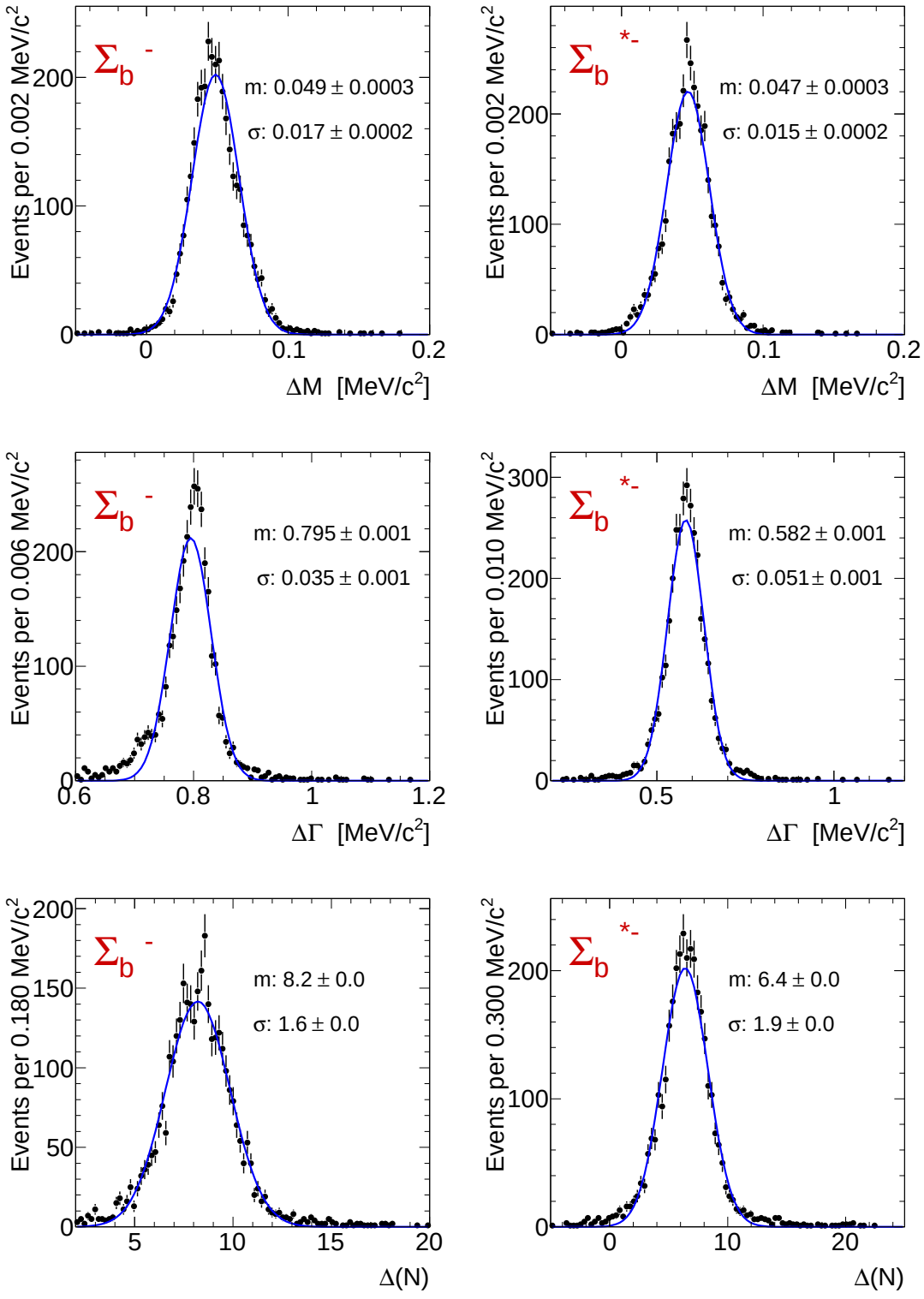

Figure 6.18: *Impact on the signal floating parameters due to* **the decrease** *by* 20% *in the gaussian sigma narrow and by* 40% *in the gaussian sigma wide describing the resolution detector to estimate the effect on the overestimation in the resolution of the* $\Sigma_b^{(*)}$ *states decaying to negative charged soft pions.*

Signal Parameters	$\Sigma_b^{(*)-} \to \Lambda_b^0 \pi^-_{\Sigma_b}$	$\Sigma_b^{(*)+} \to \Lambda_b^0 \pi^+_{\Sigma_b}$
Σ_b pole, Q_{01}	56.24	52.02
Σ_b width, Γ_{01} MeV/c^2	5.1	8.3
Σ_b yield. N_{s1}	353	430
Σ_b^* pole, Q_{02}, MeV/c^2	75.81	72.83
Σ_b^* width, Γ_{02} MeV/c^2	7.5	11.5
Σ_b^* yield, N_{s2}	547	817

Table 6.15: *Signal parameters returned by the fitter to $\Lambda_b^0 \pi^-_{\Sigma_b}$ and $\Lambda_b^0 \pi^+_{\Sigma_b}$ signs when using RooDstD0BG distribution (Equation 6.1) as the background model. All the masses and widths are in units of* MeV/c^2.

Signal Parameters	Systematic shift
Σ_b^+ pole, Q_{01}	0.05
Σ_b^+ width, Γ_{01}	0.4
Σ_b^+ yield, N_{s1}	9
Σ_b^{*+} pole, Q_{02}	0.1
Σ_b^{*+} width, Γ_{02}	0.5
Σ_b^{*+} yield, N_{s2}	24

Table 6.16: *Systematic errors in the signal floating parameters for the $\Lambda_b^0 \pi^+_{\Sigma_b}$ sign due to the uncertainty on the true background model. All the masses and widths are in units of* MeV/c^2.

The 500 toy samples are fitted with both fitters (the one used to generate the samples and our base line fitter). For every signal parameter, we obtain two distributions with the differences between the fitted and the generated values for this parameter for both fitters. We fit these two distributions with a gaussian fit. The difference between the two gaussian means plus its error is our estimation for the systematic error associated to this parameter.

The results of these studies are shown in Figs. 6.20 and 6.21, and the estimated systematic errors are summarized in Tabs. 6.16 and 6.17.

6.2.3 Summary of the Systematics

We added in quadrature all the systematic errors to quote the total systematic uncertainties on our measurements.

- For the mass measurements, the highest contribution to the systematic error comes from the mass scale uncertainty.

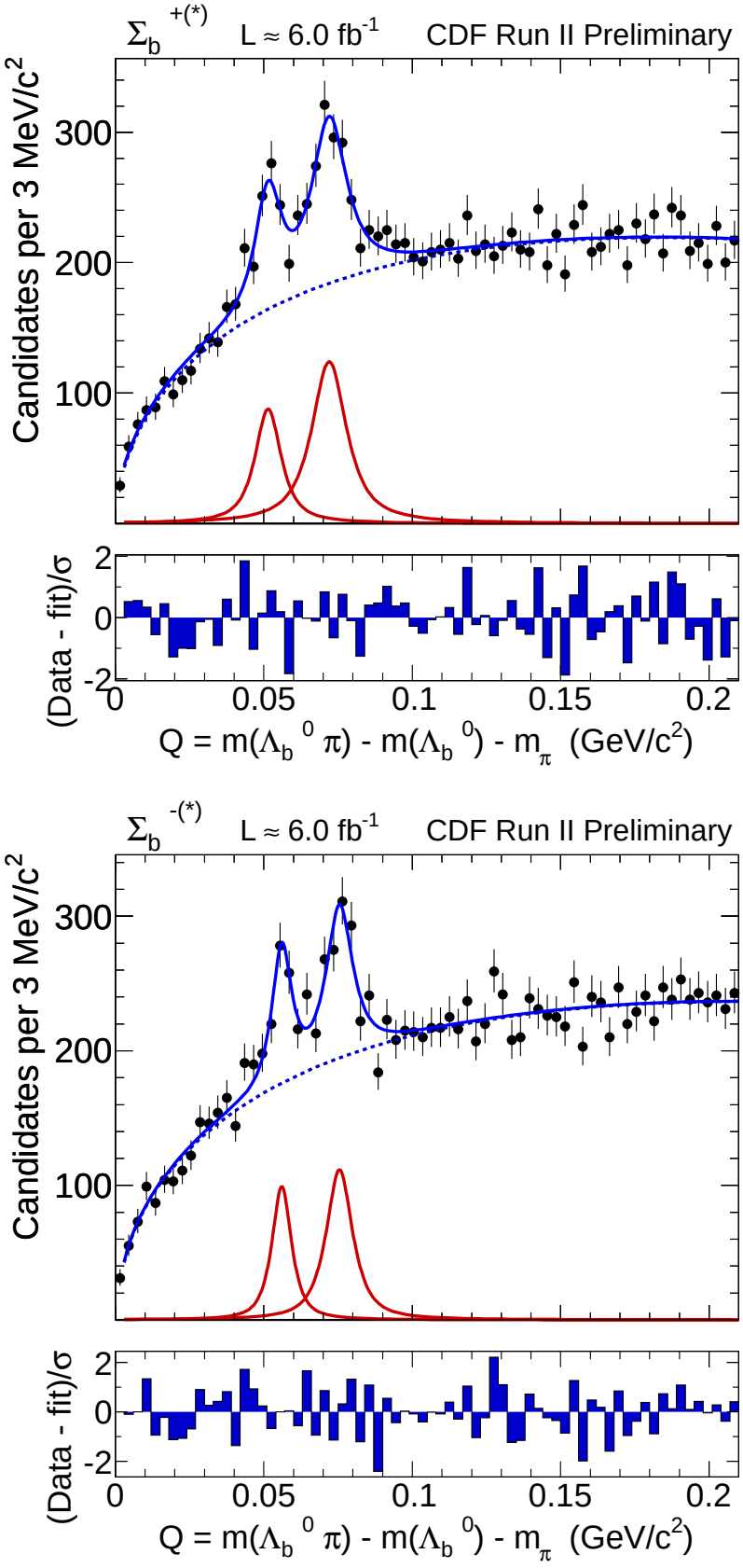

Figure 6.19: *Fits of $\Lambda_b^0\pi^+_{\Sigma_b}$ sign (upper) and $\Lambda_b^0\pi^-_{\Sigma_b}$ (bottom) using the RooDstD0BG distribution (Equation 6.1) to describe the background.*

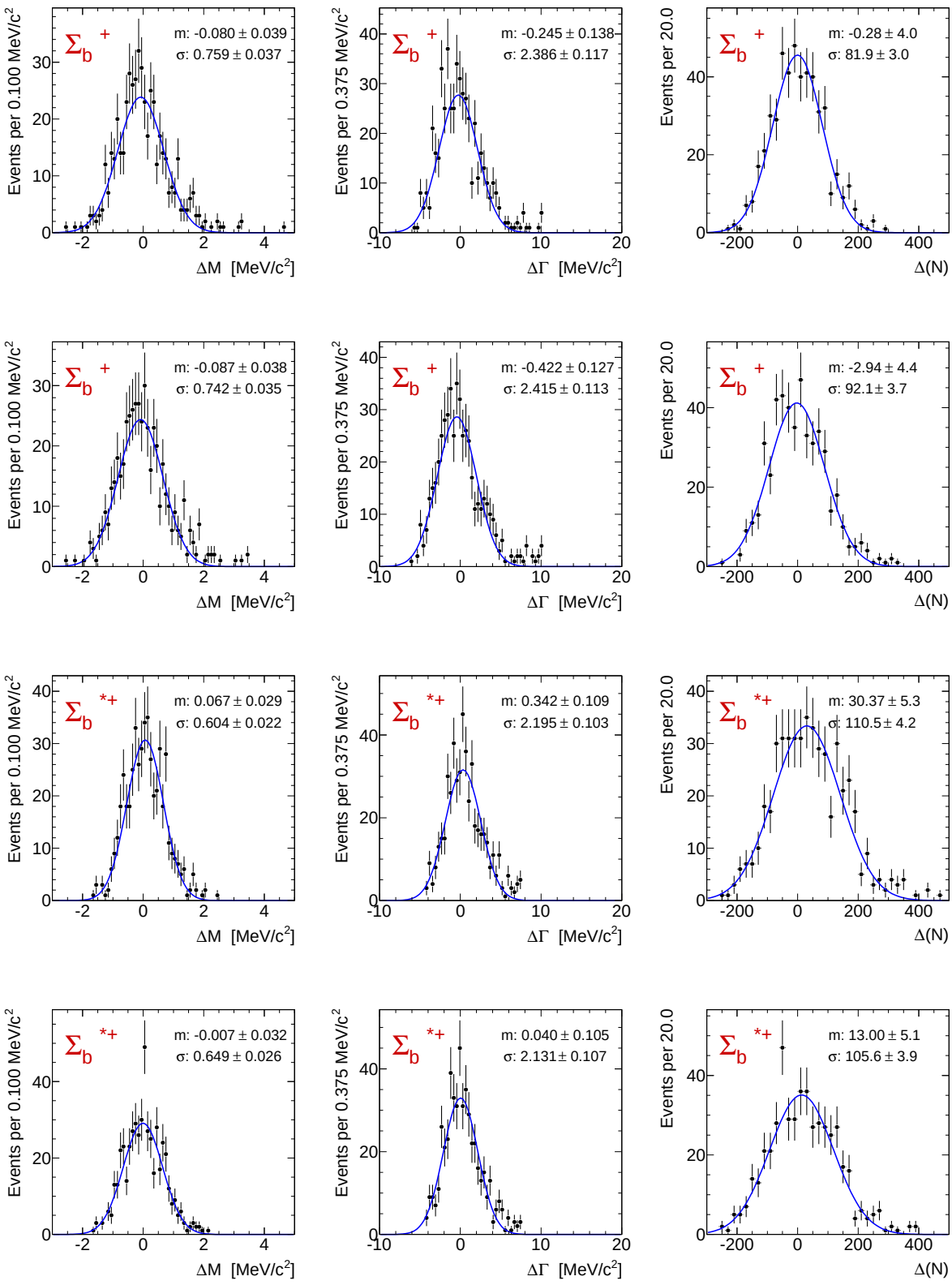

Figure 6.20: *Impact on the signal floating parameters due to the uncertainty on the background model chosen ($\Lambda_b^0\pi^+_{\Sigma_b}$). First and third rows correspond with fitting generated samples using the same PDF used to generate the samples. The second and fourth rows correspond with fitting the samples using our default fitter. In Table 6.16 the assigned systematic errors are shown.*

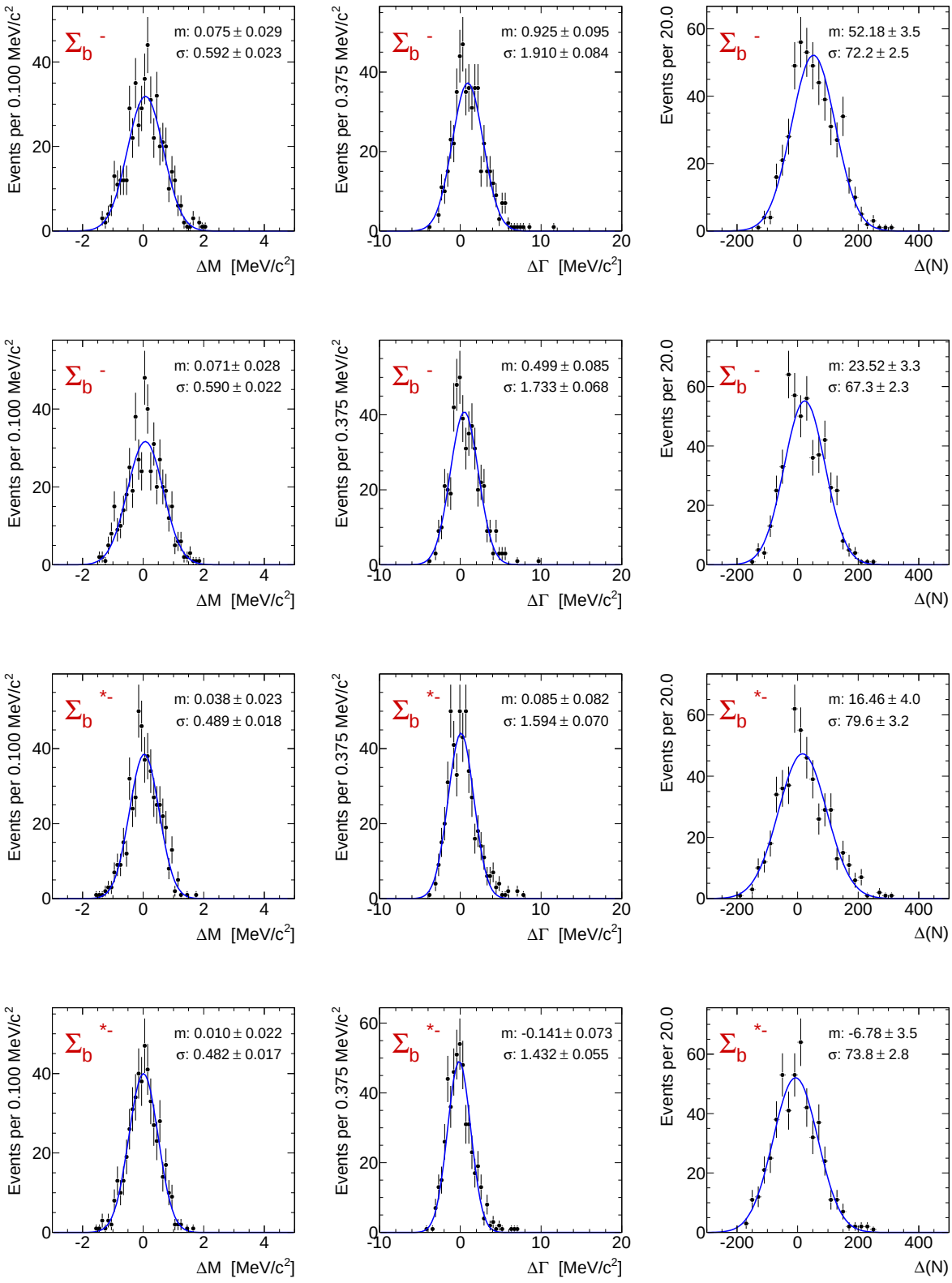

Figure 6.21: *Impact on the signal floating parameters due to the uncertainty on the background model chosen ($\Lambda_b^0\pi^-_{\Sigma_b}$). First and third rows correspond with fitting generated samples using the same PDF used to generate the samples. The second and fourth rows correspond with fitting the samples using our default fitter. In Table 6.17 the assigned systematic errors are shown.*

Signal Parameters	Systematic shift
Σ_b^- pole, Q_{01}	0.04
Σ_b^- width, Γ_{01}	0.5
Σ_b^- yield, N_{s1}	34
Σ_b^{*-} pole, Q_{02}	0.06
Σ_b^{*-} width, Γ_{02}	0.3
Σ_b^{*-} yield, N_{s2}	28

Table 6.17: *Systematic errors in the signal floating parameters for the $\Lambda_b^0\pi^-_{\Sigma_b}$ sign due to the uncertainty on the true background model. All the masses and widths are in units of* MeV/c^2.

- For the width measurements, the uncertainty in the resolution detector dominates the systematic error.

Table. 6.18 summarizes the assigned systematic errors for all the considered uncertainty sources affecting our measurements.

Signal Pars.	Mass Scale	Fitter Bias	Res.	Res.Charge	Back.	Weight	Total	%
Σ_b^+ Q			0.03	0.05	0.05	0.04	0.09	0.2
	−0.35		−0.12		−0.05	−0.01	−0.37	1
Σ_b^+ Γ	0.20		0.28	0.80	0.40	0.41	1.04	11
	−0.20	−0.38	−0.89		−0.40	−0.10	−1.07	12
Σ_b^+ events			3	8	9	13	18	4
			−7		−9	−9	−15	3
Σ_b^- Q			0.02	0.05	0.04	0.01	0.07	0.1
	−0.38		−0.07		−0.04	−0.01	−0.39	1
Σ_b^- Γ	0.20		0.27	0.80	0.50	0.11	1.01	23
	−0.20	−0.27	−0.85		−0.50	−0.19	−1.06	25
Σ_b^- events			3	8	34	1	35	11
			−7		−34	−3	−35	10
Σ_b^{*+} Q			0.03	0.05	0.10	0.01	0.12	0.2
	−0.52		−0.13		−0.10	−0.01	−0.55	1
Σ_b^{*+} Γ	0.20		0.20	0.60	0.50	0.08	0.83	8
	−0.20	−0.29	−1.00		−0.50	−0.14	−1.18	11
Σ_b^{*+} events			3	6	24	1	25	3
			−13		−24	−3	−27	4
Σ_b^{*-} Q			0.02	0.05	0.06	0.02	0.08	0.1
	−0.56		−0.08		−0.06	−0.01	−0.57	1
Σ_b^{*-} Γ	0.20		0.19	0.60	0.30	0.15	0.74	12
	−0.20	−0.23	−0.95		−0.30	−0.10	−1.05	16
Σ_b^{*-} events			2	6	28	3	29	6
			−8		−28	−1	−29	6

Table 6.18: *Summary of the systematics errors. For every parameter, the total systematic error is obtained adding all the errors in quadrature. The order of the systematic errors, in these table are: mass scale, fitter bias, detector resolution, differences in resolution for states decaying into positive and negative charge soft pions, assumed background model, and the effect on variations on the resolution weight fraction. Masses and widths are in* MeV/c^2.

Chapter 7

Results

Once that all the systematics uncertainties have been estimated (see Table 6.18), we quote the results. We measure the Q-values of Σ_b^-, Σ_b^{*-}, Σ_b^+ and Σ_b^{*+} to be:

- $m(\Sigma_b^+) - m(\Lambda_b^0) - m(\pi) = 52.0^{+0.9}_{-0.8}\,(\text{stat})^{+0.09}_{-0.4}\,(\text{syst})\,\text{MeV}/c^2$
- $m(\Sigma_b^-) - m(\Lambda_b^0) - m(\pi) = 56.2^{+0.6}_{-0.5}\,(\text{stat})^{+0.07}_{-0.4}\,(\text{syst})\,\text{MeV}/c^2$
- $m(\Sigma_b^{*+}) - m(\Lambda_b^0) - m(\pi) = 72.7 \pm 0.7\,(\text{stat})^{+0.12}_{-0.6}\,(\text{syst})\,\text{MeV}/c^2$
- $m(\Sigma_b^{*-}) - m(\Lambda_b^0) - m(\pi) = 75.7 \pm 0.6\,(\text{stat})^{+0.08}_{-0.6}\,(\text{syst})\,\text{MeV}/c^2$

From these Q-values we extract the isotopic mass differences between opposite charged states within the two isotriplets $J^P = \frac{1}{2}^+$ and $J^P = \frac{3}{2}^+$:

- $m(\Sigma_b^+) - m(\Sigma_b^-) = -4.2^{+1.1}_{-0.9}\,(\text{stat})^{+0.07}_{-0.09}\,(\text{syst})\ \ \text{MeV}/c^2$
- $m(\Sigma_b^{*+}) - m(\Sigma_b^{*-}) = -3.0 \pm 0.9\,(\text{stat})^{+0.12}_{-0.13}\,(\text{syst})\ \ \text{MeV}/c^2$

Where the statistical errors have been added in quadrature. To quote the systematic errors for the isospin splittings, the correlation between systematic uncertainties for isopin partners has to be taken into account. We say that two systematic errors, related with the systematic variation of one parameter of the model, are correlated if the Q-value of both isospin partners change in the same direction under the systematic variation of that parameter.

It is clear that adding in quadrature the systematic uncertainties associated with these variables would give an overestimation of the systematic uncertainty of the mass difference.

According to the evaluation of the systematic errors in Section 6, all the systematic uncertainties are correlated except the uncertainty in the assumed background model.

For those correlated uncertainty sources, instead of adding the associated systematic errors in quadrature, we added in quadrature the differences.

We measure the natural widths of these states to be:

- $\Gamma(\Sigma_b^+) = 9.2^{+3.8}_{-2.9}\,(\text{stat})^{+1.0}_{-1.1}\,(\text{syst})\ \ \text{MeV}/c^2$

- $\Gamma(\Sigma_b^-) = 4.3^{+3.1}_{-2.1}\,(\text{stat})^{+1.0}_{-1.1}\,(\text{syst})$ MeV/c^2
- $\Gamma(\Sigma_b^{*+}) = 10.4^{+2.7}_{-2.2}\,(\text{stat})^{+0.8}_{-1.2}\,(\text{syst})$ MeV/c^2
- $\Gamma(\Sigma_b^{*-}) = 6.4^{+2.2}_{-1.8}\,(\text{stat})^{+0.7}_{-1.1}\,(\text{syst})$ MeV/c^2

To go from Q values to absolute masses for $\Sigma_b^{(*)\pm}$, we add the PDG value of the $\pi^\pm$ mass [17] and the best CDF II mass measurement for Λ_b^0, which is $m(\Lambda_b^0) = 5619.7 \pm 1.2\,(\text{stat}) \pm 1.2\,(\text{syst})$ MeV/c^2 [81]. The error on the mass of the Λ_b^0 must also be added to the systematic error.

We measure the absolutes masses of these states to be:

- $m(\Sigma_b^+) = 5811.2^{0.9}_{-0.8}\,(\text{stat}) \pm 1.7\,(\text{syst})\,\text{MeV}/c^2$
- $m(\Sigma_b^-) = 5815.5^{+0.6}_{-0.5}\,(\text{stat}) \pm 1.7\,(\text{syst})\,\text{MeV}/c^2$
- $m(\Sigma_b^{*+}) = 5832.0 \pm 0.7\,(\text{stat}) \pm 1.8\,(\text{syst})\,\text{MeV}/c^2$
- $m(\Sigma_b^{*-}) = 5835.0 \pm 0.6\,(\text{stat}) \pm 1.8\,(\text{syst})\,\text{MeV}/c^2$

Chapter 8

Conclusions

In a conclusion, we have observed the $\Sigma_b^{(*)\pm}$ bottom baryons using a sample of ~ 16300 Λ_b^0 candidates identified in $\Lambda_b^0 \to \Lambda_c^+\pi^-$ mode. The sample corresponds to an integrated luminosity of $6\,\mathrm{fb}^{-1}$.

The first observation of $\Sigma_b^{(*)\pm}$ bottom baryons made by CDF Collaboration [3] has been confirmed with the every individual signal reconstructed at a significance of $\gtrsim 7\sigma$ in Gaussian terms.

The direct mass difference measurements have been found with the statistical precision by a factor of $\gtrsim 2.3$ better w.r.t. to the published [3] numbers and according to the amount of the statistics available. The measurements are in a good agreement with the previously found results [3].

The isospin mass splittings within $I = 1$ triplets Σ_b and Σ_b^* have been extracted for the first time. The precision of the experimental values is as good as the ones quoted by PDG [17] for Σ_c states. The $\Sigma_b^{(*)-}$ states have a higher mass value than their $\Sigma_b^{(*)+}$ partners following a well known pattern [84] of any known isospin multiplet and contrary to their charm partners [17], Σ_c where the supposedly natural order of masses within isotriplets is still violated [82].

The natural widths of both $\Sigma_b^{\pm}$ and $\Sigma_b^{*\pm}$ states have been measured for the first time. The measurements are in a agreement with the theoretical expectations, see the Table 1.2.

We are interested in non-perturbative QCD effects because they have the potential to obscure or confuse the effects in indirect searches for physics beyond the Standard Model. The best means of studying these non-perturbative QCD effects is to investigate the interactions of quarks bound in hadrons. Due to the symmetries invocked when the hadron contains one heavy quark, QCD effects are most easily studied by finding and measuring as many heavy hadrons as possible. We then compare the measurements to the predictions from a number of theoretical models.

The Σ_b measurement show good agreement with the theoretical predictions based on heavy quark effective theories. The quantum numbers (I, J, and P) still need confirmation for all these states, which will require much more data. It is encouraging that thus far

the states have been found with the properties (such as mass and intrinsic width) that we expect. This shows us that the heavy quark effective theories are a good approximation to QCD in the non-perturbative regime. However, at this point no one theoretical model stands out as preferred for predicting the properties of heavy hadrons.

The study of heavy hadrons should continue in the future. It is important to improve measurements of the known members or the spectrum-accurate measurements of the masses, widths, and lifetimes of each state, confirming the quantum numbers, and measuring the polarization of the Σ_b states are only a few possibilities.

Appendix A

Hadronic Two Displaced Track SVT Trigger

The three separate trigger paths for the hadronic two displaced tracks SVT trigger are: the nominal (B_CHARM), the low p_T (B_CHARM_LOWPT), and the high p_T (B_CHARM_HIGHPT). The trigger criteria for each path are described in detail in Ref. [52], and summarized in the following sections. Table A.1 compiles the specific requirements for these paths at each trigger level. Common notations include:

- p_T^{XFT} and p_T^{SVT}: the transverse momenta as measured by either the XFT ot SVT devices,
- $\sum p_T^{XFT}$ and $\sum p_T^{SVT}$: the scalar sum of the transverse momenta of the two displaced tracks,
- $\Delta\phi_6^{XFT}$: the separation in azimuthal angle ϕ between two tracks as measured at COT superlayer 6 by the XFT system,
- $\Delta\phi_0^{SVT}$: the separation in azimuthal angle ϕ between two tracks as extrapolated to the primary vertex position by the SVT system,
- Δz_0: the separation between two tracks along the beam axis as extrapolated to their points of closest approach.

A.1 The B_CHARM Trigger Path

This is the nominal b hadronic two displaced track SVT trigger (TTT). In order to be used at high luminosities, it must be severely prescaled. At the highest luminosities ($> 250 \times 10^{30}$ s^{-1} cm^{-2}), the TTT path is not included in the trigger selection.

Level-1

At L1, this trigger path looks for:

- Two tracks with opposite charge
- 4 XFT hit layers for each track
- XFT $p_T > 2.04$ GeV/c for each track
- Opening angle between the tracks of $0° < \Delta\phi_0 < 135°$
- Scalar p_T sum: $\Sigma_{p_T} > 5.5$ GeV/c

Level-2

At L2 the silicon SVT information is added. The requirements are:

- Two tracks with opposite charge
- SVT $\chi^2 < 25$
- SVT $p_T > 2$ GeV/c for each track
- 120 μm $< |d_0| < 1$ mm for each track
- Opening angle between the tracks of $2° < \Delta\phi_0 < 90°$
- Scalar p_T sum: $\Sigma_{p_T} > 5.5$ GeV/c
- $L_{xy} > 200$ μm

Level-3

At L3, the SVT tracks are matched to COT tracks by requiring proximity in curvature and ϕ_0. The SVT measurement is used for the track d_0 with the other four track parameters taken from the COT measurement. Pairs of these hybrid tracks are then subject to the following requirements:

- Two tracks with opposite charge
- 120 μm $< |d_0| < 1$ mm for each track
- $p_T > 2$ GeV/c for each track
- $|\eta| < 1.2$ for each track
- $|\Delta z_0 < 5$ cm between the tracks
- Opening angle $2° < \Delta\phi_0 < 90°$
- Scalar p_T sum: $\Sigma_{p_T} > 5.5$ GeV/c
- $L_{xy} > 200$ μm

A.2 The B_CHARM_LOWPT Trigger Path

The B_CHARM_LOWPT trigger path is designed to complement the B_CHARM trigger path by filling the trigger bandwidth at low luminosities. The requirements are similar but not quite as strict; for example, the tracks are not required to have opposite charge and no requirement is made on the scalar sum p_T of the two tracks.

Level-1

The requirements at L1 are:

- Two tracks
- 4 XFT hit layers for each track
- XFT $p_T > 2.04$ GeV/c for each track
- Opening angle $\Delta\phi_0 < 90°$

Level-2

The requirements are:

- Two tracks
- SVT $\chi^2 < 25$
- SVT $p_T > 2$ GeV/c for each track
- 120 μm $< |d_0| < 1$ mm for each track
- Opening angle $\Delta\phi_0 < 90°$
- $L_{xy} > 200$ μm

Level-3

The requirements at L3 are:

- Two COT tracks matched to SVT tracks
- 120 μm $< |d_0| < 1$ mm for each track
- $p_T > 2$ GeV/c for each track
- $|\Delta z_0| < 5$ cm between the tracks

- Opening angle $2^\circ < \Delta\phi_0 < 90^\circ$
- Scalar p_T sum: $\Sigma_{p_T} > 4.0$ GeV/c
- $L_{xy} > 200$ μm

A.3 The B_CHARM_HIGHPT Trigger Path

The B_CHARM_HIGHPT trigger path was originally added as a lower rate TTT path which did not need to be prescaled at high luminosities. However, even this trigger cannot be included at the highest luminosity running. The requirements are similar to the B_CHARM but with higher p_T and scalar sum p_T requirements to lower the rate.

Level-1

The requirements at L1 are:

- Two tracks with opposite charge
- 4 XFT hit layers for each track
- XFT $p_T > 2.46$ GeV/c for each track
- Opening angle $\Delta\phi_0 < 135^\circ$
- Scalar p_T sum: $\Sigma_{p_T} > 6.5$ GeV/c

Level-2

The requirements at L2 are:

- Two tracks with opposite charge
- SVT $\chi^2 < 25$
- SVT $p_T > 2.5$ GeV/c for each track
- 120 μm $< |d_0| < 1$ mm for each track
- Opening angle $2^\circ < \Delta\phi_0 < 90^\circ$
- Scalar p_T sum: $\Sigma p_T > 6.5$ GeV/c
- $L_{xy} > 200$ μm

Level-3

The requirements at L3 are:

- Two tracks with opposite charge
- 120 μm $< |d_0| <$ 1 mm for each track
- $p_T > 2$ GeV/c for each track
- $|\eta| < 1.2$ for each track
- $|\Delta z_0| < 5$ cm between the tracks
- Opening angle $2^\circ < \Delta\phi_0 < 90^\circ$
- scalar p_T sum: $\Sigma_{p_T} > 5.5$ GeV/c
- $L_{xy} > 200$ μm

		Scenario		
	Requirement	B_CHARM	B_CHARM_HIGHPT	B_CHARM_LOWPT
L1	Two XFT tracks with:	opp. charge	opp. charge	any charge
	4 XFT hits for each trk	$\surd$	$\surd$	$\surd$
	p_T^{XFT} >[GeV/c^2]	2.0	2.5	2.0
	$\sum p_T^{XFT}$ > [GeV/c^2]	5.5	6.5	0
	$\Delta\phi_6^{XFT} \in$	[0,135]°	[0,120]°	[0,120]°
L2	XFT tracks matched to SVT tracks	$\surd$	$\surd$	$\surd$
	p_T^{SVT} > [GeV/c^2]	2.0	2.5	2.0
	$\sum p_T^{SVT}$ > [GeV/c^2]	5.5	6.5	0
	$\Delta\phi_0^{SVT} \in$	[2,90]°	[2,90]°	[2,90]°
	$\lvert d_0^{SVT}\rvert \in$ [μm]	[120,1000]	[120,1000]	[120,1000]
	L_{xy}^{SVT} > [μm]	200	200	200
L3	SVT tracks matched to COT+silicon trks	$\surd$	$\surd$	$\surd$
	p_T^{SVT} > [GeV/c^2]	2.0	2.5	2.0
	χ^2_{SVT}(trk1),χ^2_{SVT}(trk2)	< 25	< 25	< 25
	$\sum p_T^{SVT}$ > [GeV/c^2]	5.5	6.5	0
	$\Delta\phi_0 \in$	[2,90]°	[2,90]°	[2,90]°
	$\lvert d_0^{SVT}\rvert \in$ [μm]	[120,1000]	[120,1000]	[120,1000]
	L_{xy}^{SVT} > [μm]	200	200	200
	$\lvert\Delta z_0\rvert$ < [cm]	5.0	5.0	5.0
	Prescaled?	$\surd$	-	$\surd$

Table A.1: *Specific requirements for the two-track trigger scenarios at each of the three trigger levels (L1/L2/L3). The notations are defined in the text.*

Appendix B

Analysis Quality Requirements

B.1 Default Track Selection

The `defTracks` requirements are made on all tracks used in these analysis; tracks which pass these requirements are considered to be of good quality. Tracks which fail the more stringent cuts are demoted to the next lower class and retested.

- COT and silicon tracking (OIZ):
  - COT requirements:

    1. Two or more axial superlayerx (SL) with 5 or more hits each
    2. Two or more stereo SL with 5 or more hits each
    3. If (1) and (2) are not satisfied, track will still be accepted if there are two axial SL and one stereo SL with 5 or more hits, as long as the track exits the COT in the z direction before the last wire layer.

  - Silicon requirements:

    1. Three or more silicon $r\phi$ hits if COT requirements are met
    2. if COT requirements are not met, track must have five or more silicon $r\phi$ hits to be accepted.
    3. One or more axial silicon hits and one or more 90° silicon hits.
    4. If (3) is not satisfied, track is accepted if it has three or more 90° silicon hits.

  - z_0 error less than 0.05 cm
- COT stand-alone tracking:
  - Same COT requirements as OIZ.

  - One or more axial sislicon hits.
  - z_0 error less than 0.5 cm

- Outside-in tracking:
  - Cot requirements:
    1. Two or more axial SL with 5 or more hits each
    2. Two or more stereo SL with 5 or more hits each
    3. If (1) and (2) are not satisfied, track will still be accepted if it has 5 or more axial COT hits and 2 or more stereo COT hits, as long as the track exits the COT in the z direction before the last wire layer.
  - Duplicate COT tracks are detected and removed

- COT only tracking:
  - Same COT requirements as for OIZ.
  - χ^2 per degree of freedom is less than 10

- Silicon only tracking:
  - If track passes through the forward region of the detector, it must have 5 or more axial silicon hits
  - If track passes through the central region of the detector, it must have 4 or more axial silicon hits
  - track does not traverse the entire COT volume (otherwise it should have fallen under the Outside-in category)

B.2 Good Run Criteria

The definition of a "good run" has been set for various physics analysis by the CDF II Data Quality Management group. For each data run, the good run bits are set true or false by the shift crew or in offline analysis, and are saved to a database. Most of the good run bits are set by a shift crew member called the Consumer Operator (CO) whose job is to monitor the online data quality plots. For b physics, the following good run bits are required to be true:

- `RUNCONTROL_STATUS`: The Run Control software starts and stops the data taking run. This bit is automatically set to true by Run Control if a run lasts long enoughh for 100 million collisions, 10,000 Level-1 acceptd, 1,000 Level-2 accepts, and at least 1 nb^{-1} of integrated luminosity.

- SHIFTCREW_STATUS: This bit is filled by the shift crew member operating the Run Control software at the end of every run.

- CLC_STATUS: This bit is set to true by the CO if the online data quality plots of luminosity and beam conditions are normal.

- L1T_STATUS and L2T_STATUS are set to true by the CO after verifying that the Trigger Monitoring plots are normal.

- L3T_STATUS is set to true if the L3 SVX II reformatter error is less that 1 %.

- COT_ONLINE bit is set to true by the CO if the COT high voltage was on for the entire run and the COT Monitoring plots look normal. COT_OFFLINE status is determined after the data has been examined offline by experts. the criteria for setting it true is that there were fewer than 1 % of bad COT channels during the run and that the integrated luminhosity was at least 10 nb^{-1}.

- SVX_ONLINE bit is set to true by the CO if the SVX II high voltage was on for the entire run and the SVX II Monitoring plots look normal. SVX_OFFLINE status is determined after the data has benn examined offline by experts. the criteria for setting it true is that the D^0 and D^{*+} yields are within the expected ranges. These particles decay at secondary vertices and thus will fire the TTT, and are produced at a high enough rate to give meaningfull statistics for any good run.

- CMU_OFFLINE bit is set to true by the CO if the CMU high voltage was on for the entire run and the CMU Monitoring plots look normal. CMU_OFFLINE status i sdetermined after the data has been examined offilen by the expertes. the criteria for setting it true is that the CMU occupancy looks normal.

- SVT_ONLINE bit is set true by the CO if the SVT Monitoring plots look normal. SVT_OFFLINE status is determined after the data has been examined offline by experts. The criteria for setting it true is that the online beam position subtraction was done correctly and the SVT occupancy looks normal.

- CAL_ONLINE bit is set true by the CO if all the elctromagnetic and hadronic calorimeter high voltages were on for the entire run and the associated monitoring plots all look normal. CAL_OFFLINe status is determined after the data has abeen examined offline by experts. the criteria for setting it true is taht the occupancy looks normal.

Appendix C

Additional Checks on the Fitter

In this appendix we present two additional checks of the fitter complementary to those checks showed within Section 5.5. Both checks consist basically in two copies of the toy MC study showed in Section 5.5 using different input values.

C.1 Toy MC I

The Q-value spectra individually for $\Sigma_b^{(*)-} \to \Lambda_b^0 \pi^-_{\Sigma_b}$ and for $\Sigma_b^{(*)+} \to \Lambda_b^0 \pi^+_{\Sigma_b}$ are generated according to the full baseline fit model consisting of the signal expressed by Eq. 5.1 with Eq. 5.4 on top of the background expressed by a form in Eq. 5.8. The input values with which the trials (or "toy MC" samples) have been generated, for every state $\Sigma_b^{(*)\pm}$, are arranged in Table C.1.

The values specified in the table correspond to the experimental data results yielded by an unbinned fitter over a subsample of the data.

We generate 10000 toy MC Q-spectra for both $\Sigma_b^{(*)-}$ and $\Sigma_b^{(*)+}$. These generated samples are then fitted by unbinned likelihood fits.

The next **9 parameters** Q_{01}, Γ_{01}, N_{s1}, Q_{02}, Γ_{02}, N_{s2}, C, b_1 and N_b are left floating in the fits, while the other ones from the Table C.1 are fixed to its originally generated values. Only converged in `MIGRAD` unbinned likelihood fits are saved. The parabolic errors are calculated by `HESSE`.

Performance Plots: $\Sigma_b^{(*)-}$

The distribution of all converged $-log(LH)$ is shown on the upper plot of Fig. C.1 with the experimental data value overlapped. The perfect Gaussian shape is observed with the mean value practically the same as the experimental data fit yields. The bottom 2×2 plot of the same Fig. C.1 demonstrates a fitter performance for a first peak Q_{01} (left column) and width Γ_{01} (right column) values.

The fitter response to Q_{02} and Γ_{01} is shown at Fig. C.2. The distributions and pulls of the fitted yields, N_{s1}, N_{s2} are at Fig. C.3.

Signal parameters	$\Sigma_b^{(*)-} \to \Lambda_b^0 \pi^-_{\Sigma_b}$	$\Sigma_b^{(*)+} \to \Lambda_b^0 \pi^+_{\Sigma_b}$
Σ_b pole, Q_{01}, MeV/c^2	56.3	51.7
Σ_b width, Γ_{01} MeV/c^2	5.74	8.4
Σ_b yield, N_{s1}	359	398
Σ_b resolution, σ_{11} MeV/c^2	1.17	1.17
Σ_b resolution, σ_{21} MeV/c^2	3.00	3.00
Σ_b fraction of σ_{11}, g_{11}	0.92	0.92
Σ_b^* pole, Q_{02}, MeV/c^2	75.8	72.8
Σ_b^* width, Γ_{02} MeV/c^2	7.00	11.4
Σ_b^* yield, N_{s2}	509	756
Σ_b^* resolution, σ_{12} MeV/c^2	1.17	1.17
Σ_b^* resolution, σ_{22} MeV/c^2	3.00	3.00
Σ_b^* fraction of σ_{12}, g_{12}	0.88	0.88
Background, *thr*	0.140	0.140
Background, α	0.5	0.5
Background, C	4.0	4.0
Background, b_1	-3.55	-4.23
Background, b_2	3.15	2.89
Background yield, N_b	13035	12400

Table C.1: *The list and values of the fit model parameters set to generate statistical trials or "toy MC" Q- spectra for both $\Sigma_b^{(*)-}$ and $\Sigma_b^{(*)+}$.*

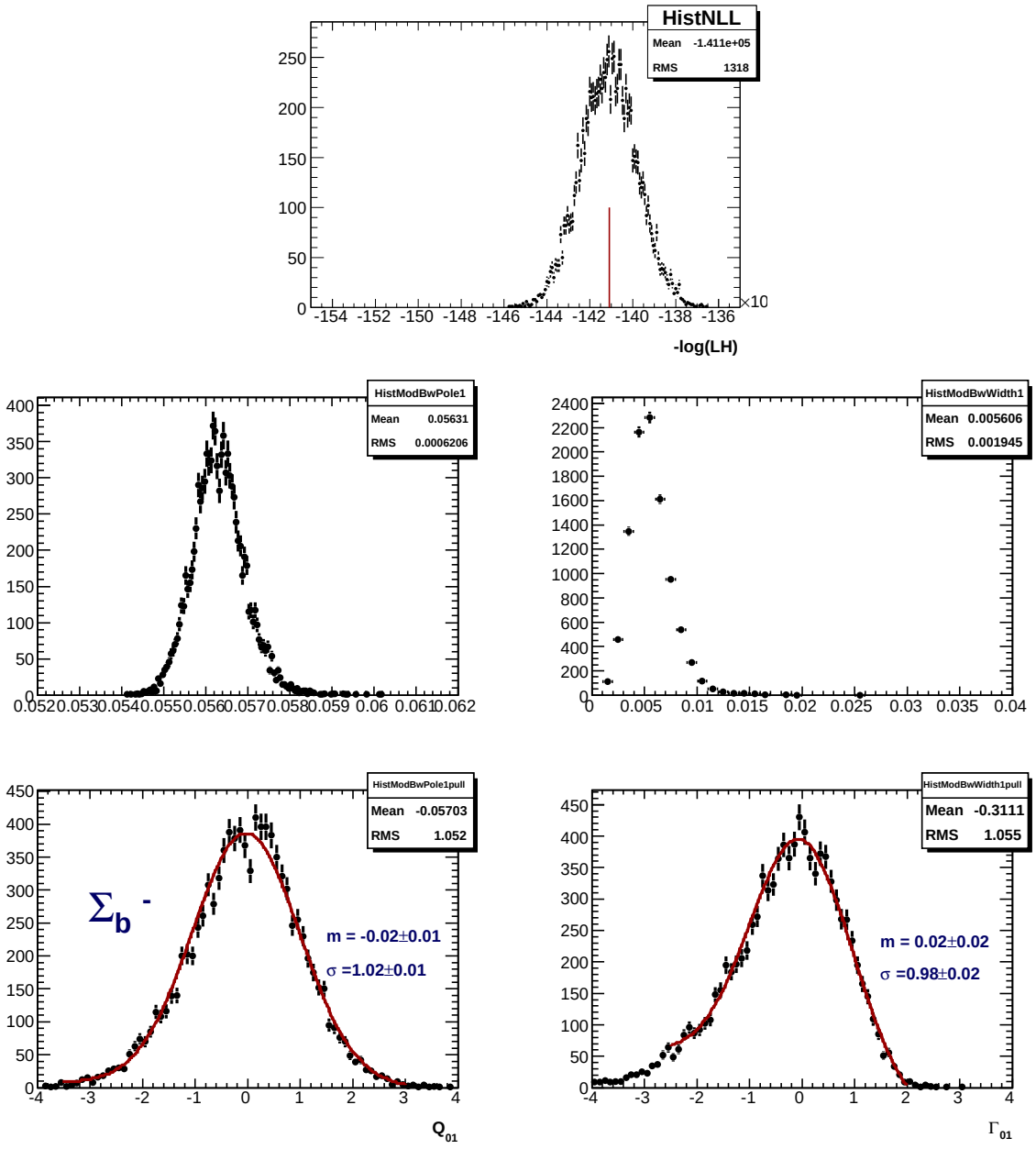

Figure C.1: *The upper plot shows the distribution of NLL resulted by unbinned LH fits of 10000 trials. Σ_b^- statistical trials for Q_{01}, GeV/c^2 and for Γ_{01} GeV/c^2 yielded the bottom plots showing the distribution of fitted values and their pulls.*

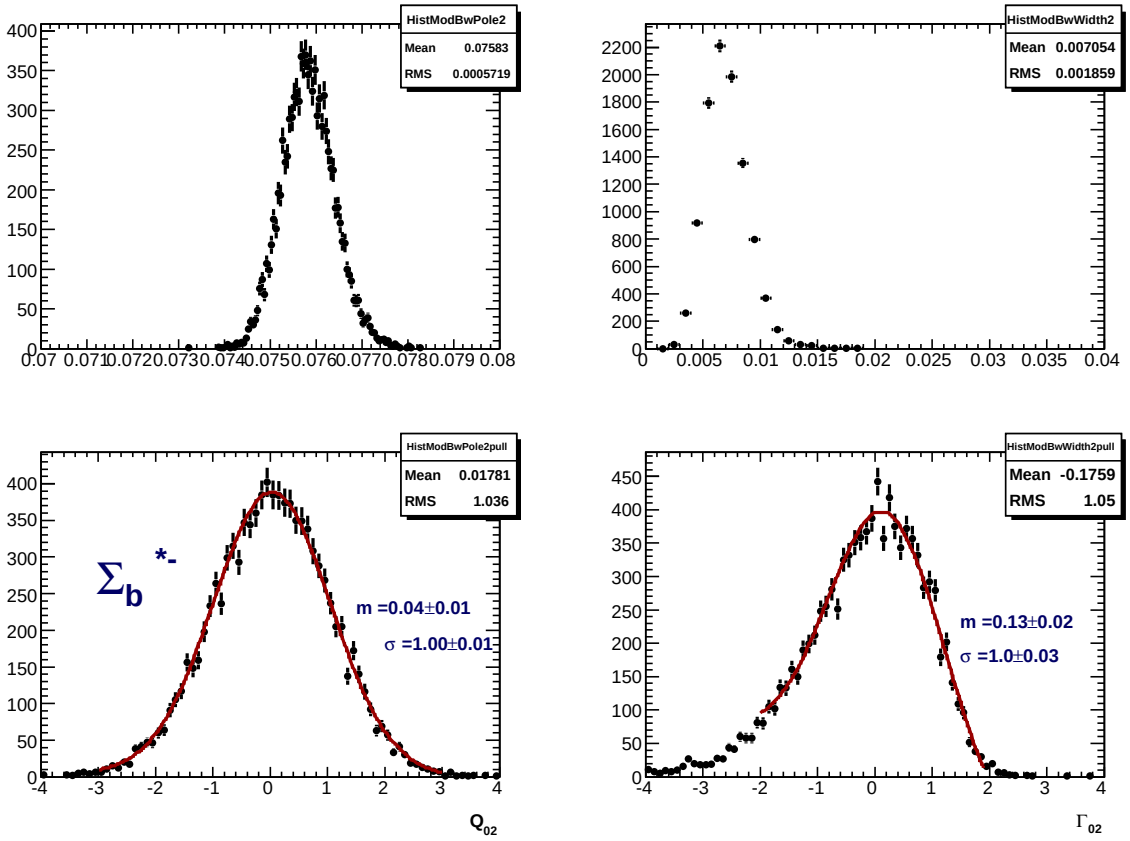

Figure C.2: *Σ_b^{*-} 10000 statistical trials for Q_{02}, GeV/c^2 and for Γ_{02} GeV/c^2. The plots show the distribution of fitted values and their pulls resulted from the same toy MC samples.*

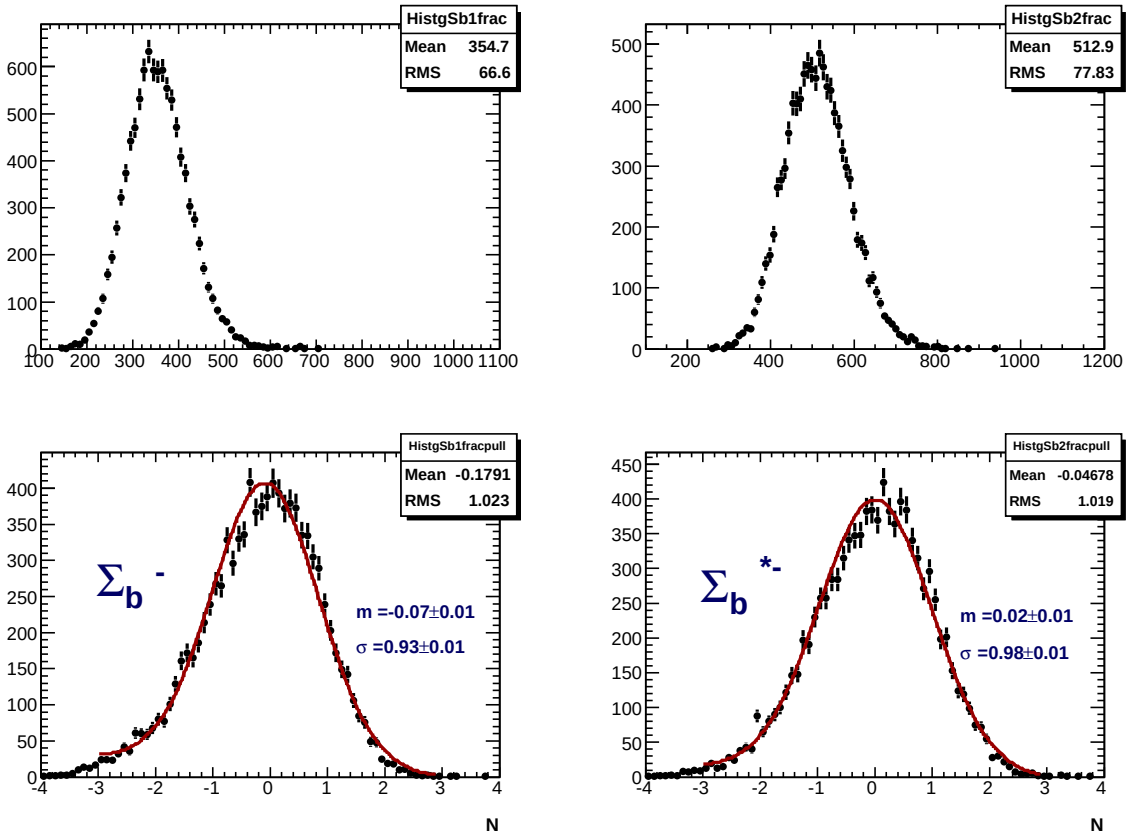

Figure C.3: $\Sigma_b^{(*)-}$ *10000 statistical trials for yields* N_{s1} *and* N_{s2}*. The plots show the distribution of fitted values and their pulls resulted from the same toy MC samples.*

The results on absolute differences extracted from plots are summarized in a Table C.2. For possible bias estimates we use the statistical means and RMS since the number of the statistical trials, 10000, is pretty high.

Signal parameters	Stat. Mean	Mean−Orig.	Stat. RMS
Σ_b^- pole, Q_{01}, MeV/c^2	56.31	0.02	0.62
Σ_b^- width, Γ_{01} MeV/c^2	5.61	−0.14	1.94
Σ_b^- yield, N_{s1}	355	−4	67
Σ_b^{*-} pole, Q_{02}, MeV/c^2	75.83	0.03	0.57
Σ_b^{*-} width, Γ_{02} MeV/c^2	7.05	0.05	1.86
Σ_b^{*-} yield, N_{s2}	513	4	78

Table C.2: $\Sigma_b^{(*)-}$ *fitter performance: the absolute differences of the fitted values and their originally preset (see Table C.1) values as extracted from high-statistics "toy MC" study of 10000 generated and fitted trials.*

The results on pulls extracted from plots and fits are summarized in Table C.3.

Signal parameters	Stat. Mean	Stat. RMS	Gauss. μ	Gauss. σ
Σ_b^- pole, Q_{01}, MeV/c^2	−0.06	1.05	-0.02 ± 0.01	1.02 ± 0.01
Σ_b^- width, Γ_{01} MeV/c^2	−0.31	1.06	-0.02 ± 0.02	0.98 ± 0.02
Σ_b^- yield, N_{s1}	−0.18	1.02	-0.08 ± 0.01	0.93 ± 0.01
Σ_b^{*-} pole, Q_{02}, MeV/c^2	0.02	1.04	0.04 ± 0.01	1.02 ± 0.01
Σ_b^{*-} width, Γ_{02} MeV/c^2	−0.18	1.05	0.13 ± 0.02	1.00 ± 0.03
Σ_b^{*-} yield, N_{s2}	−0.05	1.02	0.02 ± 0.01	0.98 ± 0.01

Table C.3: $\Sigma_b^{(*)-}$ *fitter performance: the pull distributions and their fits with Gaussian.*

The data in Table C.2 show the possibility of slight shift in Γ_{01} but still much smaller than the statistical fit error. The longer positive tail of the Γ_{01} fitted values distribution w.r.t. the shorter negative one (and an inverse behavior at pull distribution plots) can be explained by the expected correlation of Γ_{01} with N_{s1}. The stability of the fitter is assured by Gaussian σ or its RMS analog being always very close to unit.

Performance Plots: $\mathbf{\Sigma_b^{(*)+}}$

The distribution of all converged $-log(LH)$ is shown on the upper plot of Fig. C.4 with the experimental data value overlapped. The perfect Gaussian shape is observed with the mean value practically the same as the experimental data fit yields. The bottom 2×2 plot of the same Fig. C.4 demonstrates a fitter performance for a Σ_b^{*+} peak at Q_{01} (left column) and its width Γ_{01} (right column).

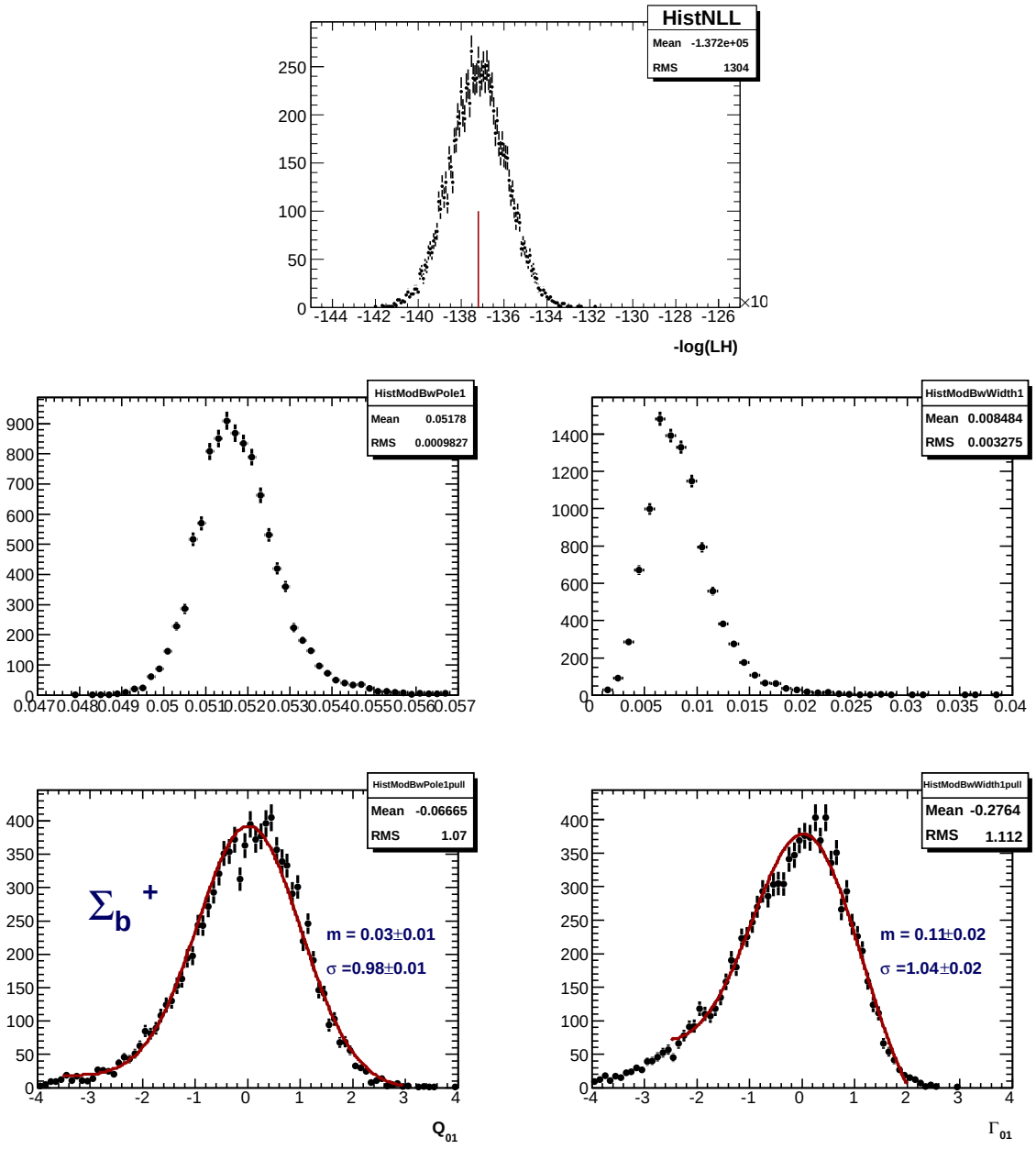

Figure C.4: *The upper plot shows the distribution of NLL resulted by unbinned LH fits of 10000 trials. Σ_b^+ statistical trials for Q_{01}, GeV/c^2 and for Γ_{01} GeV/c^2 yielded the bottom plots showing the distribution of fitted values and their pulls.*

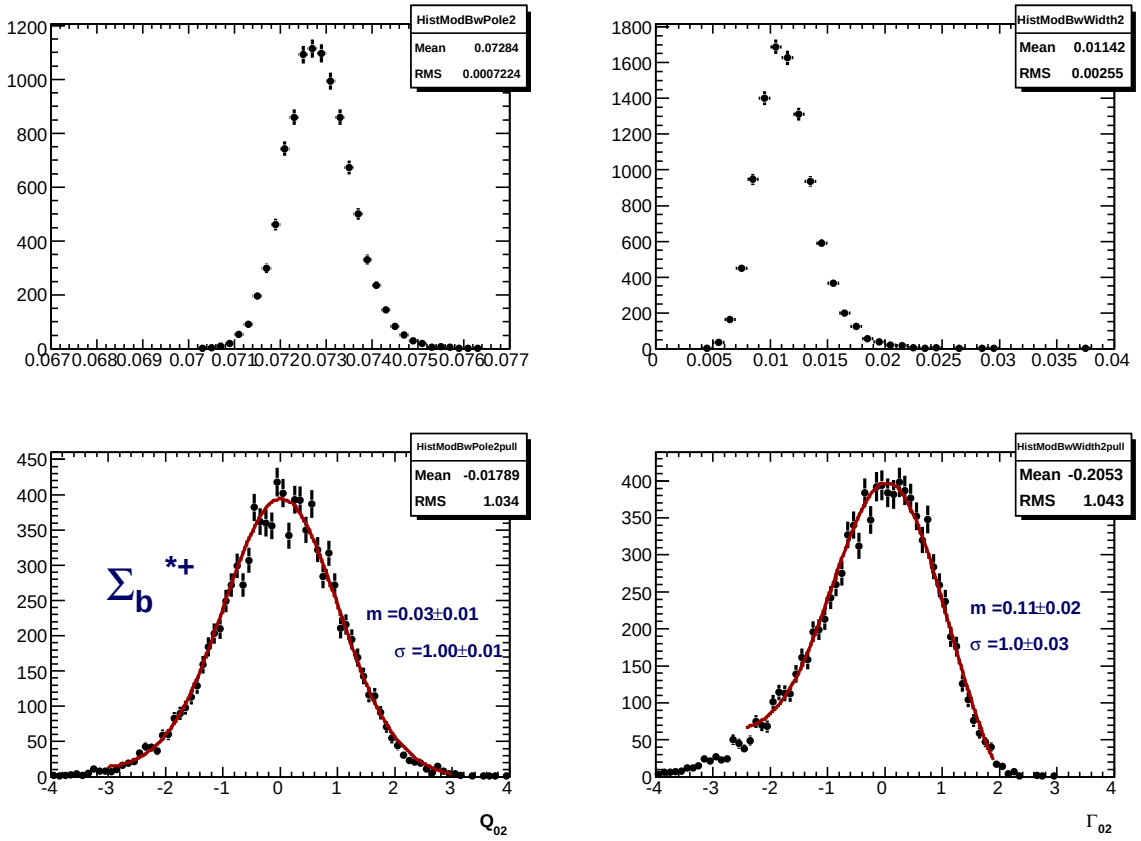

Figure C.5: Σ_b^{*+} *10000 statistical trials for* Q_{02}, GeV/c^2 *and for* Γ_{02} GeV/c^2. *The plots show the distribution of fitted values, their fit errors and their pulls resulted from the same toy MC samples.*

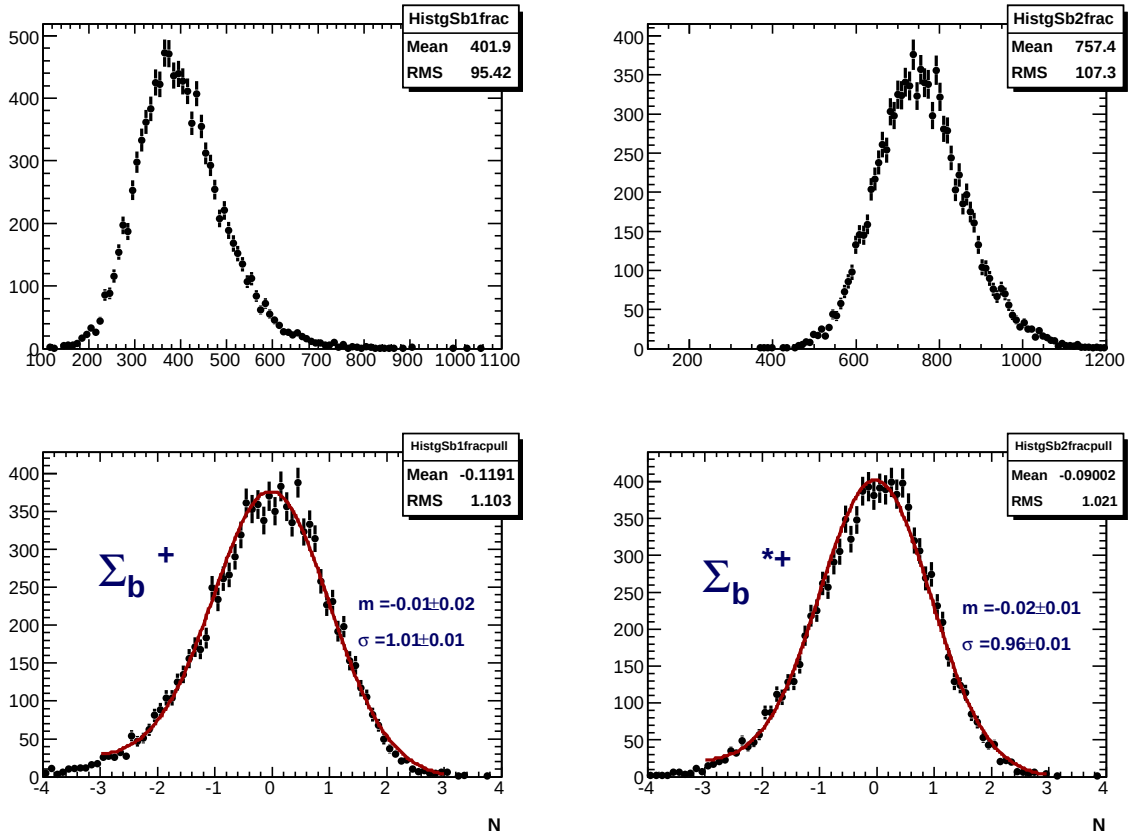

Figure C.6: $\Sigma_b^{(*)+}$ *10000 statistical trials for yields* N_{s1} *and* N_{s2}*. The plots show the distribution of fitted values, their fit errors and their pulls resulted from the same toy MC samples.*

Results for other measurables can be found in the Fig. C.5, C.6.

The results on absolute differences extracted from plots are summarized in Table C.4. For possible bias estimates we use the statistical means and RMS since the number of the statistical trials, 10000, is pretty high.

Signal parameters	Stat. Mean	Mean−Orig.	Stat. RMS
Σ_b^+ pole, Q_{01}, MeV/c^2	51.79	0.09	0.98
Σ_b^+ width, Γ_{01} MeV/c^2	8.48	−0.02	3.27
Σ_b^+ yield, N_{s1}	402	4	96
Σ_b^{*+} pole, Q_{02}, MeV/c^2	72.84	0.04	0.72
Σ_b^{*+} width, Γ_{02} MeV/c^2	11.42	−0.04	2.55
Σ_b^{*+} yield, N_{s2}	757	1	107

Table C.4: $\Sigma_b^{(*)+}$ *fitter performance: the absolute differences of the fitted values and their originally preset (see Table C.1) values as extracted from high-statistics "toy MC" study of 10000 generated and fitted trials.*

The results on pulls extracted from plots and fits are summarized in a Table C.5.

Signal parameters	Stat. Mean	Stat. RMS	Gauss. μ	Gauss. σ
Σ_b^+ pole, Q_{01}, MeV/c^2	−0.07	1.07	0.03 ± 0.01	0.98 ± 0.01
Σ_b^+ width, Γ_{01} MeV/c^2	−0.28	1.11	0.10 ± 0.02	1.04 ± 0.03
Σ_b^+ yield, N_{s1}	−0.12	1.10	-0.01 ± 0.02	1.02 ± 0.01
Σ_b^{*+} pole, Q_{02}, MeV/c^2	−0.02	1.03	0.03 ± 0.01	1.00 ± 0.01
Σ_b^{*+} width, Γ_{02} MeV/c^2	−0.21	1.04	0.11 ± 0.02	1.01 ± 0.03
Σ_b^{*+} yield, N_{s2}	−0.09	1.02	-0.02 ± 0.01	0.96 ± 0.01

Table C.5: $\Sigma_b^{(*)+}$ *fitter performance: the pull distributions and their fits with Gaussian.*

The data in Table C.4 show practically no bias in masses, widths or yields for $\Sigma_b^{(*)+}$ Q-spectra. The stability of the fitter is assured by Gaussian σ or its RMS analog being always very close to unit. The tails have a Gaussian behavior. The fitter performed stable and peaceful over a large number of 10000 trials consuming $\sim 1.7 - 2.0$ CPU minutes per trial.

C.2 Toy MC II

In this section we present the results of a further fitter stability studies when the input Q_0 values are moved down and up in the next way:

- for $\Sigma_b^{(*)-}$: $Q_{01,02} = Q_{01,02} - \sim \Gamma_{01,02}$

- for $\Sigma_b^{(*)+}$: $Q_{01,02} = Q_{01,02}+ \sim \Gamma_{01,02}$

The input values are arranged in Table C.6.

Signal parameters	$\Sigma_b^{(*)-} \to \Lambda_b^0\pi^-_{\Sigma_b}$	$\Sigma_b^{(*)+} \to \Lambda_b^0\pi^+_{\Sigma_b}$
Σ_b pole, Q_{01}, MeV/c^2	50.0	61.0
Σ_b width, Γ_{01} MeV/c^2	4.5	8.7
Σ_b yield, N_{s1}	324	443
Σ_b resolution, σ_{11} MeV/c^2	1.17	1.17
Σ_b resolution, σ_{21} MeV/c^2	2.92	2.92
Σ_b fraction of σ_{11}, g_{11}	0.70	0.70
Σ_b^* pole, Q_{02}, MeV/c^2	70.0	82.0
Σ_b^* width, Γ_{02} MeV/c^2	7.3	11.0
Σ_b^* yield, N_{s2}	530	781
Σ_b^* resolution, σ_{12} MeV/c^2	1.40	1.40
Σ_b^* resolution, σ_{22} MeV/c^2	3.80	3.80
Σ_b^* fraction of σ_{12}, g_{12}	0.73	0.73
Background, *thr*	0.140	0.140
Background, α	0.5	0.5
Background, C	4.01	4.20
Background, b_1	-3.55	-4.71
Background, b_2	3.12	2.89
Background yield, N_b	13621	12883

Table C.6: *The list and values of the fit model parameters set to generate statistical trials or "toy MC" Q- spectra for both $\Sigma_b^{(*)-}$ and $\Sigma_b^{(*)+}$ with the pole values moved down for $\Sigma_b^{(*)-}$ and up for $\Sigma_b^{(*)+}$ w.r.t. to the baseline fit.*

7000 trials and unbinned likelihood fits have been produced for both $\Sigma_b^{(*)-}$ and $\Sigma_b^{(*)+}$.

Only converged in `MIGRAD` unbinned likelihood fits with return code 0 are saved. The parabolic errors are calculated by `HESSE`.

Performance Plots: $\Sigma_b^{(*)-}$

The distribution of all converged $-log(LH)$ is shown on the upper plot of Fig. C.7 with the experimental data value overlapped. The perfect Gaussian shape is observed with the mean value practically the same as the experimental data fit yields. The bottom 2×2 plot of the same Fig. C.7 demonstrates a fitter performance for a first Σ_b^- peak Q_{01} (left column) and width Γ_{01} (right column) values. The similar plots are shown at a Fig. C.8 for the second, Σ_b^{*-} peak. The fitter response to yields with their pulls is shown at Fig. C.9.

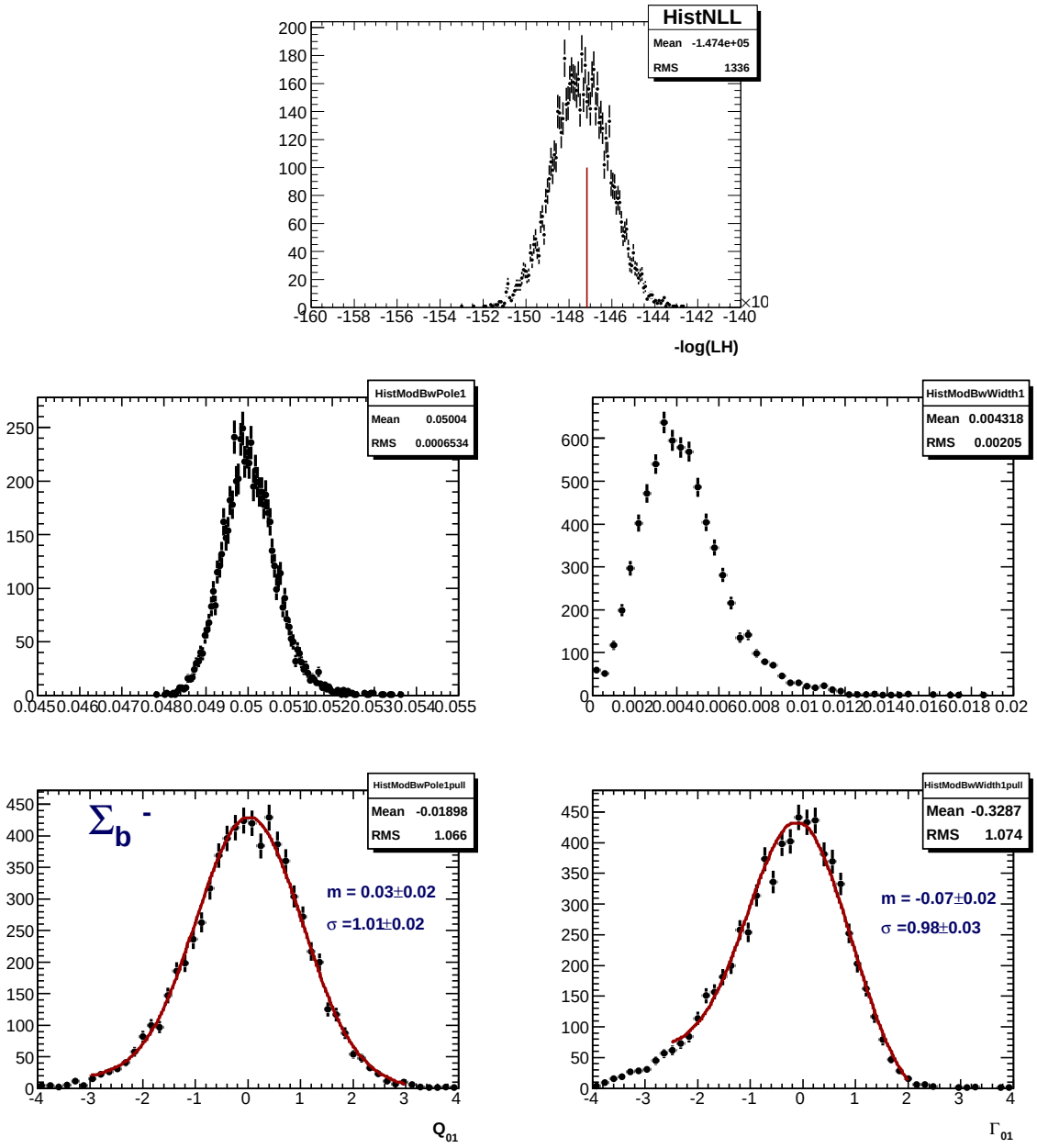

Figure C.7: *Shifted down input Q_{01} values: the upper plot shows the distribution of NLL resulted by unbinned LH fits of 7000 trials. Σ_b^- statistical trials for Q_{01}, GeV/c^2 and for Γ_{01} GeV/c^2 yielded the bottom four plots showing the distribution of fitted values and their pulls.*

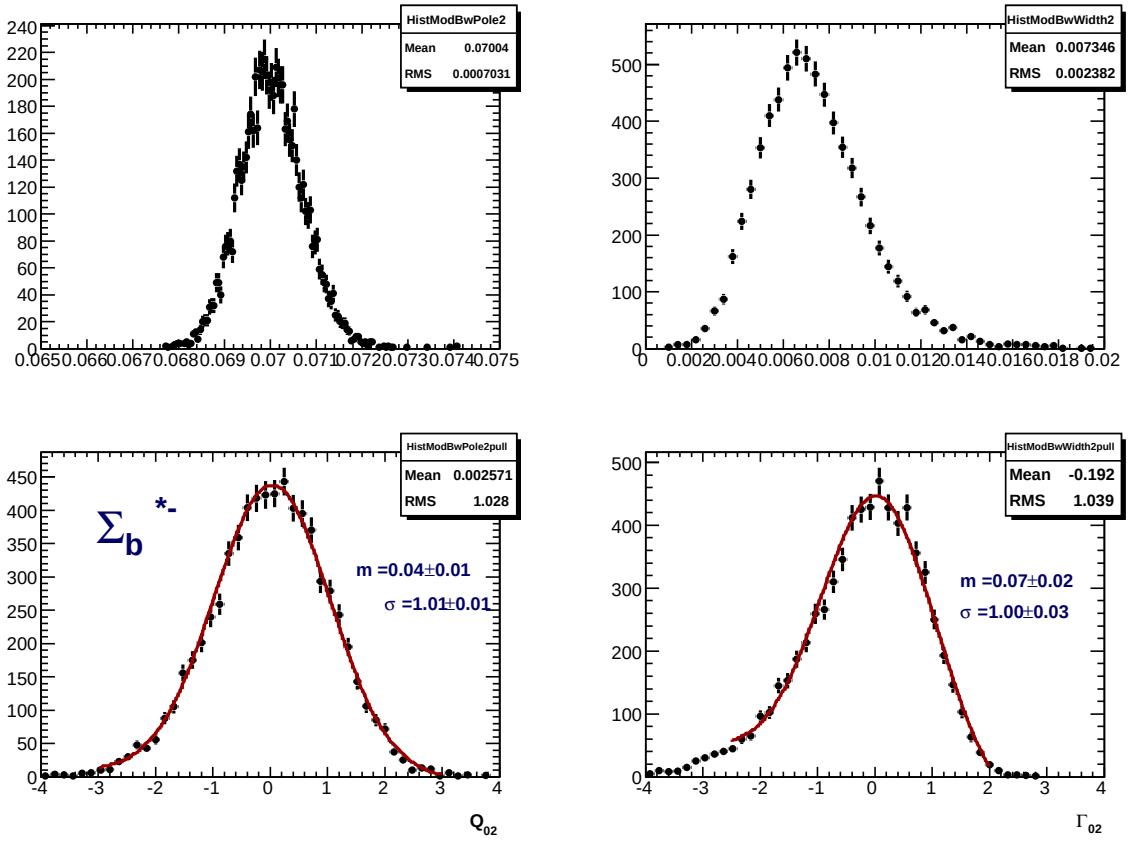

Figure C.8: *Shifted up input Q_{02} values: Σ_b^{*-} 7000 statistical trials for Q_{02}, GeV/c^2 and for Γ_{02} GeV/c^2. The plots show the distribution of fitted values and their pulls resulted from the same toy MC samples.*

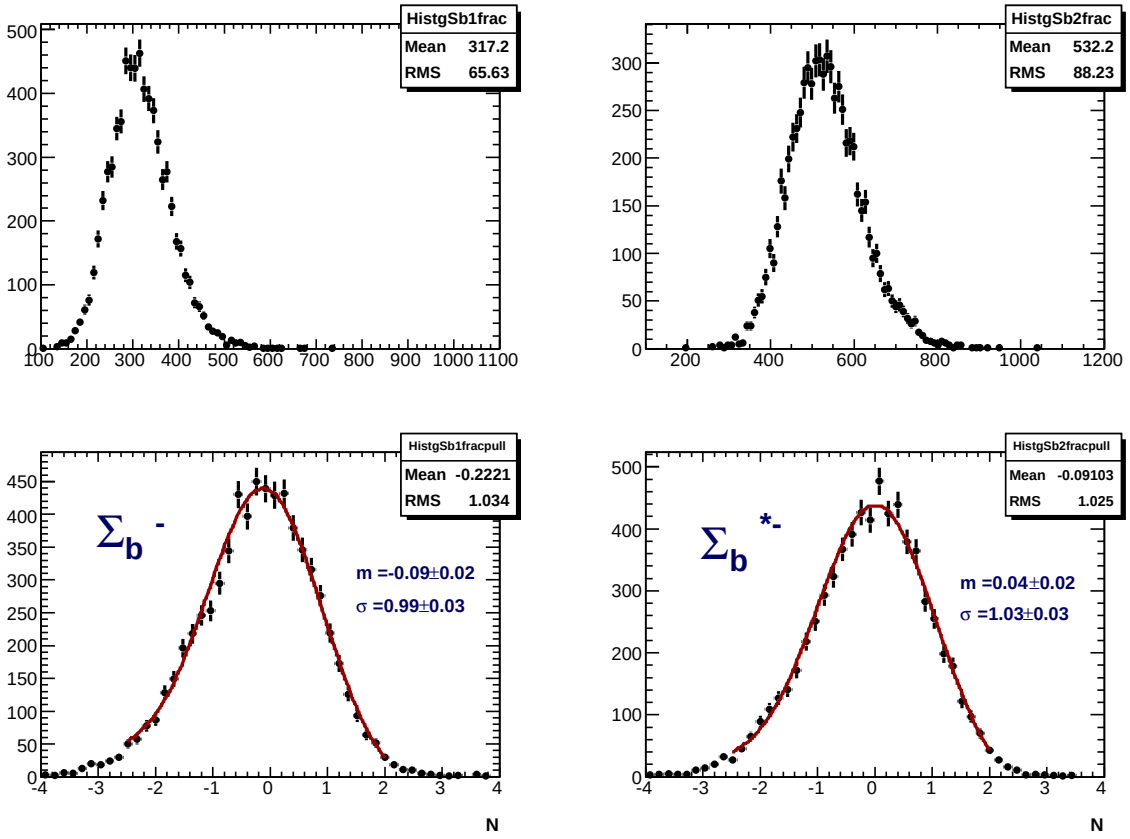

Figure C.9: *Shifted input $Q_{01,02}$ values: $\Sigma_b^{(*)-}$ 7000 statistical trials for yields N_{s1} and N_{s2}. The plots show the distribution of fitted values, and their pulls resulted from the same toy MC samples.*

The results on absolute differences extracted from plots are summarized in Table C.7. For possible bias estimates we can use the statistical means and RMS since the number of the statistical trials, 7000, is pretty high.

Signal parameters	Stat. Mean	Mean−Orig.	Stat. RMS
Σ_b^- pole, Q_{01}, MeV/c^2	50.04	0.04	0.65
Σ_b^- width, Γ_{01} MeV/c^2	4.32	−0.18	2.0
Σ_b^- yield, N_{s1}	317	−7	66
Σ_b^{*-} pole, Q_{02}, MeV/c^2	70.04	0.04	0.70
Σ_b^{*-} width, Γ_{02} MeV/c^2	7.34	0.04	2.38
Σ_b^{*-} yield, N_{s2}	532	2	88

Table C.7: *Shifted input $Q_{01,02}$ values and the corresponding $\Sigma_b^{(*)-}$ fitter response: the absolute differences of the fitted values and their originally preset (see Table C.6) values as extracted from high-statistics "toy MC" study of 7000 generated and fitted trials.*

The results on pulls extracted from plots and fits are summarized in Table C.8.

Signal parameters	Stat. Mean	Stat. RMS	Gauss. μ	Gauss. σ
Σ_b^- pole, Q_{01}, MeV/c^2	−0.02	1.07	0.03 ± 0.02	1.01 ± 0.02
Σ_b^- width, Γ_{01} MeV/c^2	−0.33	1.07	-0.07 ± 0.02	0.98 ± 0.03
Σ_b^- yield, N_{s1}	−0.22	1.03	-0.09 ± 0.02	0.99 ± 0.03
Σ_b^{*-} pole, Q_{02}, MeV/c^2	0.003	1.03	0.04 ± 0.01	1.01 ± 0.01
Σ_b^{*-} width, Γ_{02} MeV/c^2	−0.19	1.04	0.07 ± 0.02	1.00 ± 0.03
Σ_b^{*-} yield, N_{s2}	−0.09	1.03	0.04 ± 0.02	1.03 ± 0.03

Table C.8: *$\Sigma_b^{(*)-}$ fitter performance: the pull distributions and their fits with Gaussian.*

The data in Table C.7 show the possibility of slight shift in Γ_{01} but still much smaller than the statistical fit error. The longer positive tail of the Γ_{01} fitted values distribution w.r.t. the shorter negative one (and an inverse behavior at pull distribution plots) can be explained by the fact that parabolic errors are not quite right and the MINOS errors would do a better job. Another important factor is the expected positive correlation of the fitted widths with the corresponding fitted yields. Unfortunately the CPU time of fits with full MINOS is prohibitive, $10 - 15$ CPU (2.8 GHz) minutes per trial. Still the stability of the fitter is assured by Gaussian σ or its RMS analog being always very close to unit. The tails have a Gaussian behavior. The fitter performed stable and peacefully over a large number of 7000 trials consuming $\sim 1.7 - 2.0$ CPU (2.8 GHz)minutes per trial.

Performance Plots: $\Sigma_b^{(*)+}$

The distribution of all converged $-log(LH)$ is shown on the upper plot of Fig. C.10 with the experimental data value overlapped. The perfect Gaussian shape is observed with the mean value practically the same as the experimental data fit yields. The bottom 2×2 plot of the same Fig. C.10 demonstrates a fitter response for a Σ_b^+ peak at Q_{01} (left column) and its width Γ_{01} (right column). Result of this study for Σ_b^{*+} is in the C.11 and the fitter response for yields is shown at C.12.

The results on absolute differences extracted from plots are summarized in Table C.9.

Signal parameters	Stat. Mean	Mean−Orig.	Stat. RMS
Σ_b^+ pole, Q_{01}, MeV/c^2	61.07	0.07	1.03
Σ_b^+ width, Γ_{01} MeV/c^2	8.71	0.01	3.52
Σ_b^+ yield, N_{s1}	447	4	107
Σ_b^{*+} pole, Q_{02}, MeV/c^2	82.03	0.03	0.78
Σ_b^{*+} width, Γ_{02} MeV/c^2	11.05	0.05	2.96
Σ_b^{*+} yield, N_{s2}	785	4	121

Table C.9: $\Sigma_b^{(*)+}$ *fitter performance: the absolute differences of the fitted values and their originally preset (see Table C.6) values as extracted from high-statistics "toy MC" study of 7000 generated and fitted trials.*

The results on pulls extracted from plots and fits are summarized in Table C.10.

Signal parameters	Stat. Mean	Stat. RMS	Gauss. μ	Gauss. σ
Σ_b^+ pole, Q_{01}, MeV/c^2	-0.07	1.06	0.03 ± 0.01	0.98 ± 0.01
Σ_b^+ width, Γ_{01} MeV/c^2	-0.28	1.09	0.07 ± 0.02	0.95 ± 0.03
Σ_b^+ yield, N_{s1}	-0.13	1.08	0.002 ± 0.02	0.96 ± 0.01
Σ_b^{*+} pole, Q_{02}, MeV/c^2	-0.007	1.03	0.02 ± 0.02	1.01 ± 0.02
Σ_b^{*+} width, Γ_{02} MeV/c^2	-0.20	1.06	0.12 ± 0.03	1.15 ± 0.05
Σ_b^{*+} yield, N_{s2}	-0.08	1.04	0.03 ± 0.02	0.95 ± 0.02

Table C.10: $\Sigma_b^{(*)+}$ *fitter performance: the pull distributions and their fits with Gaussian.*

The data in Table C.9 show practically no bias in masses, widths or yields for $\Sigma_b^{(*)+}$ Q-spectra. The longer positive tail of the Γ_{02} fitted values distribution w.r.t. the shorter negative one (and an inverse behavior at pull distribution plots) can be explained by the naturally expected positive correlation with the yield and by parabolic errors. The stability of the fitter is assured by Gaussian σ or its RMS analog being always very close to unit. The tails have a Gaussian behavior. The fitter performed stable and peaceful over a large number of 7000 trials consuming $\sim 1.7 - 2.0$ CPU (2.8 GHz) minutes per trial.

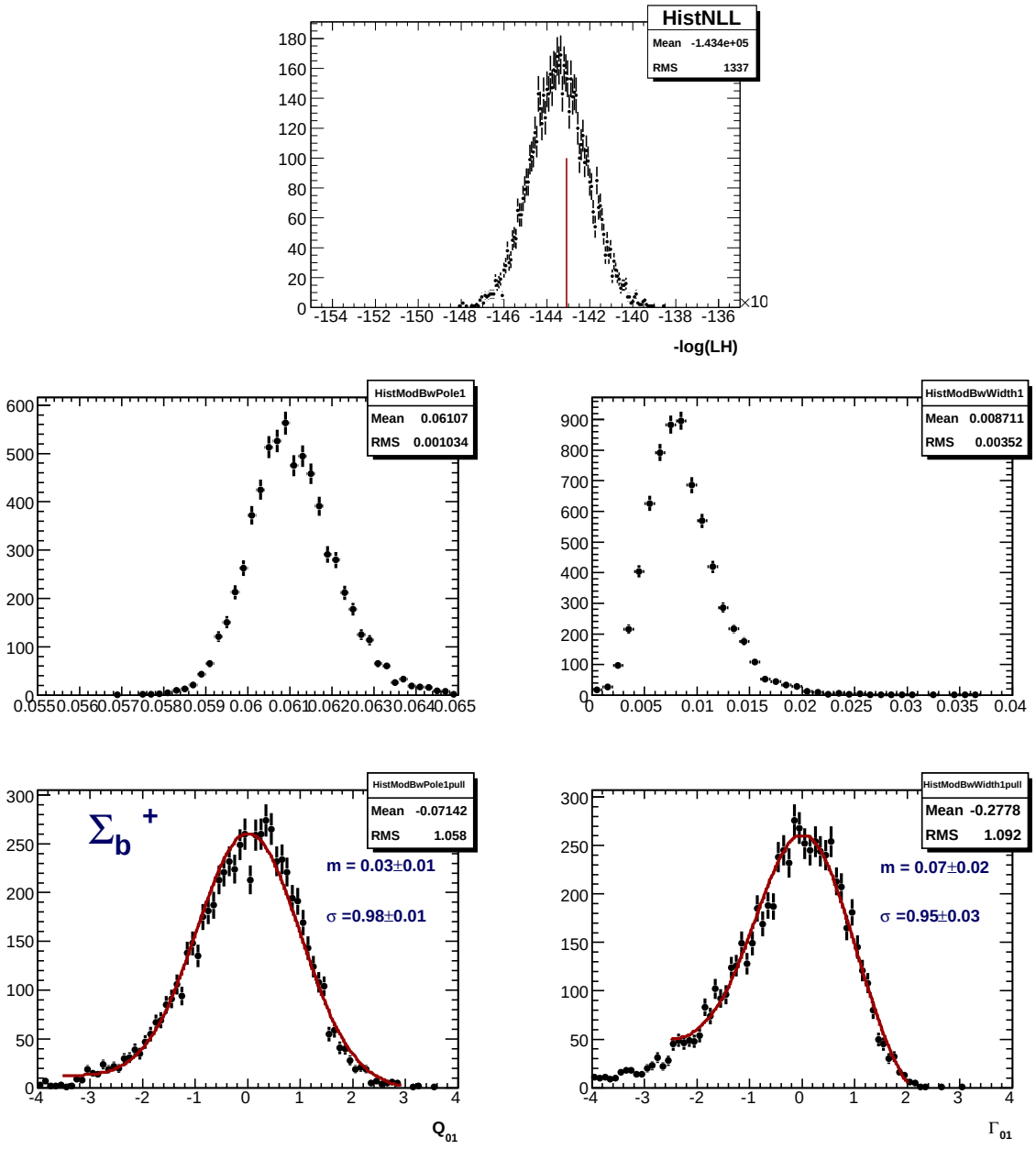

Figure C.10: *The upper plot shows the distribution of NLL resulted by unbinned LH fits of 7000 trials. Σ_b^+ statistical trials for Q_{01}, GeV/c^2 and for Γ_{01} GeV/c^2 yielded the bottom plots showing the distribution of fitted values and their pulls.*

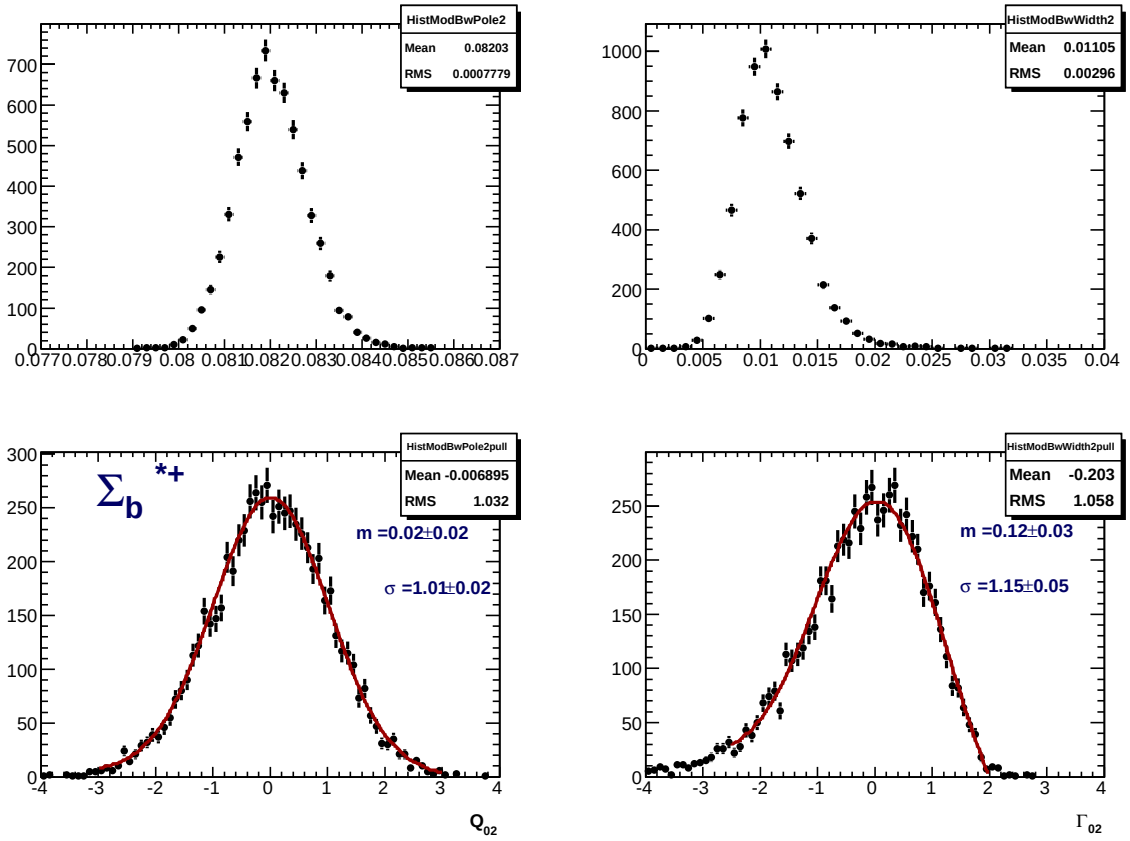

Figure C.11: Σ_b^{*+} *7000 statistical trials for* Q_{21}, GeV/c^2 *and for* Γ_{02} GeV/c^2. *The plots show the distribution of fitted values and their pulls resulted from the same toy MC samples.*

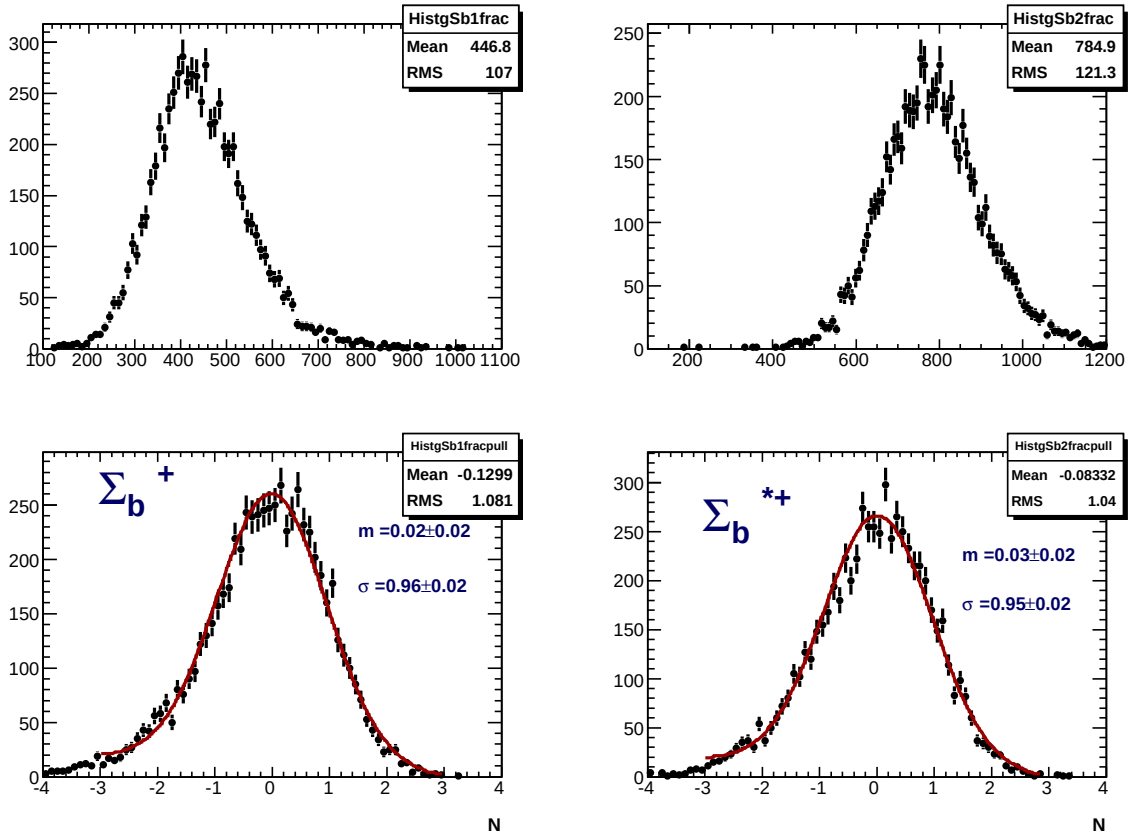

Figure C.12: $\Sigma_b^{(*)+}$ *7000 statistical trials for yields* N_{s1} *and* N_{s2}*. The plots show the distribution of fitted values, their fit errors and their pulls resulted from the same toy MC samples.*

Appendix D

Contribution to the CDF collaboration

In a large colaboration such as the CDF one, all the members have to carry on some work for the collaboration, other than physics analysis. Performing data taking shifts is one of this contributions to the collaboration. All the CDF members has to take periodically (usually one per year) these shifts.

Besides performing data taking shifts, all the people belonging to CDF have to be enrolled in a hardware group or a software group. The people enrolled in a hardware group are responsible of a subdetector, while the people collaborating within a software group perform several tasks, as monitoring of the data or maintenance and development of the CDF code.

In this appendix it is explained my contribution for the collaboration.

D.1 Work for the Silicon Group

During my stay at Fermilab I joined to the silicon group, being a member of the monitoring group, which is responsible of the monitoring of the data taken from the silicon detector.

In this appendix I explain my responsabilities as a member of the silicon group.

D.1.1 Common Tasks

The main task as a silicon member is to keep safe the silicon detector and to keep it running efficiently. Any silicon member has to cover a minimum of 8 shifts. This number of shifts is usually completed during one year. Each shift have a duration of one entire week. The people on shift (the Main Pager Carrier, MPC) must be available at any time during the full week by a pager.

Some of the duties of the MPC are:

- Attend the daily operations meeting: this is a brief ($\sim 5\,\mathrm{min}$) meeting where it is summarized the data taking of the previous day, and it is mentioned any detector

problem found. In this meeting it is also presented the plan for the current day.

- Be aware of the store setup (shot setup) schedule.

- Be aware of the schedule for any trigger tests that the trigger experts want to perform. The MPC must be present during these tests because they have the potential to damage the silicon detector.

- Draft plans for access and quite time studies: during quite time it is possible to access the detector to perform any pending reparation.

A good silicon MPC must promptly reply any call from the control room reporting incidents on the silicon detector. Tipically, there are 1-2 stores per day at Tevatron. That means that the silicon MPC receives at least two calls per day, because the MPC has to be present during the shot setup. The silicon MPC is responsible to give the confirmation to the shift crew to turn on the high voltage on the silicon detector.

Due to the proximity of the CDF silicon detector to the Tevatron beam line, it is particulary sensitive to any abnormal or unstable beam conditions. The beam incidents can generate a shower of medium energy secondary particles hitting the silicon detector.

The MPC takes the decision to turn on the high voltage based on several tools monitorizing the stability of the beam. If the silicon MPC observes unsafe conditions for the silicon, usually due to unstable beam, he must delay the inclusion of the silicon detector in the data taking.

During the store, usually well known problems happen affecting the data adquisition (DAQ), and the MPC has to take action to resume the data taking. Examples of this kind are corrupted readback from the power supplies and power supply trips. These problems have the origin in the location of the power supplies in an environment continuously exposed to radiation.

D.1.2 Silicon Monitoring

Aging effects due to long term irradiation are the primary concern for the lifetime of the detector. The main limiting factors are the inability to deplete the sensors or the decreased S/N ratio which seriously reduces the efficiency of the SVT and b-tagging. Sufficient charge collection efficiency is achieved by applying a bias voltage between the two sides of each silicon sensor. The radiation has the effect that the required voltage to fully deplete the silicon sensors increases. The Silicon Monitoring Group monitorize the S/N and the efficiency of the silicon detector and also perform periodically studies of the depletion voltage of the sensors [**?**].

As a member of the silicon monitoring group, I was responsible to monitorize the efficiency and signal-to-noise (S/N) of the silicon detector. I have also participated in the data taking for the depletion voltage studies.

Selection Criteria

The data to perform the S/N and efficiency studies are collected from events selected with a J/ψ trigger, as this trigger utilizes no silicon information, and provide a clean track sample.

We select tracks with at least one silicon hit and at least 5 hits in each of the 4 super layers of the COT. We also require a transverse momentum $p_T > 1\,\mathrm{GeV}/c$ and $|\eta| < 1$.

The signal is defined as the summed charge of a cluster of strips associated with a track in the event and it is path corrected. This is necessary since the deposited charge is proportional to the path-length. The noise, N, is estimated using special calibration runs with beam, and is defined as the noise averaged over the strips belonging to the cluster.

Signal-to-noise

Figure D.1 shows the S/N for the ϕ side of every layer of the SVX II. As expected, we observe the decrease of the S/N with the integrated luminosity due to normal detector aging. In particular we see as the layer showing the faster aging is the closest to the beam pipe (L0). These plots are useful to predict the aging effects on the silicon detector by performing extrapolations of the data histograms.

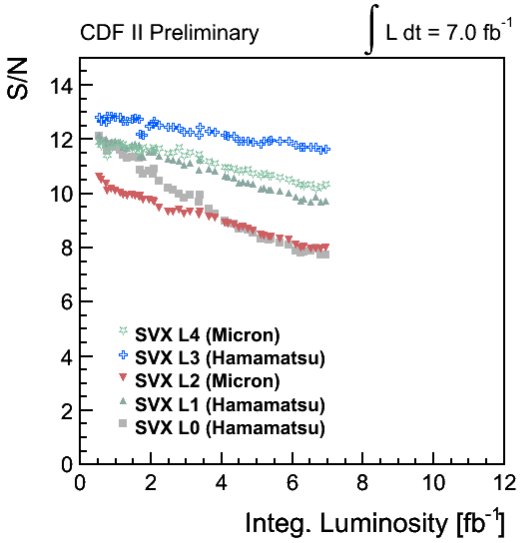

Figure D.1: Signal-to-noise of the first layer of the SVX II.

Efficiency

For each ladder of the SVX II, we define the efficiency putting in the denominator all the COT tracks intersecting that ladder which passed our selection criteria, and in the

numerator, all the previous COT tracks with at least one hit in that ladder at a distance from the track intersection with the buffer less than 50 μm. If there are more hits, we require that they be at least at 300 μm from the buffer intersection. In order to get a global efficiency for every SVX layer, we just average this efficiency over all the opperating ladders in the layer.

For the L00 the definition is the following: we take as the denominator all the COT tracks passing the selection criteria having a at least a hit in SVX L0. For the numerator we select all the previous tracks which also have a hit in L00.

Monitoring the efficiency is important because allow us to promptly detect problems on the hardware or the software reconstructing the data.

Figure D.2 shows the average efficiency over the SVX L0. In this figure is seen a net decrease of the efficiency over the last 8 years of Run II. This is expected due to the aging of the detector. The gaps in the showed histogram correspond with the shutdown periods, when several important repairs are performed.

Although the average of the efficiency is an interesting distribution, it could mask in the average a few ladders expecting problems. In practice is much better to monitorize every efficiency ladder separately. The individual monitorization of the efficiency ladders allowed us in the past to diagnose several under-depleted ladders.

When a ladder is under-depleted collects less charge and its efficiency decrease. After raising the depletion voltage, the efficiency for these under-depleted ladders is recover. Figure D.3 shows an example of a detected drop in the efficiency for one ladder due to under-depletion. As it is shown in the figure, after raising the voltage the efficiency for this ladder is recovered.

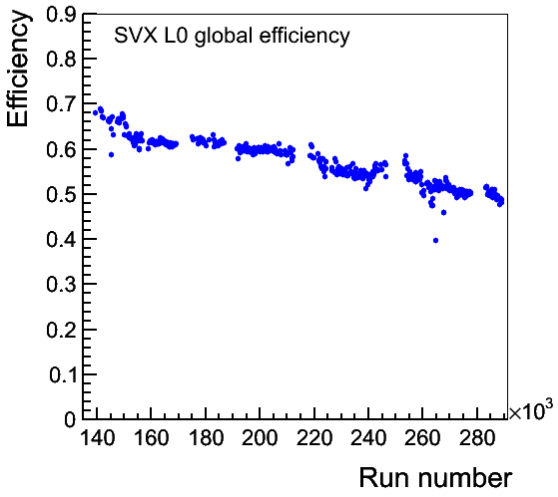

Figure D.2: Efficiency of the first layer of the SVX II.

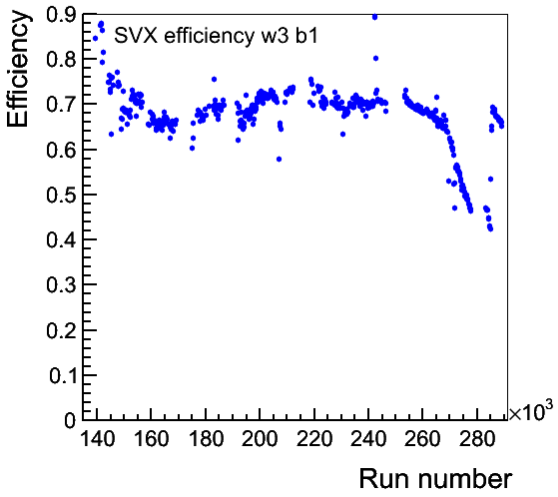

Figure D.3: *Example of efficiency drop of a SVX II ladder due to underdepletion of the voltage.*

Appendix E

Conferences and Papers

E.1 Conferences

The information included in this thesis has contributed to the following talks:

"New Results on Bottom Baryons $\Sigma_b^{(*)\pm}$ with the CDF II Detector"
XXXV International Conference on High Energy Physics (ICHEP), Paris, 22-28 July 2010.

"Latest results on quarkonia and charmoniumlike spectroscopy from Tevatron"
IX Quark Confinement and the Hadron Spectrum (QCHS), Madrid, August 30-September 3, 2010.

"Bottom Spectroscopy at CDF"
XII International Conference on Meson-Nucleon Physics and the Structure of the Nucleon (MENU), Williamsburg, Virginia, May 31-June 4, 2010.

"Study of the Σ_b Baryon with the CDF Detector",
APS April Meeting, Denver, Colorado, May 2-5, 2009.

"Measurement of Σ_b Baryons with the CDF II Detector",
APS April Meeting, Washington, DC, February 13-16, 2010.

"Observation of the heavy baryons $\Sigma_b^{\pm}$ in the decay channel $\Sigma_b^{\pm} \to \Lambda_b^0 \pi^{\pm}$, $\Lambda_b^0 \to J/\psi\, \Lambda$"
XXXII Bienal de Física, Ciudad Real, September 7-11, 2009.

E.2 Papers

The following paper is being prepared to be published in *Physical Review Letters*:

"Measurement of the Bottom Baryon Resonances Σ_b and Σ_b^*"

Appendix F

Resumen en castellano

El estado actual de nuestro conocimiento sobre la estructura y origen de la materia, se condensa en el Modelo Estándar (ME) de las partículas elementales. Dentro del marco del Modelo Estándar, existen dos tipos de constituyentes fundamentales de la materia: bosones y fermiones. los fermiones forman la materia ordinaria que nos rodea, mientras que los bosones ejercen de mediadores de las interacciones entre fermiones. Los fermiones, a su vez, se dividen en dos clases, los quarks y los leptones, formando una estructura de tres familias. Cada fermión y cada bosón tiene asociada su antipartícula.

A pesar de su notable éxito explicando las observaciones, varias dificultades teóricas apuntan a que el Modelo Estándar se trate en realidad de una teoría válida a bajas escalas de energía. De acuerdo con esta visión, el Modelo Estándar deber ser sustituido por otra teoría más completa que explique las anteriores dificultades.

Para conocer las interacciones entre las partículas es esencial realizar medidas de precisión de las propiedades de estas partículas, como la masa o la anchura de desintegración. La medida de estas propiedades permite elegir ente diversas teorías efectivas, la que mejor se ajusta a las observaciones, así como usar estas observaciones para realizar nuevas predicciones.

En particular, son de gran interes aquellos observables para los que no es posible aplicar los métodos usuales de la teoría de perturbaciones. El estudio de los bariones pesados constituye unos de estos sistemas no perturbativos. Los bariones pesados con dos bariones ligeros, forman una estructura análoga al familiar átomo de helio, con la interacción fuerte haciendo el papel del Electromagnetismo para mantener el sistema ligado. Dentro de esta analogía, el quark pesado Q constituiría el análogo del núcleo, mientras que los dos quarks ligeros serítil an el equivalente de los dos electrones orbitantes. Estos sistemas se describen por medio de teorías conteniendo la simetría del quark pesado (HQS, de sus siglas en inglés). Estas teoríse conocen conjuntamente como teorías efectivas de quark pesado (HQET, de sus siglas en inglés).

En esta tesis se describe la medida de las masas y anchuras de los hadrones $\Sigma_b^{(*)\pm}$. Estos estados estan compuestos de dos quarks ligeros y un quark pesado b formando dos tripletes de isospin:

- (Σ_b^+, Σ_b^-), $J^P = (1/2)^+$

- $(\Sigma_b^{*+},\Sigma_b^{*-})$, $J^P = (3/2)^+$

siendo los miembros del segundo isotriplete estados excitados de los miembros del primero.

Los bariones $\Sigma_b^{(*)\pm}$ fueron descubiertos por CDF en el año 2007. En dicho anĺisis, debido a la limitación en estadística, se midieron conjuntamente los estados de carga eléctrica opuesta dentro de un mismo triplete, imponiendo la condición $\Sigma_b^{*+} - \Sigma_b^{*-} = \Sigma_b^{+} - \Sigma_b^{-}$. Debido a esto no fue posible determinar la separación isotópica de masas entyre los compañeros dentro de un triplete. Además, las señales de los cuatro estados se observaron con una significancia total por encima de 5 σ, tradicionalmente el umbral que limita una observación, pero la significancia de cada uno de los estados por separado estaba alrededor de las 3 σ.

El análisis presentado en esta tesis constituye la primera confirmación del descubrimiento de estos nuevos hadrones pesados, así como la primera medida de las anchuras de desintegración de estos estados. La medi¡da de las masas se realiza independiente para cada compañero dentro de un isotriplete, lo que permite realizar la primera medida de las diferencias isotópicas de masa entre estados.

F.1 Dispositivo experimental

El acelerador Tevatron, situado en el laboratorio nacional Fermi (Fermilab) en Batavia (Illinois, EEUU), es un colisionador protón-antiproton con una energía en el centro de masas de 1.96 TeV. Durante muchos años, este acelerador fue el de mayor energía operando en el mundo. Estas instalaciones tienen cinco aceleradores y anillos de almacenamiento (*Cockcroft-Walton, Linac, Booster, Main Injector* and *Tevatron*) usados en etapas sucesivas para acelerar las partículas hasta 980 GeV.

El ciclo de aceleración empieza con la producción a partir de hidrógeno ionizado, que se aceleran hasta 750 keV por un Cockroft-Walton. Estos iones preacelerados se inyectan en el Linac donde se aceleran hasta 400 MeV. Al final de este proceso, los iones pasan a través de una hoja de carbono para arrancar sus electrones y producir protones. Dentro del Booster, los protones se agrupan en paquetes y se aceleran hasta una energía de 8 GeV. En el Main Injector, estos protones se aceleran hasta 150 GeV y se inyectan en el paso final dentro del Tevatron.

La producción de antiprotones es significativamente más complicada. El ciclo empieza con la extracción de protones a 120 GeV del Main Injector y su posterior colisión contra un blanco de acero inoxidable. Este proceso produce una amplia variedad de partículas entre als que se encuentran los antiprotones. Las partículas emergen del blanco con diferentes ángulos y son focalizadas hacia la línea de aceleración. Con el objeto de seleccionar solo antiprotones, el haz de partículas se envía a través de un imán pulsado que actúa como espectrómetro. Los antiprotones asi producidos son inyectados en el *Debuncher*, un acelerador que aumenta su energía hasta 8 GeV. Después de este proceso, el haz de antiprotones se dirige al *Accumulator*, un anillo de almacenamiento. Desde ahí, los antiprotones son finalmente inyectados en el Main Injector y acelerados hasta 150 GeV, desde donde se transfieren al Tevatron de la misma manera que se hace con los protones.

El detector CDF II se encuentra en operación desde 2001. Es un detector multipropósito que combina varios subdetectores dispuestos de forma cilíndrica y concéntrica respecto al eje del haz de partícula. Este dectector está formado por:

- Un sistema de identificación de trazas que proporciona la medida del momento de las partículas cargadas, la posición del vértice primario de la interacción en el eje z, y permite, a su vez, reconstruir vértices secundarios.
- Un calorímetro cuyo propósito es medir la energía de las partículas cargadas producidas en la interacción.
- Cámaras de deriva y centelleadores para la detección de muones.

A continuación se detallan cada uno de los subdetectores empezando por los más cercanos a la tubería del haz y siguiendo hacia el exterior en dirección radial.

Los sistemas de identificación de trazas se encuentran dentro de un solenoide superconductor de 1.5 m de radio y 4.8 m de longitud que genera un campo magnético de 1.4 T paralelo al eje del haz de patículas. la parte más interna del sistema de identificación de trazas es un detector de microtirasd de silicio resistente a la radiación. Se extiende desde un radio de 1.2 cm hasta 28 cm, cubriendo las regiones centrales del detector.

La capa más interna de silicio se conoce como L00 y está formada por microtiras activas solo por uno de sus lados. Las siguientes cinco capas de silicio despueués del L00, constituyen el SVXII. Finalmente, las dos capas maás externas forman el ISL. Las siete capas que forman el SVXII y el ISL contienen material sensible por los dos lados y proporcionan información de la posición de las partículas con una precisisón de 9 micras en el mejor de los casos.

Rodeando el detector de silicio se encuentra la *Central Outer Tracker* (COT), la pieza fundamental del sistema de detección de trazas de CDF II. La COT es una cámara de deriva cilídrica de 3.1 m de longitud, que cubre en la zona radial una región desde los 40 a los 137 cm. Esta formada por 96 capas de hilos sensibles que están agurpados de forma radial en 8 supercapas. El número total de hilos sensibles de la COT es 30240. Aproximadamente la mitad de estos hilos van en la dirección z y la otra mitad están inclinados un pequeño ńgulo (2 grados) con respecto a la dirección z. La combinación de estos dos tipos de hilos permite la medida de posiciones en z.

El sistema de calorímetros de CDF II se encuentra rodeando el sistema de detección de trazas en la parte exterior del solenoide. Los distintos calorímetros que componen el sistema son detectores basados en centelleadores segmentados en torres proyectivas que apuntan a la región de interacción.

El calorímetro está dividido en dos regiones: la región central y el *plug*. Cada una de estas regiones está dividida en parte electromagnética y hadrónica. La parte electromagnética proporciona información para reconstruir objectos como electrones o fotones, mientras que la parte hadrónica se usa para la reconstrucción de jets.

Por último, en la parte más externa de CDF II se encuentran las cámaras de muones. El sistema de deteccioón de muones consiste en un conjunto de cámaras de deriva y centelleadores que están instalados en la parte exterior del calorímetro.

Como complemento a los sistemas de detección, CDF II cuenta con un complejo sistema de adquisición de datos. La tasa media de interacciones en el Tevatron es de 2.53 Mhz. Esta tasa de interacción es órdenes de magnitud superior a la mx́ima tasa que el sistema de adquisición de datos puede soportar. Además, la mayoría de las colisiones producidas son de un intereés nulo para el análisis de datos. Debido a esto, CDF cuenta con un sistema automático de selección de sucesos a tiempo real, *trigger*. El trigger decide si el correspondiente suceso medido por el detector va a ser almacenado en cinta para su posterior anaálisis o descartado definitivamente.

El sistema de trigger de CDF consiste en tres niveles de decisión. Los dos primeros niveles están basados en hardware y el tercero consiste en una granja de procesadores. Las decisiones tomadas por el sistema están basadas en información de los sucesos con complejidad creciente. El nivel 1 del trigger es un sistema síncrono que lee suscesos y toma decisiones cada vez que se produce un cruce de protones y antiprotones. El nivel 1 del trigger reduce la tasa de sucesos de 2.53 Mhz a menos de 50 kHz. El hardware de este nivel 1 consiste en tres líneas paralelas de procesado que alimentan a la unidad global de decisión de nivel 1. Una de las lías se encarga de encontrar objectos basados en medidad del calorímetro, L1 CAL, ota encuentra muones, L1 MUON, mientras que la tercera encuentra trazas en la COT, L1 TRACK. Puesto que los muones y electrones necesitan la presencia de una traza apuntando al correspondiente detector, la información de estas trazas se envía a las líneas de calorímetro, muones y trazas.

Finalmente, la unidad global de decisión de nivel 1 toma una decisión basada en los objetos de interés encontrados por diferentes procesos del nivel 1.

Como segundo paso en sistema de decisión tenemos el nivel 2 del trigger que es un sistema astíl ncrono que procesa sucesos recibidos desde el nivel 1. Después del nivel 2, la tasa de sucesos se reduce a 1 kHz.

Una vez que el suceso es aceptado a nivel 2, tiene que ser procesado completamente con toda la información disponible en el detector. Esta operación tiene lugar en la granja de procesadores a nivel 3. El nivel 3 reconstruye el suceso utilizando algoritmos que usan toda la información disponible en el detector y mejoran la resolución utilizada en los niveles anteriores.

Esto incluye una reconstrucción tridimensional de las trazas, el emparejamiento entre trazas y calorímetro o sistema de muones. Los sucesos que pasan satisfactoriamente loe requisitos del nivel 3 son trasnferidos al sistema de almacenado en cinta magnética. La tsa media de procesado a nivel 3 por suceso es de unos pocos segundos. La tasa de sucesos cumpliendo los requisitos de nivel 3 se reduce a 50 Hz.

F.1.1 The Two-Track Trigger

La vida media de los hadrones pesados que se desintegran por medio de la interacción débil es larga comparada con la de los hadrones más ligeros [17]. Este hecho implica que el vértice de desintegración de estos hadrones pesados estará desplazado una cantidad apreciable del vértice primario de interacción. Por tanto, las trazas dejadas en el detector por partículas cargadas provenientes de la desintegración de estos hadrones pesados,

se caracterizan por tener parámetros de impacto inconsistentes con cero. La precisa información proveniente del detector de silicio y la electrónica del SVT, proporcionan al trigger una resolución en el parámetro de impacto de las trazas de alta energía de unos 35 μm. Esta singular característica, la primera de su clase en colisionadores hadrónicos, y única en Tevatron, permite usar la presencia de trazas desplazadas del vértice primario en el trigger. Seleccionando con el trigger eventos con trazas desplazadas crea muestras de datos enriquecidas en desintegraciones de hadrones conteniendo quarks b y c. Este trigger recibe el nombre de *two-track trigger* (TTT).

F.2 Reconstrucción

Para realizar un análisis de datos, la información obtenida del detector tiene que ser procesada con el objecto de reconstruir observables. Esta reconstrucción implica algoritmos matemáticos y definiciones muy alejadas de la información que obtenemos del detector.

La reconstrucción final de cada modo de desintegración se realiza una vez que los datos han sido escritos en cinta magnética. La reconstrucción requiere un preciso conocimiento del detector.

A continuación se discute la reconstrucción del canal estudiado en esta tesis, aunque todos los conceptos desarrollados se aplican igualmente a la reconstruccción de otros canales de desintegración.

F.2.1 Reconstrucción de trazas

Las trayectorias de partículas cargadas se reconstruyen (en primera aproximación) usando la información contenida en la COT. Estas trayectorias se extrapolan al detector de silicio y se reajustan incorporando la información de este detector.

De especial relevancia es la recontrucción del vértice primario de interacción. El vértice no es un objecto de análisis como tal, sin embargo, es la referencia inicial para la reconstrucción de cualquier otro objecto final. El vértice primario de un evento particular se localiza ajustando trayectorias de partículas cargadas medidas con precisión a un punto de origen común. El vértice primario se determina para cada evento.

Las trayectorias obtenidas de la información del detector deben ser recalculadas de forma que se consideren dos efectos inducidos por el detector mismo:

- la dispersión multiple de Coulomb dentro del volumen de la COT
- la distribución de material del detector

El primero de los efectos es una descripción estadística del ángulo de dispersión de una partícula como resultado de las interacciones con los electrones atómicos. Este efecto es mayor para partículas con baja energía. si este efecto no es tenido en cuenta, se obtiene una minusvaloración en los errores de los parámetros que describen la trayectoria.

El segundo efecto a tener en cuenta es la energía perdida por las partículas al interaccionar con los materiales del detector. Al perder energía, el momento lineal de la partícula decrece, y por tanto la curvatura de la trayectoria va cambiando a lo largo del recorrido de la partícula.

F.2.2 Reconstrucción de la desintegración de $\Sigma_b^{(*)}$

Una vez que se tienen colecciones de trazas para cada evento, estas trazas se combinan para formar varios niveles de partículas *padre*. Para ello se utiliza la herramienta *CTVMFT*, un paquete de software desarrollado para ajustar trazas a vértices [55]. La reconstrucción se realiza *de atrás adelante*, es decir, a partir de las trazas del estado final se va recomponiendo la desintegración hasta llegar al estado inicial. Para el caso particular de esta tesis, el canal de desintegración estudiado es: $\Sigma_b^{(*)\pm} \to \Lambda_b^0\pi^\pm$, $\Lambda_b^0 \to \Lambda_c^+\pi^-$, $\Lambda_c^+ \to PK^-\pi^-$

La recontrucción empieza reconstruyendo el vértice de desintegración del Λ_c^+, esto es, la desintegración $\Lambda_c^+ \to PK^-\pi^-$. Esto se hace por medio de un ajuste de tres trazas, que se asume que son un proton, un kaon y un pion, a un vértice común. A continuación se reconstruye el vértice del Λ_b^0 haciendo un ajuste de una traza e imponiendo la condición de que la masa del candidato Λ_c^+ sea igual a su masa en el PDG [17]. Por último, el candidato Λ_b^0 se combina con una traza de bajo momento transversal por medio de un ajuste.

F.3 Medida de $\Sigma_b^{(*)\pm}$

El presente análisis realiza una medida de las masas y las anchuras de desintegración de los cuatro estados $\Sigma_b^{(*)\pm}$. El análisis se realiza en la variable Q, es decir, la energía liberada en el proceso, $Q = m(\Lambda_b^0\pi^\pm) - m(\Lambda_b^0) - m(\pi^\pm)$, porque al analizar esta diferencia de masas, la mayoria de los efectos sistemáticos relacionados con la resolución en masa del Λ_b^0 se cancelan.

EL fondo de la distribución en la variable Q se espera que muestre una forma típica de $\sqrt{Q - thr}$.

F.3.1 Optimizacióm

Del análisis anterior [68] sabemos que las combinaciones aleatorias de candidatos Λ_b^0 con trazas de bajo momento transversal, constituyen el fondo dominante bajo las $\Sigma_b^{(*)\pm} \to \Lambda_b^0\pi^\pm$ señales [3]. La elección de los cortes finales del análisis se hizo en base a la optimización de la señal de Λ_b^0 observada. La señal se maximizó con respecto al fondo de acuerdo con la figura de mérito $S/\sqrt{S+B}$ donde S y B son respectivamente la señal y el fondo obtenidos en un ajuste de la distribución de masa invariante del Λ_b^0. La señal S se determina como el número de entradas obtenidas del ajuste a la distribución dentro de un intervalo de $\pm 3 \cdot \sigma$ respecto al valor central del pico de la distribución. El fondo B

se determina como el número de entradas obtenidas del ajuste para el fondo dentro del mismo intervalo de $\pm 3 \cdot \sigma$ centrado en el pico.

Los cortes sometidos al proceso de optimización son los siguientes:

- $c\tau(\Lambda_b^0)/\sigma_{c\tau}$
- $c\tau(\Lambda_b^0)$
- $c\tau(\Lambda_c^+ \leftarrow \Lambda_b^0)$
- $|d_0|(\Lambda_b^0)$
- $p_T(\pi_b^-)$

El proceso de optimización se llevó a cabo simultáneamente para todos los cortes. Figura F.1 muestra el proceso de optimización, mientras que la Tabla F.1 resume los valores obtenidos para los cortes.

Variable	Cut value
$c\tau(\Lambda_b^0)$	$> 200\,\mu$m
$c\tau(\Lambda_b^0)/\sigma_{c\tau}$	> 12.0
$\lvert d_0(\Lambda_b^0)\rvert$	$< 80\,\mu$m
$c\tau(\Lambda_c^+ \leftarrow \Lambda_b^0)$	$> -150\,\mu$m
$c\tau(\Lambda_c^+ \leftarrow \Lambda_b^0)$	$< 250\,\mu$m
$p_T(\pi_b^-)$	$> 1.5\,\mathrm{GeV}/c$

Table F.1: *Valores para los cortes obtenidos como resultado de la optimización.*

F.3.2 Descripción del modelo

El modelo usado para ajustar el espectro experimental de los estados $\Sigma_b^{(*)\pm}$ se compone de dos partes: una parte describiendo la señal y otra el fondo.

La señal se describe por medio de distribuciones de Breit-Wigner convolucionadas con dos distribuciones de Gauss describiendo la resolución del detector, como se muestra en Eq. F.1.

$$\mathcal{S}(Q; Q_0, \Gamma, \sigma_1, g_1, \sigma_2) = \mathcal{BW}(Q; Q_0, \Gamma) \otimes (g_1 \cdot \mathcal{G}(q; 0, \sigma_1) + (1 - g_1) \cdot \mathcal{G}(q; 0, \sigma_2)) \quad \text{(F.1)}$$

donde la distribución de Breit-Wigner (Eq. F.2) y la distribución de Gauss (Eq. F.3) son bien conocidas

$$\mathcal{BW}(Q; Q_0, \Gamma) = \frac{\Gamma/2\pi}{(Q - Q_0)^2 - (\Gamma/2)^2}, \quad \text{(F.2)}$$

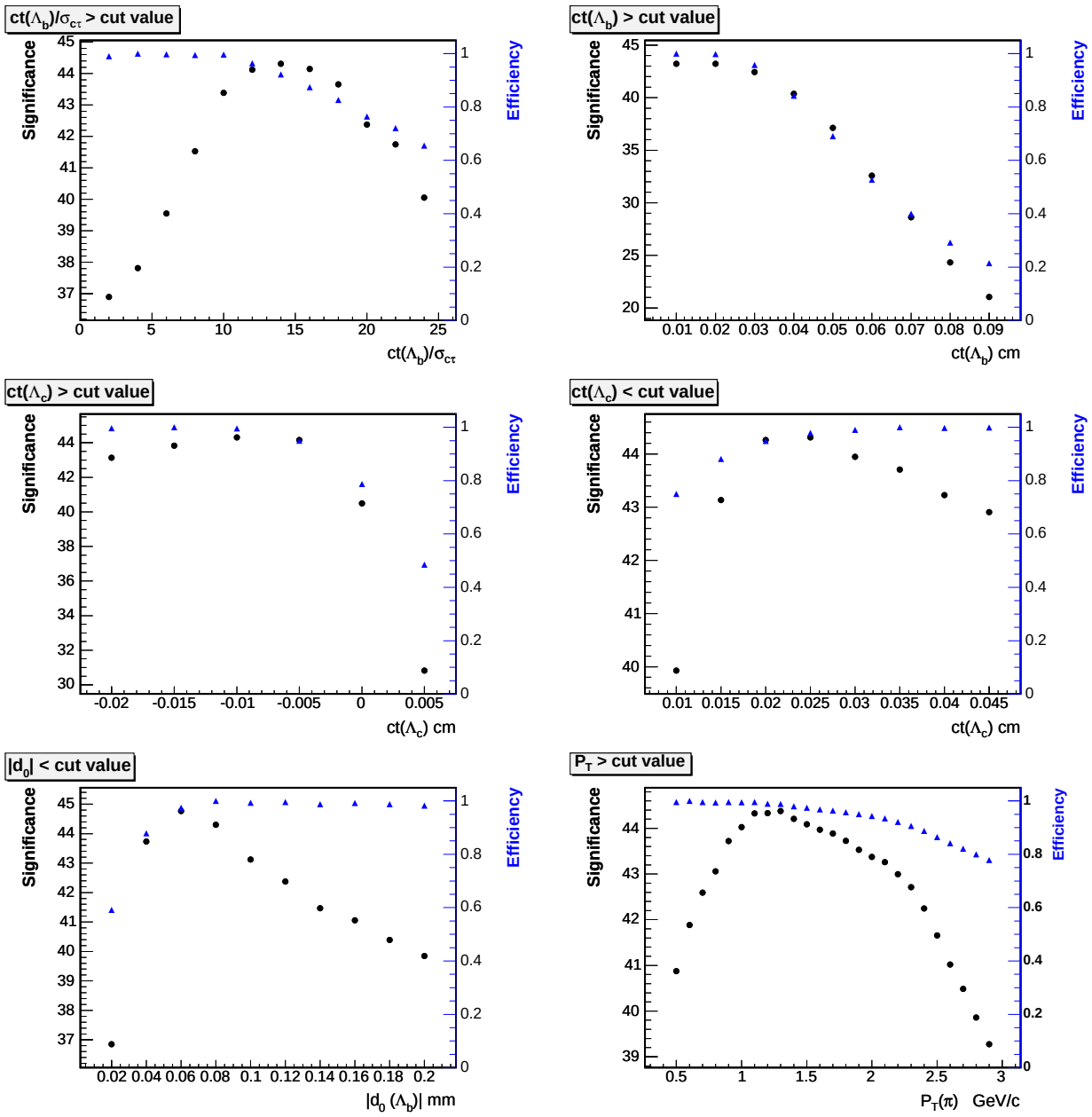

Figure F.1: *Proceso de optimización de las variables $c\tau(\Lambda_b^0)/\sigma_{C\tau}$, $c\tau(\Lambda_b^0)$ (primera fila), $c\tau(\Lambda_c^+ \leftarrow \Lambda_b^0)$ (segunda fila), $|d_0|(\Lambda_b^0)$ y $p_T(\pi_b^-)$ (tercera fila). Los círculos negros (escala de la izquierda) corresponden a la F.O.M. como función del corte en una variable en cuestión. Los triángulos azules (escala de la derecha) muestran la eficiencia de la señal obtenida de un ajuste binado. La elección de los cortes se muestra en la Tabla F.1.*

$$\mathcal{G}(q;0,\sigma) = \frac{1}{\sigma\sqrt{2\pi}} \cdot \exp\left(-\frac{q^2}{2\sigma^2}\right) \tag{F.3}$$

Las distribuciones de Breit-Wigner incorporan una correción de momento angular debida a que el pion emitido en la desintegración $\Sigma_b^{(*)\pm} \to \Lambda_b^0\pi^\pm$ se emite en una onda P. Esta correción incorpora al parmetro describiendo la anchura de la desintegración, esto es, Γ el factor $(\frac{p_\pi^*}{p_\pi^{*0}})^{2\cdot L+1}$, donde p_π^* , p_π^{*0} es el momento lineal del pion emitido en el sistema de referencia centro de masa del $\Sigma_b^{(*)}$, refiriendose el segundo a la misma cantidad evaluada en el polo de la resonancia. El exponente es $2 \cdot L + 1 = 3$, ya que el pion se emite en una onda P.

F.4 Errores sistemáticos

Se consideraron las tres siguientes fuentes de incertidumbres sistemáticas afectando a nuestras medidas:

- Incertidumbre introducida por el ajuste.
- Efecto introducido por la incertidumbre en la escala de momentos.
- Efecto de las asunciones hechas en el modelo que ajusta los datos.

F.4.1 Incertidumbre introducida por el ajuste

Antes de ajustar la distribución Q de los $\Sigma_b^{(*)\pm}$ se realizaron varios pruebas para detectar cualquier posible sesgo introducido por el método de ajuste. Estas pruebas consisten en la generación de múltiples pseudoexperimentos distribuidos según los espectros experimentales. Estos pesudoexperimentos se ajustan con el mismo procedimiento que se usa con los datos. Usando los valores iniciales de los parámetros del modelo y los valores devueltos por el método de ajuste, se construye la distribución de las diferencias entre los parámetros de entrada, y los parámtros medidos, asi como la distribución de estas diferencias divididas por el error (*pulls*) del parámetro devuelto por el método.

Para todas las variables, la distribución de las diferencias entre los valores de entrada y los de salida presentan aspecto gaussiano centrado en cero, poniendo de manifiesto que el método no introduce sesgos en las medidas.

Los pulls también presentan aspecto gaussiano centrado en 0 con $\sigma \approx 1.0$, salvo en el caso de los parámetros midiendo las anchuras, en los que se observa una cola positiva en la distribución que ocasiona que los pulls estén centrados en un valor ligeramente por encima de 0. Esto se traslada en que el valor medido para este parámetro estará ligeramente por encima de su valor nominal, de modo que asignamos un error sistemático que tenga en cuenta este efecto. Siendo conservadores, tomamos el mayor de los sesgos hayados (-0.13 para el caso de $\Gamma(\Sigma_b^{*+})$) y asignamos a las cuatro anchuras el mismo error sistemático:

$$-0.13 \cdot \sigma_{stat}$$

donde σ_{stat} denota el error estadístico devuelto por el método para ese parámetro.

Figuras F.2–F.4 muestran los resultados de los tests para $\Sigma_b^{(*)-}$, mientras que las Figuras F.5–F.7 muestran los resultados para $\Sigma_b^{(*)+}$.

Tablas F.2 y F.3 resumen los resultados de estos tests.

Signal parameters	Stat. Mean	Stat. RMS	Gauss. μ	Gauss. σ
Σ_b^+ pole, Q_{01}, MeV/c^2	-0.11	1.08	-0.02 ± 0.02	1.02 ± 0.01
Σ_b^+ width, Γ_{01} MeV/c^2	-0.28	1.11	0.08 ± 0.02	1.07 ± 0.03
Σ_b^+ yield, N_{s1}	-0.12	1.10	0.06 ± 0.03	1.08 ± 0.04
Σ_b^{*+} pole, Q_{02}, MeV/c^2	0.01	1.03	0.04 ± 0.02	1.00 ± 0.03
Σ_b^{*+} width, Γ_{02} MeV/c^2	-0.16	1.03	0.13 ± 0.02	1.07 ± 0.03
Σ_b^{*+} yield, N_{s2}	-0.08	1.03	0.09 ± 0.03	1.04 ± 0.04

Table F.2: *Resultados de los tests al método de ajuste para $\Sigma_b^{(*)+}$: distribuciones de pull y sus ajustes gaussianos.*

Signal parameters	Stat. Mean	Stat. RMS	Gauss. μ	Gauss. σ
Σ_b^- pole, Q_{01}, MeV/c^2	-0.05	1.07	0.05 ± 0.02	0.99 ± 0.02
Σ_b^- width, Γ_{01} MeV/c^2	-0.27	1.07	0.02 ± 0.02	1.02 ± 0.03
Σ_b^- yield, N_{s1}	-0.14	1.06	0.04 ± 0.02	1.01 ± 0.03
Σ_b^{*-} pole, Q_{02}, MeV/c^2	0.02	1.04	0.05 ± 0.02	1.00 ± 0.02
Σ_b^{*-} width, Γ_{02} MeV/c^2	-0.21	1.06	0.07 ± 0.02	1.02 ± 0.03
Σ_b^{*-} yield, N_{s2}	-0.09	1.04	0.06 ± 0.02	1.01 ± 0.03

Table F.3: *Resultados de los tests al método de ajuste para $\Sigma_b^{(*)-}$: distribuciones de pull y sus ajustes gaussianos.*

F.4.2 Incertidumbre en la escala de momentos

El efecto de la incertidumbre en la escala de momentos sobre los valores Q de los estados $\Sigma_b^{(*)\pm}$ lo estimamos comparando los valores Q medidos por CDF y los listados en el PDG [17] para varias desintegraciones liberando similares energías. Concretamente se analizaron las desintegraciones siguientes: $\Sigma_c^{++} \to \Lambda_c^+\pi^+$, $\Sigma_c^0 \to \Lambda_c^+\pi^-$, $\Lambda_c^{*+} \to \Lambda_c^+\pi^+\pi^-$ y $D^{*\pm} \to D^0\pi^\pm$.

Las diferencias entre los valores Q medidos por CDF y los listados en el PDG se representaron en el eje de abscisas de una gráfica, poniendo los valores Q medidos por CDF en el eje de abscisas. La distribución resultante se ajustó a una línea recta. La incertidumbre sistemática de cada estado $\Sigma_b^{(*)}$ debida a la escala de momentos se extrajo evaluando esta función en cada uno de los valores Q de los estados $\Sigma_b^{(*)}$.

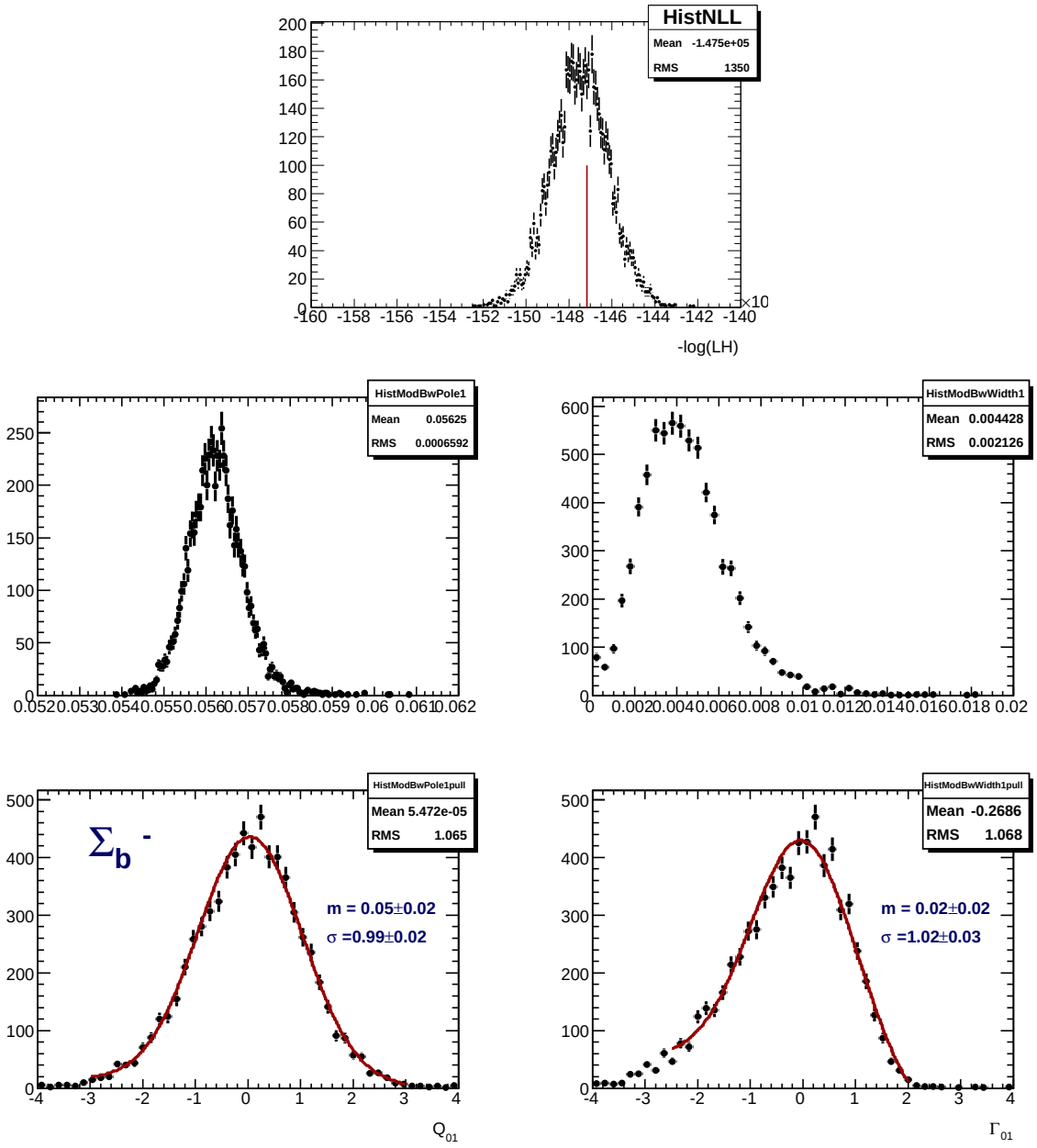

Figure F.2: *La figura de arriba muestra la distribución del NLL resultado de ajustar 7000 pesudoexperimentos para Σ_b^-. Las dos siguientes figuras muestran las distribuciones de los valores medidos de Q_{01}, GeV/c^2 y Γ_{01} GeV/c^2. Las dos figuras de abajo muestran los pulls de estas dos variables.*

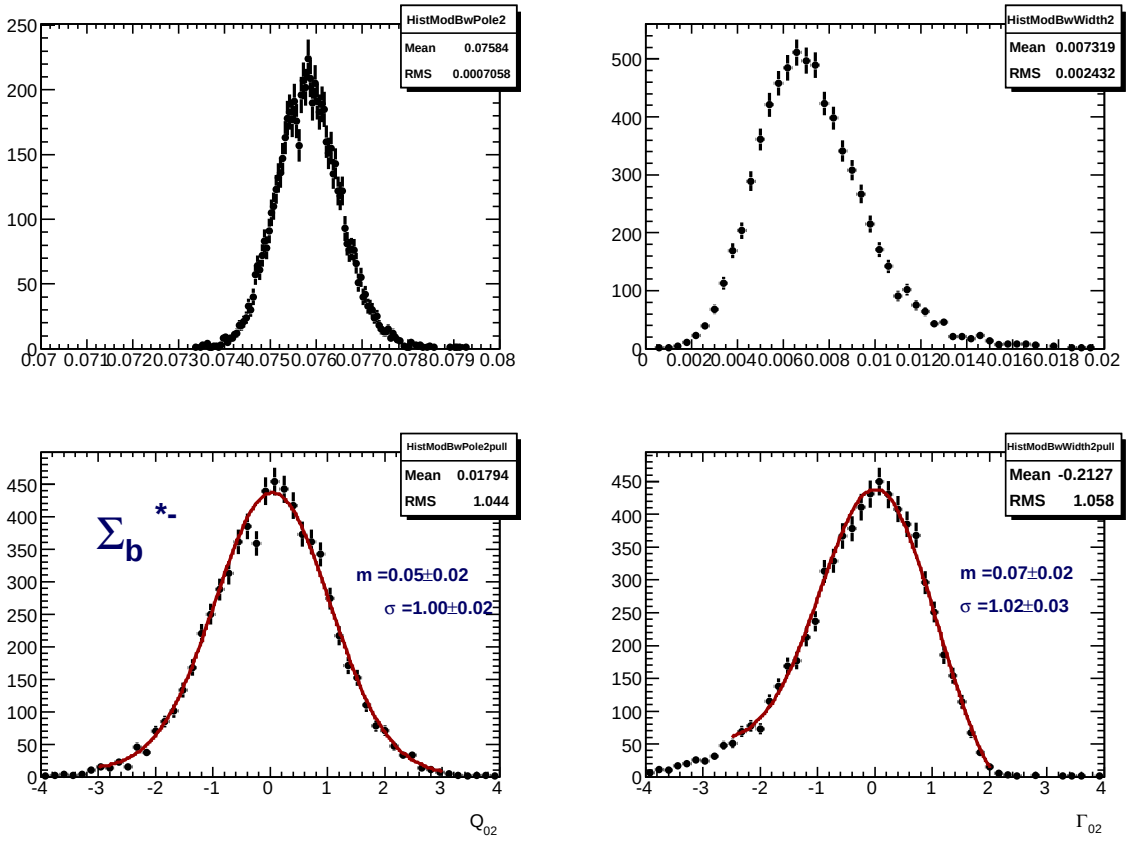

Figure F.3: *Resultados de los tests realizados al modelo de ajuste para los parḿetros* Q_{02}, GeV/c^2 *y* Γ_{02} GeV/c^2 *de* Σ_b^{*-}. *Las dos figuras de arriba muestran las distribuciones de los valores medidos para estos parḿetros, y las dos figuras de abajo mustran sus pulls.*

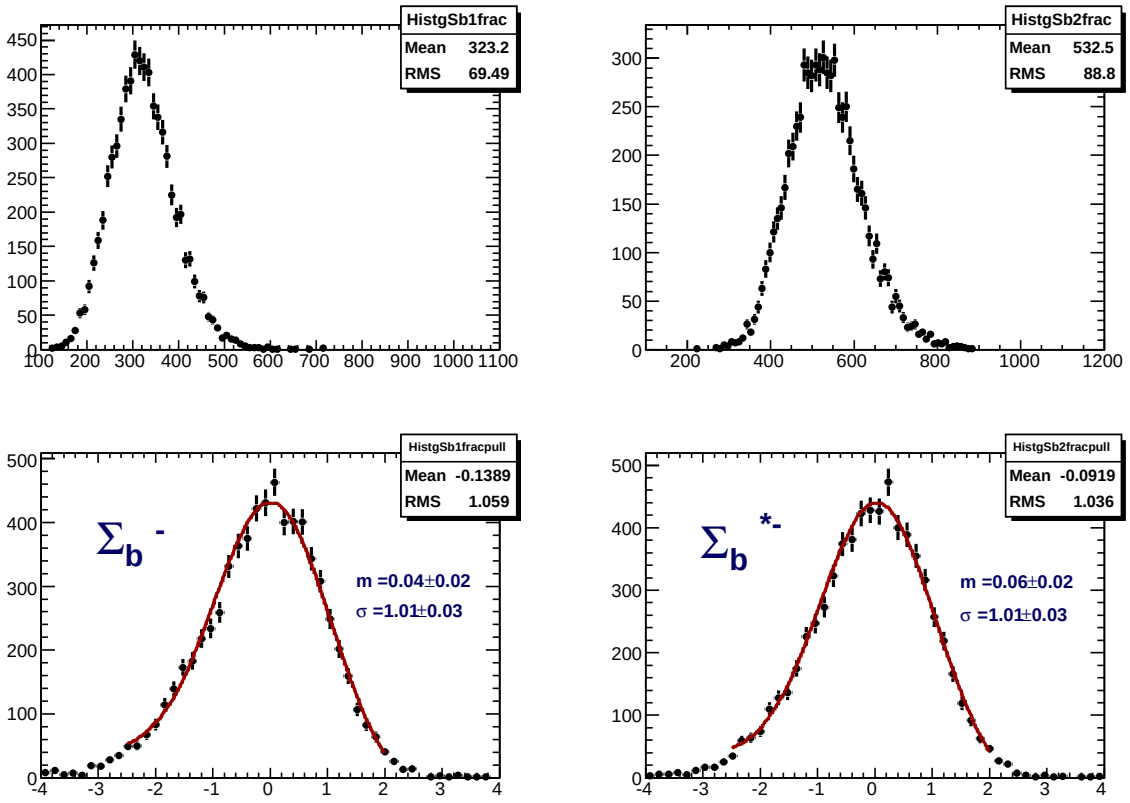

Figure F.4: *Las figuras muestran los valores medidos y sus pulls para los paramétros* N_{s1} *and* N_{s2} *para* Σ_b^{*-}.

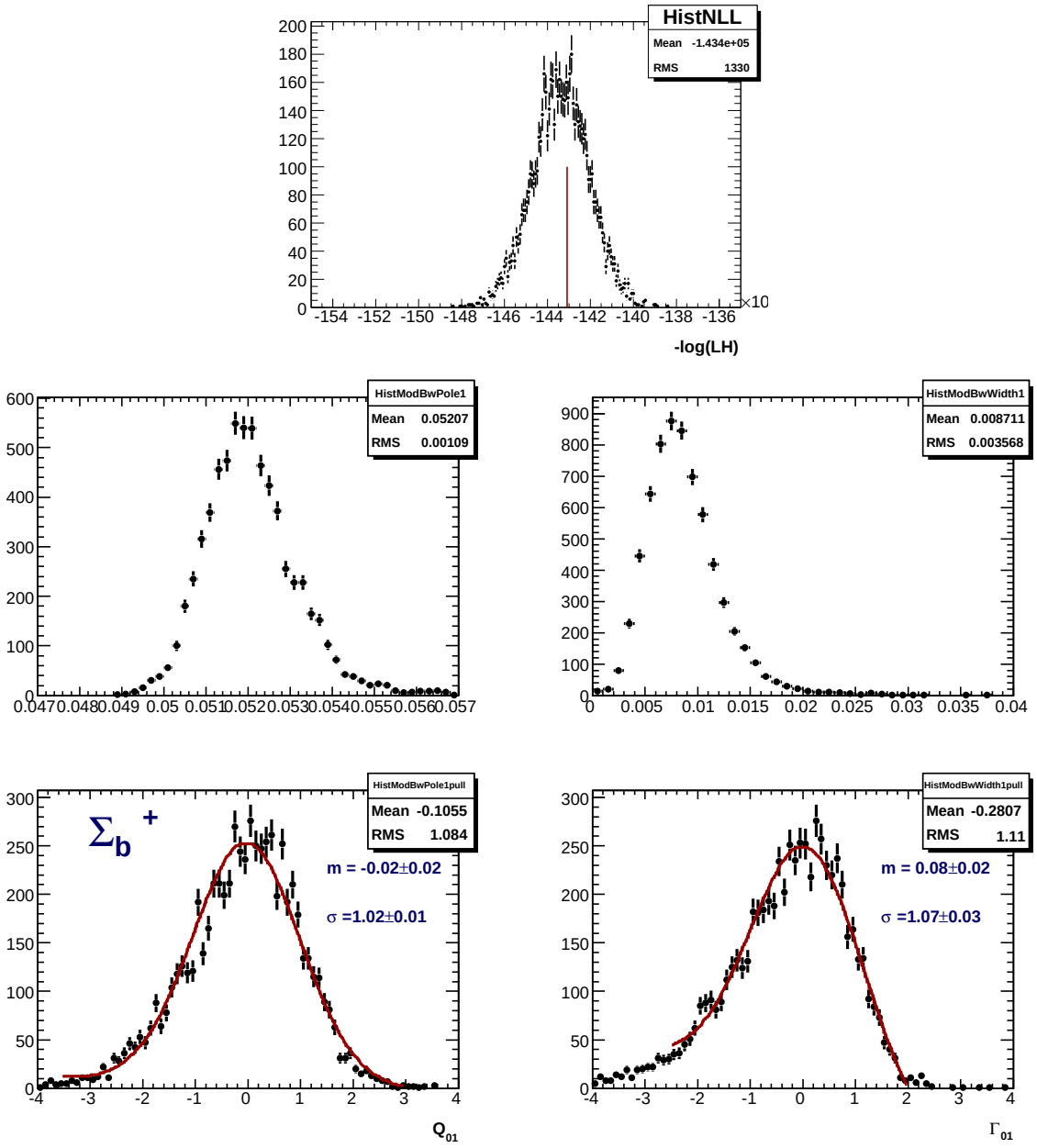

Figure F.5: *La figura de arriba muestra la distribución del NLL resultado de ajustar 7000 pesudoexperimentos para Σ_b^+. Las dos siguientes figuras muestran las distribuciones de los valores medidos de Q_{01}, GeV/c^2 y Γ_{01} GeV/c^2. Las dos figuras de abajo muestran los pulls de estas dos variables.*

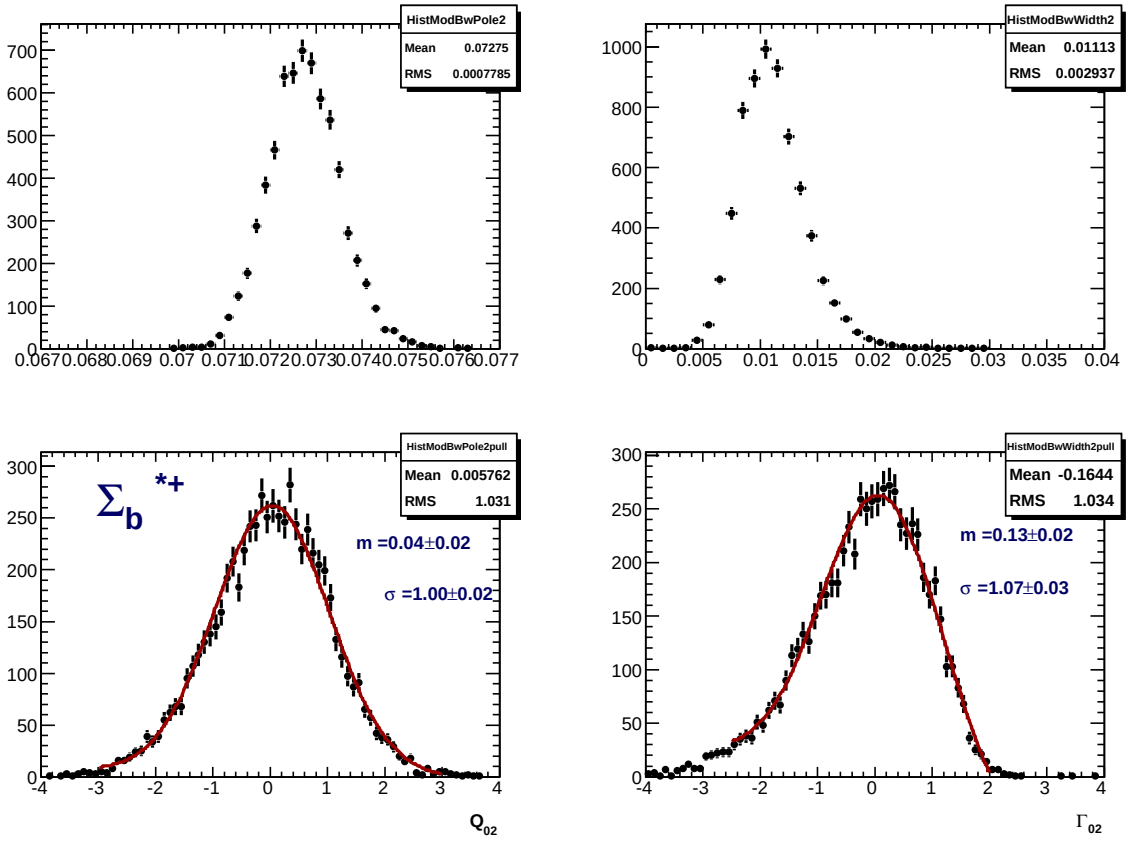

Figure F.6: *Resultados de los test realizados al modelo de ajuste para los parḿetros* Q_{02}, GeV/c^2 *y* Γ_{02} GeV/c^2 *de* Σ_b^{*+}. *Las dos figuras de arriba muestran las distribuciones de los valores medidos para estos parḿetros, y las dos figuras de abajo mustran sus pulls.*

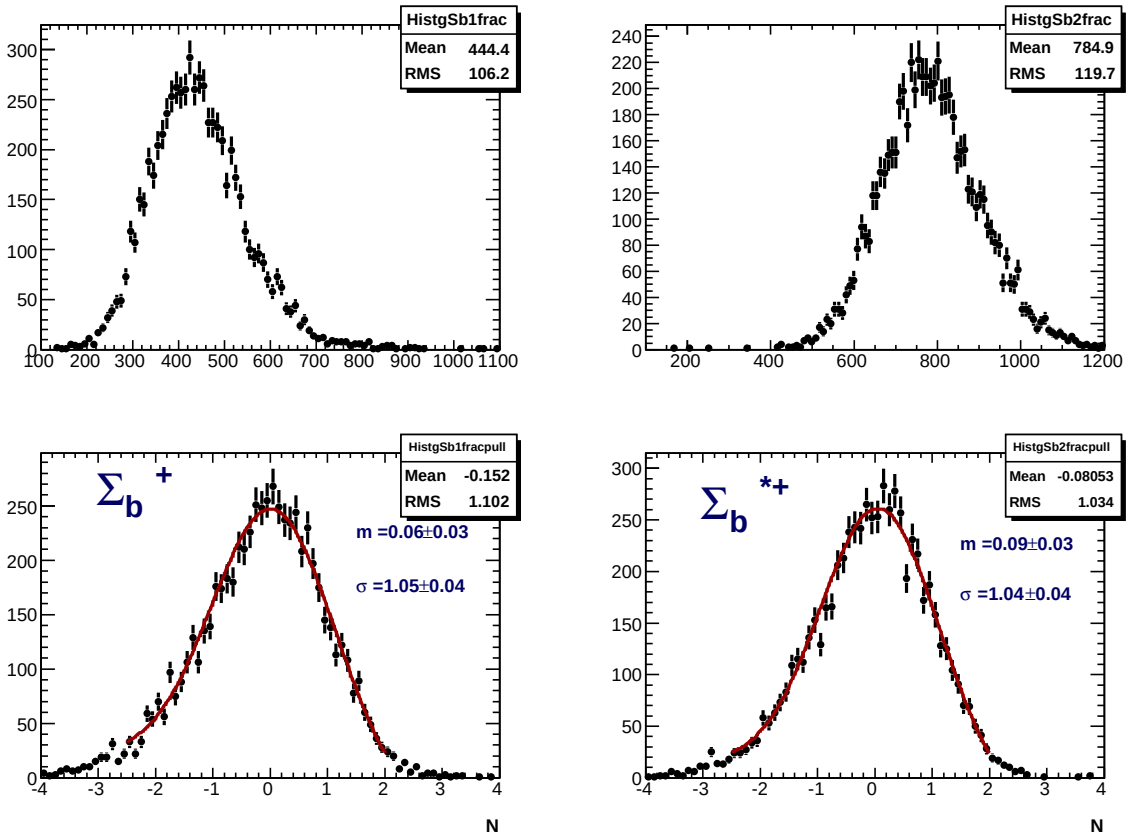

Figure F.7: *Las figuras muestran los valores medidos y sus pulls para los paramétros N_{s1} and N_{s2} para Σ_b^{*+}.*

El efecto de la incertidumbre en la escala de momentos sobre la medida de la anchura de los estados $\Sigma_b^{(*)}$ también fue consideraba. Se estudió la distribución de la variable Q en la desintegración $D^{*\pm} \to D^0\ \pi^\pm$ para rangos diferentes del momento transversal del pion. Se ajustaron las señales con distribuciones de Breit-Wigner convolucionadas con distribuciones de Gauss describiendo la resolución del detector. Todos los valores medidos de la anchura natural fueron menores que 0.2 MeV/c^2, que es el valor que tomamos como error sistemático.

F.4.3 Efecto de las asunciones en el modelo de ajuste

En el modelo de ajuste, los parámetros describiendo la resolución del detector se mantienen fijos a valores extraidos de simulación. El efecto sobre las medidas de la incertidumbre en estos parámetros se estudió mediante la generación y posterior ajuste de múltiples pseudoexperimentos.

El efecto en las medidas debido al modelo asumido para el fondo de la desintegración se estimó generando múltiples pseudoexperimentos usando un modelo alternativo para describir el fondo de la desintegración. Las muestras fueron ajustadas con el procedimiento base y con el modelo alternativo usado para generlas para estimar el error sistemático.

F.4.4 Resumen errores sistemáticos

Para obtener la incertidumbre sistemática total de nuestras medidas se extrajo la raíz cuadrada de la suma cuadrática de las incertidumbres sistemáticas.

- Para la medida de los valores Q, la incertidumbre sistemática dominante es la debida a la incertidumbre en la escala de masas.
- Para la medida de las anchuras, la incertidumbre dominante es la debida a la resolución del detector.

Tabla F.4 resume los errores sistemáticos del análisis.

F.5 Resultados

Los valores Q medidos para los estados $\Sigma_b^{(*)\pm}$ son los siguientes:

- $m(\Sigma_b^+) - m(\Lambda_b^0) - m(\pi) = 52.0^{+0.9}_{-0.8}\,(\text{stat})^{+0.09}_{-0.4}\,(\text{syst})\,\text{MeV}/c^2$
- $m(\Sigma_b^-) - m(\Lambda_b^0) - m(\pi) = 56.2^{+0.6}_{-0.5}\,(\text{stat})^{+0.07}_{-0.4}\,(\text{syst})\,\text{MeV}/c^2$
- $m(\Sigma_b^{*+}) - m(\Lambda_b^0) - m(\pi) = 72.7 \pm 0.7\,(\text{stat})^{+0.12}_{-0.6}\,(\text{syst})\,\text{MeV}/c^2$
- $m(\Sigma_b^{*-}) - m(\Lambda_b^0) - m(\pi) = 75.7 \pm 0.6\,(\text{stat})^{+0.08}_{-0.6}\,(\text{syst})\,\text{MeV}/c^2$

Signal Parameter	Escala masas	Procedimiento	Res.	Fondo	Total	%
Σ_b^+ Q, MeV/c^2			0.07	0.05	0.09	0.2
	-0.35		-0.12	-0.05	-0.37	1
Σ_b^+ Γ, MeV/c^2	0.20		0.94	0.40	1.04	11
	-0.20	-0.38	-0.89	-0.40	-1.07	12
Σ_b^+ events			16	9	18	4
			-11	-9	-15	3
Σ_b^- Q, MeV/c^2			0.05	0.04	0.07	0.1
	-0.38		-0.07	-0.04	-0.39	1
Σ_b^- Γ, MeV/c^2	0.20		0.85	0.50	1.01	23
	-0.20	-0.27	-0.87	-0.50	-1.06	25
Σ_b^- events			9	34	35	11
			-8	-34	-35	10
Σ_b^{*+} Q, MeV/c^2			0.06	0.10	0.12	0.2
	-0.52		-0.13	-0.10	-0.55	1
Σ_b^{*+} Γ, MeV/c^2	0.20		0.64	0.50	0.83	8
	-0.20	-0.29	-1.01	-0.50	-1.18	11
Σ_b^{*+} events			7	24	25	3
			-13	-24	-27	4
Σ_b^{*-} Q, MeV/c^2			0.06	0.06	0.08	0.1
	-0.56		-0.08	-0.06	-0.57	1
Σ_b^{*-} Γ, MeV/c^2	0.20		0.65	0.30	0.74	12
	-0.20	-0.23	-0.96	-0.30	-1.05	16
Σ_b^{*-} events			7	28	29	6
			-8	-28	-29	6

Table F.4: Resumen de los errores sistemáticos. Para cada parámetro, se listan cada uno de los errores sistemáticos en el orden siguiente: escala de masas, procedimiento, resolución del detector y modelo asumido para describir el fondo. El error sistemático total se obtiene extrayendo la raíz cuadrada de la suma cuadrática de todos los errores. La última columna muestra el tanto por ciento del error sistemático total sobre la medida.

De estos valores Q extraemos las diferencias isotópicas de masas entre compañeros dentro de los dos isotripletes. $J^P = \frac{1}{2}^+$ and $J^P = \frac{3}{2}^+$:

- $m(\Sigma_b^+) - m(\Sigma_b^-) = -4.2^{+1.1}_{-0.9}\,(\text{stat})^{+0.07}_{-0.09}\,(\text{syst})\ \text{MeV}/c^2$
- $m(\Sigma_b^{*+}) - m(\Sigma_b^{*-}) = -3.0 \pm 0.9\,(\text{stat})^{+0.12}_{-0.13}\,(\text{syst})\ \text{MeV}/c^2$

donde la incertidumbre estadística es la raíz cuadrada de la suma cuadrática de las incertidumbres estadísticas.

Para obtener la incertidumbre sistemática se suman cuadráticamente las diferencias en los errores sistemáticos entre ambos compañeros del isotriplete, menos para la incertidumbre en el modelo de fondo, que se suma cuadráticamente sin hacer la diferencia. La raíz cuadrada de esta suma es el error sistemático total.

Medimos las siguientes anchuras naturales para los estados:

- $\Gamma(\Sigma_b^+) = 9.2^{+3.8}_{-2.9}\,(\text{stat})^{+1.0}_{-1.1}\,(\text{syst})\ \text{MeV}/c^2$
- $\Gamma(\Sigma_b^-) = 4.3^{+3.1}_{-2.1}\,(\text{stat})^{+1.0}_{-1.1}\,(\text{syst})\ \text{MeV}/c^2$
- $\Gamma(\Sigma_b^{*+}) = 10.4^{+2.7}_{-2.2}\,(\text{stat})^{+0.8}_{-1.2}\,(\text{syst})\ \text{MeV}/c^2$
- $\Gamma(\Sigma_b^{*-}) = 6.4^{+2.2}_{-1.8}\,(\text{stat})^{+0.7}_{-1.1}\,(\text{syst})\ \text{MeV}/c^2$

Para pasar de valores Q a masas absolutas, añadimos la masa del pion [17] y el valor de CDF para la masa del Λ_b^0, $m(\Lambda_b^0) = 5619.7 \pm 1.2\,(\text{stat}) \pm 1.2\,(\text{syst})\ \text{MeV}/c^2$ [81]. El error en la masa del Λ_b^0 se incluye en el error sistemático. Las masas absolutas resultantes son:

- $m(\Sigma_b^+) = 5811.2^{0.9}_{-0.8}\,(\text{stat}) \pm 1.7\,(\text{syst})\,\text{MeV}/c^2$
- $m(\Sigma_b^-) = 5815.5^{+0.6}_{-0.5}\,(\text{stat}) \pm 1.7\,(\text{syst})\,\text{MeV}/c^2$
- $m(\Sigma_b^{*+}) = 5832.0 \pm 0.7\,(\text{stat}) \pm 1.8\,(\text{syst})\,\text{MeV}/c^2$
- $m(\Sigma_b^{*-}) = 5835.0 \pm 0.6\,(\text{stat}) \pm 1.8\,(\text{syst})\,\text{MeV}/c^2$

Las Figuras F.8 y F.9 muestran las distribuciones del valor Q para los estados $\Sigma_b^{(*)\pm}$ con el resultado del ajuste superimpuesto.

F.6 Conclusiones

En esta tesis se describe la medida de los bariones pesados $\Sigma_b^{(*)\pm}$ usando una muestra de ~ 16300 Λ_b^0 candidatos identificados en el modo de desintegración $\Lambda_b^0 \to \Lambda_c^+\pi^-$. La muestra corresponde a una luminosidad integrada de $6\,\text{fb}^{-1}$.

Se ha confirmado la primera observación de estos estados hecha por la Colaboración CDF [3]. Cada una de las señales se ha reconstruido con una significancia de $\gtrsim 7\sigma$ en términos gaussianos.

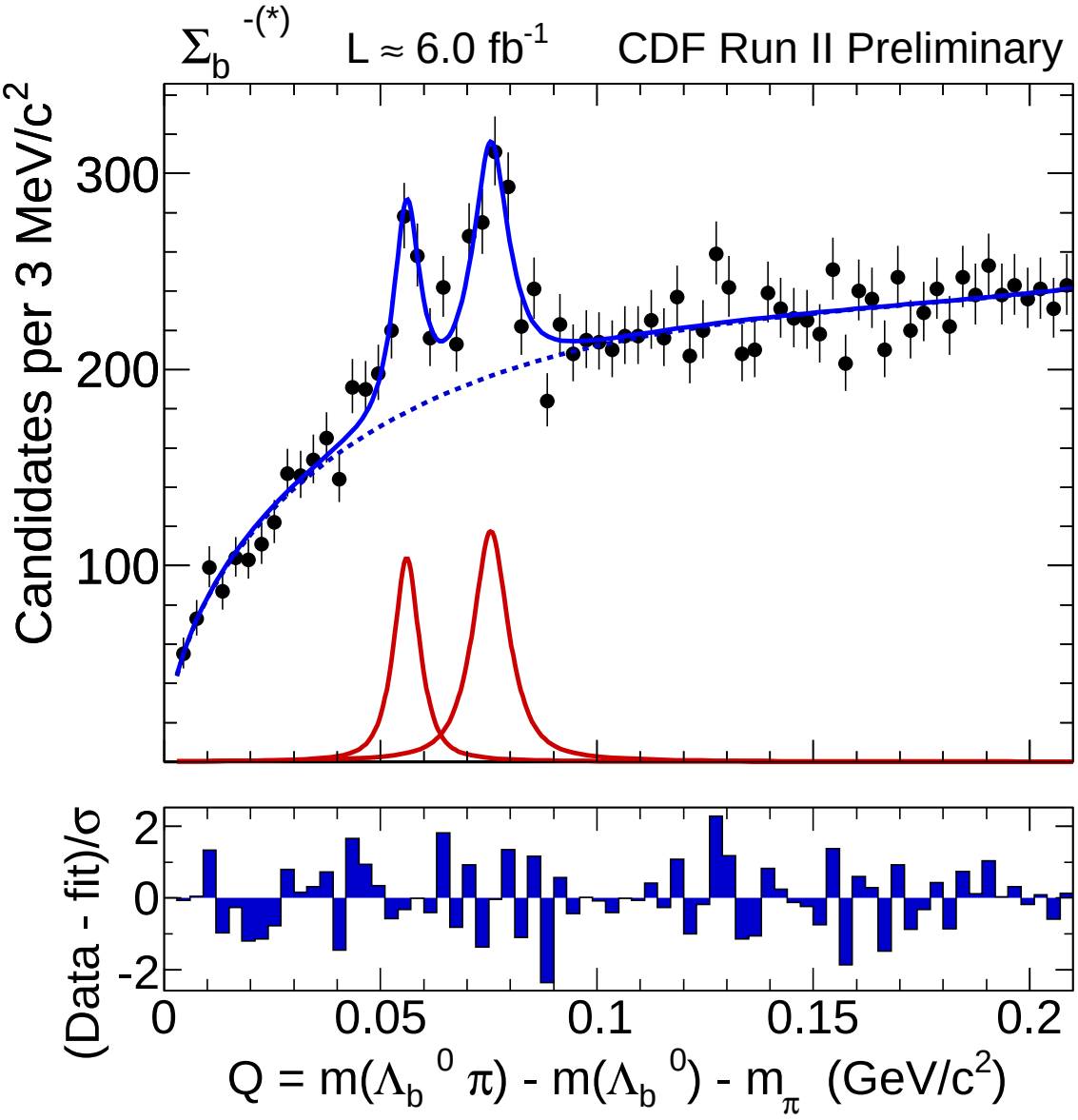

Figure F.8: *Candidatos $\Sigma_b^{(*)-}$: espectro en la variable Q, donde $Q = M(\Lambda_b^0\pi^-) - M(\Lambda_b^0) - m_\pi$, con el resultado del ajuste no binado superimpuesto*

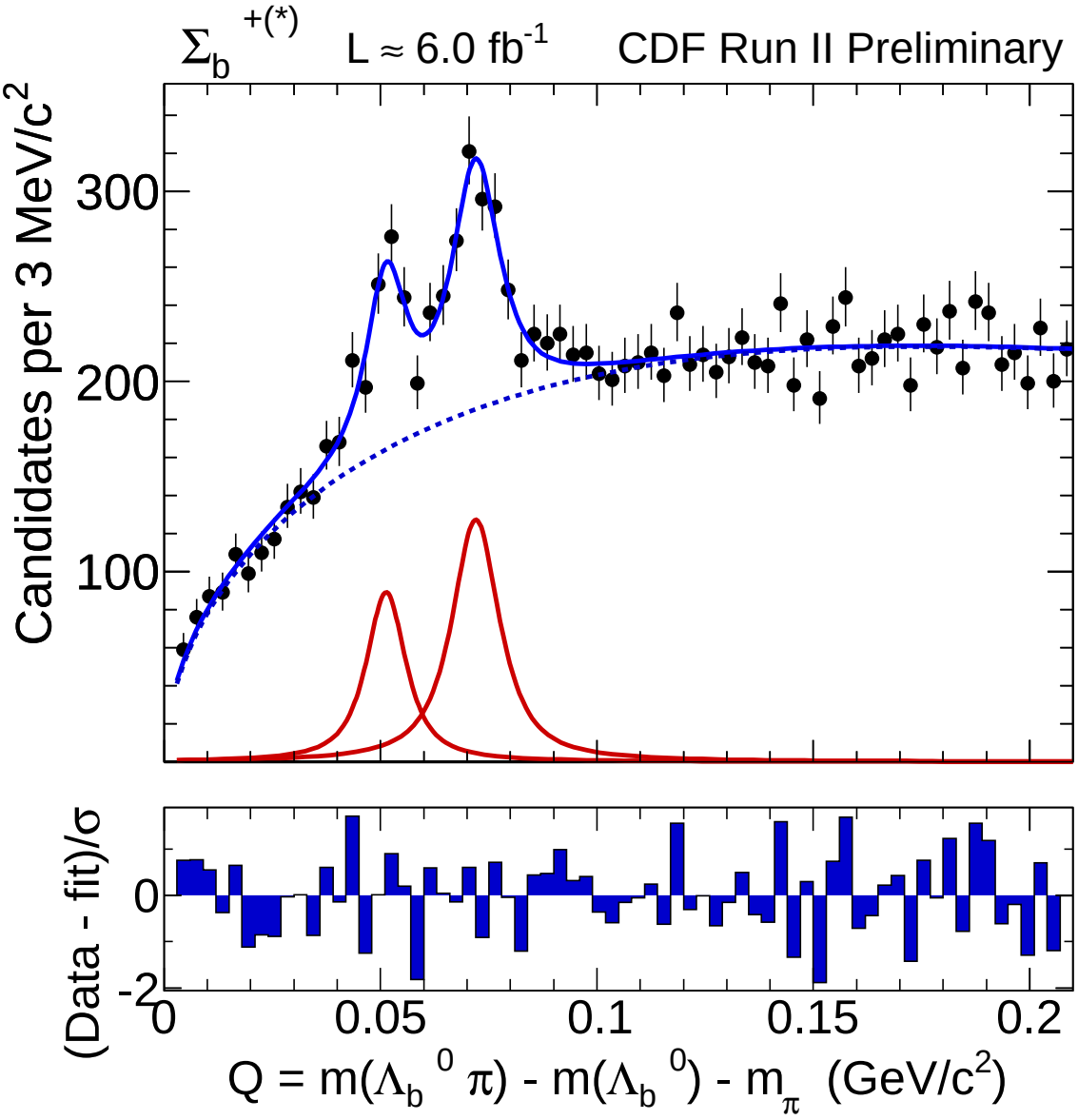

Figure F.9: *Candidatos $\Sigma_b^{(*)+}$: espectro en la variable Q, donde $Q = M(\Lambda_b^0\pi^-) - M(\Lambda_b^0) - m_\pi$, con el resultado del ajuste no binado superimpuesto*

La medida de las diferencias de masa (valors Q) presenta una precisión estadística un factor $\gtrsim 2.3$ mejor con respecto al análisis anterior [3], en concordancia con la cantidad de estaística disponible. Los valores Q medidos son consistentes con los observados en el descubrimiento [3].

Se han extraido por primera vez las diferencias isotópicas de masas dentro de los dos isotripletes $I = 1$ (Σ_b and Σ_b^*), con una precisión comparable a la que se muestra en el PDG [17] para los estados Σ_c. Los estados $\Sigma_b^{(*)-}$ muestran masas mayores que los estados $\Sigma_b^{(*)+}$ siguiendo un conocido patrón [84] en los multipletes de isospin, contrariamente a lo que se observa en sus análogos Σ_c, donde no se verifica este supuesto orden natural de las masas [82].

Se han medido por primera vez las anchuras naturales de desintegración de estos estados. Las anchuras medidas están de acuerdo con las predicciones teóricas (see Table 1.2).

Bibliography

[1] N. Isgur and M.B. Wise, *Phys. Lett.* **B232** (1989) 113, **B237** (1990) 527; H. Georgi, *Phys. Lett.* **B240** (1990) 447; N. Isgur and M.B. Wise, *Phys.* **D42**, 2388 (1990); N. Isgur and M.B. Wise, *Phys. Lett.* **66**, 1130 (1991); N. Isgur and M.B. Wise, *Nucl. Phys.* **B348**, 276 (1991).

[2] M. Neubert, Phys. Rept. **245**, 259 (1994) [arXiv:heo-ph/9306320]; A.V. Manohar and M.B. Wise, *Camb. Monogr. Part. Phys. Nucl. Phys. Cosmol.* **10**, 1 (2000).

[3] T. Aaltonen *et al.* [CDF Collaboration], *Phys. Rev. Lett.* **99**, 202001 (2007) [arXiv:0706.3868 [hep-ex]].

[4] C. Albertus, J. E. Amaro, E. Hernandez and J. Nieves, *Nucl. Phys.* **A740**, 333 (2004) [arXiv:nucl-th/0311100].

[5] D. Ebert, R. N. Faustov and V. O. Galkin, *Phys. Rev.* **D72**, 034026 (2005) [arXiv:hep-ph/0504112].

[6] D. Ebert, R. N. Faustov and V. O. Galkin, *Phys. Lett.* **B659**, 612 (2008) [arXiv:0705.2957 [hep-ph]].

[7] S. Capstick and N. Isgur, *Phys. Rev.* **D34**, 2809 (1986).

[8] E. E. Jenkins, *Phys. Rev.* **D54** (1996) 4515, **D55** (1997) R10, **D77** (2008) 034012.

[9] R. Roncaglia, D. B. Lichtenberg and E. Predazzi, *Phys. Rev.* **D52**, 1722 (1995) [arXiv:hep-ph/9502251].

[10] M. Karliner and H. J. Lipkin, *Phys. Lett.* **B660**, 539 (2008) [arXiv:hep-ph/0611306].

[11] I. M. Narodetskii, C. Semay and A. I. Veselov, *Eur. Phys. J.* **C55**, 403 (2008) [arXiv:0801.4270 [hep-ph]].

[12] H. Garcilazo, J. Vijande and A. Valcarce, *J. Phys.* **G34**, 961 (2007) [arXiv:hep-ph/0703257].

[13] J. R. Zhang and M. Q. Huang, *Phys. Rev.* **D77**, 094002 (2008) [arXiv:0805.0479 [hep-ph]].

[14] R. Lewis and R. M. Woloshyn, *Phys. Rev.* **D79**, 014502 (2009) [arXiv:0806.4783 [hep-lat]].

[15] A.D. Martin F. Halzen. *Quarks and Leptons: An Introductory Course in Modern Particle Physics.* Wiley Text Books, 1984.

[16] Y. Fukuda *et al.* [Super-Kamiokande Collaboration] *Phys. Rev. Lett.* **81**, 1562-1567 (1998) [arXiv:9807003 [hep-ex]].

[17] C. Amsler *et al.* [Particle Data Group], *Phys. Lett.* **B667**, 1 (2008) (URL: http://pdg.lbl.gov).

[18] G. 't Hooft, *Nucl. Phys.* **B72** (1974) 461; E. Witten, *Nucl. Phys.* **B160** (1979) 57; S. Coleman, in Aspects of Symmetry (Cambridge University Press, Cambridge, 1989).

[19] R. F. Dashen, E. E. Jenkins and A. V. Manohar, *Phys. Rev.* **D49** (1994) 4713.

[20] E. E. Jenkins and R. F. Lebed, *Phys. Rev.* **D52** (1995) 282.

[21] X. Liu, H. X. Chen, Y. R. Liu, A. Hosaka and S. L. Zhu, *Phys. Rev.* **D77**, 014031 (2008) [arXiv:0710.0123 [hep-ph]].

[22] N. Mathur, R. Lewis and R. M. Woloshyn, *Phys. Rev.* **D66**, 014502 (2002) [arXiv:hep-ph/0203253].

[23] Fermilab Beam Division. Run II Handbook. http://www-bd.fnal.gov/runII/index.html.

[24] R.Blair, *et al.*, The CDF II Detector Technical Design Report, FERMILAB-Pub-96/390-E, November, 1996.

[25] D. Acosta *et al.* [CDF Collaboration], "Measurement of the J/ψ meson and b-hadron production cross sections in $p\overline{p}$ collisions at $\sqrt{s} = 1960$ GeV", Phys. Rev. D **71**, 032001 (2005) [arXiv:hep-ex/0412071].

[26] Fermilab Beam Division. http://www-bd.fnal.gov.

[27] C.W.Schmidth, The Fermilab 400-MeV Linac upgrade, FERMILAB-CONF-93/111(1993).

[28] J. Marriner, Stochastic Cooling Overview, FERMILAB-CONF-03/158 (2003).

[29] http://www-bdnew.fnal.gov/operations/rookie_books/rbooks.html

[30] CDF Collaboration, F. Abe *et al.*,"The CDF Detector: An Overview", *Nucl. Instr. Meth.* **A271** (1988), 387-403.

[31] F. Abe *et al.* [CDF Collaboration],"Measurement of the W-boson mass", *Phys. Rev.* **D52** (1995), 4784-4827.

[32] R. Wagner et. al, "CDF Central Outer Tracker", *CDF internal Note* **6227** (2002), 6267 (2003).

[33] W.Riegler et. at, "COT Detector Physics Simulations", *CDF internal Note* **5050** (2000).

[34] A. Sill, *Nucl. Instrum. Meth.* **A447**, 1 (2000).

[35] D. Amidei *et al.*, *Nucl. Instrum. Meth.* **A350**, 73 (1994); S. Cihangir E_T et al., *Nucl. Instrum. Meth.* **A360**, 137 (1995).

[36] S. Leone for the ISL group, "The Intermediate silicon Layers (ISL) Detector for the Collider Detector at Fermilab", CDF internal Note 5129 (1999).

[37] The CDF II Collaboration, Proposal for Enhancement of the CDF II Detector: "An Inner Silicon Layer and A time Of Flight Detector", Fermilab-Proposal-909, presented to the Fermilab Director and PAC, October, 1998.

[38] M. Bishai *et al.*,"An SVX3D Chip User's Companion", CDF internal Note 5062 (1999).

[39] A. Bardi *et al.*, *Nucl. Instrum. Meth.* **A409**, 658 (1998).

[40] W.Ashmanskas *et al.*, "The CDF Silicon Vertex Tracker", FERMILAB-CONF-00/238-E.

[41] W.Ashmanskas *et al.*, "The CDF Silicon Vertex Trigger", FERMILAB-CONF-03/198-E.

[42] W.Ashmanskas *et al.*, 'Performance of the CDF Online Silicon Vertex Tracker", IEEE Trans. *Nucl. Sci.*, **49**, 1177-1184 (2002).

[43] J. Antos *et al.*, *Nucl. Instrum. Meth.* **A383**, 13 (1996), **A360**, 118 (1995). M. Garcia-Sciveres *et al.*, *Nucl. Instrum. Meth.* **A435**, 58 (1999).

[44] P Gatti, COT Integrated Tracking, http://www-cdf.fnal.gov/internal/ people/links/PaoloGatti/my.html

[45] K.Bloom, Outside-In Tracking Description, http://www-cdf.fnal.gov/upgrades/ computing/projects/reconstruction/tracking/user-docs/OIoverview.html

[46] C.M. Ginsburg *Eur. Phys. J. C33*, s1002-s1004 (2004).

[47] C. Grozis *et al.*, "The Time-of-Flight Detector for CDF", *Nucl. Phys. Proc. Suppl.* vol. **47** (2001) 344; *Int. J. Mod. Phys.* **A16S1C** (2001) 1119; G.Gomez for the TOF group, "The CDF-II Time of Flight Detector", CDF internal Note 6258 (2003).

[48] D. Acosta *et al. Nucl. Instrum. Method.* **A461**, 540-544 (2001).

[49] David Saltzberg, "Run-II Trigger Table and Datasets Plan", *CDF internal Note* **4718** (1998).

[50] J. Gartner *et al.*, "The Performance of the XFT in Run II", *CDF internal Note* **6766** (2003).

[51] E.J.Thompson et. al, "Online Track Processor for the CDF Upgrade", IEEE Transactions on Nuclear Science, 49 No. 3, (2002).

[52] A. Belloni, I. K. Furić, and C. Paus, "Multibody Trigger Paths in the Two Track Trigger Data", CDF Note 6526 (2003).

[53] M. Campanelli and E. Gerchtein, "Calibration of the momentum scale for Kalman reffiter using J/ψ events", *CDF internal Note* **6905** (2004).

[54] S. Menzemer, "TrackingKal-A Tracking and Alignment Software Package for the CDF II Silicon Detector", *CDF internal Note* **5968** Rev.4 (2003).

[55] J. Marriner, "Secondary Vertex Fit with Mass and Pointing Constraints (CTVMFT)", *CDF internal Note* **1996** (1993).

[56] http://www-cdf.fnal.gov/htbin/twiki/bin/view/BStntuples/WebHome.

[57] P. Sphicas, "A $b\bar{b}$ Monte Carlo Generator", *CDF internal Note* **2655** (1994); K. Anikeev, C. Paus, and P. Murat, "Description of Bgenerator II: Bgenerator in its Run II Incarnation", *CDF internal Note* **5092** (1999).

[58] A. Heiss, *et. al.*, "A new measurement of exclusive B lifetimes using Run 1 data", CDF note 5331.

[59] K.Anikeev, *et. al.*, "Calibration of Energy Loss and Magnetic Field using J/psi Events in Run II", CDF note 5958.

[60] K.Anikeev, *et. al.*, "The Inclusive B Lifetime using Run II Data at CDF", CDF note 6023.

[61] J. Boudreau *et al.*, "Yields and cut optimization for $B^{\pm} \to J/\psi K^{\pm}, J/\psi \to \mu^{+}\mu^{-}$, CDF note 6226.

[62] P. Sphicas "A $b\bar{b}$ Monte Carlo Generator", CDF/DOC/BOTTOM/CDFR/2655

[63] K. Anikeev, Christoph Paus, Pasha Murat, "Description of Bgenerator II", *CDF internal Note* **5092**

[64] J.D. Lewis P. Avery, "Cleomc: The CDF interface to the CLEO monte carlo (QQ)", *CDF internal Note* **2724**

[65] K. Anikeev, A. Korn, Ch. Paus "Generator Level Dimuon Trigger Simulation" *CDF internal Note* **5686**

[66] L. Demortier and L. Lyons, "Everything you always wanted to know about pulls", *CDF internal Note* **5776**.

[67] Ray Culbertson, private communication.

[68] I.Gorelov, S.Seidel, E.Vataga, "Measurement of Properties of the Bottom Baryon Resonances Σ_b and Σ_b^*", *CDF internal Note* **9076**

[69] Arkady Bolshov, Igor Gorelov, Christoph Paus, Sally Seidel, Elena Vataga, "Search for Σ_b Using the Two Track Trigger Dataset", *CDF internal Note* **8166**

[70] I.Gorelov, D.Litvintsev, P.Maksimovic, M.Martin, J.Pursley, M.Schmidt, S.Seidel, R.J.Tesarek, E.Vataga, "Search for New Heavy Baryons Σ_b and Σ_b^* in the Two Track Trigger Data Using $1\,\mathrm{fb}^{-1}$", *CDF internal Note* **8396**.

[71] The CDF Collaboration, Observation of New Heavy Baryons Σ_b and Σ_b^*, *CDF internal Note* **8523**

[72] Shin-Shan Yu, Rick Tesarek, Dmitri Litvintsev, Joel Heinrich, Nigel Lockyer, "Ratio of $\mathcal{B}(\Lambda_b^0 \to \Lambda_c^+ \mu^- \overline{\nu}_\mu)$ to $\mathcal{B}(\Lambda_b^0 \to \Lambda_c^+ \pi^-)$ in the Two Track Trigger", *CDF internal Note* **7559**

[73] Y. Le, M. Martin, and P. Maksimovi?c, Observation of $\Lambda_b^0 \to \Lambda_c^+ \pi_b^-$ and the Measurement of $f_{\Lambda_b^0} \cdot \mathcal{B}(\Lambda_b^0 \to \Lambda_c^+ \pi_b^-)/f_{B^0} \cdot \mathcal{B}(B^0 \to D^- \pi^+)$, *CDF internal Note* **6396**

[74] J. G. Korner, M. Kramer and D. Pirjol, "Heavy Baryons", *Prog. Part. Nucl. Phys.* **33**, 787 (1994) [arXiv:hep-ph/9406359].

[75] J. D. Jackson, *Nuovo Cim.* **34**, 1644 (1964).

[76] J. D. Jackson, Private communication, 11.06.07.

[77] M. Artuso *et al.* [CLEO Collaboration], *Phys. Rev.* **D65**, 071101 (2002) [arXiv:hep-ex/0110071].

[78] G. Brandenburg *et al.* [CLEO Collaboration], *Phys. Rev. Lett.* **78**, 2304-2308 (1997).

[79] T. J. V. Bowcock *et al.* [CLEO Collaboration], *Phys. Rev. Lett.* **62**, 1240 (1989).

[80] E. Klempt and J. M. Richard, arXiv:0901.2055 [hep-ph].

[81] D. Acosta *et al.* [CDF Collaboration] *Phys. Rev. Lett.* **96**, 202001 (2006).

[82] F. Wick (for the CDF Collaboration), "Charm baryon spectroscopy at CDF", talk at ICHEP 2010, Paris, 22-28 July 2010, to be published in the Proceedings; see also the public web page: http://www-cdf.fnal.gov/physics/new/bottom/100701.blessed-Charm_Baryons/

[83] A. Abulencia *et al.* [CDF Collaboration], "Measurement of mass and width of the excited charmed meson states D_1^0 and D_2^{*0} at CDF", *Phys. Rev.* **D73**, 051104 (2006).

[84] F.K. Guo, C. Hanhart and U.G. Meissner, *JHEP* **0809**, 136 (2008) [axVix:0809.2359 [hep-ph]].